

UNCLASSIFIED

AD NUMBER
ADB263763
NEW LIMITATION CHANGE
TO Approved for public release, distribution unlimited
FROM Distribution authorized to U.S. Gov't. agencies only; Proprietary Info.; Aug 2000. Other requests shall be referred to U.S. Army Medical Research and Materiel Command, 504 Scott St., Fort Detrick, MD 21702-5012.
AUTHORITY
USAMRMC ltr, dtd 15 May 2003

THIS PAGE IS UNCLASSIFIED

AD \_\_\_\_\_

Award Number: DAMD17-99-1-9475

TITLE: Tissue Engineering Initiative

PRINCIPAL INVESTIGATOR: Vincent C. Hascall, Ph.D.

CONTRACTING ORGANIZATION: The Cleveland Clinic Foundation  
Cleveland, Ohio 44195

REPORT DATE: August 2000

TYPE OF REPORT: Annual

PREPARED FOR: U.S. Army Medical Research and Materiel Command  
Fort Detrick, Maryland 21702-5012

DISTRIBUTION STATEMENT: Distribution authorized to U.S. Government agencies only (proprietary information, Aug 00). Other requests for this document shall be referred to U.S. Army Medical Research and Materiel Command, 504 Scott Street, Fort Detrick, Maryland 21702-5012.

The views, opinions and/or findings contained in this report are those of the author(s) and should not be construed as an official Department of the Army position, policy or decision unless so designated by other documentation.

20010301 111

## NOTICE

USING GOVERNMENT DRAWINGS, SPECIFICATIONS, OR OTHER DATA INCLUDED IN THIS DOCUMENT FOR ANY PURPOSE OTHER THAN GOVERNMENT PROCUREMENT DOES NOT IN ANY WAY OBLIGATE THE U.S. GOVERNMENT. THE FACT THAT THE GOVERNMENT FORMULATED OR SUPPLIED THE DRAWINGS, SPECIFICATIONS, OR OTHER DATA DOES NOT LICENSE THE HOLDER OR ANY OTHER PERSON OR CORPORATION; OR CONVEY ANY RIGHTS OR PERMISSION TO MANUFACTURE, USE, OR SELL ANY PATENTED INVENTION THAT MAY RELATE TO THEM.

### LIMITED RIGHTS LEGEND

Award Number: DAMD17-99-1-9475  
Organization: The Cleveland Clinic Foundation  
Location of Limited Rights Data (Pages):

Those portions of the technical data contained in this report marked as limited rights data shall not, without the written permission of the above contractor, be (a) released or disclosed outside the government, (b) used by the Government for manufacture or, in the case of computer software documentation, for preparing the same or similar computer software, or (c) used by a party other than the Government, except that the Government may release or disclose technical data to persons outside the Government, or permit the use of technical data by such persons, if (i) such release, disclosure, or use is necessary for emergency repair or overhaul or (ii) is a release or disclosure of technical data (other than detailed manufacturing or process data) to, or use of such data by, a foreign government that is in the interest of the Government and is required for evaluational or informational purposes, provided in either case that such release, disclosure or use is made subject to a prohibition that the person to whom the data is released or disclosed may not further use, release or disclose such data, and the contractor or subcontractor or subcontractor asserting the restriction is notified of such release, disclosure or use. This legend, together with the indications of the portions of this data which are subject to such limitations, shall be included on any reproduction hereof which includes any part of the portions subject to such limitations.

THIS TECHNICAL REPORT HAS BEEN REVIEWED AND IS APPROVED FOR PUBLICATION.

---

---

---

---

**REPORT DOCUMENTATION PAGE**Form Approved  
OMB No. 074-0188

Public reporting burden for this collection of information is estimated to average 1 hour per response, including the time for reviewing instructions, searching existing data sources, gathering and maintaining the data needed, and completing and reviewing this collection of information. Send comments regarding this burden estimate or any other aspect of this collection of information, including suggestions for reducing this burden to Washington Headquarters Services, Directorate for Information Operations and Reports, 1215 Jefferson Davis Highway, Suite 1204, Arlington, VA 22202-4302, and to the Office of Management and Budget, Paperwork Reduction Project (0704-0188), Washington, DC 20503

1. AGENCY USE ONLY (Leave blank)		2. REPORT DATE August 2000	3. REPORT TYPE AND DATES COVERED Annual (1 Aug 99 - 31 Jul 00)	
4. TITLE AND SUBTITLE Tissue Engineering Initiative			5. FUNDING NUMBERS DAMD17-99-1-9475	
6. AUTHOR(S) Vincent C. Hascall, Ph.D.				
7. PERFORMING ORGANIZATION NAME(S) AND ADDRESS(ES) The Cleveland Clinic Foundation Cleveland, Ohio 44195  E-MAIL: hascall@bme.ri.ccf.org			8. PERFORMING ORGANIZATION REPORT NUMBER	
9. SPONSORING / MONITORING AGENCY NAME(S) AND ADDRESS(ES)  U.S. Army Medical Research and Materiel Command Fort Detrick, Maryland 21702-5012			10. SPONSORING / MONITORING AGENCY REPORT NUMBER	
11. SUPPLEMENTARY NOTES Report contains color graphics.				
12a. DISTRIBUTION / AVAILABILITY STATEMENT Distribution authorized to U.S. Government agencies only (proprietary information, Aug 00). Other requests for this document shall be referred to U.S. Army Medical Research and Materiel Command, 504 Scott Street, Fort Detrick, Maryland 21702-5012.				12b. DISTRIBUTION CODE
13. ABSTRACT ( <i>Maximum 200 Words</i> )  <p>The Cleveland Clinic Foundation Tissue Engineering Initiative was proposed to initiate novel tissue engineering projects as a collaboration between connective tissue biochemists, bioengineers, prototype engineers and physician researchers from the Department of Biomedical Engineering. The primary focus of these projects was to test applications of gels consisting of purified hyaluronan, covalently crosslinked by di-vinyl sulfone (hylans). The gel formulations tested were obtained via collaboration with Biomatrix, Inc. During the first year of this project, considerable effort has been expended evaluating the biochemical makeup of these gels, as well as their biomechanical properties. Additionally, a set of experiments was designed to evaluate the ability of cells to attach to the gels and proliferate. It was found that untreated gels did not support good cell attachment. However, when surface coated with cell adhesion proteins (collagen I, extracellular matrix (ECM) gel, laminin, fibronectin), cells attach and proliferate actively. The mechanical property evaluations and cell attachment studies show properties necessary for the use of hylans as substrates for the development of tissue engineered cell-hylan composites. However, current hylan formulations have demonstrated some limitations to the proposed applications. Methods are currently under investigation to improve the properties of hylans to better suit the proposed tissue engineering applications.</p>				
14. SUBJECT TERMS  hylan, hyaluronan, matrix, bone, epidermis, tendon, endothelium			15. NUMBER OF PAGES 373	16. PRICE CODE
17. SECURITY CLASSIFICATION OF REPORT Unclassified	18. SECURITY CLASSIFICATION OF THIS PAGE Unclassified	19. SECURITY CLASSIFICATION OF ABSTRACT Unclassified	20. LIMITATION OF ABSTRACT Unlimited	

NSN 7540-01-280-5500

Standard Form 298 (Rev. 2-89)  
Prescribed by ANSI Std. Z39-18  
298-102

## Table of Contents

Cover.....	1
SF 298.....	2
Introduction.....	4
Body.....	5
Key Research Accomplishments.....	59
Reportable Outcomes.....	60
Conclusions.....	61
References.....	62
Appendices.....	64

## INTRODUCTION

---

As stated in the initial proposal, the Department of Biomedical Engineering has proposed investigation of a novel biomaterial, crosslinked hyaluronan (hylan), as a substrate for cells involved in the formation and maintenance of the matrix of soft tissues (*i.e.* vascular, tendon, and epidermal tissues). This task has been undertaken by a multidisciplinary team with expertise in biomaterials science, cellular and molecular biology, connective tissue biochemistry, structural engineering, biomechanics and imaging.

Briefly, hyaluronan is a highly anionic biopolymer comprised of a disaccharide chain (-4-glucuronic acid- $\beta$ 1,3-N-acetylglucosamine- $\beta$ 1-) repeated thousands of times to attain an average molecular weight of several million. It is synthesized by almost all cells and forms a structural element of most extracellular matrices in the body. Highly purified hyaluronan has been shown to be a biocompatible, efficacious supplement in a variety of surgical procedures, as a vitreous replacement in eye surgery and as a synovial fluid supplement in osteoarthritis (Balazs and Denlinger, 1989; Larsen *et al.*, 1995). The developer of this technology, Dr. Endre Balazs, CEO of Biomatrix and a collaborator on this project, has now developed methods to introduce covalent di-vinyl sulfone crosslinks between hyaluronan molecules. It is this class of hyaluronan based materials (hylans) that has been, and continues to be the focus of this work.

## **TISSUE ENGINEERING OF SOFT TISSUES**

---

Prior to this study, hylans had not been investigated as a matrix for tissue engineering. The first step in this study was to determine the mechanical properties as well as the cellular interactions of a variety of hylan formulations, provided by Biomatrix, Inc. (Ridgefield, NJ) as substrates for the engineering of soft tissue replacements.

### **DETERMINATION OF SUBSTRATES – Project 1 (PI: Ivan Vesely)**

---

The purpose of this project is to determine the correlation between the biomechanical properties of hylan preparations and two parameters of the material, namely the concentration of hyaluronan in the preparation and the extent of bifunctional crosslinking from the di-vinyl sulfone reagent. This aspect of the Tissue Engineering Initiative has been carried out as an ongoing collaboration with Dr. Hascall's lab. Ms. Maida Ludwig, a graduate student in the Department of Bioengineering at Case Western Reserve University, undertook this task as her research component for an MS degree, under the co-direction of Dr. Vincent Hascall (for the biochemistry) and Dr. Ivan Vesely (for the biomechanics). Ms. Ludwig successfully completed her MS degree this summer, and her thesis is included with this report (See Appendix, pp. 65-143).

Several series of hylans were prepared by Biomatrix, Inc. (Ridgefield, NJ) for evaluation in our laboratories. The following individuals have been responsible for the development and production of hylans for this project:

- Dr. Endre Balazs, CEO
- Dr. Nancy Larsen, Director of Research
- Julie Whetstone, a research technician at Biomatrix, Inc. under the supervision of Dr. Balazs

Each series was prepared with either a constant concentration of hyaluronan with increasing concentrations of the di-vinyl sulfone crosslinker, or a constant amount of di-vinyl sulfone with increasing concentrations of the hyaluronan. Except at the highest crosslinking density, the mechanical properties of the hylan preparations precluded testing by tensile stress-strain methods because of the difficulty in clamping ends of the pliant materials. Thus, only compressive stress-strain curves were measured for most preparations. The compressive and tensile testing of saline-washed hylans was performed using an Instron servohydraulic-testing machine (Instron, Inc., Canton, MA). The degree of crosslinking was

determined (via Fluorophore-Activated Carbohydrate Electrophoresis; FACE), and hyaluronan content was also determined (via a hexuronic acid assay) for the various hylan formulations. These properties of the polymer were correlated to the modulus of the material (Figure 1).

Test hylan samples contained between 0.05 and 3.2 mg/ml of hyaluronan (HA) and a HA/ cross-linking agent ratio between 0.7 and 5.0. In general, HA content per wet weight of hylan decreased as the degree of cross-linking was reduced. Compressive moduli determined at 25% strain were higher for gels containing higher amounts of di-vinyl sulfone crosslinking reagent as illustrated in Figure 2 and Table 2. For all hylan sample types, the compressive modulus was one order of magnitude higher than the modulus determined via tensile testing (Table 1). The difference in compressive and tensile moduli is due to the non-linear behavior of hylan in compression and its highly linear behavior in tension. Subjecting gels to alcohol treatment increased the modulus of hylans one order of magnitude greater than that of saline washed samples (*e.g.*,  $15.1 \pm 4.0$  kPa vs.  $2.0 \pm 0.5$  kPa, alcohol wash vs. saline wash for the compressive modulus; Table 1). Alcohol washing increases the rigidity of hylan and roughly doubles the modulus (Table 1). In direct comparison with other materials, the tested hylan samples have moduli two orders of magnitude less than that of the highly elastic native heart valve cusps (600-1000 kPa) (Table 3, see also Project 4).

Sections 4.1-4.5 of the thesis (see Appendix, pp. 121-4) summarize the biochemical analyses. The results indicate that the hexuronic acid assay can provide a reasonable estimate of the hyaluronan content in weighed samples of the hylan preparations. In the hyaluronidase treatments, preparations with lower crosslinking were completely solubilized by the digestion protocol. The products were fluorotagged and displayed on FACE gels, which revealed bands characteristic of bifunctional and monofunctional crosslinks (see Fig. 3-1, see Appendix, p. 104). The disaccharide digestion product is the only band present in the original hyaluronan preparation, and its content in the crosslinked preparations provides a measure of the mass of the polymer in unsubstituted regions. Some preparations were made with radioactive di-vinyl sulfone, and FACE analyses of these preparations were used to confirm the bands resulting from the crosslinks. However, hylan preparations with higher crosslinking density were not completely solubilized by the hyaluronidase. In these cases, the proportion of unsubstituted hyaluronan is much less, and stretches with multiple crosslinks most likely create a network that retains much of the polymer in an insoluble form.



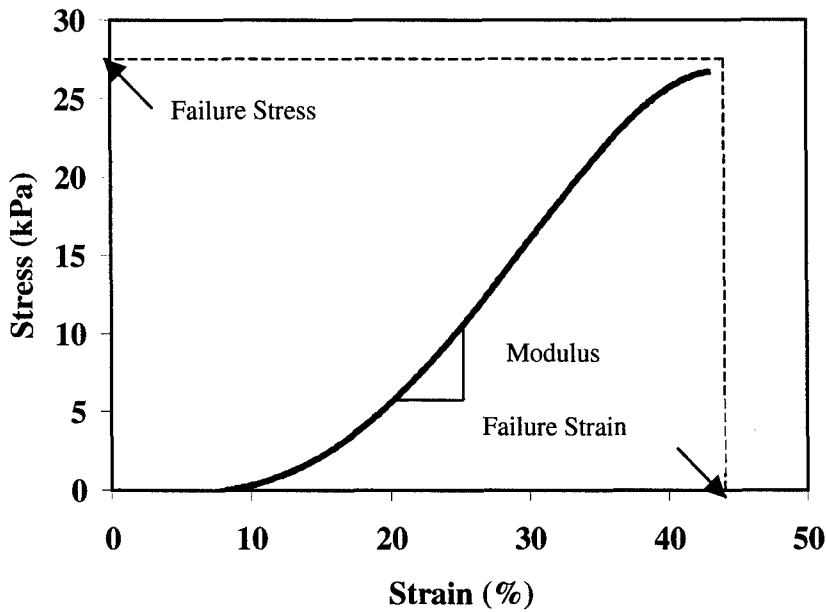


**Figure 1.** Stress vs. strain curve defining parameters for mechanical testing of materials.

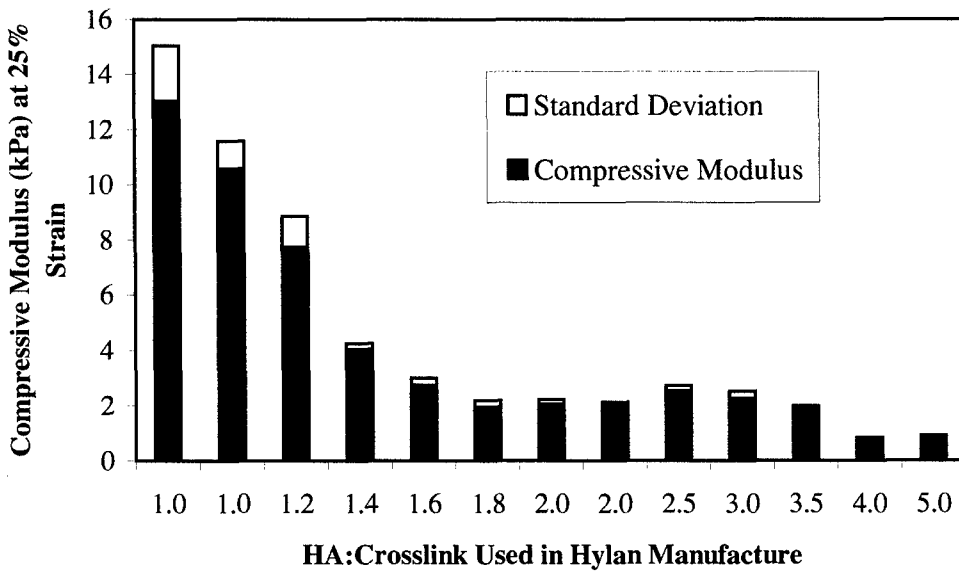


**Figure 2.** Effect of Hyaluronic acid to crosslink ratio on compressive modulus of saline-washed hylan gels. A lower ratio indicates a higher level of cross-linking, which provides greater strength to the material [Ludwig, M.A., 2000].

Sample	Testing Method	Modulus, 10% Strain		Modulus, 25% Strain	
		Mean (kPa)	Std. Dev.	Mean (kPa)	Std. Dev.
B170-1.8	Tension	0.4	0.32	0.54	0.23
B170-1.8	Compression	2.03	0.47	2.77	0.34
B173-1.8	Tension	7.13	0.93	8.15	0.69
B173-1.8	Compression	15.11	3.98	45.64	22.06

**Table 1.** Comparison of elastic moduli determined by differential testing methods for saline-washed (B170-1.8) and alcohol-washed (B173-1.8) hylan gels. For both gel types, the HA to crosslink ratio was 1.8 [Ludwig, M.A., 2000].

Hylan B173 (Alcohol-washed hylan) tensile test			
Sample	Modulus, 25% Strain (kPa)	Failure Strain (%)	Failure Stress (kPa)
B173-0.7P	18.90 ± 1.31	114.58 ± 15.96	20.99 ± 3.69
B173-1.4P	5.23 ± 3.10	154.80 ± 16.45	21.65 ± 2.42
B173-1.8P	1.84 ± 0.88	129.48 ± 20.54	14.00 ± 5.93

**Table 2.** Comparison of mechanical parameters for alcohol-washed gels as a function of the degree of cross-linking. Gel nomenclature indicates HA to crosslink ratios [Ludwig, M.A., 2000].

Specimen	Modulus (kPa)	Source
Human Abdominal Skin	1 to 2	Bader & Bower, 1983
Hylan (Saline Wash, High Crosslink)*	10	Experimental Results
Hylan (Alcohol Wash, High Crosslink)	19	Experimental Results
Collagen Gel, 2.2 mg/ml	20	Experimental Results
Collagen Gel, 3 mg/ml	40	Osborne, 1998
Elastin	600	Fung, 1993
Collagen (along fiber)	1,000,000	Fung, 1993

**Table 3.** Comparison of moduli for various biomaterials and biological tissues.

\* Determined via compression testing; all others tested in tension [Ludwig, M.A., 2000].

## **Significance**

Hylans show non-linear behavior similar to native valvular tissues. While the strength of gels in the present form is insufficient for their use as primary tissue replacements, they have sufficient properties to serve as a substrate for cell culture, as an epidermal replacement or other applications that do not require a high modulus of elasticity. This aspect of the project is discussed in greater detail later in this report (Project 4). Further chemical/structural modifications of hylan gels are necessary to improve their strength. It is believed that some of these compositional changes will also lend properties more advantageous to cell attachment and proliferation. Additionally, we believe that gel reinforcement via synthesis of a collagen and elastin-rich matrix by attached cells can contribute to added gel strength and/or elasticity. The mechanical properties of the current hylan preparations fall short of levels which would be satisfactory for long term use in cell culture models, in which controlled, variable strain would be a parameter under study (Projects 3, 4, and 5).

## **Future Work**

In summary, Project 1 has met the objectives of measuring the mechanical properties of several series of formulations, and has developed methods to measure the concentration of hyaluronan in the preparations as well as important parameters relating to crosslink structures and crosslink density. To date none of the formulations has optimal mechanical properties for meeting some of the objectives in other Projects in the overall proposed study. The highest crosslinked hylans have properties approaching those desired, and we will continue to explore additional materials in this range. Some methods to be investigated for the improvement of the hylan matrix are increased concentrations of hyaluronan and increased levels of crosslinking. The use of radiolabeled di-vinyl sulfone will also be explored to provide an alternative method for evaluating the degree of crosslinking in formulations that resist digestion with the hyaluronidase.

## **KERATINOCYTE MODEL – Project 2 (PI: Vincent Hascall)**

---

The ability of the rat epidermal keratinocyte cell line to form an organotypic epidermis on a collagen substrata directly or on a basement membrane-coated collagen substrata has been fully evaluated and the results published this year (see Appendix, pp. 144-156). The morphology of the epidermis with the underlying basement membrane is indistinguishable from that of a thin murine epidermis *in vivo*, with hemidesmosome attachments and a smooth plasma membrane interface. Thus, the model is well established for the experiments proposed in this project.

Several attempts were made to culture the keratinocytes on various hylan preparations. In each case, the cells were unable to attach to the material properly with the most common result being clusters of cells adhering primarily to each other. This indicates that the basal surface of the basal cells will not anchor properly on the hyaluronan surface of the material. This may inhibit cell division and prevent subsequent differentiation and stratification. As for the studies with aortic smooth muscle cells in Project 4, surface modification of the hylan preparations will be necessary to meet some of the objectives of this project.

### **Future Work**

Dependent upon the outcome of the modifications in Project 4, we will initiate cultures of keratinocytes on hylan preparations that prove satisfactory with the smooth muscle cells. We expect that preparations conditioned with basement membrane molecules such as laminin will prove feasible. In the meantime, experiments to define the role of hyaluronan in the differentiation and stratification of the keratinocytes will continue.

## VASCULAR ENDOTHELIAL CELL MODEL – Project 3 (PI: Hiroaki Harasaki)

---

Vascular grafts smaller than 6 mm in diameter fail prematurely due to thrombosis and intimal hyperplasia. Endothelialization appears to be critical to their long term patency and success. Endothelial seeding of vascular grafts has shown inconclusive results mainly due to poor adhesion and resultant detachment of endothelial cells under flow. It was initially hypothesized that hylans possessing a surface coat of collagen type IV, a component of basement membrane, will provide a substrate for endothelial cell (EC) seeding. The focus of this project is to develop and optimize the seeding technology and its evaluation *in vitro*. In an actual application of this approach in a vascular graft configuration, it is required that either the graft is completely covered by a confluent layer of EC or, if the endothelialization is incomplete, EC used for seeding is altered to promote its antithrombogenic properties to minimize initial surface thrombus formation. We took an approach to genetically alter the capillary-derived EC to over-express nitric oxide (NO). NO is known to improve the blood compatibility of EC by suppressing platelet aggregation. It is also known that NO relaxes smooth muscle contraction and prevents vascular smooth muscle cell (SMC) proliferation. Work is in progress to transfect EC with pSPORT-NOS using viral and non-viral vectors. EC thus transfected showed *in vitro* a significant suppression of platelet aggregation and SMC proliferation (Kaderr *et al.*, in press). The retention rate of transfected EC is being studied under flow using conventional vascular graft materials as the substrate.

As stated in Project 1, the mechanical properties of the current hylan preparations fall short of levels which would be satisfactory for long term use in cell culture models in which controlled, variable strain would be a parameter under study (*i.e.* evaluation under flow, as in this study). For this reason, appropriate development work is being carried out in parallel until the hylan formulations have been optimized.

As a result of this limited mechanical property of current hylans, a composite graft approach should be sought for in the development of vascular grafts. The inertness of unmodified hyaluronan is an attractive characteristic to prevent SMC proliferation when it is used as a layer of a composite, multilayered vascular grafts. One of the leading causes of graft occlusion in the chronic phase of implantation is SMC proliferation, preferentially occurring at the anastomotic sites. The origins of SMC are two folds; transmurally from the tissue capsule formed around the graft and directly from the native arterial stump through the anastomosis. The hyaluronan layer used as a subendothelial cell layer could prevent SMC proliferation due, at least, to the former mechanism. This hyaluronan layer will be

supported outside by a substrate of a sufficient mechanical strength, such as an e-PTFE or woven Dacron graft.

As an alternative, we have tested the feasibility of locally delivering nuclear factor kappa-B (NF-kB) antisense oligodeoxynucleotide (ODN) to inhibit SMC proliferation (Collaboration with Prof. R. Bellamkonda, Department of Biomedical Engineering, Case Western Reserve University). NF-kB expression is essential for SMC activation and proliferation, and it has been shown *in vitro* that antisense ODN to NF-kB actually inhibit SMC proliferation. We have developed the poly (DL-lactide co-glycolide) based drug delivery system in an injectable form. Dr. Bellamkonda's group has also developed a lipid microcylinder system as a vehicle as a means of local drug delivery. This system is consist of helically wrapped bilayers of diacetylenic lipid, 1,2-bis (tricoso-10, 12-diynoyl-*sn*-glycero-3-phosphocholine. These delivery systems have been shown to be usable for NF-kB antisense ODN and are available for animal experiments of vascular grafts with EC lined hyaluronan surfaces.

#### **Future Work**

The personnel and methods necessary to begin this project are currently in place. As soon as a suitable hylan substrate is identified through the efforts of Dr. Vesely's lab (Project 1), EC seeding will be commenced. Additionally, careful attention will be paid to the outcomes of Projects 2 and 4, as they assess and optimize surface pretreatments necessary to facilitate successful cell attachment to the hylan substrates. While awaiting the progress in Projects 1, 2, and 4, an independent effort will be made to develop the gene therapy for EC over expression of NO. Additionally, we will begin the development of a prototype composite vascular graft. As a final progression of this project, the application of endothelial cells seeded on this substrate onto various vascular grafts will be evaluated *in vivo* in our well established dog carotid artery interposition model (Uchida, *et al.*, 1993).

## **AORTIC SMOOTH MUSCLE CELL MODEL – Project 4 (PI: Ivan Vesely)**

---

The overall objective of this sub-project is to develop suitable biological substrates for fabrication of a composite artificial heart valve. The goal is to develop a viscoelastic, mechanically anisotropic material, populated with cells, using tissue-engineering principles. Hylan is a versatile and highly biocompatible biopolymer formed by crosslinking the connective tissue component hyaluronan. It is therefore a potential candidate for use as cellular scaffolds. Dr. Vesely's lab has extensive background with smooth muscle cells for use in the development of bioartificial heart valves. For this reason, the defined neonatal rat aortic smooth muscles cells (NRASMCs) used in his work were an obvious choice to evaluate cellular interactions with hylans. Information gathered from these studies may then be applied to future work with other cell lines/types. The multifaceted approach towards evaluating hylans as cellular scaffolds for tissue engineering encompasses the following specific aims:

**Aim # 1.** Develop a system for generating highly elastic matrices via long-term cell culture *in vitro*.

**Aim # 2.** Investigate the feasibility of cell attachment and proliferation on untreated and modified hylan substrates. Additionally, assess material reinforcement via extracellular matrix synthesis by attached cells, in static or dynamic systems. Our primary objectives are being realized via knowledge gained from several independent but closely associated studies as stated above. The results of each study are summarized below.

### **Aim #1. Development of Elastin-Rich Substrates**

---

Collagen, elastin, and glycosaminoglycans (GAGs) are the primary structural components of valvular tissues. We are in the process of developing a system for *in vitro* cellular synthesis of natural polymers that would possess strength and compliance similar to native tissues. We have made significant progress in determining the factors and the conditions necessary for stimulating cells to synthesize large quantities of insoluble (cross-linked) elastin. The ultimate goal is to attain a highly aligned matrix/sheet of elastin fibers possessing the desired level of strength and compliance.

For this study, we selected neonatal rat aortic smooth muscle cells (NRASMCs) as the source of elastin since they synthesize elastin prolifically. A protocol was developed for harvesting smooth muscle cells from aortic explants from 3-day old rats (Harlan Sprague-Dawley, Indianapolis, IN). Primary cell cultures were established and passaged repeatedly to establish numerous colonies of cells. We quantified the total elastin synthesized by cell cultures (passages 3-11) over culture periods ranging from 1- 5 weeks. Cells synthesize soluble tropoelastin, and insoluble elastin, which is deposited into the extracellular

matrix. In view of the goals of our study, we are interested in maximizing the synthesis of insoluble elastin. A protocol was developed for sequential assays of cell layers for analysis of cell numbers (via DNA Analysis), collagen synthesized by smooth muscle cells (via hydroxyproline assays) and the measurement of soluble and insoluble elastin. Elastin was measured using a commercially available Fastin-Elastin assay (Biocolor, Ltd., Belfast, N. Ireland). In the absence of specific growth factors/vitamins influencing elastin synthesis (control), we determined that a major fraction of elastin synthesized was released into the medium as soluble tropoelastin. Control cultures produced approximately 0.5 ng of insoluble elastin per cell over a period of 3 weeks. The production of soluble tropoelastin during the same period ranged between 1.3 and 3 mg/ml.

In an attempt to drive elastin synthesis towards generation of insoluble elastin, we have initiated controlled studies wherein specific growth factors were added as additives to the culture medium. The factors added include transforming growth factor- $\beta$  (TGF- $\beta$ ), retenoic acid, interleukin-1 $\beta$ , vitamin C, and copper as  $\text{Cu}^{2+}$ . Specifically, we expect to determine the effect of addition of growth factors on extracellular matrix development and cell proliferation. Our experiments strongly suggest that in the presence of  $\text{Cu}^{2+}$  ions (2.5-5  $\mu\text{M}$ ) crosslinking of soluble elastin is promoted. Over 3 weeks, cell cultures with 5  $\mu\text{M}$   $\text{Cu}^{2+}$  generated 2.8 times more insoluble elastin than control cultures.

The structural form of elastin secreted into the extracellular matrix is of importance in determining the mechanical properties of tissues. Insoluble elastin appears either in an amorphous form or is highly organized as fibers. Elastin fibers are made up of highly crosslinked elastin fibrils and provide greater elasticity to the tissue. In contrast, amorphous elastin is weakly crosslinked and can be solublized relatively easily. We subjected our cell layers to transmission electron microscopy (TEM). The TEM images confirm an increased deposition of insoluble elastin in the presence of  $\text{Cu}^{2+}$  (Figures 3a. and b.). Additionally, most of the extracellular elastin is in the amorphous form. In contrast, a TEM image of the ventricular layer of porcine aortic valve cusps shows organized elastin fibers (Figure 4). Accordingly, future work in this area will focus on the study of mechanisms involved in the crosslinking and fibrillation of extracellular elastin. Over the last few months, we have also developed and optimized protocols for visualization of elastin within tissues, or in cell layers. Figure 5 shows a confocal image of a 3 week-old layer of smooth muscle cells cultured on glass slides. Immunohistochemical techniques (fluorescent-labeled antibodies) were used to identify cellular actin, nuclei, and extracellular elastin. Significantly,



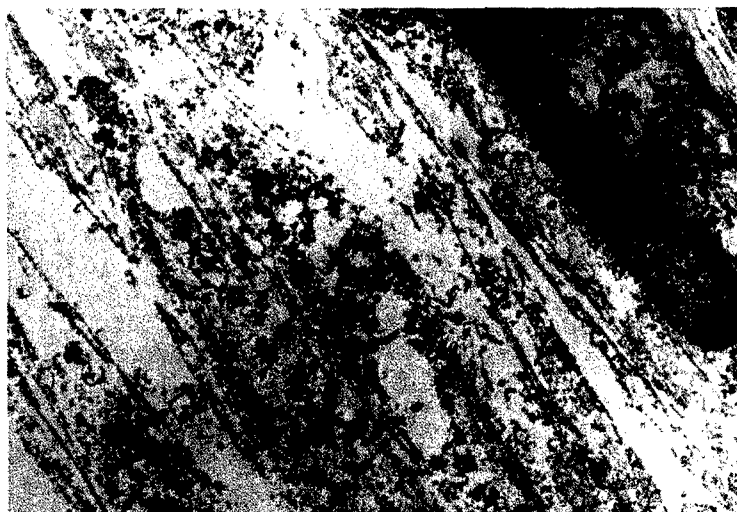


**Figure 3a.** TEM of neonatal rat aortic smooth muscle cell layer (4600 $\times$ ). Cells were cultured for 3 weeks. A very low percentage of the elastin synthesized by the cells is present in the form of insoluble elastin.



**Figure 3b.** TEM of neonatal rat aortic cell layer showing the presence of amorphous (non-fibrillar) elastin. Cells were cultured for 3 weeks in the presence of 5  $\mu\text{M}$   $\text{Cu}^{2+}$  in the culture medium. Copper promotes crosslinking of elastin synthesized by cells and renders it insoluble. Magnification: 13,000 $\times$ .



**Figure 4.** TEM of ventricular layer of porcine aortic valve cusp (6000 $\times$ ). Photograph indicates the substantial presence of highly oriented fibrillar insoluble elastin. Collagen fibrils are also seen. The significant elastin content is responsible for the highly elastic nature of this layer.

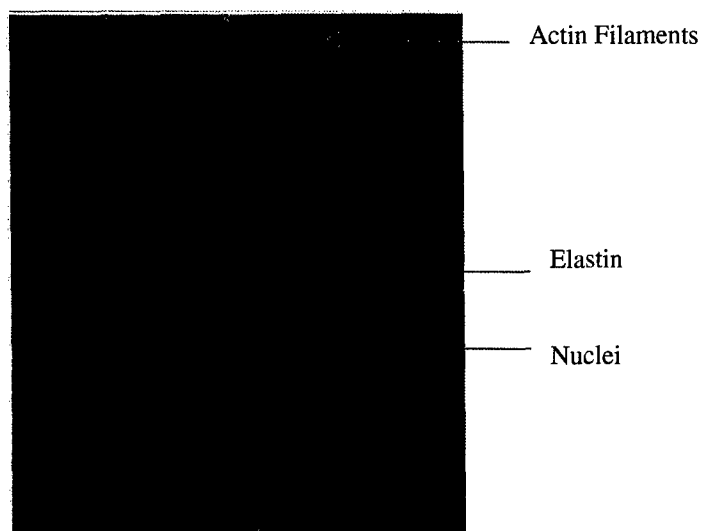


**Figure 5.** Confocal microscope image of neonatal rat aortic smooth muscle cells cultured on glass slides for 3 weeks in the presence of 5  $\mu\text{M}$   $\text{Cu}^{2+}$ . Immunohistochemical techniques were used to label cellular actin (Alexa 488 Phalloidin), extracellular elastin (Texas Red) and nuclei (DAPI). Image shows significant synthesis of insoluble elastin (partially in fibrillar form). Magnification: 200 $\times$ .

cells cultured on glass slides synthesize elastin of which a significant fraction is organized into fibers (Figure 5).

### **Significance**

NRASMCs were demonstrated to synthesize large amounts of elastin, as previously shown. However, we determined that a low fraction of synthesized elastin is incorporated as a structural component of the extracellular matrix. Culturing cells in the presence of copper ions and other growth factors/stimulants can significantly enhance insoluble extracellular elastin production. The importance of this study lies in the determination of factors influencing insoluble (structural) elastin synthesis. Such knowledge is useful in manipulating culture conditions so as to replicate the elastin chemistry and structure in native aortic heart valve cusps.

### **Aim #2. Investigate hylans as scaffolds for cell attachment and proliferation**

---

Previously, aortic valve interstitial cells were shown to have considerable biosynthetic activity in some animal models [Mulholland and Gottleib, 1996]. Further, the degradation or absence of structural tissue components such as collagen and glycosaminoglycans in human aortic valve allografts and even xenografts has been related to post-implantation acellularization of tissues. Thus, our rationale for having viable cells in/on a material to be implanted at the site of a heart valve is based on the above two arguments. The objectives of this study were to investigate the conditions necessary for cell attachment, proliferation, and matrix synthesis on several different hylan gel formulations, obtained from Biomatrix, Inc. These included particulate hylan gels (B10, JB21 G, JB21D), solid saline-washed gels (B181-B, B186, B190), and solid alcohol-treated gels (B181-C2). In the hydrated state, these gels contained up to 1.5% (w/v) of HA and the remainder, water. The particulate gels were provided in the form of dehydrated films and were reconstituted with serum-free culture medium. These gels contained uniform hylan particulates ranging in size between 460 and 1060 microns. Saline-washed solid hylans were optically clear and ranged in thickness between 5 and 8 mm. As discussed previously (Project 1), some gels were also washed with alcohol to provide greater stiffness.

Prior to cell seeding, gels were equilibrated overnight with serum-free culture medium (DMEM: F12, Gibco Laboratories, Rockville, MD). Gels were then sectioned into round pieces, each 1.9 cm<sup>2</sup> in area and introduced into wells of a 24-well plate.  $20 \times 10^5$  cells (passages 3-5) were seeded per well and cultured in the presence of DMEM: F12 containing 10% (v/v) fetal bovine serum. Initial studies conclusively showed that untreated hylans, irrespective of their formulation, did not support attachment or

viability of cells. Accordingly, subsequent to equilibration gels were surface-coated with known cell adhesion proteins including collagen I or collagen IV, fibronectin, fibrinogen, reconstituted extracellular matrix gel or laminin. Protein concentrations in bulk suspensions ranged between 10 and 100  $\mu\text{g}$  of protein /100  $\mu\text{l}$ . NRASMCs were then seeded on the gel surface and cultured for up to 21 days. Irrespective of the coating concentration, fibrinogen did not promote cell attachment to the hylan. This may have been either due to ineffective adherence onto the hylan surface or failure of cells to recognize the agonist. Cells on particulate gels appeared irregularly shaped (ECM gel, fibronectin and laminin), or highly spread (collagen I, IV). For all treatments, gel surfaces were confluent with cells by 2 weeks (Figure 6). Cells attached on solid gels were mostly rounded although spread cells were also observed on gels treated with collagen type I or ECM gel (Figure 7). Figure 8 contrasts the highly spread nature of smooth muscle cells attached on collagen I-treated hylans with the normal phenotype. Cell attachment was quantified using the MTT assay, described previously [Miller and McDevitt, 1992]. Briefly, this is a spectrophotometric assay based on release of a blue formazan product by the mitochondria of live attached cells on exposure to MTT (3-(4,5-dimethylthiazol-2-yl)-2,5-diphenyl tetrazolium bromide) reagent. Cell attachment was found to depend on bulk protein concentration and the type of adhesion protein. At four weeks, cell attachment on particulate gels coated with Collagen type I, ECM, laminin, and fibronectin was enhanced by 2.7, 4.2, 3.0, and 2.6 times respectively over attachment at one week [ $n = 3$ ] (Figure 9). On solid gels, cell counts were similar at one and two weeks for all pretreatments except with ECM where cell attachment was enhanced to 1.9 times (Figure 10). This suggests that cells attach but do not proliferate on treated solid hylan gels. Further investigation is necessary to determine if the failure of cells to proliferate on solid gels is related to the inefficient deposition of adhesion protein prior to cell seeding. In the experiments performed, cells attached to all non-collagen treated solid gels did not survive beyond 3 weeks. We also performed a short-term study to investigate if protein treated alcohol washed gels respond favorably to cell attachment. Preliminary results indicate that cell attachment on alcohol-washed gels is similar to those on the solid gels for similar protein pre-coats (Figure 11). Further long-term culture studies on all the above hylan formulations are currently in progress.

### **Significance**

The results obtained clearly indicate that smooth muscle cells may be successfully cultured on hylans. Cell attachment and multiplication was most prolific on particulate hylan gels, possibly due to their comparatively rough surface, which promotes protein adherence and provides greater anchorage for attaching cells. For the same reason, we think cells attached on such gels show a highly spread

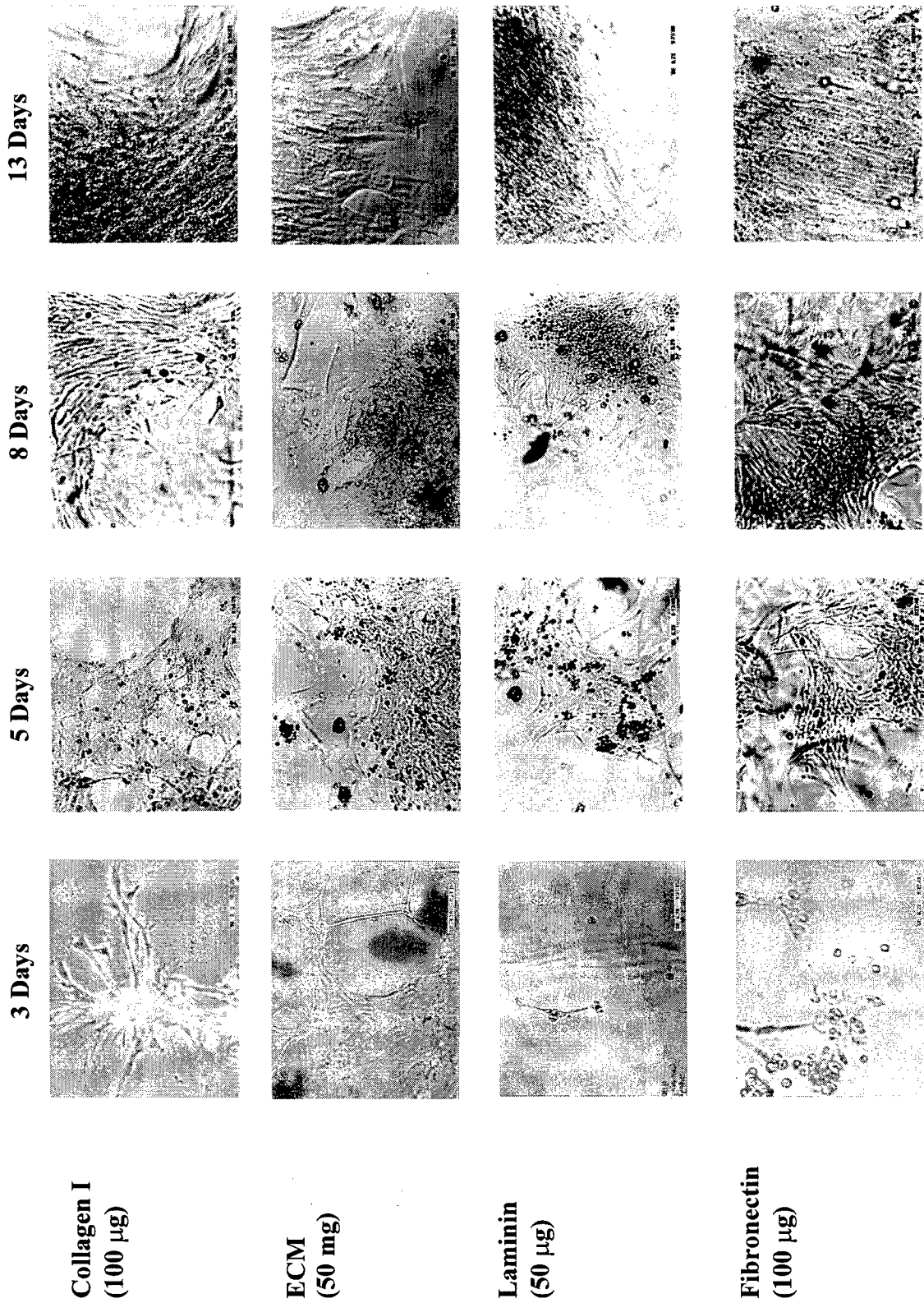
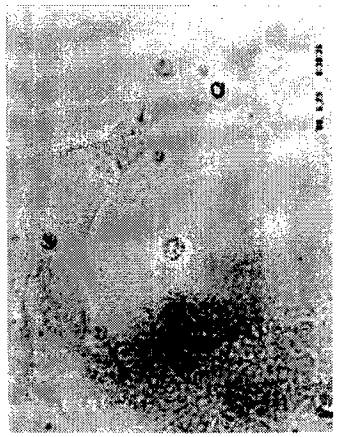


**Figure 6.** Neonatal rat aortic smooth muscle cells (NRASMC) cultured on particulate hylan gels. Gel surfaces were coated with adhesion proteins to facilitate cell attachment. Culture area was 1.9 cm<sup>2</sup>. Magnification: 40x.



5 Days

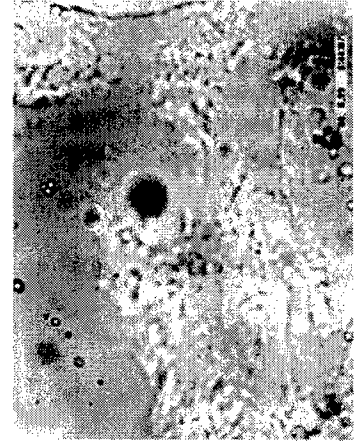


8 Days

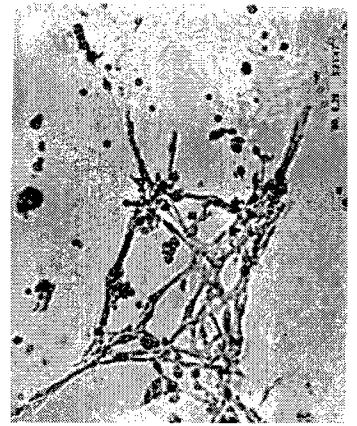


13 Days

**Collagen I  
(100 µg)**



5 Days

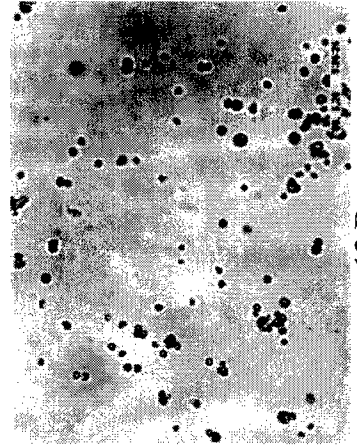


8 Days



13 Days

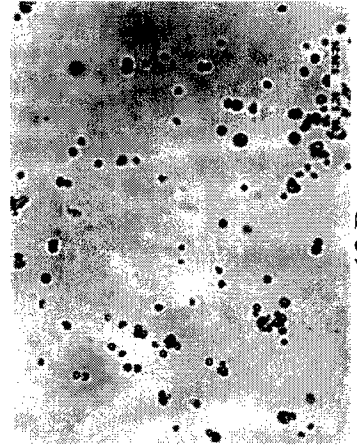
**ECM  
(50 µg)**



5 Days



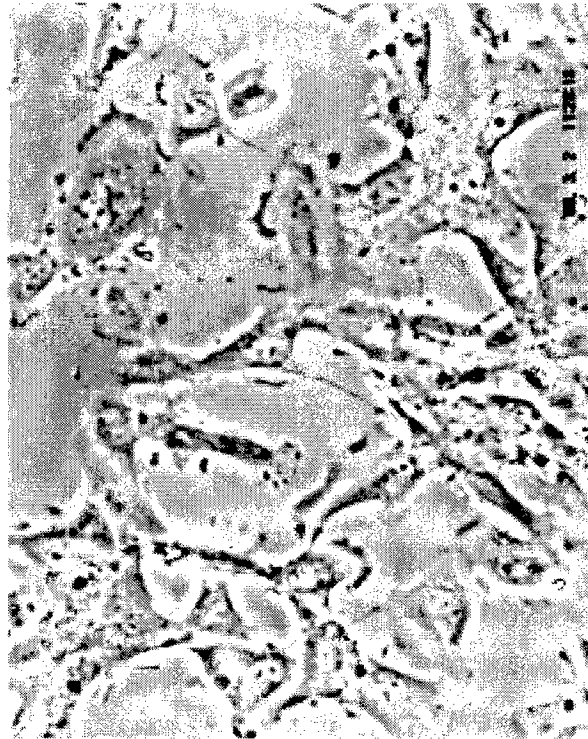
8 Days



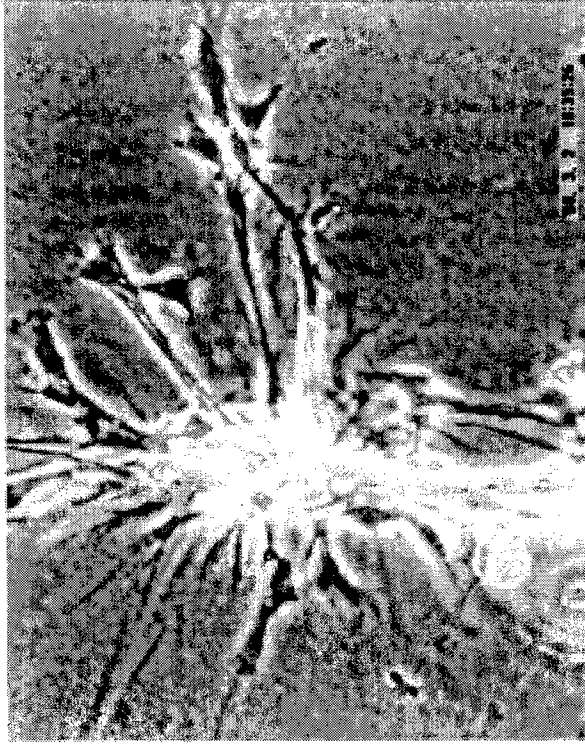
13 Days

**Laminin/  
Fibronectin  
(50 µg/100 µg)**

**Figure 7.** Neonatal rat aortic smooth muscle cells (NRASMC) cultured on solid hylan gels (5-8 mm thick). Gel surfaces were coated with adhesion proteins to facilitate cell attachment. Culture area was 1.9 cm<sup>2</sup>. Magnification: 40x.



### Culture Dish



### Hylan

**Figure 8.** Neonatal rat aortic smooth muscle cells are shown at 3 days at 20 $\times$  magnification. The gel surface were coated with collagen type I (100 mg/100 ml) and each substrate was separately seeded with  $2 \times 10^5$  cells. Cells on the collagen/hylan surface were stretched highly and aligned to form cord like structures.

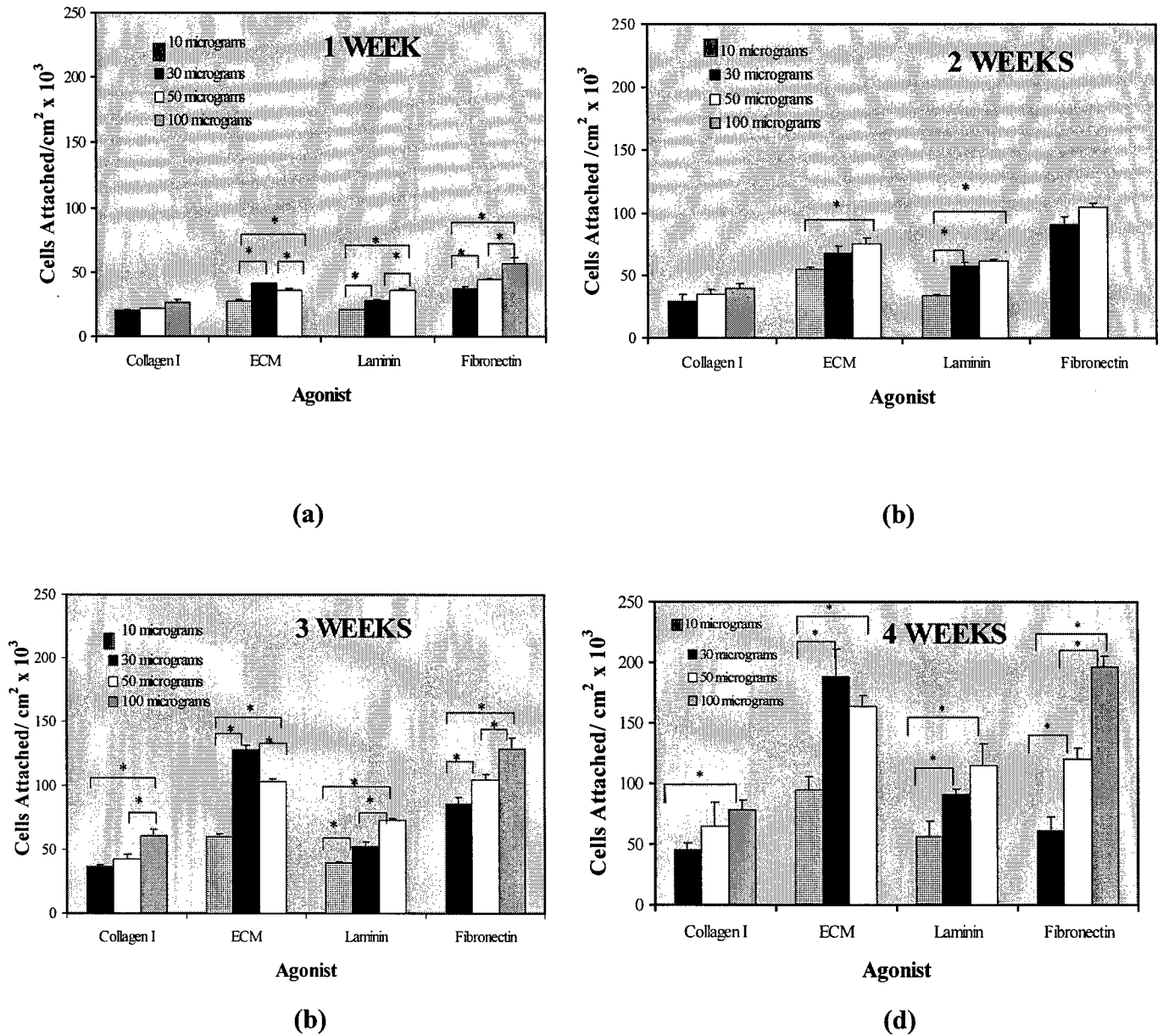


**Figure 9.** Proliferation of rat aortic smooth muscle cells on surface-treated particulate hylan gels (B10). Cells were cultured for between 1 and 4 weeks (Figs. a - d) respectively. Columns and bars represent Mean  $\pm$  SE of  $n = 3$  trials (\* $p < .05$ ). Note: ECM/Laminin = 10, 30, 50  $\mu$ g and Collagen I/Fibronectin = 30, 50, 100  $\mu$ g.



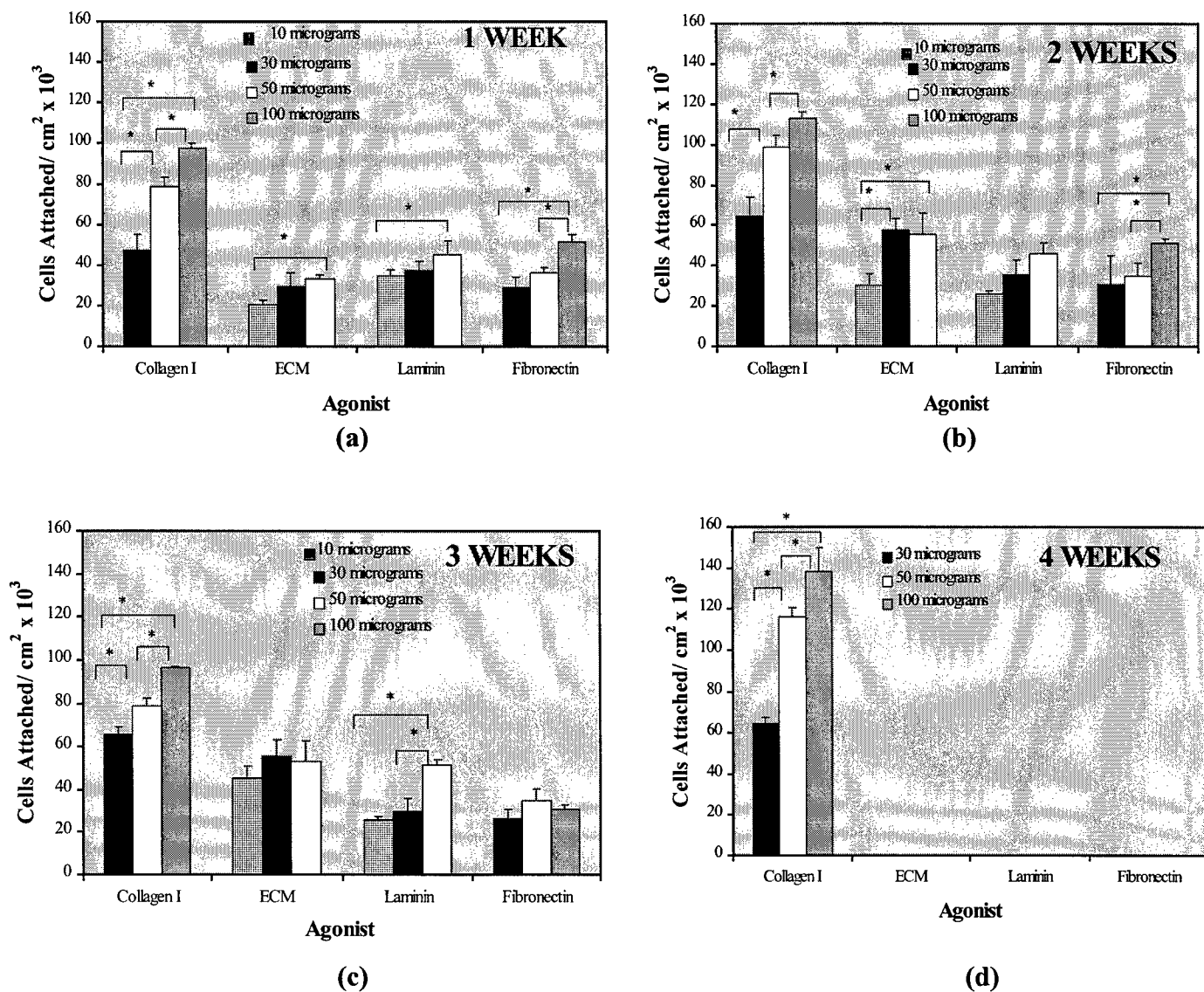
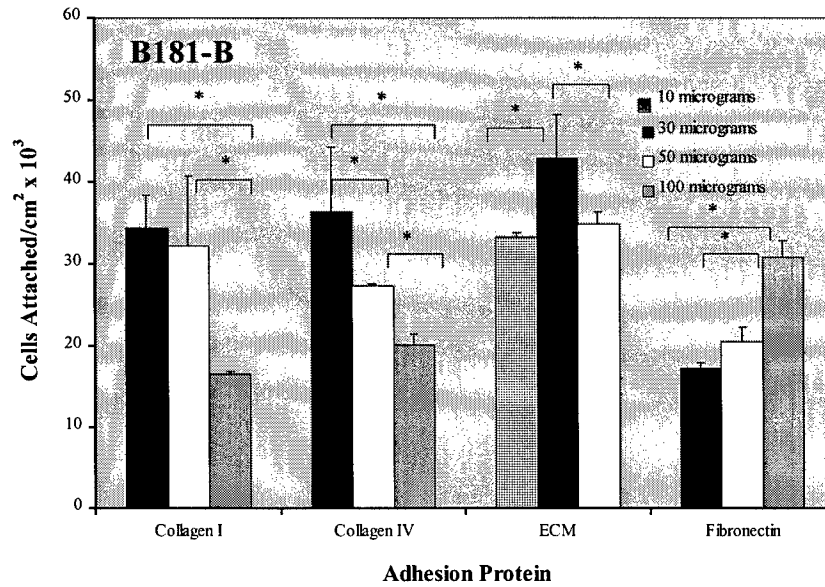
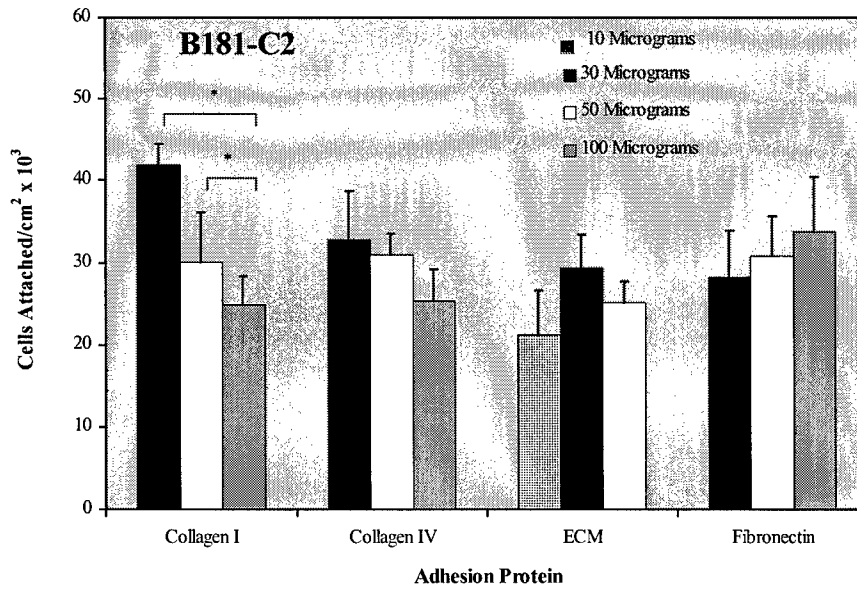


**Figure 10.** Proliferation of rat aortic smooth muscle cells on surface-treated solid hylan gels (B186/B190; saline-washed). Cells were cultured for between 1 and 4 weeks (Figs. a - d). In this study, cells on gels coated with ECM, laminin, and fibronectin did not survive beyond 3 weeks. Results represent the mean  $\pm$  SE of  $n = 3$  trials (\* $p < .05$ ). Note: ECM/Laminin = 10, 30, 50  $\mu\text{g}$  and Collagen I/Fibronectin = 30, 50, 100  $\mu\text{g}$ .



(a)



(b)

**Figure 11.** Comparison of cell attachment on surface-treated solid hylan gels which were either saline-washed (B181-B; Fig. a) or alcohol-treated (B181-C2; Fig. b). Culture period = 7 days (\* $p < .05$ ). Note: ECM = 10, 30, 50  $\mu\text{g}$  and Collagen I/Collagen IV/Fibronectin = 30, 50, 100  $\mu\text{g}$ .

morphology. In contrast, solid gels have relatively smooth surfaces, which may not provide sufficient anchorage for cells. However, the current study clearly demonstrates that cell-hylan composites show promise towards the successful development of bioengineered materials.

### **Supporting work**

In the past year, we have also initiated a study to develop non-leaflet tissue components of heart valves. In specific, we are attempting to engineer a bioartificial replacement for mitral valve chordae. Chordae are collagenous bundles that connect the mitral valve cusps to the aortic root and prevent ballooning of leaflets during ventricular systole. The longitudinal orientation of collagen fibers in chordae is crucial to its mechanical strength. Although not a part of the original grant proposal, we mention this study due to its relevance to tissue engineering of heart valve leaflets. A collagen sheath was reconstituted from acid-soluble collagen type I (rat tail) in an *in vitro* device wherein the ends of the sheath were attached to porous holders by fibrillar entrapment. Human fibroblasts or neonatal rat aortic smooth muscle cells were seeded within the collagen sheet. Sheath contraction (due to cell attachment and elongation) in the axial direction was restricted due to attachment to the holders. Accordingly, the collagen sheath tended to contract along the transverse axis. Our goal was to investigate if application of unidirectionally oriented mechanical stresses can promote unidirectional cell alignment and thence production of extracellular matrix proteins. Thus, we hope to develop highly oriented composites resembling mitral valve chordae in structure and function. Our initial studies show that upon application of axial constraints cells are stimulated to proliferate and align themselves in the axial direction and also synthesize collagen oriented similarly. Through this study, we hope to understand the kinetics of matrix contraction and the parameters influencing the process. The device developed here for studying matrix alignment will be adapted to studies of hylan-cell composites in the following year. We expect to reinforce the composites by guided cellular synthesis of extracellular matrix and thus improve upon their mechanical properties.

### **Future Studies**

Our immediate aims are to carry out long-term (> 4 weeks) culture of smooth muscle cells on hylans and to perform qualitative and quantitative analysis of the extracellular matrix synthesized by attached cells. We plan to attempt micro machining of surface irregularities on solid hylans so as to provide greater anchorage for cell attachment and spreading. This would be relevant since solid hylans are preferable to particulate hylans as implant materials from a mechanical standpoint. Once characterization of extracellular matrix on hylans (in a static system) is complete, we plan to develop a device for

investigating guided matrix synthesis and gel reinforcement by application of uniaxial strain. We have already initiated a parallel study to investigate cell attachment and proliferation within rather than on hylan gels. The ability of cells to populate and metabolize within hylans is expected to lead to the development of bioartificial composites much more closely resembling native heart valve cusps.

### **Infrastructure**

- Hired part-time student in spring of 1999 to establish tissue culture facilities at our laboratory.
- Hired one postdoctoral fellow in September 1999 to take on the development of hylan technology.
- Hired a doctoral student for 6 months to initiate elastin-based research (Aim #2).
- Currently 1 full time and 5 part-time (students/ summer interns) are engaged in tissue engineering in our laboratory.
- We have developed active research collaboration with several personnel within the Lerner Research Institute, The Cleveland Clinic Foundation. They include:
  - Judith Drazba, Ph.D.- Director Imaging Core
  - Carol de la Motte, M.S. – Technician, Department of Colorectal Surgery
  - Kathleen Derwin, Ph.D. – Project Staff, Department of Biomedical Engineering
  - Vincent C. Hascall, Ph.D. – Director, Connective Tissue Biology, Department of Biomedical Engineering
  - Jim McMahon, Ph.D. – Division of Pathology

### **Conclusions**

Our work over the previous year has shown that gels based on cross-linked hyaluronan (hylan) are suitable materials for development of biological implants. The mechanical properties of hylans make them suitable for the development for epidermal replacements and non-stress intensive physiological applications. However, further chemical/structural modifications are necessary to enhance their stiffness/elasticity for use in the development of heart valve tissues. Developing a cell-hylan composite wherein the gel is strengthened by elastin and collagen secreted by cultured cells is one method of reinforcing the material. We have identified the conditions under which neonatal rat aortic smooth muscle cells prolifically synthesize elastin or collagen in large quantities. We have also shown that such cells attach and proliferate actively on hylan gels treated with cell adhesion proteins. The results of this work are of prime importance in the development of bioengineered materials based on cell-hylan composites.

## **TENDON CELLS – Project 5 (PI: Kathleen Derwin)**

---

We have proposed to establish *in vitro* culture models of tendon fascicles and cells to investigate various metabolic parameters and their relationship to the mechanical loading environment. The first step in this investigation has been to establish baseline properties of native tendon tissue in the selected animal model. To date, our efforts have focused on *flexor digitorum superficialis* (FDS) tendons in a canine *ex vivo* model. After determination of their baseline parameters, we have proposed establishing cultures of primary tendon explants under no load or subjected to static and dynamic tensile loads, according to established protocols (Hannafin *et al*, 1995). As a final progression, we have proposed the development of bioartificial tendon analogs comprised of isolated primary fibroblasts cultured on and within hylan scaffolds (see Project 4). Baseline parameters for these analogs will also be determined and compared with those of native tendon tissue. These tendon/cell composites will also be subjected to the same loading protocols as the primary tendon explants, and the effects of mechanical loading will be evaluated.

### **Establishment of Primary Tissue *Ex Vivo* Model**

Canine pelvic limbs have been retrieved from male, mongrel dogs (25-30 kg) at the time of sacrifice. These animals were obtained from animals in an approved but unrelated study at The Cleveland Clinic Foundation (“Anesthesia and Pulmonary Vascular Signal Transduction”, Dr. Paul Murray, Anesthesiology, NIH Award HL38291-14). For all preliminary studies, the distal third of the FDS tendon was investigated. Specifically, the four tendon branches from the region of the tendon between the distal tarsal bones and the metacarpophalangeal joints were utilized (Figure 12). We have adopted the terminology medial outer (MO), medial inner (MI), lateral inner (LI), and lateral outer (LO) to describe these four tendons based on their anatomical location.

### **Determination of Baseline Properties**

Several techniques have been developed to determine the baseline properties of FDS tendon explants. These procedures will also be applied to evaluate the effects of mechanical load on tendon tissues and cells in future aspects of the proposed project.

#### Dissection

Tendon segments were isolated from the hindpaw of a single mongrel canine (n=8) and cleaned of any attached muscle and sheath material with the aid of a stereomicroscope. Based upon visual inspection, a 3.5 cm length of uniform tendon tissue could be harvested from the mid-region of the isolated tendon segments (Figure 12C, 12D).

## Geometry

Isolated tendons were mounted in a device that allowed them to be tensioned and rotated about their long axis while viewed under a stereomicroscope (Figure 13). Calibrated cross-sectional images of each tendon segment were captured and used to compute a cross-sectional area. Results demonstrated that inner FDS tendons were significantly larger in cross-section ( $4.4 \pm 0.2 \text{ mm}^2$ ) than outer tendons ( $2.3 \pm 0.2 \text{ mm}^2$ ).

## Water Content

Cleaned tendon segments (as described above) were blotted and weighed on an analytical balance (n=8). The segments were then dried at 60°C for 48 hours and reweighed. Water content was determined by calculating the percent decrease in weight due to drying. Results demonstrate that the water content of outer and inner FDS tendons was similar. The average water content of FDS tendons was  $64.5 \pm 1.0\%$  (Table 4).

## Hydroxyproline Content

Cleaned tendon segments (as described above) were dried at 60°C for 48 hours and weighed (~10 mg dry). Hydroxyproline content was determined from these dried segments using a standardized spectrophotometric technique (Stegeman and Stalder, 1967) using a SpectraMAX Plus microplate reader (Molecular Devices, Inc., Sunnyvale, CA). From these results, collagen content was calculated based on the premise that hydroxyproline is solely derived from collagen, and that it represents 13% of this protein by weight (Cetta *et al*, 1982). Results demonstrated the hydroxyproline and content of outer and inner FDS tendons was similar. The average hydroxyproline content of FDS tendons was  $97.2 \pm 6.6 \text{ } \mu\text{g/mg dry wt}$  (Table 4) which translates to a collagen content of  $747.6 \pm 51.1 \text{ } \mu\text{g/mg dry wt}$  (74.8%).

**Table 4.** FDS tendon biochemical and mechanical properties (mean  $\pm$  s.d.)

	FDS tendons (n=8)
Water Content (%)	$64.5 \pm 1.0$
Hydroxyproline Content ( $\mu\text{g/mg dry wt}$ )	$97.2 \pm 6.6$
S-GAG Content ( $\mu\text{g/mg dry wt}$ )	$0.33 \pm .10$
Failure Stress (MPa)	$76.7 \pm 16.6$

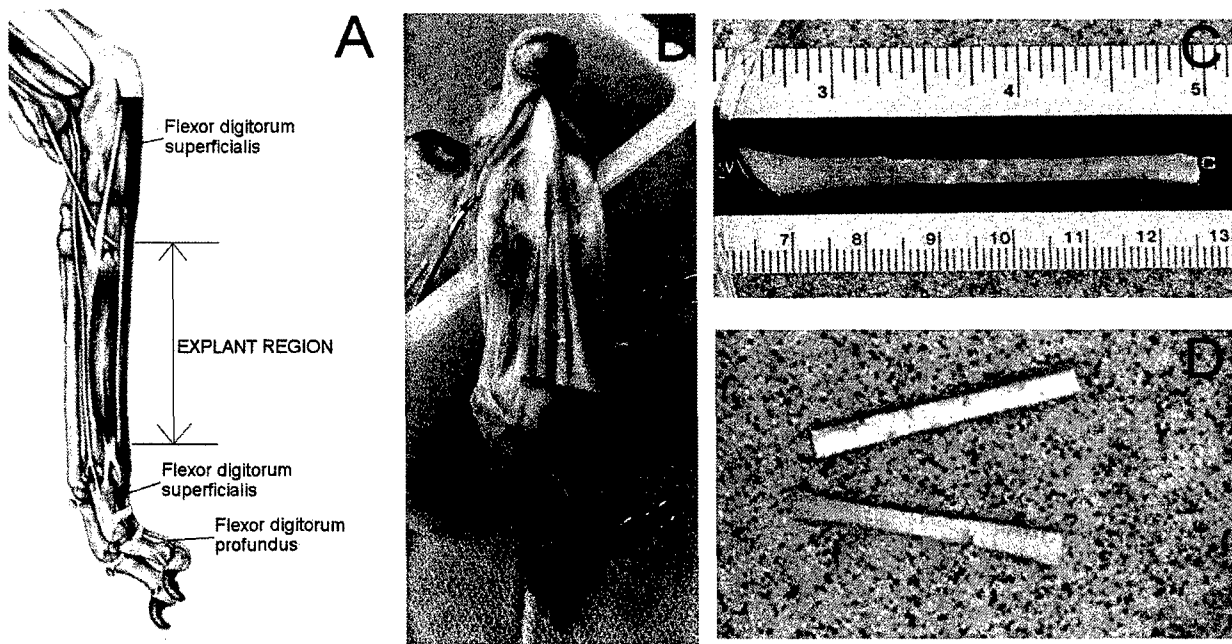


**Figure 12.** Anatomy and dissection of canine FDS tendons. (A) Lateral view of the canine hindpaw depicting the *flexor digitorum superficialis* (FDS) tendon. Arrows denote region of tendon used for preliminary studies. (B) Palmar view of canine hindpaw with the four branches of the FDS tendon exposed. (C) An isolated FDS tendon segment (D) Two FDS tendon segments after being cleaned of muscle and sheath material and cut to 3.5 cm in length.

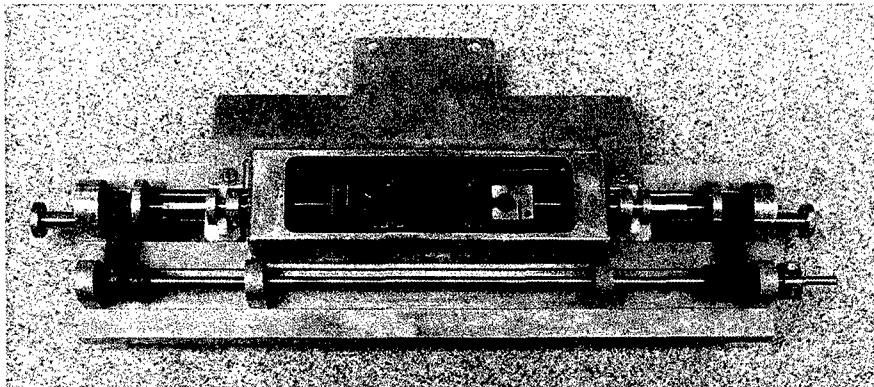


**Figure 13.** Gripped tendon mounted into device for cross-section viewing under microscope

### Sulfated Glycosaminoglycan (S-GAG) Content

Cleaned tendon segments (as described above) were dried at 60°C for 48 hours and weighed (~10 mg dry). The sulfated glycosaminoglycan content (S-GAG) of the dried tendon segments was determined using fluorophore-assisted carbohydrate electrophoresis (FACE) technology (Calabro *et al.*, 2000). FACE analysis of FDS tendons is shown in Figure 14 where  $\Delta\text{Di2S}$  has been added as a standard. (Previous studies have indicated that FDS tendons do not contain measurable amounts of endogenous  $\Delta\text{Di2S}$ ). Results demonstrate that  $\Delta\text{Di4S}$  is the predominant disaccharide present in the chains, although small amounts of  $\Delta\text{Di6S}$  were also present. Digital analysis of the FACE gel allowed the amounts of each saccharide product to be quantitated. The S-GAG content of FDS tendons was defined as the sum of the  $\Delta\text{Di4S}$  and  $\Delta\text{Di6S}$  products and averaged  $0.33 \pm .10 \mu\text{g/mg}$  dry wt (Table 4).

### Mechanical Properties

Tendon segments were placed into grips (Figure 15A) and their cross-sectional area determined as described above. Tendons were then immediately transferred to an Instron 5543 materials testing machine (Figure 15B, 15C). Tendons were initially mounted in a slack position, and a nominal preload of 2 N was applied. The specimens were then subjected to 5-10 cycles of preconditioning between 0 and 0.5 mm at 10 mm/min. Following pre-cycling, the “zero-point” or the position where the specimen is just about to resist load was manually determined. Specimens were then immediately tested to failure at 10 mm/min. During the procedure, tendons were kept moist with culture medium as required. Typical preconditioning and failure curves for FDS tendons are shown in Figure 16. In all cases, tendons achieved stable hysteresis curves in less than 10 cycles of preconditioning. Loads were normalized by the initial specimen cross-sectional area of each tendon in order to compute stresses. The stress at failure was similar for inner and outer FDS tendons and averaged  $76.7 \pm 16.6 \text{ MPa}$  (Table 4). However, it is noted that all specimens failed at the grip region. Therefore, the measured failure stresses likely underestimate the actual tensile strength of the material.

### **Future Work**

Currently, we are fine-tuning the protocols for the above-mentioned assays and will use these techniques to evaluate the effects of mechanical load on tendon tissues and cells in future aspects of the proposed project. Further, we have begun to investigate methods for sterile tissue harvest and gripping the tendon explants in organ culture. Design of a device to apply *in vitro* loads to tendon explants in



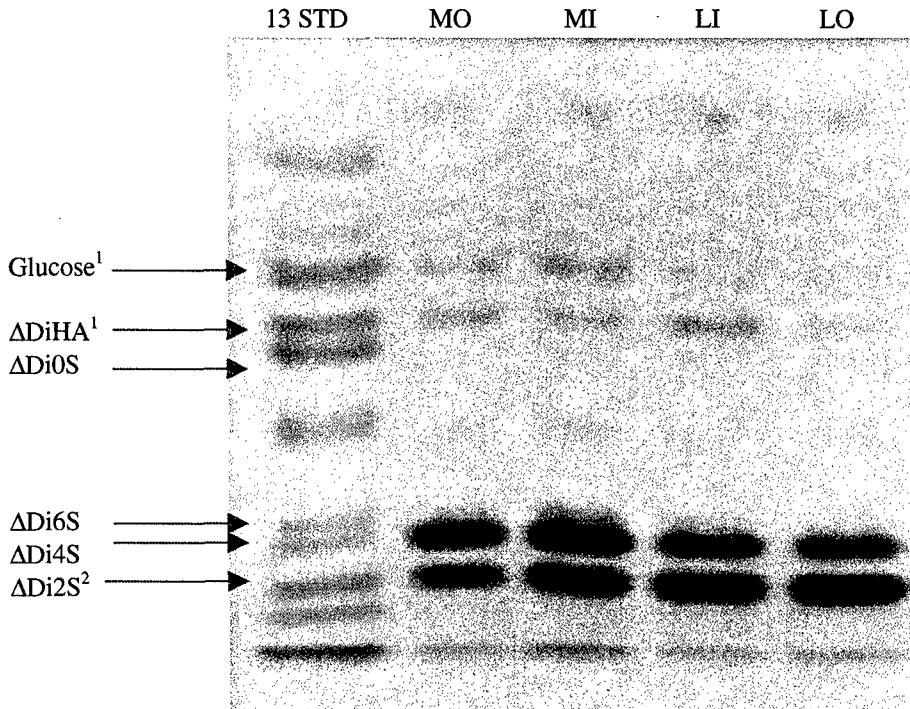


**Figure 14.** FACE analysis of canine FDS tendons allows for determination of the sulfated glycosaminoglycan content (1= Endogenous glucose and hyaluronic acid were largely removed during sample preparation; 2= FDS tendons contain undetectable amounts of endogenous  $\Delta$ Di2S, hence it was added for quantitation).

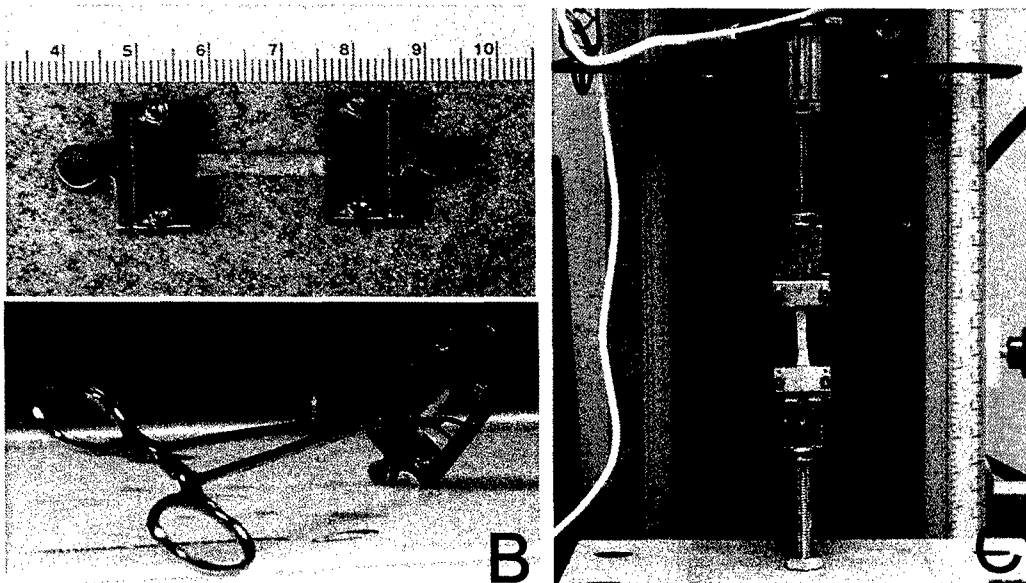


**Figure 15.** (A) Isolated tendon mounted onto custom grips. (B) Device used to transport and mount the gripped tendon sample onto the Instron. (C) Tendon mounted onto Instron 5543 materials testing machine (Instron, Inc., Canton, MA).

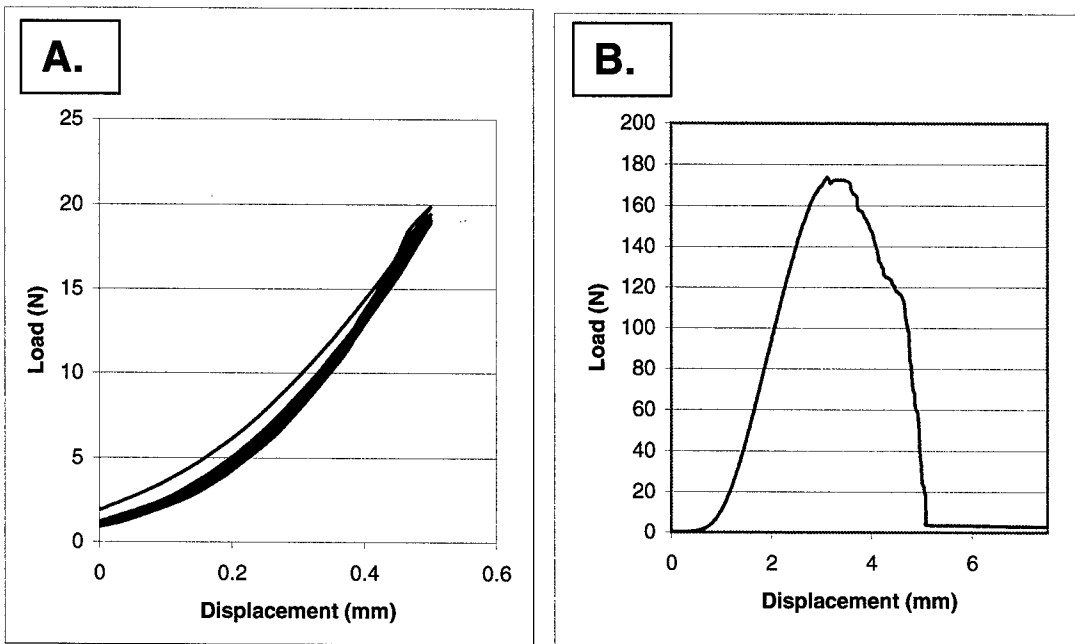


**Figure 16.** Typical (A) preconditioning and (B) failure curves for FDS tendons.

organ culture is underway (See Engineering Analysis and Prototype Support Facility). This model system will allow us to study directly the effects of physical forces on tendon cells in which the spatial relationship of the cells with their extracellular matrix is maintained. We are also developing procedures for tendon cell isolation and cell culture. We will soon begin to culture cells on hylan and collagen gels and investigate the effects of mechanical loads on isolated cells. We intend to investigate tendon cell adhesion to hylan material containing various water contents. Further, we will investigate the possibility of using tendon cell-collagen constructs within hylan tubes for *in vivo* tissue engineering applications.

### **Infrastructure**

- I started my position at The Cleveland Clinic Foundation coincident with the submission of this proposal (Summer 1998). Since that time, I have spent considerable effort establishing my laboratory.
- I have purchased specialty equipment necessary to facilitate both biological and mechanical testing assays (*i.e.* SpectraMAX Plus Spectrophotometer, Instron 5543 materials testing machine with accompanying software and non-contacting video extensometer system).
- I have hired 2 technical support staff, one of whom is specifically devoted to this project.
- I have taken on 2 graduate students, whose projects will draw directly from this research program.

## **EVALUATION OF ENGINEERED SOFT TISSUES – Project 6 (PI: Brian Davis)**

---

The scope of this project was to develop means for the evaluation of the mechanical properties of engineered soft tissue constructs. It was initially proposed that these methods would be evaluated using skin of normal subjects and burn victims (of various age groups, various anatomical sites) via spectroscopic autofluorescence and video imaging techniques, the purpose being to evaluate changes that occur due to the natural aging and location on the body in the normal subjects. The burn victims would provide information about the differences, if any, between normal and regenerated skin. However, this project was disapproved by the Department of Defense, as they and the Cleveland Clinic Foundation were unable to resolve issues of patient injury liability associated with the study of live subjects. For this reason, a secondary proposal for this project was submitted on March 24<sup>th</sup>, 2000.

The second proposal involved the use of cadaveric tissue to eliminate the liability issues associated with the initial proposal. The same technique of laser fluoroscopy as initially proposed will be employed in this study. Previous studies (Jurgens *et al.*, 1995; Pierard and Lapiere, 1977) which have assessed mechanical properties of skin, have not related physiologically relevant skin properties to data collected via non-invasive optical methods. By employing cadaveric tissue samples, autofluorescence data could be collected from a specimen, which could then be subjected to mechanical testing. Both sets of parameters can be obtained from the same specimen in this manner.

In addition to the change in tissue source with the second proposal, the focus was shifted as well. Rather than examining regenerated skin in burn victims, the effects of aging in normal skin versus the effects of diabetes was proposed to be investigated. Despite this shift in focus, the same methods of laser fluoroscopy and video imaging techniques would still be employed.

Despite the change in protocol to the use of cadaveric tissue, this protocol still was not approved for use by the Department of Defense. In the second submission, the tissue source was identified as the Cooperative Human Tissue Network, Western Division, Case Western Reserve University (CWRU, Cleveland, OH). Persons reviewing the proposal were not familiar with this tissue bank and requested that we switch to a source they were familiar with, or provide further information on CWRU. Additionally, there were concerns as to the confidentiality of the tissue donor's identity. For these reasons, the secondary proposal was also denied, pending resolution of these issues. For these reasons, no progress has been made on this project.

During the preparation of this report, there were several communications between Dr. Davis (CCF) and Catherine Smith (DOD) regarding the status of this protocol. After many telephone calls,

faxes, and e-mails, we received word from Ms. Smith that the protocol had been cleared for approval, via a telephone conversation August 17<sup>th</sup>, 2000. This was confirmed by speaking with Sacelia Heller (DOD) on August 18<sup>th</sup>, 2000. Ms. Heller informed us that a formal written approval was being prepared and that work could begin on this project.

### **Future Work**

The study will now be initiated as laid out in the second submission (March 24<sup>th</sup>, 2000). The methods described in the proposal will be refined using cadaveric skin samples obtained from an approved source. Once these techniques are refined, and baseline data are collected from the cadaveric skin samples, these methods may be applied to tissue engineered skin and other soft tissues, as they become available.

## TISSUE ENGINEERING OF BONE

---

We have defined methods for harvesting bone precursor cells from aspirates of human bone marrow (Muschler *et al.*, 1997) and have characterized their ability to undergo osteoblastic differentiation in culture (Majors *et al.*, 1997). Bone precursor cells that can form osteoblastic colonies (Colony Forming Units – Osteoblastic, or CFU-Os) are relatively rare in human bone marrow aspirates. For this reason, the initial thrust of this project has been to selectively concentrate these cells, for use in developing tissue engineered bone constructs.

### **SELECTION AND CONCENTRATION OF BONE PRECURSOR CELLS - Project 7 (PI: Maciej Zborowski)**

---

Bone precursor cells have a potential, under suitable culture conditions, to differentiate into bone-forming cells (osteoblasts) *in vitro*, and therefore are a necessary cellular component of any future bone replacement therapy. The bone precursor cells are rare, approximately at 1/20,000 nucleated cells. Moreover, the molecular makeup of the cell surface of the early bone precursor cell distinguishing them from committed osteoblastic cells is poorly understood. Those two factors contribute to significant technical difficulties of isolating the bone precursor cells from the bone marrow aspirates.

We have identified a candidate molecular marker of the bone precursor cell, and perfected the cell separation technology suitable for bone precursor cell isolation experiments. The candidate molecular marker, hyaluronan, and its presence on rare cells in the bone marrow have been indicated in preliminary studies by Carol de la Motte (CCF, Colorectal Surgery), a collaborator on this project. The cell separation technology most suitable for the rare cell separation experiments is based on the method of the magnetic deposition on microscope slides.

There are indications that hyaluronan is present on the surface of early bone precursor cells (mesenchymal stem cells). Hyaluronan on the cell surface can be detected by its reaction with a highly specific, biotinylated protein. The bound protein is then identified by fluorescein isothiocyanate (FITC)-tagged avidin. This method was used to identify the very rare cells in bone marrow aspirated with a hyaluronan coat, under the fluorescence microscope (de la Motte). The human bone marrow cell suspension was obtained from normal donors through the collaboration with Dr. Muschler (Project 9). Cell smears were prepared on the microscope glass slides and stained for hyaluronan. Only a few cells were observed to fluoresce (Figure 17). The morphology of the fluorescent cells was consistent with that of an early progenitor cell (small, round cell without the characteristic features of the mature cell).

A prototype magnetic cell deposition system has been developed, with the assistance of the Engineering Analysis and Prototype Support Facility. The distinguishing feature of this prototype is that it allows for direct deposition of the magnetically labeled cells on the microscope slide. This system has been selected as being most suitable for isolation of rare cells, such as the bone precursor cell, because of its high recovery of the separated cells. A schematic illustration of the magnetic deposition system is presented in Figure 18. The system comprises a syringe pump with a set of five syringes, a magnet, and a set of five flow channels with connecting tubing. A characteristic feature of the magnet is a narrow interpolar gap which generates a highly non-uniform, well-defined fringing field. The interpolar gap, the source of the fringing field, is a strong attractor of magnetically susceptible material, in particular, the magnetically labeled cells. Before operation, the target cells are tagged using a suitable magnetic label; the flow channel is assembled, placed on the magnet and filled with the carrier medium. The flow channels are oriented in a perpendicular fashion to the interpolar gap. The test procedure consists of loading the cell samples into the syringes and activating the syringe pumps. The stream of cells passing across the interpolar gap is exposed to a strong, highly localized magnetic field that deflects the magnetic cells from the sample stream towards the channel wall facing the magnet. As a result, the magnetized cells are precipitated from the flowing solution onto the glass slide, forming a narrow band at the interpolar gap. Once the entire volume of the cell sample has been pumped across the interpolar gap, the flow channels are disassembled and the glass slide is detached from the flow channel (Figure 19). Cell adhesion to the glass slide prevents cell losses from the deposition band during fixation and staining steps or for subsequent culture. The non-tagged cells are washed away from the slide, thus providing a clear and unobstructed view of the few, deposited target cells (bone precursor cells). The stained slide is mounted on a standard microscopic substrate slide and is available for analysis.

The selective pre-enrichment of the bone precursor cells was accomplished by substitution of the FITC-avidin for ferromagnetic avidin (Miltenyi Biotec, Bergisch Gladbach, Germany). This then deposited cells with hyaluronan coats on the microscopic glass slides and provided a convenient, first step for further analysis of bone cell differentiation. Targeting the cell surface markers (hyaluronan) rather than intracellular markers in bringing the cells down on the microscope slide in the magnetic field ensures the viability of the target cells isolated on the slide. The type of the magnetic label proposed in this study, colloidal rather than the particulate one, ensures lack of interference from the label during the optical

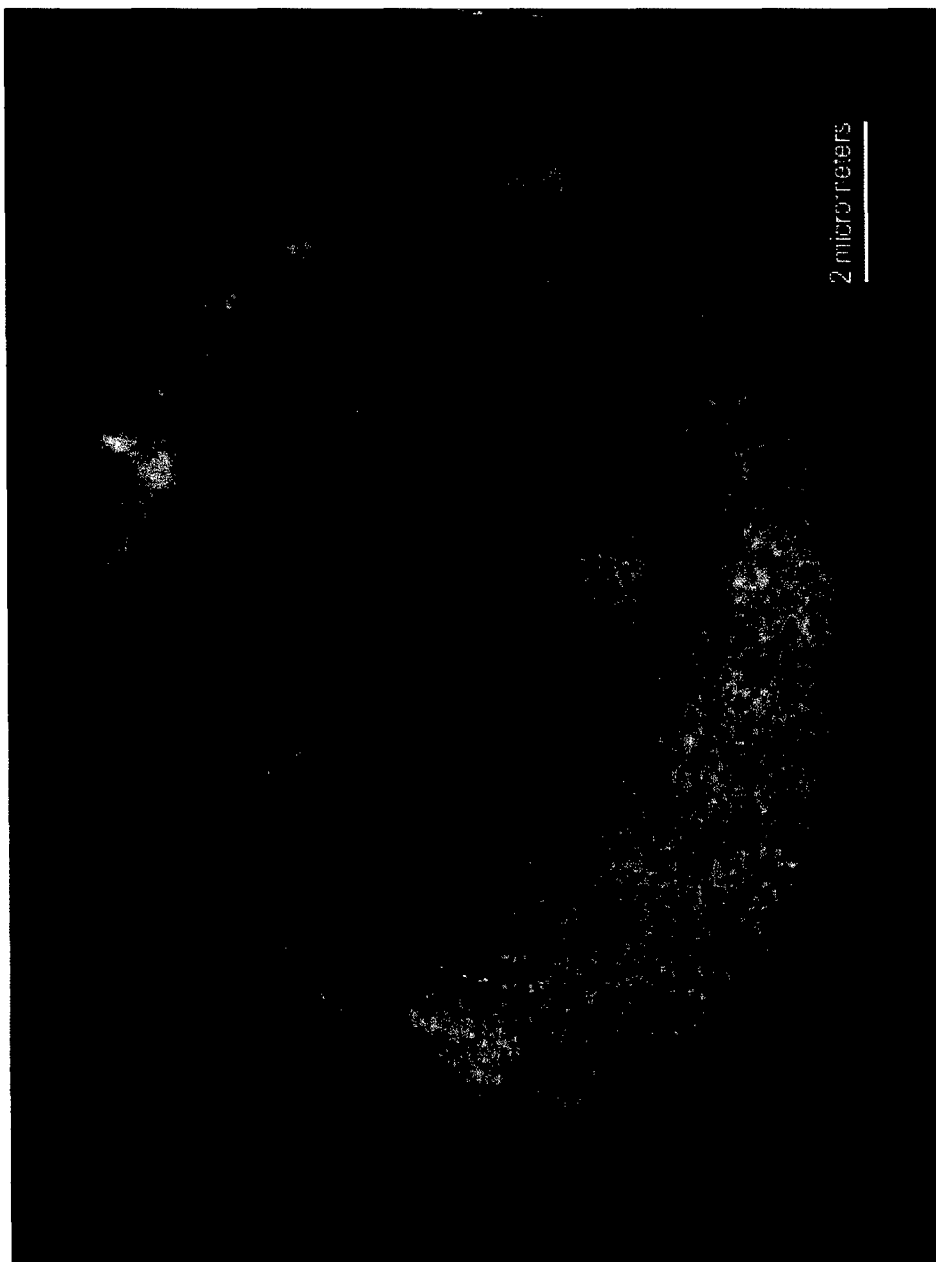


**Figure 17.** A microscopic image of the putative bone precursor cell stained with biotinylated protein and FITC-tagged avidin (de la Motte).



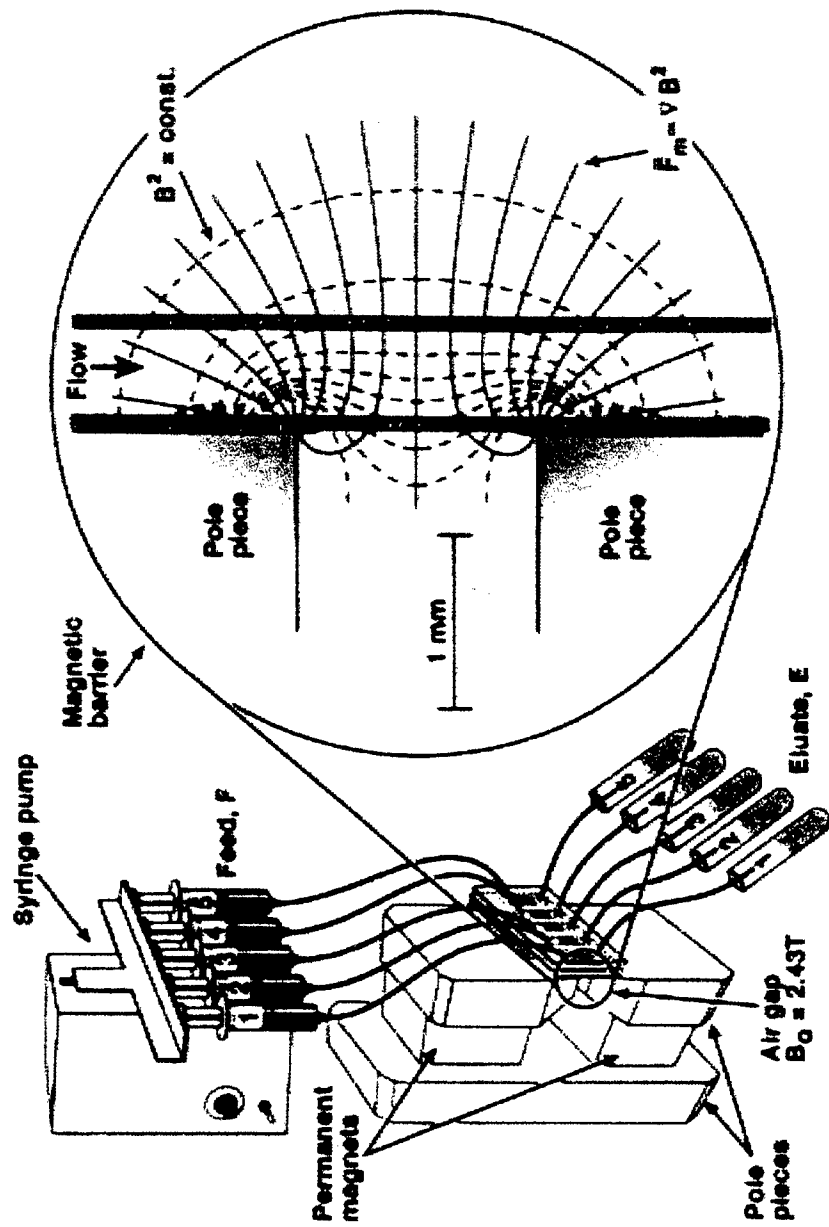


Figure 18. Magnetic slide deposition system

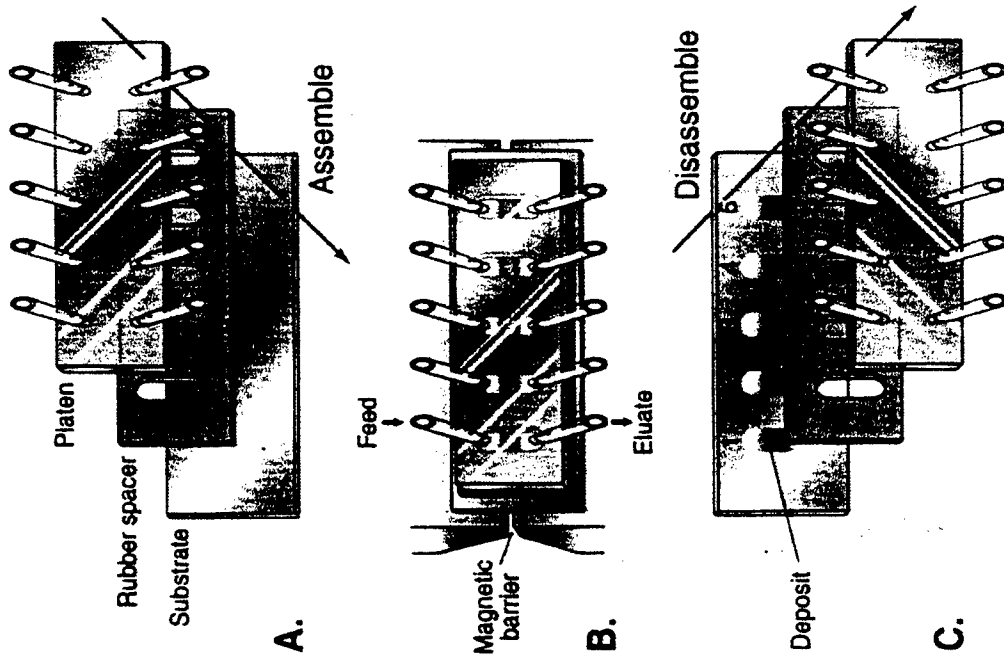


Figure 19. Magnetic deposition slide setup

analysis of the cell. In addition, the colloidal magnetic labels are known not to interfere with subsequent cell proliferation (unpublished results). The deposited cells may be further permeabilized and analyzed for the intracellular markers. These could include cytosolic and nuclear targets. Alternatively, the magnetically deposited cells could be transferred immediately into the tissue culture medium and allowed to proliferate under typical tissue culture conditions. Thus, the magnetic cell deposition on the microscope slide may offer a convenient platform for the molecular analysis of the precursor cell differentiation.

The capability of the magnetic cell deposition on the glass slides for isolation of rare bone precursor cell has been initially evaluated on an unrelated cell model system developed in our laboratory. It consisted of a mixture of cells of epithelial origin with the peripheral blood mononuclear cell (MNC) fraction. The distinguishing marker of the epithelial cells is the presence of the epithelial membrane antigen (EMA) on those cells and not on the circulating blood cells. Small, predetermined numbers of the epithelium-derived cells were added to a known number of the MNCs and the mixture was sequentially labeled with the anti EMA antibody and a secondary antibody conjugated to the magnetic, colloidal particle. The cell mixture was pumped through the magnetic deposition system, and the slides were stained for nucleated cells. The slides were subsequently evaluated for the presence of the epithelial-like cells that have significantly different morphology from that of the MNCs. Even at a very low frequency of 1/1,000,000 of the epithelium-derived cells to the MNCs in the mixture, the epithelium-derived cells could be seen on the magnetic deposition slides, with most of the MNCs washed-off of the slides. The estimated enrichment ratio of the epithelium-derived to the MNC on the slide was 100,000.

The current work focuses on the enrichment of the bone precursor cells on the magnetic glass slide using the biotin-tagged hyaluronan-binding protein, and a streptavidin-tagged magnetic colloid as a magnetizing agent. The initial experiments were performed by using the same experimental protocol developed for the mixture of the epithelium-derived cells in the MNCs (with the exception of the cell targeting reagent). The typical results show very few cells retained on the slides (Figure 20). The frequency and the morphology of the magnetically-selected cells on the slide are consistent with the properties of the bone precursor cells.

### **Future Work**

The research plan for year 2 of this project includes positive identification of the cells selected on the slide as bone precursor cells. This will be accomplished by the additional analysis of the deposited cells for the presence of hyaluronan on their surface, by blocking experiments (in which the hyaluronan



**Figure 20.** An example of the putative bone precursor cell selected on the magnetic deposition slide.

sites will be blocked by the non-biotinylated probe), and by determination of the expansion of the cells selected on the magnetic deposition slide in culture.

## **OPTIMIZING MATRIX FOR ATTACHMENT AND DIFFERENTIATION OF BONE PRECURSOR CELLS *IN VITRO* – Project 8 (PI: Ron Midura)**

---

Design of cell-matrix composites for tissue engineering of bone requires that the bone precursor cells attach to the matrix at a sufficient concentration to create an optimal environment for the cells to proliferate and differentiate into mature bone. The cell-matrix composite must also be designed to optimize the attachment of these cells and to support later stages of bone regeneration *in vivo*. Therefore, it was proposed that matrix materials with defined surfaces be tested *in vitro* for their ability to selectively attach bone progenitors and to support subsequent proliferation and terminal differentiation.

As stated previously (Projects 1, 2, and 4), it has been shown that current formulation of hylan gel do not support optimal cell attachment or proliferation without surface modification. Additionally, it has been shown that these gels lack sufficient mechanical strength and ability to handle to be adequately in a mechanically demanding structure such as bone (Projects 1 and 9). Therefore, the work that has been done on this project has been to refine techniques and evaluate osteoblastic cellular interactions with specific extracellular matrix molecules *in vitro*. This work was carried out in parallel to these other projects, such that when suitable hylan formulations are made available, this project can progress.

While efforts have been made in Project 4 to define the cellular interactions of NRASMCs with surface treated hylans; these interactions are cell type specific and must be clearly defined for bone precursor cells. To this point, two general classes of matrix adhesion molecules found in bone (collagen I and fibronectin) have been tested and shown to adhere both primary and cell line osteoblastic cells *in vitro*. Under controlled *in vitro* conditions, osteoblasts adhere quantitatively to both of these substrates. Additionally, osteoblast adhesion discriminates between these two matrix substrates using distinct integrin receptors. Osteoblast proliferation, differentiation and functional ability to deposit bone mineral *in vitro* are influenced greatly by their attachment to these matrix substrates. Thus, osteoblast attachment to type I collagen versus fibronectin results in different biological outcomes. It is presumed that the signal transduction processes induced by these adhesion reactions are distinct and provide different information content presented to the cells. This information will be useful for clearly defining the surface pretreatments necessary, if any, for application in the tissue engineering of bone.

### **Future Work**

We are poised to test osteoblast adherence to hylan gels *in vitro* and measure functional outcomes with respect to proliferation, differentiation and mineral deposition, once suitable substrate formulations are identified. Since hyaluronan exists around most osteocytes and preosteocytes but only a few

osteoblasts *in vivo*, we hypothesize that osteoblast adhesion to Hylan gels *in vitro* should induce their differentiation into osteocytes.

Further investigation into the specific aspects of these cellular interactions with extracellular matrix molecules will be continued in parallel to the other projects of the Tissue Engineering Initiative. Meanwhile the efforts of other collaborators (Projects 1, 2, 4, and 9) focus on the refinement and development of more appropriate hylan gels.

## **OPTIMIZING CELL-MATRIX COMPOSITES FOR BONE REGENERATION *IN VIVO* – Project 9 (PI: George Muschler)**

---

Performance of a cell-matrix composite *in vivo* will be influenced by several parameters which cannot be adequately modeled *in vitro*, including 1) the rate of diffusion of nutrients from extracellular fluid through the implanted matrix following implantation, 2) the metabolic activity of implanted cells prior to revascularization, 3) the volume of the defect and distance from the vascular perimeter to the center of the implant, 4) the vascularity of local soft tissue, 5) the quality and viability of local osseous and periosteal tissue, and 6) the capacity of the cell-matrix composite to induce prompt revascularization of the grafted defect.

Evaluation of these variables requires a model system in which the volume of the grafted defect is of sufficient size to make the limitations of diffusion and revascularization a limiting factor in at least parts of the defect (at least 1 cm in size). Furthermore, the anatomic site must be relevant to the bone environment in which most grafting for trauma is performed (*i.e.* the diaphysis of a long bone). To satisfy these model design requirements, we have developed the following canine femoral defect model.

### **Canine Femoral Defect Model**

*In vivo* experiments will utilize the canine femoral defect model employing *in vivo* oxygen tension monitoring that has been developed in our laboratory and was described in the initial DOD proposal. Outcome will be assessed based on bone formation (CT analysis), histology (decalcified histology), and oxygen tension history (early environment and rate of revascularization). Briefly, four identical (1 cm dia) defects are created in the lateral aspect of the straight proximal segment of the femur of male beagles (10-18 months, 12-16 kg). Through a lateral incision over the femur, a linear template is affixed to the lateral aspect of the femur (Figure 21). The template fixation screws are left in place to serve as defined markers for precise location of the defect grafts at the time of harvest. After placing the graft, the site is sealed with a snap fit cap. Each cap is designed to position and hold an oxygen sensing electrode (0.5 mm dia) in the precise center of the defect. The set of four caps and electrode wires are protected by a cover held with proximal and distal screws. Oxygen tension is reported telemetrically using a custom implanted device developed in the Department of Biomedical Engineering at the Cleveland Clinic, taking advantage of technologies and expertise gained in the Total Artificial Heart Program. (Figures 21 and 22).



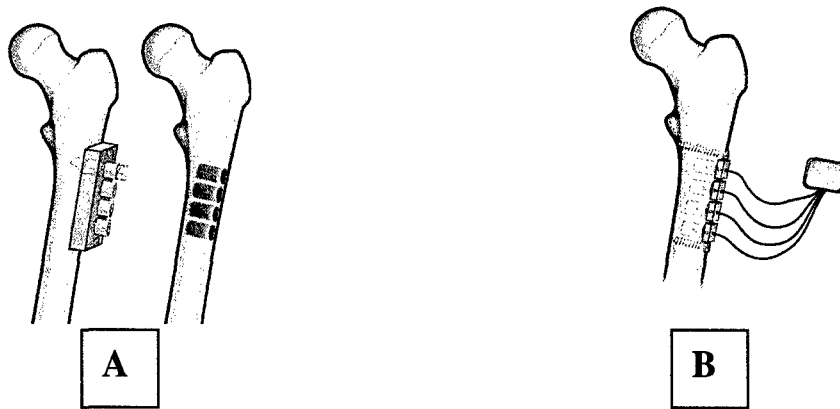


**Figure 21.** A) Schematic representing placement of the defect template over the lateral aspect of the femur and a representation of the femur following placement of the 4 grafts. B) Schematic of the defect caps with oxygen sensors in place.

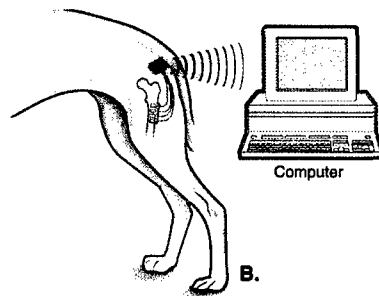


**Figure 22.** Schematic of the data collection system designed by the Cleveland Clinic Foundation, Department of Biomedical Engineering.

## **Selection of Graft Matrix Materials**

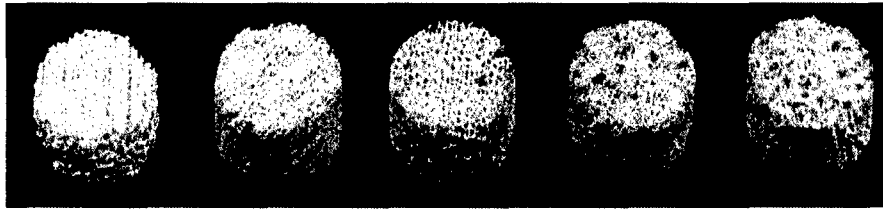
Prior to the onset of this current project we were stimulated by our observations of rapid adherence of connective tissue precursor cells (CTPs) to tissue culture plastic. We therefore investigated the use of available porous bone graft matrices as a surface for rapid concentration of CFU-Os. Completing a series of experiments, proposed in 1995, we found that ~40% of nucleated marrow cells and ~80% of CTPs will attach to either coralline hydroxyapatite or allograft bone matrix, a 2 to 1 selection of CTPs over other marrow cells. If placed into culture, CTPs will proliferate to cover these matrices with alkaline phosphatase (AP) producing colonies. (See Figure 23 and 24.) Similar attachment and proliferation can be achieved on polymeric surfaces (See Figure 25).

Using allograft cancellous bone (funded by NIH RO1 AR42997) and allograft bone powder (funded by Musculoskeletal Transplant Foundation), we have defined specific methods for use in an operating room setting which begin to optimize this method for selection and concentration of bone marrow derived cells. Important parameters include: pore size ( $\geq$  a 425-850 micron powder bed, to avoid entrapment of and sludging of cells in the matrix); linear flow rate (12-50 mm/min); and dilution of fresh marrow sample prior to loading (10:1, reducing viscosity and improving flow). Using these methods, CTPs can be rapidly concentrated 20 fold (~25,000/cc) in an allograft matrix, approaching the concentration of CTPs in native autogenous bone. This results in ~4 fold greater concentration than that shown on the far right in Figure 23.

As described in the initial proposal, we are now investigating the use of hyaluronan based matrices using these same methods. The materials initially selected in a meeting with Endre Balazs on April 11<sup>th</sup>, 2000 were hylan B beads. These beads were selected because it was believed that they possessed sufficient physical stiffness to maintain their shape when packed as a column or in a bone defect, with only moderate deformation. Furthermore, the chemistry of hylan gels preserve active functional groups which will allow selective surface modification during later phases of the project. The beads were evaluated having a mean diameter of approximately 1000  $\mu\text{m}$ .

## **Results**

Initial evaluation of the hylan B beads has been completed. This experience found that the hylan B beads could not be used effectively as a component in an affinity column. The beads proved to be too deformable, and as a result, progressively limited the flow of fluid and cells through the column and also resulted in clogging of the porous filters used to retain the beads in the column. Furthermore, when cells and matrix were mixed as a slurry, we found that that we were unable to separate the beads from the non-



Cells Loaded ( $\times 10^6$ )	0	10	20	40	100
Cells Retained ( $\times 10^6$ )	0	4.7	8.8	16	44
CTPs Retained	0	425	1100	1900	5400

**FIGURE 23.** Loading on Coralline Hydroxyapatite (HA) Ceramic Disks (15 mm dia. x 5 mm) – 9 days in culture .

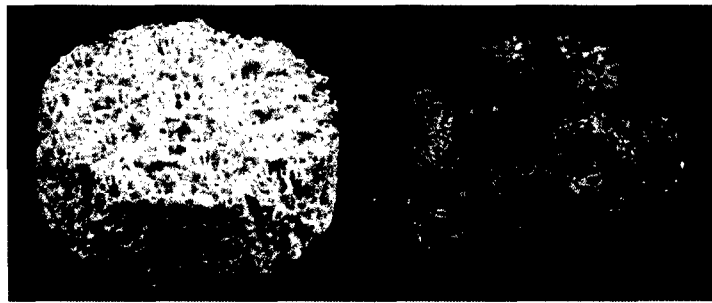


**FIGURE 24.** Proliferation of CTPs and Expression of AP on Coralline HA disks. Loading performed as in far right sample of Figure 23 above. Culture period: 9 Days (left) 24 Days (Right).



**FIGURE 25.** 3D confocal microscopy of a polystyrene bead (300 $\mu$  dia). This bead was loaded as part of a bead affinity column, similar to disks in Figure 23 above. Culture period: 9 days. Autofluorescence of the Fast Red stain localizes regions of cells expressing alkaline phosphatase (AP).

attached suspended cells, because the beads were isodense with the cells (*i.e.* did not settle from solution, nor was centrifugation effective). Subsequently, and most recently, a much denser fibrous freeze dried HA matrix was prepared at Biomatrix and evaluated. This preparation demonstrated improved function in a column. Fibrous clumps of matrix rehydrated leaving channels of sufficient size to allow fluid and cells to flow. However, clogging was still prevalent, as longer periods of rehydration were used, the matrix showed continued swelling making it progressively less able to support fluid flow and softening the gel to a state which was sufficiently deformable to clog the porous filter (as above). Further effort is being invested in designing other suitable modifications to generate a porous, open, high surface area HA matrix that is better suited for this application. No control preparations of bone have been prepared to date, as it is known from previous efforts that the bone matrix poses no such problems.

### ***In Vivo* Experiments**

Prior to initiating any *in vivo* experiments, it was required that the Cleveland Clinic Foundation Research Animal Facilities undergo a site visit by a veterinarian from the DOD. Following Dr. Calvin B. Carpenter's May 25<sup>th</sup> site visit, there were issues brought into question regarding the socialization and exercise regimens for dogs intended for use in this study. As a result, all *in vivo* experiments were put on temporary hold pending resolution of these concerns. These issues were addressed in a letter dated July 28, 2000 to Sacelia L. Heller at the DOD from Daniel R. Beyer, Research Division Administrator, Cleveland Clinic Foundation (see Appendix, pp. 159-162). We were recently informed that this letter sufficiently addressed Dr. Carpenter's concerns, and the temporary hold on *in vivo* experiments has been lifted. Therefore, once suitable replacements for the hylan B beads are identified, canine *in vivo* experiments will commence.

### **Future Work**

We are now investigating means of making the hylan matrix bed more rigid, so as to allow for the flow of cells through the matrix. As mentioned in Project 1, methods to be investigated for the improvement of the hylan matrix are increased concentrations of hyaluronan and increased levels of crosslinking. Of additional interest to this study would be the investigation of alternate geometries and physical forms of hylan. Examples to be investigated instead of beads include large diameter threads with a woven conformation, a porous "sponge-like" plug similar to those shown in Figures 23 and 24, and a hylan coating applied on a stiffer underlying matrix such as bone matrix or polymer beads. As already stated, once suitable replacements for the hylan B beads are identified, canine *in vivo* experiments will commence.

## **A MULTI-AXIAL EXTENSOMETER FOR GLOBAL MEASUREMENT OF BONE STRAIN – Project 10 (PI: Brian Davis)**

---

An extensometer that measures displacements in 3D and converts the data into global bone strain magnitudes and rates is described. This device is capable of monitoring physiological strains *in vivo*, and because of its 3D configuration can differentiate between bending and axial strains. The extensometer uses six paired capacitive sensors mounted to intraosseous pins and allows measurement of principal strain magnitudes and their direction, and maximum shear strain. Data are presented for validation of the device against a surface-mounted 60 degree strain gage rosette in an acrylic specimen under dynamic 4-point bending, with sinusoidal and square wave loading inputs up to 4700  $\mu\epsilon$  and 20 Hz. Pearson's correlation coefficient ( $r$ ) between extensometer and strain gage ranged from 0.711 (at 20 Hz) to 0.999 (at 1 Hz). This type of device is capable of tracking strain up to strain rates in excess of 90,000  $\mu\epsilon/\text{sec}$ .

### **Mechanical Assessment**

Researchers on this project have focused on measurement of strain in bone to more fully understand the adaptation of bone to its functional environment. Knowledge of strains experienced during normal daily activities has direct implications in the study of age related bone loss, post-menopausal osteoporosis, fracture healing, and disuse osteoporosis. Both (i) surgical staples and (ii) resistance-type strain gages have been used *in vivo* in humans and animals. However, these methods of strain measurement have certain limitations, namely, requirements for surgery and use of materials that could irritate the surrounding tissues.

The device described is an extensometer, which uses non-contact capacitive probes as the displacement sensing technique. The probes are mounted on acrylic bodies to three intraosseous pins that are implanted into and protrude from the bone (Figure 26). The probes, situated in pairs, are oriented to each other pair by 60°, as such the term “delta extensometer” is used to distinguish the device from an axial extensometer. Both the device described here and staple-type gages eliminate the need for degreasing agents, chemical bonding agents, or surface preparation such as drying, sanding, and filling associated with resistance-type bonded strain gages; an advantage for *in vivo* applications. A further advantage offered by the delta extensometer is the ability to distinguish axial strains from strains due to bending from one measurement site. Calculation of strains due to bending require that strain gage instrumentation, including staple-type gages, be mounted to opposing faces of the specimen, which is not always feasible *in vivo*.

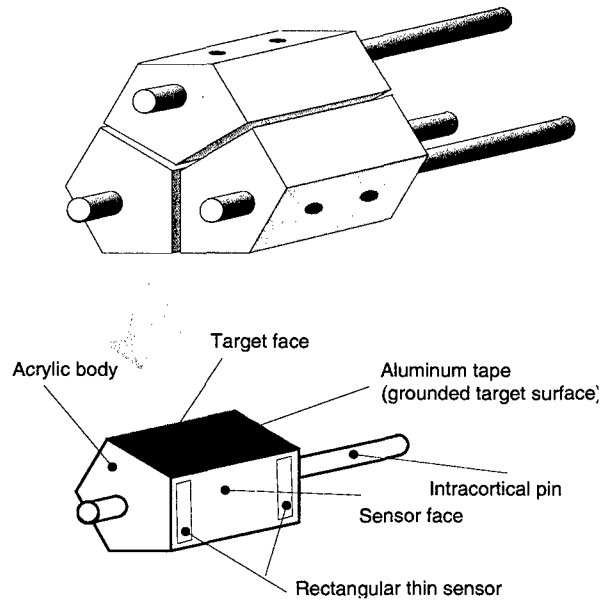


**Figure 26.** Extensometer uses six capacitive sensors mounted to acrylic bodies which are attached to intraosseous pins. The acrylic bodies are mounted to the protruding ends of the pins after implantation.

Validation tests of the extensometer were performed in dynamic four point bending up to 20 Hz in an acrylic specimen (measuring 25.4 X 25.4 X 304.8 mm long), instrumented with the capacitive extensometer and, as a comparison strain measurement, a delta rosette strain gage (Measurements Group, WA-03-030WY-120). The strain gage rosette was mounted to the specimen surface next to the extensometer insertion site but within the load span. The strain gage was placed outside the area formed by the intraosseous pins due to the size of the rosette (gage length for the extensometer was 7.1 mm), and to minimize the possibility of strain gradients due to stress concentrations from the mounting holes from interfering with the strain gage output. The grid 1 (reference grid) direction for both gage and extensometer was oriented 22.5 ° from the long axis of the specimen to maximize signal from each of the three grids. Principal strain levels in the specimen reached 4700  $\mu\epsilon$ .

Sensors (HPS-1X4C-A-200-FX, Capacitec, Inc., Ayer, MA) were calibrated at the factory over an air gap of 0 to 1.016 mm, corresponding to -5 to +5Vdc, or a linear range of +/- 71,000 $\mu\epsilon$  with a 7.1-mm gage length. Amplifier resolution (Model 4100-S, Capacitec, Inc., Ayer, MA) is +/-0.01% of full scale, or +/- 1 mV. The engineering unit conversion is  $1.016 \times 10^{-4}$  mm/mV. Data were collected with a 16-bit

A/D board (AT-MIO-16E-10, National Instruments, Austin, TX), and processed through a custom LabVIEW™ data acquisition and analysis program (National Instruments, Austin, TX) running on a personal computer. Data were oversampled at 5000 Hz, and plotted as 10 sample averages, giving an effective sampling rate of 500 Hz. Capacitive sensor resolution is improved by oversampling and averaging due to the oscillatory nature of the modulation /demodulation circuitry (carrier frequency =15 kHz) used by the amplifiers. A gain stage and anti-aliasing filter (8300 XWB, Preston Scientific, Anaheim, CA) with cutoff frequency of 100 Hz was used prior to digitizing extensometer data.

Strain at the specimen plane of interest (*e.g.*, the bone surface) is calculated from measurements obtained from sensor pairs that lie outside of the specimen plane. The basic concept is that vectors describing the direction and position of each pin relative to an adjacent pin can be determined by two measurements of the distances between the pins. (If the pins always remained parallel to each other, only one distance measurement would be needed to ascertain if the pins had moved towards, or away, from each other.)

The calculated strain at the surface of the acrylic validation specimen tracked strain gage response to sinusoidal and square wave inputs up to 20 Hz and a maximum strain rate of 50,000  $\mu\epsilon$ /sec in four-point bending with the maximum mean percent error between extensometer and strain gage output ranging up to 11.6 % (measured as a % of maximum strain for that trial, not as a % of full scale). Pearson's correlation coefficient (*r*) ranged between 0.711 (for the 20 Hz sinusoidal condition) to 0.9996 (for the 1 Hz sinusoidal condition.)

### **Significance**

Based on these data, the extensometer is suited for measuring strains above 100  $\mu\epsilon$ . It is possible to change the linear range and associated resolution (and thereby measure smaller strains) by using different sensor models and calibrations depending on the application. Where access to the specimen is limited, surfaces are rough, porous, or not able to be absolutely clean, where strain magnitudes are expected to be relatively high, and for *in vivo* measurements, this device has significant advantages over current methods.

### **Future Work**

As tissue engineered bone becomes available for testing, this technology can be applied to the novel constructs for strain evaluation. These measurements can then be compared to strain readings taken from native bone for direct comparison.

## TISSUE ENGINEERING SUPPORT FACILITIES

---

### **Imaging Support Facility**

---

The Imaging Support Facility is developing and employing technologies necessary to serve the needs of all relevant projects. The Facility provides prompt and definitive histologic, immunologic, and *in situ* analysis for bioengineered tissue specimens.

#### **Confocal Laser Microscope Imaging**

As described in the initial proposal, engineered tissues need to be evaluated for their spatial and temporal expression of specific biological markers that are present in native tissue. For reasons previously stated, the confocal laser microscope is the ideal tool for this analysis. A Leica TCS SP Confocal Microscope was purchased with the funds allocated. The instrument arrived at the Cleveland Clinic Foundation mid August 2000. Facilities Engineering is currently making renovations to the space allocated for its installation. Target date for the system to be operational is mid September 2000.

#### **Phosphoimager**

As described in the initial proposal, engineered tissues will need to be evaluated for the quality and quantity of specific gene expression patterns unique to their native tissue homologues. When combined with specific DNA and RNA probes, a phosphoimager can unambiguously identify and accurately measure these gene expression patterns. The Storm 860 phosphoimager (Molecular Dynamics, Inc.) described in the initial proposal, has not yet been purchased. Instead, Molecular Dynamics, Inc. now has a new model, Typhoon, which can handle chemoluminescence, fluorescence, as well as phospholuminescence. Both systems come with a pentium workstation as previously described. Since it would take some time to have tissue engineered constructs to evaluate by this method, the purchase of the phosphoimager has been pushed back to year two of the project.

#### **Micro CT Station**

As outlined in the initial proposal, a Micro CT Station and an Octane/SSE Workstation were to be purchased as capital equipment for support of the Image Analysis Core. The Micro CT will allow us to analyze tissue engineered constructs with 3D volume imaging at a high spatial resolution (~10  $\mu\text{m}$ ). Rather than purchasing a commercially available Micro CT Station, the funds allocated for the Micro CT and Octane/SSE Workstation were combined to allow for the purchase of components to build a more sophisticated Micro CT Station. In place of the Octane/SSE Workstation, a high powered Pentium Workstation was purchased to support the custom Micro CT. To date, all major components for the



construction of the Micro CT Station have been purchased and are on site. The Micro CT Station should be functional and available for use by all investigators on this project by December 2000.

### **Automated Quantitative Microscopy**

The traditional method of analysis of tissue sections and cellular data has been, and continues to be, manual light microscopic interpretation. The accuracy of such tedious and laborious manual methods depends largely on the skill of the user, and these methods do not allow further analysis of cell shapes and locations. In recent years, however, advanced histologic techniques have been combined with computerized image processing and analysis. These techniques continue to evolve in response to the recognized limitations of subjective or semi-quantitative data analysis and growing needs for obtaining large amounts of objective, quantitative data.

Our Department's Biomedical Imaging Group (<http://www.ccf.org/ri/bme/image>) has developed and continues to refine an automated image analysis system for use in quantitative microscopy. This system is versatile, allowing analysis of stained tissue sections, *in situ* hybridizations, confocal images, or cell cultures and provides the data in unambiguous statistical terms. This system also provides information that is difficult or impossible to obtain from manual assessment (*e.g.* size, shape, and orientation). The system will have immediate application in this proposal for quantification of the following:

- Cell morphology, including total cell counts, determination of cell area, cell color, shape analysis, and position/location data. These analyses will be aided by routines that perform opening and closing operations, boundary detection, global filling and decomposition.
- Immunochemical or routine stain analysis, by chromagen color, purity, and intensity.
- Gross morphologic features such as cellularity, blood vessel luminal area, vascular density, extent of collagen infiltration, and continuity of elastin fibers.
- Grain counting techniques using grey-scale analysis of *in situ* hybridizations.
- *In situ* hybridization chromagen distribution using advanced color segmentation algorithms.
- Quantification of fluorescence intensity in immunohistochemically stained tissue.

The software for this automated image analysis system is nearly complete. It is currently functional on high-powered workstations and is being adapted for application and usage on Windows NT systems. This adaptation will allow nearly everyone in our Department to implement this technology.

## **File Server**

Finally, a highly sophisticated F520-8N-256-14D9 File Server (StorNet, Inc., West Chester, PA) was purchased and is currently being used by all investigators in the Tissue Engineering Initiative and Imaging Core. This equipment is installed and functional. It has been networked to support multiple image data collection systems within the scope of the Tissue Engineering Initiative.

## **Engineering Analysis and Prototype Support Facility**

---

As described in the initial proposal, the Department of Biomedical Engineering houses an Engineering Design and Analysis Group as well as Mechanical and Electrical Prototype Facilities. Through the first year of this award period, these groups have contributed several novel implements to our tissue engineering research efforts.

## **Engineering Design and Analysis Group**

---

### **Mark VI Magnetic Flow Sorter**

This cell separation flow chamber was designed for use in separating and selectively concentrating bone precursor cells (see Project 7 – Zborowski). The Engineering Design and Analysis Group and Prototype Support Facility were brought into the project to begin moving the technology from a research focus to a product development focus. The end result of their work being the design and fabrication of a “clinical”, full-scale disposable prototype. In the course of designing this prototype, guided by computational fluid dynamics simulations, many considerations and design criteria were evaluated. These items included the desired cell sorting performance goals, the manufacturability of the design, the internal flow characteristics and biocompatibility of surfaces and materials.

### **Tendon Tissue Slicing Apparatus**

Initially, the patellar tendon was investigated for material property evaluation in support of the tendon cell project (Project 5 – Derwin). The primary objective of this work was to develop a technique for creating uniform tissue samples from a single patellar tendon. The Engineering Design and Analysis Group developed a design concept using Pro/Engineer modeling software (Parametric Technologies Corporation, Waltham, MA), for an apparatus that would allow for up to 4 uniform sections to be taken from a single patellar tendon while under tension. From Dr. Derwin’s work, it was found that tendon material from different regions of these specimens did not necessarily appear uniform in mechanical or

biochemical properties, despite their uniform geometry. For this reason, this project is currently on hold, pending investigation of the baseline properties of canine *flexor digitorum superficialis* (FDS) tendons.

### **Tendon Tissue Cyclic Loading Apparatus**

Preliminary design work was begun on a device to perform cyclic loading of tendon tissue samples maintained in culture media, with the entire system contained in an incubator to maintain physiologic conditions. Several key design requirements include small overall tendon displacements (1-2 mm), a gripping mechanism to prevent tissue necrosis from compression of the tendon, components which can be disassembled for cleaning and sterilization between tests, ability to run multiple samples simultaneously, and test units which will maintain sterility of the media through the duration of the tests (several weeks). This project will proceed following final selection of the tendon source, its corresponding dimensions, and final determination of the functional requirements.

### **Infrastructure**

- Two Dell personal computers (Dell Dimension XPS T600 Pentium III, Dell Dimension XPS T600 Workstation 410, Dell Computer Corporation, Round Rock, TX) were purchased in place of the originally proposed Integraph TDZ-2000 NT Workstation. The primary reason for this change was the recent advances in the processor (computational) speed and graphics capabilities for the personal computers. These new personal computers are capable of either running computational fluid dynamics software locally on the PC or interfacing with the CCF/BME departmental Unix network for very high end computations via x-windows emulators (run and view computations from PC). The Dell computers also provide the capability for performing daily word processing, spreadsheet calculations, and e-mail operations.
- A full time engineering staff member was hired as support for this project. The new hire, with an MS in Chemical Engineering, was hired to function in a "hands on" and consulting capacity for all 10 of the Tissue Engineering Initiative projects.

### **Prototype Support Facility**

---

The Prototype Support Facility has produced several custom fixtures for use in the Tissue Engineering Initiative projects. The following is the summary of the custom fixtures fabricated for use in these projects:

#### **Project 5 (Derwin)**

- Grips for mounting tendon explants in a cross sectional area device, as well as the Instron device used for mechanical testing (Figure 15A).

- Tissue mounting device for maintaining the above mentioned grips (with tendon) in tension during transport from the cross sectional area device to the Instron testing machine (Figure 15B).
- Mounting fixtures to attach custom grips to Instron mechanical testing device (Figure 15C).
- Rotational device for evaluation of tendon cross sectional area under tension (Figure 13).

#### **Project 10 (Davis)**

- Intracortical pins for mounting the capacitance based sensors into bone, used for evaluating local bone strain (Figure 26).

### **Electronics Core**

---

The Electronics Core has also produced some custom instrumentation for use in the Tissue Engineering projects. The following device is currently in use:

#### **Project 5 (Derwin)**

- Electronic control unit for rotational device, to allow for hands free operation, while evaluation under a stereomicroscope

## KEY RESEARCH ACCOMPLISHMENTS

---

1. Evaluated the biomechanical properties of various hylan gel formulations, as provided by Biomatrix, Inc. (Ridgefield, NJ), using established protocols for mechanical testing (Project 1).
2. Defined methods for determining the concentration of hyaluronan in the hylan gel preparations (Projects 1 and 4).
3. Defined methods for determination of degree of di-vinyl sulfone crosslinking, as well as establishing the effect of crosslinking on the modulus (stiffness) of the hylan gel preparations (Project 1).
4. Initiated gene therapy investigation to improve function of endothelial cell seeded vascular grafts (Project 3).
5. Implemented a well-defined investigation into the benefits of pretreatment of the hylan gel formulations to enhance cell attachment and proliferation (Project 4).
6. Established baseline biochemical and mechanical properties of native tendon tissue for comparison to future tissue engineered tendon constructs (Project 5).
7. Resolved liability issues involved with the study of live subjects, so that methods can be developed for the evaluation of engineered soft tissues (Project 6).
8. Developed prototype magnetic cell deposition system for the selective isolation and concentration of bone precursor cells (Project 7).
9. Developed methods for the assessment of bone precursor cell attachment, proliferation, and mineralization on hylan substrates (Project 8).
10. Ruled out the use of hylan beads as a substrate for use in a previously developed *in vivo* canine femoral defect model (Project 9).
11. Developed and tested prototype capacitive extensometer for the evaluation of bone strain *in vivo* (Project 10).
12. Incorporated several new imaging and image analysis systems into the Department of Biomedical Engineering's Imaging Support Facility.
13. Developed and fabricated many prototype devices to facilitate the various tissue engineering projects through collaborations between the investigators and the Department of Biomedical Engineering's Engineering Analysis and Prototype Support Facility.

## REPORTABLE OUTCOMES

---

1. An elaborated research proposal based on the current work was submitted to the American Heart Association (Ohio Valley Affiliate) by Dr. Anand Ramamurthi, a post-doctoral research associate and resulted in the granting of a 2-year postdoctoral fellowship (\$ 58,000/ 2 years, AHA ID# 0020393B).
2. Technical abstracts based on the study of cell attachment on hylans have been accepted for presentation at the Hyaluronan 2000 meeting in Wrexham, Wales, UK (Sept 2-8, 2000) and the Biomedical Engineering Society (BMES) Annual Meeting in Seattle, WA (October 13-16, 2000) (see Appendix).
3. "The effect of the degree of crosslinking on the modulus of hylan" was completed by Ms. Maida Ann Ludwig, Department of Biomedical Engineering, Case Western Reserve University, as a research requirement (Thesis, see Appendix) for the granting of an M.S. degree in Biomedical Engineering (August 2000).
4. "Design and test of an extensometer for global measurement of bone strain suitable for use *in vivo* in humans" was completed by Ms. Gail Patricia Perusek, Department of Mechanical and Aerospace Engineering, Case Western Reserve University, as a research requirement (Thesis, see Appendix) for the granting of an M.S. degree in Mechanical Engineering (May 2000).
5. Publication of the underlying work upon which Project 2 is based.

A preformed basal lamina alters the metabolism and distribution of hyaluronan in epidermal keratinocyte "organotypic" cultures grown on collagen matrices. Published in *Histochemistry and Cell Biology* (2000) 113: 265-277. By Vincent C. Hascall and Michael Hogg (CCF) in collaboration with Raija H. Tammi (lead author), Markku I. Tammi, Sanna Pasonen, and Donald K. MacCallum.

*All publications listed above are included in their entirety in the Appendices that follow.*

## CONCLUSIONS

---

Our work over the previous year has shown that gels based on cross-linked hyaluronic acid (hylan) are suitable materials for development of biological implants. While the strength of hylan gels in the present form is insufficient for their use as primary tissue replacements, they possess mechanical properties that may be suitable for the development of epidermal replacements and non-stress intensive physiological applications. Further chemical/structural modifications are necessary to improve upon the strength of these gels (*i.e.* increased hyaluronan concentration, increased crosslinking). Additionally, it is believed that gel reinforcement via synthesis of collagen-rich and elastin-rich matrices by attached cells can contribute to added gel strength and/or elasticity.

It has been shown that cells (NRASMCs, Project 4) attach and proliferate actively on hylan gels treated with cell adhesion proteins (collagen I, ECM gel, laminin, fibronectin). Cell attachment and multiplication was most prolific on particulate hylan gels, possibly due to their comparatively rough surface, which promotes protein adherence and provides greater anchorage for attaching cells. It is believed that cells attached on such gels show a highly spread morphology for the same reason. In contrast, solid gels have relatively smooth surfaces, which may not provide sufficient anchorage for cells. However, the current study clearly demonstrates that cell-hylan composites show promise towards the successful development of bioengineered materials. It is believed that the compositional changes previously mentioned will also lend properties more advantageous to cell attachment and proliferation.

As mentioned previously, methods to be investigated for the improvement of the hylan matrix are increased concentrations of hyaluronan and increased levels of crosslinking. Current formulations of hylan are available as thin films, solid gels, particulate gels, and microbeads. These conformations do not possess physical characteristics that lend themselves to application in the tissue engineering of bone. However, alternate geometries and/or physical forms (*i.e.* woven large diameter threads, porous cylindrical plugs, hylan coating on a stiffer underlying matrix) of hylan may prove useful in such applications.

While the current formulations of hylan gel have been shown to have some limitations in the applications proposed, the results of Projects 1 and 4 do show promise for their use in tissue engineering applications. Considerable effort will be spent in year 2 of this initiative to address the compositional and conformational changes described herein. The identification of substrates with greater mechanical strength and rigidity will allow for further advancement in those projects which require greater structural integrity (*i.e.* vascular tissue, tendon, bone).

## REFERENCES

---

- Balazs EA and Denlinger JL. Clinical uses of hyaluronan. In *The Biology of Hyaluronan* (Ciba Foundation Symposium #143). (Eds. Evered D and Whelan J). John Wiley & Sons, Chichester and New York: 265-280, 1989.
- Calabro A, Benavides M, Tammi M, Hascall VC, Midura RJ. Microanalysis of enzyme digests of hyaluronan and chondroitin/dermatan sulfate by fluorophore-assisted carbohydrate electrophoreses (FACE). *Glycobiology*. **10**[3]: 273-281, 2000.
- Calabro A, Hascall VC, Midura RJ. Adaptation of FACE methodology for microanalysis of total hyaluronan and chondroitin sulfate composition from cartilage. *Glycobiology* **10**[3]: 283-293, 2000.
- Cetta G, Tenni R, Zanaboni G, De Luca G, Ippolito E, De, Martino C, Castellani AA: Biochemical and morphological modifications in rabbit Achilles tendon during maturation and aging. *Biochem J* **204**: 61-67, 1982.
- Fung YC. *Biomechanics, mechanical properties of living tissues*. Springer-Verlag, New York, 1993.
- Hannafin JA, Arnoczky SP, Hoonjan A, Torzilli PA: Effect of stress deprivation and cyclic tensile loading on the material and morphologic properties of canine flexor digitorum profundus tendon: an *in vitro* study. *J Orthop Res* **13**: 907-914, 1995.
- Jurgens C, Porte T, Wolter D, Schmidt HG, Kricheldorf HR, Kreiser-Saunders I. Development and characterization of an absorbable temporary wound dressing [German]. *Unfallchirurg*, **98**[4]: 233-240.
- Kaderr KN, Akella R, Ziats NP, Lakey LA, Harasaki H, Ranieri J, Bellamkonda RV). ENOS over-expressing endothelial cells inhibit platelet aggregation smooth muscle cell proliferation *in vitro*. Accepted for publication, *J Tissue Eng*.
- Larsen NE, Leshchiner E, Balazs EA, Belmonte C. Biocompatibility of hylan polymers in various tissue compartments. In *Polymers in Medicine and Pharmacy* (Proceedings of the Materials Research Society, Spring Meeting, April 17-21, 1995, San Francisco, CA). (Eds. Mikos AG, Leong KW, Radomsky ML, Tamada JA, Yaszemski MJ). Materials Research Society, Pittsburgh, PA: 149-153.
- Ludwig MA. The effect of the degree of crosslinking on the modulus of hylan. Case Western Reserve University, *Thesis*, August 2000.
- Majors AK, Boehm CA, Nitto H, Midura RJ, Muschler GF. Characterization of human bone marrow stromal cells with respect to osteoblastic differentiation. *J Orthop Res* **15**: 546-557, 1997.
- Miller RR and McDevitt CA. *Anal Biochem*. **192**[2]: 380-383, 1992.
- Mulholland DS and Gotleib AI. Cell biology of valvular interstitial cells. *Can J Cardiol*. **12**[3]: 231-236, 1996.



Muschler GF, Boehm C, Easley K. Aspiration to obtain osteoblast progenitor cells from human bone marrow: the influence of aspiration volume. *J Bone Joint Surg* **79A**[11]: 1699-1709, 1997.

Osborne CS, Barbenel JC, Smith D. Investigation into the tensile properties of collagen/chondroitin-6-sulfate gels: the effect of crosslinking agents and diamines. *Med Biol Eng Comput*, **36**[1]: 129-134, 1998.

Pierard GE, Lapiere CM. Physiopathological variations in the mechanical properties of the skin. *Arch Derm Res* **260**: 231-239.

Stegeman H and Stalder K. TITLE. *Cin Chim Acta*. **18**: 267-273, 1967.

Tammi RH, Tammi MI, Hascall VC, Hogg M, Pasonen S, MacCallum DK. A preformed basal lamina alters the metabolism and distribution of hyaluronan in epidermal keratinocyte "organotypic" cultures grown on collagen matrices. *Histochem Cell Biol*. **113**: 265-277, 2000.

Uchida N, Kambic H, Emoto H, Chen J-F, Hsu S-L, Murabayashi S, Harasaki H, Nose Y. Compliance effects on small diameter polyurethane graft patency. *J Biomed Mater Res* **27**: 1269-1279, 1993.

Vogel KG, Keller EJ, Lenhoff RJ, Campbell K, Koob TJ. Proteoglycan synthesis by fibroblast cultures initiated from regions of adult bovine tendon subjected to different mechanical forces. *Eur J Cell Biol*. **41** [1]: 102-112, 1986.

## APPENDICES

---

Disclosure Letter	65
The Effect of the Degree of Crosslinking on the Modulus of Hylan (Masters Thesis)	66
A Preformed Basal Lamina Alters the Metabolism and Distribution of Hyaluronan in Epidermal Keratinocyte "Organotypic" Cultures Grown on Collagen Matrices	145
Cell Attachment on Surface-Treated Hylan Gels (Hyaluronan 2000 Conference)	158
Cell Attachment on Surface-Treated Hylan Gels (2000 BMES Annual Meeting)	159
Correspondence with Sacelia L. Heller	160
Design and Test of an Extensometer for Global Measurement of Bone Strain Suitable for Use <i>In Vivo</i> in Humans (Masters Thesis)	164

August 29, 2000

Commander  
U.S. Army Medical Research and Materials Command  
ATTN: MCMR-RMI-S  
504 Scott St.  
Fort Detrick, MD 21702-5012

To Whom It May Concern:

This letter is to serve as a disclosure limitation in regard to the information contained in this annual report, "Tissue Engineering Initiative," Cleveland Clinic Foundation, Department of Biomedical Engineering (Award Number: DAMD17-99-1-9475).

As stated in the Reportable Outcomes section of this report (page 60), there have been 5 publications based on the work described in this document (2 thesis, 2 presentation abstracts, 1 peer reviewed article). All of these publications are included, in their entirety, in the Appendix of this report. However, all other data contained in this document are as yet unpublished and should not be deemed suitable for public release. As requested, the abstract covers the purpose, scope, and major findings from this work. Therefore, all pages in the body of the report should be considered proprietary, and only the abstract and Appendix should be deemed suitable for public release.

Although the report requirements specify that stapling in the upper left-hand corner is the preferred method of binding, it is inappropriate in this case due to the volume of this report. Pursuant to a telephone conversation with Virginia Miller (DOD, on behalf of Judy Pawlus), it was recommended that the report be secured with several large rubber bands, as the report is approximately 300 pages in length. We apologize for our inability to meet this single requirement. Should there be any other questions regarding this report, please do not hesitate to contact us.

Sincerely,

Vincent C. Hascall

THE EFFECT OF THE DEGREE OF CROSSLINKING  
ON THE MODULUS OF HYLAN

by

Maida Ann Ludwig

Submitted in partial fulfillment of the requirements  
for the degree of Master of Science

Research Advisor: Dr. Vincent Hascall, Ph.D.

Cleveland Clinic Foundation

Academic Advisor: Dr. Ravi Bellamkonda, Ph.D.

Case Western Reserve University

Department of Biomedical Engineering

CASE WESTERN RESERVE UNIVERSITY

August, 2000

THE EFFECT OF THE DEGREE OF CROSSLINKING  
ON THE MODULUS OF HYLAN

ABSTRACT

by

Maida A. Ludwig

Biomaterials are an integral part of clinical medicine and advances made in this field are sure to have profound effects. An optimal biomaterial will not elicit an immune response by the body, is suitable for various applications, is easy to handle, and can be altered to match its intended use. Hylan is a biomaterial that may possess all of these characteristics.

If the relationship between the degree of crosslinking and the modulus of hylan can be defined, manufacturers will be able to produce hylan with an appropriate modulus for a specific application. To define this relationship, FACE (fluorescence-activated carbohydrate electrophoretic) analysis was used to explore the degree of crosslinking of hylan. Compression testing and tensile testing were performed to determine the modulus of hylan materials.

It was found that the concentration (mg/ml) of releasable hyaluronan found by FACE analysis correlated reasonably well with the compressive modulus of hylan. If the production of hylan is more tightly controlled, this relationship may be even more reliable than demonstrated here.

## DEDICATION

To my family, especially my parents, who managed to always lead me down the right path, while allowing me to believe the whole time that I was the one making the decisions.

## ACKNOWLEDGEMENTS

I would like to thank my research advisor, Dr. Vincent Hascall, for all his help, patience, and guidance. I would also like to thank Dr. Anthony Calabro, Jr., for his assistance in designing the experiments and interpreting the results. I thank Dr. Ivan Vesely and Ed Barber for guiding the mechanical testing aspects of this project. I also thank my other committee members, Dr. Ravi Bellamkonda, and Dr. Steven Eppell, for their help with my thesis, as well as being professors who motivated me to learn.

I would like to thank everyone in the lab: Maria Benavides, Aniq Darr, Csaba Fulop, Ph.D., Michael Hogg, Ph.D., and Durba Mukhopadhyay, Ph.D., for all their help and the favors they did for me without question.

I again thank my family for all their love and support throughout the years. I thank Matthew Mendez for his unfailing friendship, patience, help and support, and for always being there when I needed him most.

I thank Biomatrix, Inc. of Ridgefield, NJ, for supplying the hylan samples, and especially Julie Whetstone for working with me. Financial support was provided by the Department of Defense of the U.S.A. and the Cleveland Clinic Foundation, of Cleveland, Ohio.

## TABLE OF CONTENTS

ABSTRACT	ii
DEDICATION	iii
ACKNOWLEDGEMENTS	iv
TABLE OF CONTENTS	v
LIST OF FIGURES	ix
LIST OF TABLES	x
LIST OF ABBREVIATIONS	xi
1. INTRODUCTION	1
1.1. Specific Aims	1
1.2. Significance	2
1.3. Background of Hyaluronan and Hylan	3
1.4. Future Directions	9
1.5. Introduction of Biochemical Analysis Techniques	11
1.5.1. Background of Enzyme Digestion used in FACE analysis	11
1.5.2. Difference in HA Measurements between FACE and Uronic Acid Assay	14
1.6. Radiolabeled Hylan Experiments	14
1.7. Introduction of Mechanical Testing Techniques	14
2. MATERIALS AND METHODS	16
2.1. Materials	16
2.1.1. Hylan Samples	16



2.1.2.	Hylan Wash Methods	17
2.1.3.	Collagen Gel	17
2.2.	Biochemical Analysis	18
2.2.1.	FACE Gel Analysis	18
2.2.1.1.	Enzyme Digestion of Hylan	18
2.2.1.2.	Fluorotagging	18
2.2.1.3.	FACE Gel Analysis	19
2.2.2.	Uronic Acid Assay	19
2.3.	Radiolabeled Hylan Analysis	20
2.4.	Swelling of Hylan	21
2.5.	Mechanical Analysis	21
2.5.1.	Compression Testing	21
2.5.2.	Compression Testing Data Analysis	22
2.5.3.	Tensile Testing	24
2.5.4.	Tensile Testing Data Analysis	25
3.	RESULTS	27
3.1.	FACE Analysis of Healon and Hylan B	27
3.2.	Analysis of Radiolabeled Hylan	28
3.3.	FACE Analysis of Hylan B167	30
3.4.	FACE Analysis of Hylan B180	31
3.5.	Uronic Acid Assay on Hylan B167 and Hylan B180	34
3.6.	FACE Analysis of Hylan B170 and Hylan B173	35
3.7.	Uronic Acid Assay on Hylan B170 and B173	37

3.8. Compression Testing of Hylan B167 and B180	38
3.9. Compression Testing of a Collagen Gel	39
3.10. Tensile Testing of Hylan B173	39
3.11. Comparison of Compressive and Tensile Moduli	40
3.12. Swelling Experiments	43
4. DISCUSSION	45
4.1. FACE Analysis of Healon and Hylan B	45
4.2. Analysis of Radiolabeled Hylan	46
4.3. FACE Analysis of Hylan B167 and Hylan B180	46
4.4. Uronic Acid Assay of Hylan B167 and Hylan B180	47
4.5. FACE Analysis of Hylan B170 and Hylan B173	48
4.6. Uronic Acid Assay on Hylan B170 and Hylan B173	48
4.7. Compression Testing of Hylan B167, B180 and a Collagen Gel	49
4.8. Tensile Testing of Hylan B173	50
4.9. Relation between Amount of Releasable Hyaluronan and the Compressive Modulus of Hylan Samples	51
4.10. Swelling Experiments	53
4.11. Other Experiments	54
4.11.1. Conversion of Saline Washed Hylan to Isopropanol Washed Hylan	54
4.11.2. Seeding of Keratinocytes upon Hylan	54
4.12. Future Directions	55
5. WORKS CITED	56



## LIST OF FIGURES

FIGURE 1-1	Structure of Hyaluronan Disaccharide	3
FIGURE 1-2	Enzyme Digestion on Healon (hyaluronan)	12
FIGURE 1-3	Enzyme Digestion on Hylan (cross-linked hyaluronan)	13
FIGURE 2-1	Full Plot of Data for Hylan B180-1.2 Compression Testing	24
FIGURE 2-2	Definition of Mechanical Parameters	26
FIGURE 3-1	FACE Gel of Healon and Hylan B	28
FIGURE 3-2	Radiolabeled Hylan Gel Indicating HA Disaccharide and Crosslink Bands	29
FIGURE 3-3	FACE Analysis of Hylan B167	31
FIGURE 3-4	FACE Analysis of Hylan B180	32
FIGURE 3-5	FACE Analysis of Hylan B170 and B173	36
FIGURE 3-6	Tension and Compression Tests on Hylan B180-1.8, Saline Washed	41
FIGURE 3-7	Tension and Compression Tests on Hylan B180-1.8, Isopropanol Washed	42
FIGURE 3-8	Percent Hylan B167 and B180 Swell when in Water as compared to Saline	44
FIGURE 4-1	Compressive Modulus at 25% Strain vs. Hylan Formulation	52
FIGURE 4-2	Releasable HA mg/ml determined by FACE Analysis vs. Compressive Modulus at 25% Strain	53

## LIST OF TABLES

TABLE 3-1	Radiolabeled Hylan Comparison of Bands	29
TABLE 3-2	FACE Analysis of Hylan B167 and B180	33
TABLE 3-3	Uronic Acid Assay of Hylan B167 and B180	34
TABLE 3-4	FACE Analysis of Hylan B170 and B173	37
TABLE 3-5	Uronic Acid Assay of Hylan B170 and B173	37
TABLE 3-6	Compressive Modulus at 25% Strain for Hylan B167 and B180	38
TABLE 3-7	Material Parameters Determined by Tensile Testing of Hylan B173	39
TABLE 3-8	Comparison of Testing Methods for Isopropanol and Saline Washed Hylans	43
TABLE 4-1	Moduli of Various Biomaterials and Biological Tissues	50

## LIST OF ABBREVIATIONS

AMAC.....	2-aminoacridone
CCD.....	charged-coupled device
DMSO.....	dimethylsulfoxide
FACE.....	fluorophore-assisted carbohydrate electrophoresis
GPIB.....	General Purpose Interface Bus
HA.....	hyaluronan
SD.....	streptococcal disgalactie

THE EFFECT OF THE DEGREE OF CROSSLINKING  
ON THE MODULUS OF HYLAN

by

Maida Ann Ludwig

Submitted in partial fulfillment of the requirements  
for the degree of Master of Science

Research Advisor: Dr. Vincent Hascall, Ph.D.

Cleveland Clinic Foundation

Academic Advisor: Dr. Ravi Bellamkonda, Ph.D.

Case Western Reserve University

Department of Biomedical Engineering  
CASE WESTERN RESERVE UNIVERSITY

August, 2000

## 1. INTRODUCTION

### 1.1. Specific Aims

Although numerous biomaterials exist, the need for a better biomaterial never ceases. The proposed study is to characterize a biomaterial made from crosslinked hyaluronan, known as hylan, that is inert in the body, displays significant elastic properties, and can be used for a variety of applications. The specific goal of this project is to determine the relation between the degree of crosslinking and the modulus of hylan. This relationship will allow the specification of a certain degree of crosslinking in the manufacturing process in order to obtain the desired modulus of the hylan specimens. This is extremely useful because the modulus of hylan can be changed to suit a variety of applications.

In order to reach the goal, two main areas need to be addressed:

- 1) **The degree of crosslinking of the hylan specimens needs to be defined by biochemical analysis in terms of the specimen's moles of releasable hyaluronan (HA), and moles of functional group associated with HA crosslinking.**
- 2) **The modulus of the hylan specimens needs to be determined.**

The data from these experiments will be evaluated to quantify the relation between the degree of crosslinking and the modulus of hylan.



## 1.2. Significance

Biomaterials are an essential part of clinical medicine. Although there are presently many good biomaterials, none are perfect. A biomaterial that does not elicit an immune response by the body, is suitable for a variety of applications, can be altered to fit specific situations, and is easy to work with would be a great advance in the world of biomaterials. Hylan is a biomaterial that may possess all of these characteristics.

Hyaluronan is a polysaccharide that is produced by almost all cells of the human body. Under physiological conditions, HA exists in a highly hydrated form due to its negatively charged carboxyl groups. It can be covalently crosslinked to form a water insoluble material called hylan, that demonstrates sufficient mechanical properties for clinical applications. The useful aspect of hylan is the combination of its elastic properties and its biocompatibility. Hylan can be used for a variety of applications because its properties can be changed from a soft gel to a solid material by varying the amount of crosslinking (Band 1996). Experiments with hylan have shown it to be inert in the body. It does not elicit an immune response, or cause adverse tissue reactions when implanted (Larsen 1992).

If a relationship between the degree of crosslinking and the modulus of the hylan substrates can be defined, it will be possible to specify the characteristics desired for a certain application and then know the amount of crosslinking that is needed in the manufacturing process to produce the appropriate material. Hylan could be a candidate for applications that presently utilize collagen substrates (one example being an artificial

skin substrate) because it does not elicit an immune response by the body, demonstrates longer residence times than collagen, and there is no need for prerequisite skin tests of patients (Larsen 1992). Hylan is already used for a variety of other biomaterial applications such as soft tissue replacements, drug delivery vehicles, viscosurgery, treatment of arthritis, and post-surgical adhesion management (Balazs 1995).

### 1.3. Background of Hyaluronan and Hylan

Hyaluronan is an ubiquitous polysaccharide with a repeating disaccharide of glucuronic acid and N-acetylglucosamine (Fig 1-1).

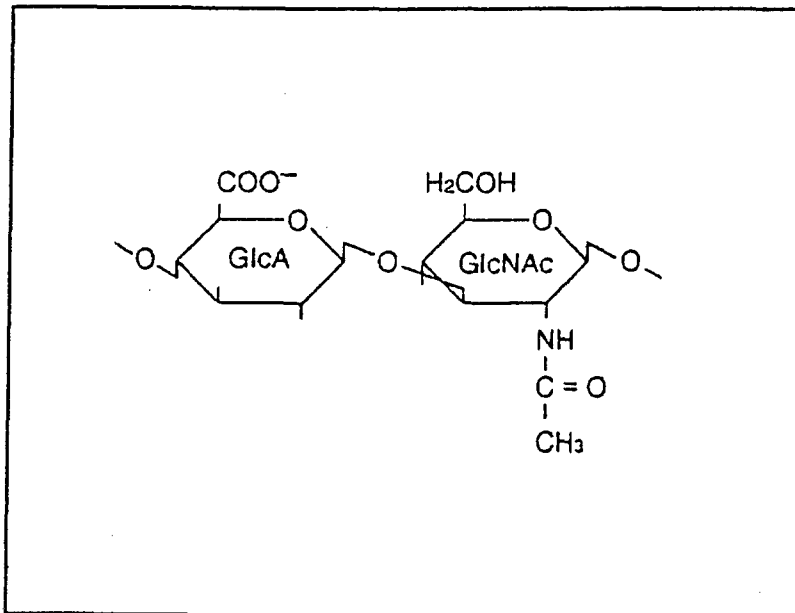


Figure 1-1: Structure of Hyaluronan disaccharide

-D-glucuronic acid-beta-1,3-D-N-acetylglucosamine-beta-1,4-

It forms large linear polymers where the number of disaccharides can reach 30,000 units, with a molecular mass of more than 10 MDa (Hascall 1989). It exists *in vivo* as a polyanion, not in the protonated acid form. Nearly all cells of the body synthesize hyaluronan. One of the highest concentrations of hyaluronan in the body is found in the epidermis. "Hyaluronan has been shown to determine skin turgor (hydration), provide viscoelasticity and shock absorption, and to play an important role in tissue regeneration during healing. More recently, its important role in epidermal function has likewise been recognized" (Balazs 1995).

HA synthesis appears to occur in a compartment associated with the cell surface, rather than in the Golgi. To date, experiments indicate that HA is elongated at its reducing end by adding UDP-N-acetylglucosamine with displacement of UDP from the UDP-glucuronosyl residue which occupies the reducing end. The HA molecule is extruded directly into the extracellular space (Hascall 1991).

"The highest concentrations of hyaluronan occur in synovial fluid, vitreous body, skin and certain specialized tissues such as umbilical cord and rooster comb, during fetal development, and in tissue repair and regeneration" (Fraser 1989). The largest amounts are in the intercellular matrix of skin and musculoskeletal tissues. During early development and before tissue differentiation, HA without or with only small amounts of proteoglycans can be the major structural macromolecule in the extracellular matrix. In this situation it can promote cell proliferation and migration (Wight 1991). HA-based extracellular matrices often provide a pathway for cells, such as neural crest cells and hematopoietic cells, to move along. The HA-based matrices also provide an environment where cells differentiate and form new matrices (Wight 1991). Elevated levels of HA are

found during wound healing (Oksala 1995) as well as during inflammation (Lesley 1997).

Metabolic degradation of HA is mainly intracellular and uptake is performed by a receptor. The endothelial cells lining the sinusoids of the liver and lymph nodes provide the main avenue for uptake and metabolism (Fraser 1989). The metabolic cycle, from polymer to acetate can be completed *in vivo* in less than 10 min (Fraser 1989).

HA has been found to be important in terms of the changes that occur in the skin of elderly people. A study by Ghersetich *et al.* found that there was a reduction in the number of electron-dense granules of HA, and of their filaments, until they were completely absent in subjects aged 60. They concluded that the different levels of HA in the dermis could result in most important changes that occur in the skin, namely, decreased turgidity, less support for microvessels, wrinkling, and altered elasticity (Ghersetich 1994). Another study found that neither the concentration nor polymer size of hyaluronan changes with age (Ludger 1994). However, they did observe that enhanced association of HA with tissue occurs, most likely through HA-binding proteins and changes in the histolocalization of HA. These findings may be the cause of the changes that occur in human skin with age (Ludger 1994).

Hyaluronan is a highly viscous solution that has an expanded random coil structure in physiological solutions and therefore occupies a large domain. Because of this structure, small molecules are free to diffuse through the solvent within the domain. Larger molecules will have much more trouble diffusing through and are more likely to be excluded the larger they are. However, the hyaluronan chains are always moving in

solution. Therefore, it is theoretically possible for a molecule of any size to pass through, where the larger molecules would pass through much more slowly.

Hyaluronan does not cause the body to react to it in a negative manner.

“Numerous *in vitro* and *in vivo* studies have shown that hyaluronic acid is a noncytotoxic, nonimmunogenic and noninflammatory macromolecule” (Larsen 1985). The hyaluronan molecule is identical in all species (Balazs 1991), which is beneficial in many respects. In terms of the body’s reaction to hyaluronan, it presents very little risk of hypersensitivity or rejection reactions, it requires no prerequisite skin test for prospective patients, and implant resorption due to tissue reaction is minimized therefore avoiding the need for repeated applications (Larsen 1992). The fact that hyaluronan is identical across species is also advantageous in terms of ease and cost effectiveness of utilizing it for applications. It is obtained from rooster comb where it is present at high concentrations (7.5 mg/ml), then purified, and sold by Pharmacia (trade name Healon) for clinical purposes. It is presently used to replace the vitreous of the eye during eye surgery and the synovial fluid of the knee joint during knee surgery (Balazs & Denlinger 1989).

Processes have been developed by Biomatrix, Inc. (CEO, Endre Balazs) to introduce covalent crosslinks between individual hyaluronan molecules, which changes their properties from viscous solution to elastic material. This class of materials is named hylans, and is the material being used in these experiments. Crosslinking can affect the optical properties, where higher crosslink density creates a less translucent material, as well as the chemical properties of hyaluronan. Crosslinking changes the solubility and rheological characteristics of the molecule, but it does not affect the biocompatibility of the hyaluronan polymer (Larsen 1995). “It has been well documented that purified,

noninflammatory hyaluronan does not elicit humoral or cell mediated immune reactions. Hylan and hylan gels have been shown to behave identically to the native polymer in this regard" (Larsen 1994). Larsen *et al.* performed an experiment where a hylan gel slurry was injected intradermally and subdermally in mice. They found that there was a minimal reaction at 24 hours, and subsequently (for seven weeks) there was no significant tissue reaction (Larsen 1994). Additionally, Larsen *et al.* evaluated the immune response to the hylan gel slurry in rabbits. Unmodified hylan gel slurry, degraded hylan gel slurry, and hylan gel slurry-ovalbumin were used to immunize rabbits, none of which produced an antibody response (Larsen 1994). Because hylan is composed of carbohydrates, it would not be expected to elicit an immune response and indeed, that was what was seen in Larsen's experiments. The results of these experiments and similar ones (Larsen 1995) "suggest that hylan materials are not recognized as 'foreign' by the cells with which they interact. Typically, hylan materials exhibit remarkable local and systemic tolerance and compatibility" (Larsen 1995).

Hylan preparations have shown to be superior to hyaluronan in medical applications in a number of different respects. In one study, radio-labeled hylan gel was injected into the dermis of guinea pigs. The study was conducted for a period of one month and it was found that the hylan gel completely remained at the site of implantation (within experimental error) (Balazs 1991, Larsen 1993). Unmodified (uncrosslinked) hyaluronan is eliminated much more rapidly by the body, especially in places of high mechanical stresses. Residence time can be controlled by the crosslinking reaction conditions used, to give anything from a soft, deformable gel to a solid membrane, with prolonged to permanent residence times (Band 1996). The hylan samples used in these

experiments have permanent residence times, although gels with shorter residence times also have applications. Saphwan *et al.* have shown that hylan is able to sustain its integrity as a viscoelastic material three times better than high molecular weight hyaluronan in environments where -OH radicals are present, such as in an inflamed joint (Saphwan 1995).

Elasticity and not eliciting an immune response are the main advantages that hylan biomaterials possess. Crosslinked hyaluronan (hylan) will be especially useful as a substrate for growing a skin replacement since it possesses elastic properties as does skin. We will be testing the mechanical properties of hylan to try to determine the modulus of elasticity and extensibility, just as has been done for *in vivo* testing of skin (Clark 1996). We will determine the maximum load in addition to the other parameters, as was done when Osborne *et al.* performed testing of crosslinked collagen substrates used as artificial skin substrates (Osborne 1998).

Presently, a typical substrate used for correction of soft tissue defects is a collagen implant. However, it has been widely shown that collagen implants often have very short residence times because they are resorbed by the body, are associated with a low incidence of hypersensitivity reactions, and prospective patients must undergo skin testing prior to collagen administration (Larsen 1993, 1995, Balazs 1995). Hylan has been shown to circumvent these problems. Because of this, future purposes of using hylan for artificial skin substrate look promising. Crosslinked collagen substrates for use as an artificial skin substrate have been tested. It has been shown that certain crosslinking reagents gave results that significantly improved the mechanical properties of the material for use in clinical applications (Osborne 1998). Hopefully, hylan will also

reveal mechanical properties appropriate for clinical use. If so, hylan could prove to be a valuable biomaterial because it does not cause the body to produce an immune response and it possesses elastic properties.

#### 1.4. Future Directions

As of yet, "there is no true replacement for healthy, intact skin, which is the body's largest organ and one of the most complex" (Strange 1997). Skin provides many important functions, including acting as a barrier to moisture loss, UV light, and microbial and chemical invasion (Gallico 1995). It also aids in the control of temperature and is an important sensory organ.

Presently, the most common solution to covering a wound is autografting (Strange 1997). Often the graft is meshed (small slits are placed in the graft) so that it can be stretched to cover a greater portion of the wound site. Despite meshing to cover more area, sometimes autografting is still not possible. This is true in severe burn cases where there is not enough undamaged skin in order to take a graft (Hansbrough 1994). Also, in elderly patients the skin is much thinner making graft excision difficult and the donor site is often slow to heal (Strange 1997). Additionally, some patients can not handle the trauma of an additional wound (Strange 1997).

In cases where autografting is not immediately possible, the wounds have to be temporarily covered. Two techniques presently employed are allografts, grafts from the same species, and xenografts, grafts from other species. In the United States, fresh or cryopreserved cadaver skin is the preferred choice, but it is often in short supply, of



variable quality, presents the possibility of transmitting both bacterial and viral diseases, and ultimately results in rejection (Hansbrough 1994). In either case, the allograft or xenograft is quickly rejected (days to weeks) by the patient's immune system and must be replaced (Strange 1997).

Because of the present complications in covering wounds, the development of a temporary artificial epidermis for use in clinical applications would be a relief for many doctors, as well as patients. There are several properties that need to be taken into account when considering the design of an artificial epidermis. It must have very small to no antigenic effect on the body, promote growth of a new epidermis, be biologically stable, have tensile strength similar to the natural epidermis, and be easy to handle. The goal is to produce a confluent sheet of cultured keratinocytes on an appropriate substance for skin grafting. Presently, the most common substrate for artificial skin is composed of collagen (Hanthamrongwit 1996).

Once optimum mechanical properties are determined by this project, we are interested in using hylan as a substrate for growing epidermal keratinocytes to form a temporary artificial epidermis. It will be determined whether these cells can form a basement membrane and undergo differentiation when grown on hylan. If successful, the result would be a fully functioning epidermal layer upon a non-immunogenic substrate. This could be implanted on a dermal layer to provide the barrier function and to prevent moisture loss as normal skin does. Fluid exchange would be permitted between the epidermal layer and the dermis but host cells would not have access to epidermal cells, therefore bypassing the possibility of a severe immune response.

## 1.5. Introduction of Biochemical Analysis Techniques

To determine the composition of hylan gels it is necessary to evaluate the amount of hyaluronan and amount of crosslinking present. A relatively new method for determining these quantities is fluorophore-assisted carbohydrate electrophoresis (FACE) gel analysis. To confirm the findings of the FACE analysis, uronic acid assays will also be performed to quantify the amount of hyaluronan in hylan, but will not relate any information about the degree of crosslinking. To ascertain that what is seen in the FACE analysis is indeed crosslinks, hylan samples with  $^{14}\text{C}$  radiolabel incorporated into the crosslinking moiety will be analyzed.

### 1.5.1. Background of Enzyme Digestion used in FACE Analysis

The first step necessary in FACE gel analysis is to digest the sample with the enzyme hyaluronidase from streptococcus dysgalactiae (SD). This enzyme is an eliminase and digests the hyaluronan polysaccharide into disaccharide units (Figure 1-2)

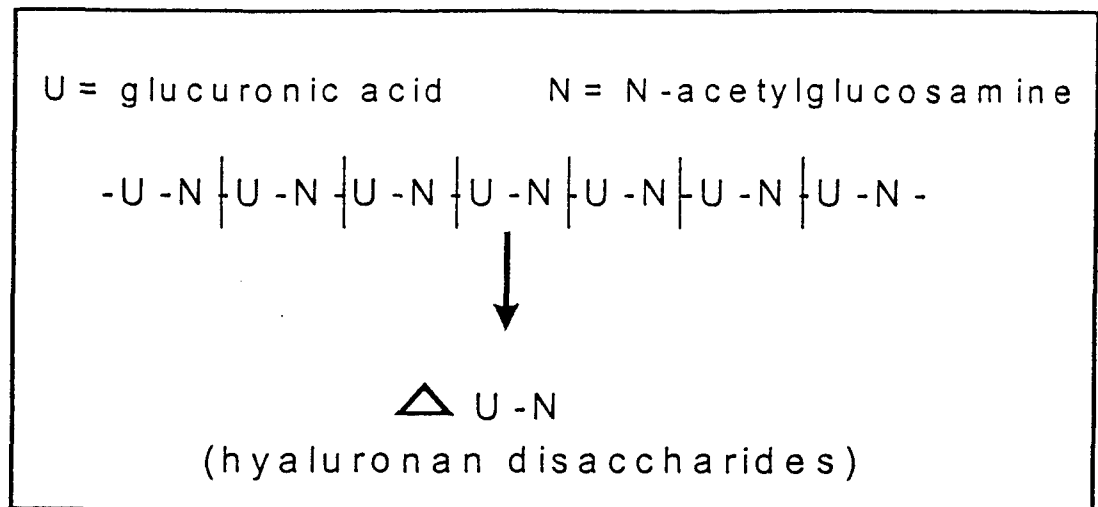
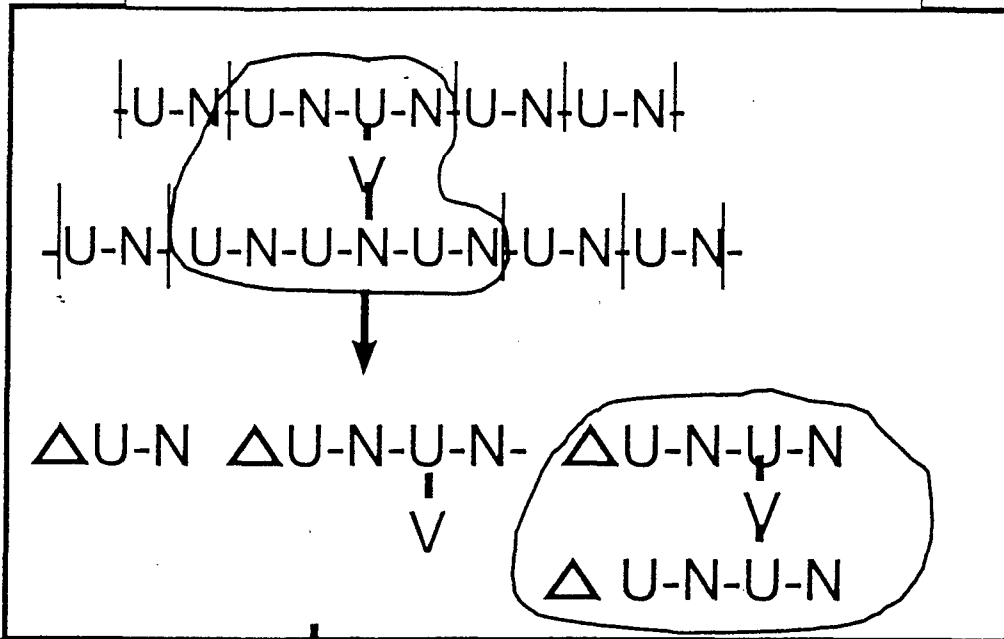


Figure 1-2 : Enzyme digestion on Healon (hyaluronan)

and units containing crosslink, if present (Figure 1-3), while also creating a reducing group on the end of each unit. The crosslinked groups contain at least one crosslink and several HA disaccharides because the enzyme is not able to cleave the divinyl sulfone crosslink and is only able to cleave near the crosslink. This results in a much larger group being created than the HA disaccharide group. Additionally, the enzyme does not always stop digesting a precise distance from the crosslink, so various sized crosslinked groups are created. Furthermore, the enzyme may create a crosslink group that contains more than one divinyl sulfone crosslink between multiple chains, creating even larger structures. Another possibility is the creation of a unit that contains a pendant group, due to the side reaction that is possible between the divinyl sulfone group and water. Pendant groups are formed when the divinyl sulfone crosslink reacts with a HA chain on one end, and reacts with water on the other end (Figure 1-3). Therefore, a pendant group is formed instead of a functional crosslink.

## Enzyme Digestion on Hylan



**HA Disaccharide    Pendant Group    Functional Crosslink**  
 U=glucuronic acid, N=N-acetylglucosamine, V=divinyl sulfone

Figure 1-3 : Enzyme digestion on hylan (cross-linked hyaluronan)

### 1.5.2. Difference in HA Measurements between FACE and Uronic Acid Assay

It is important to recognize the difference between what FACE and the uronic acid assay measure in terms of HA. When FACE mg/ml HA is reported it is the mg/ml of HA disaccharide that is *released* by enzyme digestion. If the entire sample is not digested the number given will be artificially low. Also, it relates information only about the HA disaccharide band, not the crosslinked bands containing HA. The uronic acid assay, on the other hand, relates information about the entire HA content. It is able to destroy all the crosslinks so it can evaluate the HA in total. The uronic acid assay also analyzes the released products of enzyme digestion. Therefore, just as in the FACE assay, if the entire sample is not digested the number reported will be artificially low.

### 1.6. Radiolabeled Hylan Experiments

Hylan with  $^{14}\text{C}$  labeled divinyl sulfone crosslinks were analyzed to try to determine which bands on the FACE gels contain crosslinks and which do not. Because the radioactive label is only present on the crosslinking agent, pure HA will not contain any radioactivity.

### 1.7. Introduction of Mechanical Testing Techniques

All materials testing was carried out on an Instron servohydraulic testing machine. Compression testing and tensile testing was performed on various formulations

of hylan, including saline washed hylans and isopropanol washed hylans (see 2.1.2). Additionally, a collagen gel was tested in compression. This was done so we could directly compare the compressive modulus of hylan with the compressive modulus of a collagen gel. A collagen gel was chosen because it is considered a standard substrate for cell culture, and appeared to have a somewhat similar modulus to hylan. This gives a direct comparison of hylan to a material that is well known and characterized.

## 2. MATERIALS AND METHODS

### 2.1. Materials

#### 2.1.1. Hylan Samples

Biomatrix, Inc. of Ridgefield, New Jersey, provided multiple formulations of hylan. The formulations vary with respect to the amount of crosslinking reagent used and the amount of hyaluronan present in the gels. In addition, Healon, which is a solution of hyaluronan with no crosslinks, was tested. After evaluating the first set of formulations created, additional formulations were made to meet our specifications.

To make the hylan samples, hyaluronan (HA) molecules are added to water to give 4% HA. Then, 0.1 M NaOH is added to decrease the viscosity of the solution to allow for sufficient mixing, and the divinyl sulfone crosslinking reagent is added. Pushing between two syringes connected with a barrel mixes it, which helps ensure satisfactory mixing and no air bubbles. The gel solution is then placed in a petri dish to set for about one hour.

To make hylan formulations with different amounts of crosslinking, the ratio of HA weight to divinyl sulfone weight added to the reaction mixture is varied. The formulations are named according to the ratio of these reagents added during their production, regardless of what the actual resulting material contains. For example, hylan B167-1.0 is hylan B from lot 167 with a 1:1 ratio of HA weight and divinyl sulfone weight added. Hylan B180-1.8 is hylan B from lot 180 with a 1.8:1 ratio of HA weight to divinyl sulfone weight.

### 2.1.2. Hylan Wash Methods

All hylan samples were prepared in the same manner. However, two possible wash procedures can be performed after the gel is made. One method is the standard wash, which is a wash done in saline. The other wash is done first in isopropanol overnight and then in saline. The wash method chosen produces dramatic differences in the final hylan product.

### 2.1.3. Collagen Gel

The collagen gel was prepared from type I rat tail collagen at 3.85 mg/ml (Collaborative Research). Two ml of 10X Hanks Balanced Salt Solution (HBSS) was premixed with 200  $\mu$ l of 7% sodium bicarbonate. This mixture is added to prediluted collagen (3.85 mg/ml diluted to 2.5 mg/ml in 0.02 N acetic acid) at a ratio of 0.5 ml to 4 ml collagen such that the final collagen concentration is 2.2 mg/ml. Then, 1 M NaOH is added at a ratio of 100-120  $\mu$ l per 4 ml collagen-0.5 ml HBSS/sodium bicarbonate. This is mixed well avoiding air bubbles. Five ml of this solution was quickly aliquoted into a 35 mm tissue culture dish and placed in a 37°C incubator for one hour.



## 2.2. Biochemical Analysis

### 2.2.1. FACE Gel Analysis

#### 2.2.1.1. Enzyme Digestion of Hylan

To perform the enzyme digestion, five milligrams (wet weight) of hylan is taken and added to 95  $\mu$ l of ammonium acetate with 0.005% phenol red to ascertain correct pH of 7.0. One  $\mu$ l of hyaluronidase streptococcal disgalactie (SD) is added, mixed gently by flicking with the finger, spun down, and placed in a 37°C water bath for 4 hours. Every hour the tube is gently mixed as before and spun down. After 4 hours, the digested samples are completely dried down on a speed vacuum.

#### 2.2.1.2. Fluorotagging

The reducing groups created by enzyme digestion can be fluorotagged using 2-aminoacridone (AMAC) (Calabro #1 2000). Forty microliters ( $\mu$ l) of 0.0125 M AMAC in DMSO and acetic acid (85% DMSO, 15% acetic acid) is added to the dried down sample, vortexed well, and incubated at room temperature for 10-15 minutes. Forty  $\mu$ l of 1.25 M sodium cyanoborohydride is then added, vortexed well, spun down, and incubated at 37°C for 15-16 hours.

### 2.2.1.3. FACE Gel Analysis

Once the samples are fluorotagged they can be run on a fluorescence-activated carbohydrate electrophoretic (FACE) gel. The FACE gel separates derivatives based on molecular weight and charge and thereby separates the disaccharide units and the crosslinked units produced by the enzyme digest. The FACE apparatus is prepared by cooling it with ice atop a stir plate and adding FACE gel running buffer to the chamber. The FACE gels are rinsed with purified water and inserted into the holder, which is then placed into the chamber of buffer. Twenty  $\mu\text{l}$  of glycerol are added to each fluorotagged sample, and 5  $\mu\text{l}$  of the samples are then loaded onto the gel by means of a multi-channel pipetter. There are eight available lanes on each gel, and one or two of the eight lanes are used for standards. Two gels can be run in each set-up. A power supply is connected to the FACE apparatus and set to 500V. The gel is electrophoresed for 80 min. The gel is removed from the FACE apparatus, and the intensity of the fluorescence in each band is captured digitally with a cooled, charged-coupled device (CCD) camera upon exposure to a transilluminator. Gel-pro analyzer software is used to analyze the data obtained from the digital image. The information from this analysis allows the calculation of the moles of hyaluronan and the moles of crosslinks present in the hylan samples.

### 2.2.2. Uronic Acid Assay

One hundred  $\mu\text{l}$  of previously digested hylan samples (see 2.2.1.1.) are placed in glass tubes. One hundred  $\mu\text{l}$  of each of 5 standards are added to a glass tube. To each tube, 750  $\mu\text{l}$  of concentrated sulfuric acid tetraborate is added, and the tubes are placed on

a 100°C hotplate for 5 min. The tubes are placed in a room temperature water bath for 5 min., and then 10 µl of hydroxyphenol is added. The tubes are vortexed well, and 250 µl of each sample is added to a well of a 96-well plate. A plate reader and the softmax-pro software package (Molecular Devices, Corp.) were used to read the plate. The given values can be converted into moles of hyaluronan for comparison with the information obtained from the FACE analysis.

### 2.3. Radiolabeled Hylan Analysis

For the hylan samples with radiolabeled crosslinks, this same procedure is followed for running a FACE analysis (see 2.2.1.), but in addition the bands that fluoresce are cut from the gel and put into a scintillation counter to verify which bands on the FACE gel contain crosslinks. For crosslink A, B, C, and HA bands, the gel was cut horizontally all the way across the gel, along the top and bottom edge of each row containing a specific band, as close to the band as possible (see Figure 3-2 for band locations). Crosslink D was cut in the same manner except it contained all the fluorescent material (the smeared-looking region) found below crosslink C (see Figure 3-2). Radioactivity was measured using a Beckman LS 6500 Scintillation Counter. Scintillation fluid was ScintiSafe Plus 50% from Fisher Scientific.

## 2.4. Swelling of Hylan

All hylan samples arrive from Biomatix, Inc. stored in saline solution and are kept that way for all studies except in preparation for FTIR analysis in which case they are kept in water. To analyze how much the samples swell in water as compared to saline a simple experiment was performed. A piece of hylan, approximately 500-1000 mg, stored in saline is dabbed dry with a Kimwipe and then weighed. The piece of hylan is then placed in 14 mL of water and agitated on a shaker plate set on low for 2 days. The hylan is once again dabbed dry with a Kimwipe and weighed. The percent swell is

calculated as follows: 
$$\frac{\text{waterweight} - \text{salineweight}}{\text{salineweight}} \times 100\%$$

## 2.5. Mechanical Analysis

All materials testing was carried out on an Instron servohydraulic testing machine Model#8511 with the 8500Plus controller. Machine control and data acquisition were done through custom written software routines in Labview running on a PC with the Windows NT 4.0 operating system. Communication between the PC and the 8500Plus controller was accomplished through a GPIB interface.

### 2.5.1. Compression Testing

Specimens were cut with a circular punch 10 mm in diameter. All samples were between 4 and 7 mm thick. The specimens were compressed without constraining

the edges. Compression tests were run at 1 mm/s with a data acquisition rate of 200 Hz. The rate of 1mm/s was chosen for safety of the load cell. When performing compression tests on hylan, the testing platens must be brought extremely close together because the hylan is very thin. This presents a risk of breaking the load cell. Therefore, a lower testing rate was chosen for compression than tension so that we were able to monitor the experiment, and stop it if there were problems that would result in breaking of the load cell. A 5 lb, hermetically sealed, tension/compression rated Sensotec Loadcell (Model 30) was used. Samples were placed on a 30 mm diameter aluminum loading platen that screwed into the loadcell on the bottom of the frame. An identical loading platen was mounted to the cross-head of the Instron. The top platen was lowered until it was 1-3 mm from the top of the test specimen. From this point the distance between the top and bottom platen faces was measured and was called the initial start length. Compression tests were started from this position and a ramp of 1 mm/s was run with an amplitude set to bring the platen faces to within 3 mm of each other. The test ended if either the load exceeded 1500 g, or the platens came within 3 mm of each other. All tests were done in air.

#### 2.5.2. Compression Testing Data Analysis

The load vs. displacement data were converted into stress vs. strain and plotted in Microsoft Excel. To convert load into stress in Pascals, the load in kg is multiplied by gravity in  $m/s^2$ , and that quantity is divided by the cross-sectional area in  $m^2$ . The cross-sectional area is  $\pi r^2$ . To convert displacement into strain, the chop point is subtracted

from the displacement, and that quantity is divided by the gauge length. The entire quantity is multiplied by 100 to give percent strain. The distance between the top and bottom testing platen faces is called the initial start length. The chop point is taken as the number in the raw data where the specimen first takes on load. The gauge length is defined as the initial start length minus the chop point.

The slope between 20-30% strain was taken as the compressive modulus, and named the compressive modulus at 25% strain. The slope between 5-15% strain was taken for some samples, and name the compressive modulus at 10% strain. The mean compressive modulus and standard deviation from the three samples taken is calculated and reported for each hylan formulation. The compressive modulus was taken between 20-30% because this region is relevant for clinical applications. Although at higher strains, such as 70-80%, the compressive modulus becomes much larger, this only happens after passing through a non-linear region (Figure 2-1). The data following the non-linear region are representative of a highly compressed, very thin film, and are not characteristic of a realistic material property of hylan. Therefore the data following the non-linear region will not be presented for any further samples. Only the relevant region will be plotted in the results section.

### B180-1.2 Compression Test

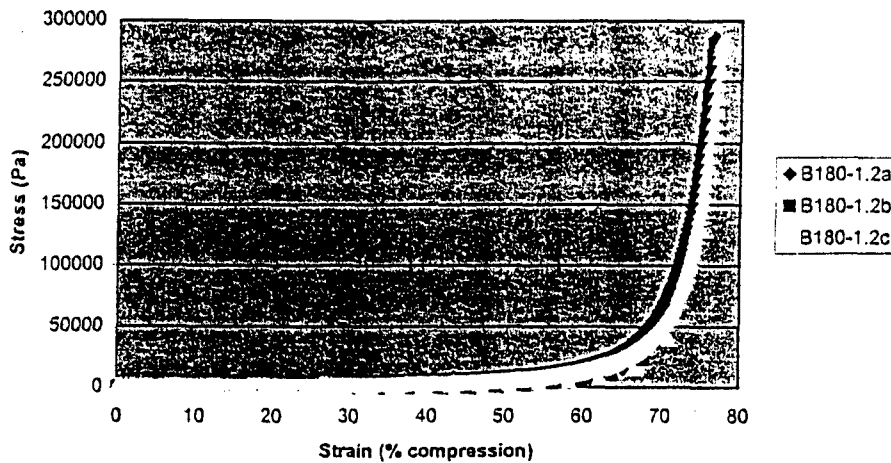


Figure 2-I: Full plot of data for hylan B180-1.2 compression testing demonstrating non-linear region of the data.

#### 2.5.3. Tensile Testing

Three samples of each isopropanol washed hylan formulation were tested in tension. Specimens were 10 mm x 25 mm, and the thickness was measured using a custom designed thickness measuring system that consists of a very light plastic plunger attached to a Mitutoyo digital indicator. The specimen was placed in the Instron machine with an initial starting length of 15 mm. Delrin grips with copper mesh lining to engage the samples were used to hold the sample. The test ramp was set to 4 mm/s with a digital acquisition rate of 200 Hz. The testing was performed in a tank of saline at 37°C. The same load cell was used in these tests as in compression tests. Each sample was preconditioned to 20 g for 3 cycles and then the 4th cycle was stored. Stress relaxation and failure tests were performed as well. Failure tests were run at 2 mm/s. Preliminary

stress relaxation experiments (data not shown) indicated that hylan is mostly an elastic material, with only a small viscous component. Therefore, the small difference in testing rates should not play much of a role since elastic materials are typically strain rate independent. Curves were plotted in Microsoft Excel.

#### 2.5.4. Tensile Testing Data Analysis

The load vs. displacement data acquired were converted into stress vs. strain, and analyzed in the same manner as the compression data. The only difference being that when the load was converted into stress, the cross-sectional area was taken as the width multiplied by the thickness, not as  $\pi r^2$ , since the hylan was cut into rectangular strips for tension testing. Failure parameters were taken directly from the raw data (Figure 2-2). The curves were plotted in Microsoft Excel.



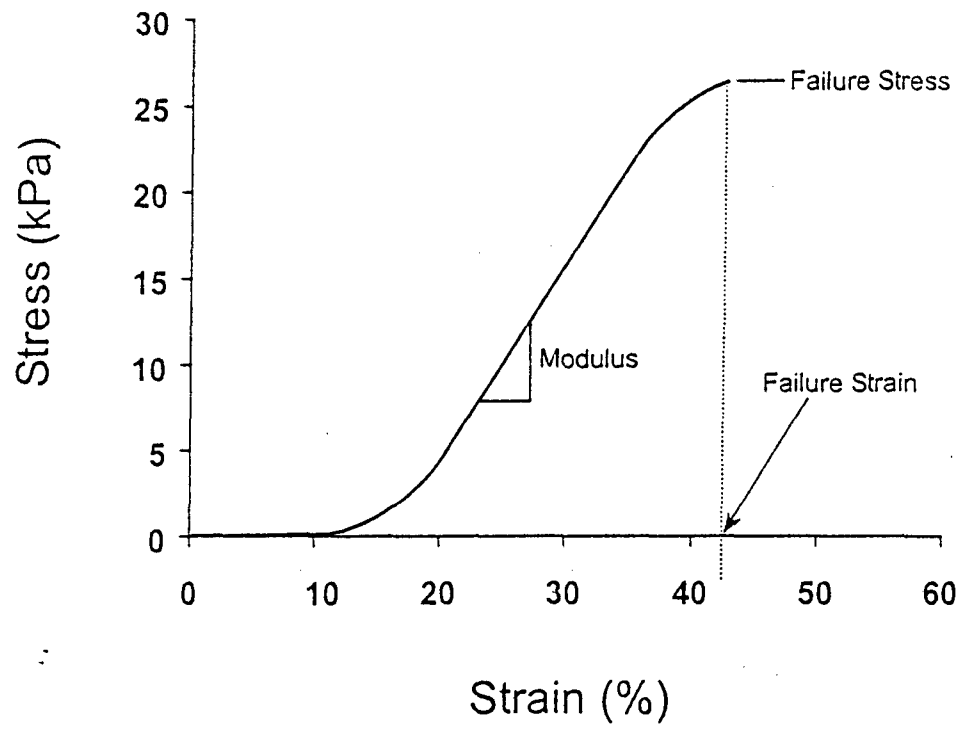


Figure 2-2: Definition of Mechanical Parameters

### 3. RESULTS

#### 3.1. FACE ANALYSIS OF HEALON AND HYLAN B

FACE analysis of Healon reveals one major band on the gel (Figure 3-1). This band is attributed to HA disaccharides. The rest of the lane is clean, indicating only HA disaccharides are present. The hylan B lane contains several bands (Figure 3-1). Again, the major band is due to HA disaccharides. The other prominent bands are indicative of larger HA pieces due to crosslinking. There is a smear in the area of Crosslink C and D, due to small amounts of various sized HA pieces. The crosslinked bands run to various places on the gel according to their molecular weight and charge, so their destination can not be easily predicted (Calabro 2000).

### FACE Analysis of Healon & Hylan B

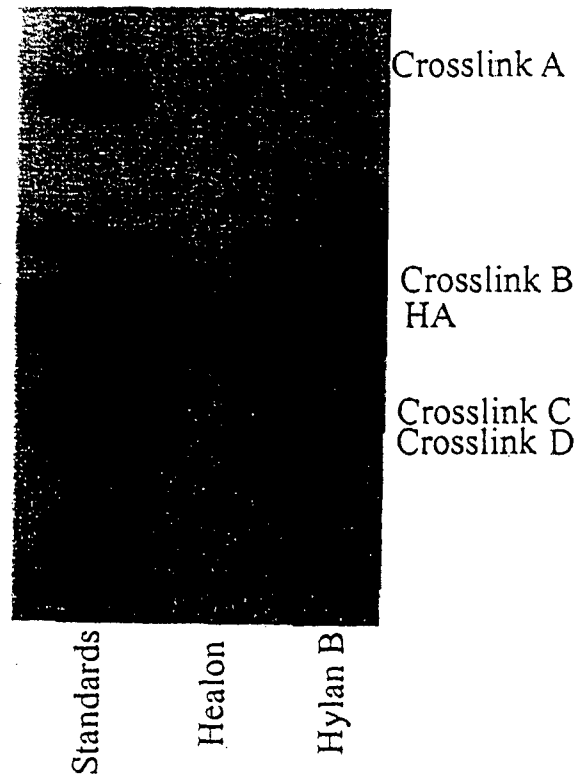


Figure 3-1: FACE gel of Healon and hylan B

### 3.2. ANALYSIS OF RADIOLABELED HYLAN

Only 46% of the total radioactivity loaded on the gel was recovered. This is due to the fact that only some sections were sampled, not the entire gel. The five major bands labeled account for 38% of the total radioactivity loaded (Figure 3-2). The ratio of radioactive counts to HA fluorescence and the percentage of the total counts expected attributed to each band was calculated (Table 3-1).

## Radiolabeled Hylan Gel

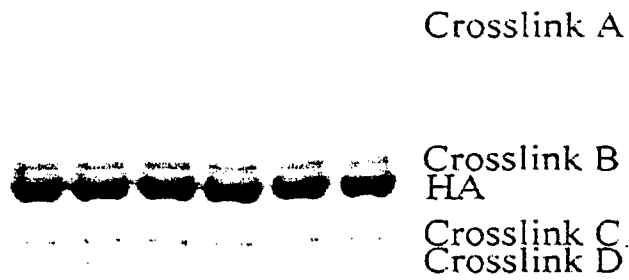


Figure 3-2: Radiolabeled hylan gel indicating HA disaccharide and crosslink bands

Table 3-1: Radiolabeled hylan comparison of bands

Band	Radioactive : HA Counts fluorescence	% in band of total counts loaded
Crosslink A	5.79 : 1	2.92
Crosslink B	0.24 : 1	10.62
HA	0.15 : 1	6.82
Crosslink C	4.00 : 1	7.26
Crosslink D	23.62 : 1	10.94

### 3.3. FACE ANALYSIS OF HYLAN B167

FACE analysis of hylan B167 shows the major band in each lane to be HA disaccharides and several smaller bands due to the larger HA pieces created by the crosslinks (Figure 3-3). Lane 1.0 has significantly less material in all bands due to incomplete solubilization of hylan. The mg/ml HA in each sample is calculated as well as the ratio of HA to crosslink B (Table 3-2).

## B167 FACE Gel

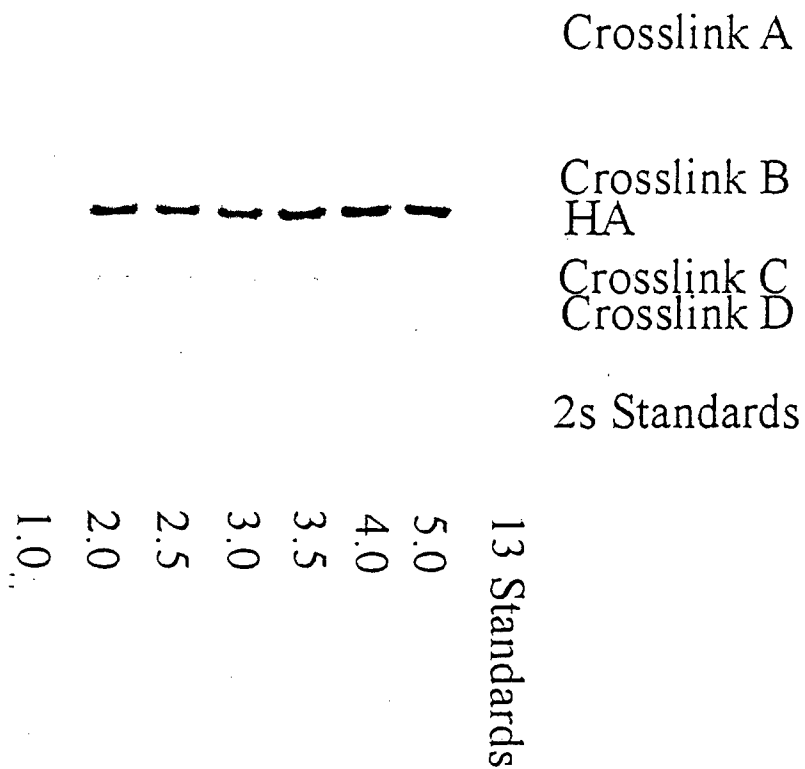


Figure 3-3: FACE analysis of hylan B167. Number labels on the bottom of the gel reflect the weight ratio of HA: crosslinking reagent added during the manufacturing of hylan.

### 3.4. FACE ANALYSIS OF HYLAN B180

FACE analysis of hylan B180 shows the major band in each lane to be HA disaccharides which are visibly increasing in amount from 1.0 to the 2.0 sample (Figure 3-4). Several smaller bands of larger HA pieces created by crosslinking are seen as well.

The mg/ml HA in each sample is calculated as well as the ratio of HA to crosslink B (Table 3-2). Hylan B180-1.0 and B180-1.2 had incomplete solubilization by the enzyme.

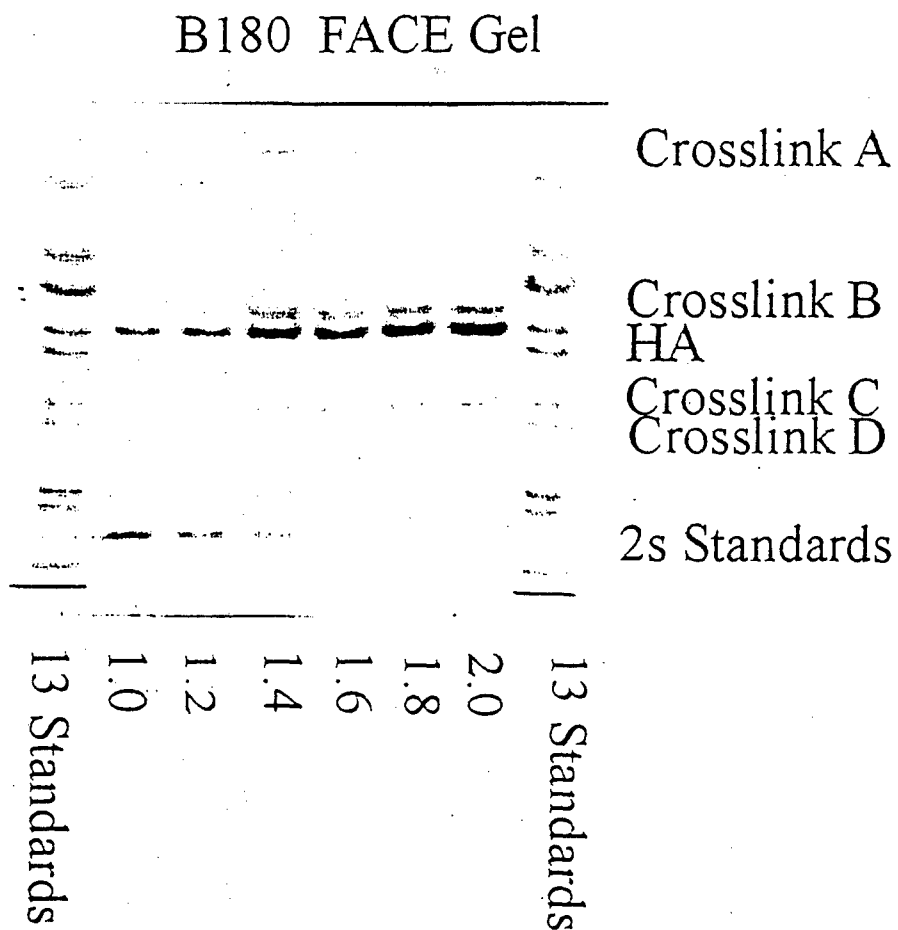


Figure 3-4: FACE analysis of hylan B180. Number labels on the bottom of the gel reflect the weight ratio of HA: crosslinking reagent added during the manufacturing of hylan.

Table 3-2: FACE analysis of hylan B167 and B180

<b>Hylan B167 &amp; B180 FACE Analysis</b>		
	<b>Concentration of HA (mg/ml)</b>	<b>HA/crosslinkB</b>
<b>B167-1.0*</b>	0.15	7.88
<b>B180-1.0*</b>	0.13	4.87
<b>B180-1.2*</b>	0.18	4.68
<b>B180-1.4</b>	0.49	5.33
<b>B180-1.6</b>	0.51	5.71
<b>B180-1.8</b>	0.77	6.14
<b>B180-2.0</b>	0.99	6.15
<b>B167-2.0</b>	2.30	8.59
<b>B167-2.5</b>	1.69	9.22
<b>B167-3.0</b>	2.06	9.20
<b>B167-3.5</b>	2.53	9.80
<b>B167-4.0</b>	3.20	14.17
<b>B167-5.0</b>	2.85	15.00

\* = visible evidence of incomplete solubilization



### 3.5 URONIC ACID ASSAY ON HYLAN B167 AND HYLAN B180

Uronic acid assays were performed on aliquots of soluble digest of hylan B167 and B180. The results are found in table 3-3.

Table 3-3: Uronic acid assay of hylan B167 and B180

<b>Hylan B167 &amp; B180 Uronic Acid Assay</b>	
<b>Sample</b>	<b>Concentration of HA (mg/ml)</b>
B167-1.0*	0.51
B180-1.0*	3.00
B180-1.2*	7.30
B180-1.4	7.66
B180-1.6	6.74
B180-1.8	5.60
B180-2.0	6.17
B167-2.0	2.21
B167-2.5	2.03
B167-3.0	2.01
B167-3.5	1.81
B167-4.0	1.50
B167-5.0	1.39

\* = visible evidence of incomplete solubilization

### 3.6. FACE ANALYSIS OF HYLAN B170 AND HYLAN B173

FACE analysis of hylan B170 and B173 shows the major band in each to be HA disaccharides (Figure 3-5). There are several smaller bands of larger HA pieces due to crosslinking. Significant differences can be seen between saline washed samples and isopropanol washed samples of the same degree of crosslinking. These differences can be seen in the calculated mg/ml HA as well (Table 3-4). All of the isopropanol washed samples had incomplete solubilization by the enzyme.

**B170 & B173 FACE Gel**  
 (Saline vs. Isopropanol Wash)

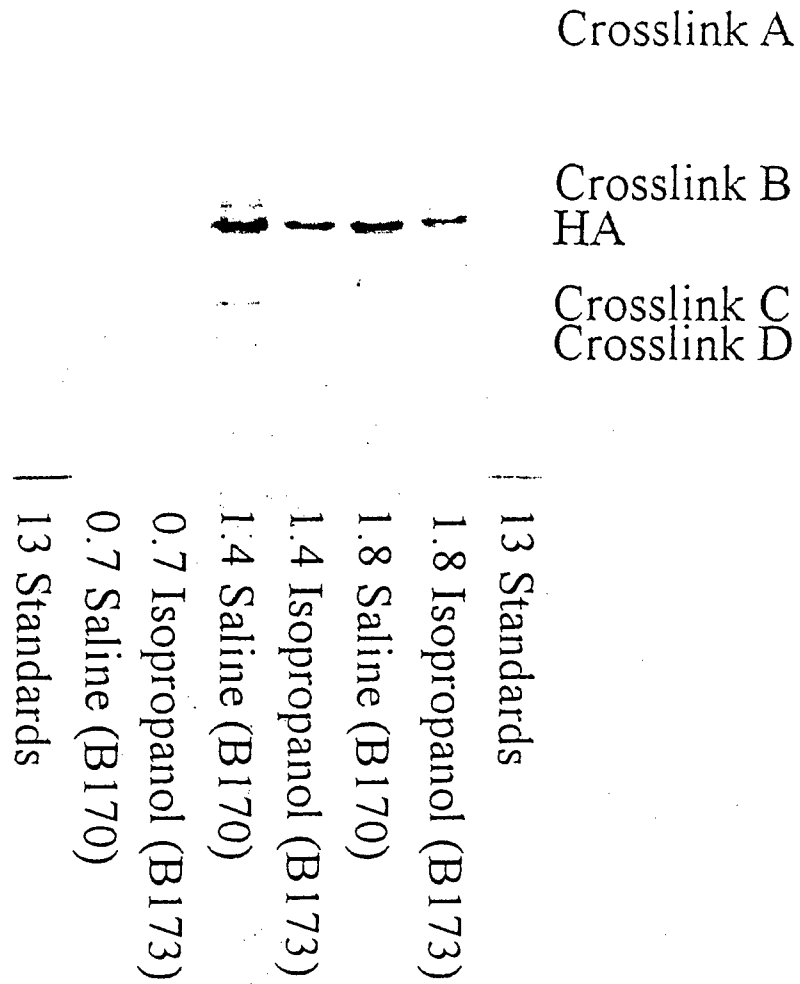


Figure 3-5: FACE analysis of hylan B170 (saline wash) and hylan B173 (isopropanol wash). Number labels on the bottom of the gel reflect the weight ratio of HA: crosslinking reagent added during the manufacturing of hylan.

Table 3-4: FACE analysis results of hylan B170 and B173

	<b>High Crosslinking (0.7)</b>	<b>Medium Crosslinking (1.4)</b>	<b>Low Crosslinking (1.8)</b>
<b>B170 saline</b>	0.12 mg/ml HA	1.44 mg/ml HA	0.92 mg/ml HA
<b>B173 isopropanol*</b>	0.05 mg/ml HA	0.62 mg/ml HA	0.45 mg/ml HA

\* = visible evidence of incomplete solubilization

### 3.7. URONIC ACID ASSAY ON HYLAN B170 AND HYLAN B173

Uronic acid assays were performed on hylan B170 and B173. The results are found in table 3-5.

Table 3-5: Uronic acid assay results of hylan B170 and B173

	<b>High Crosslinking (0.7)</b>	<b>Medium Crosslinking (1.4)</b>	<b>Low Crosslinking (1.8)</b>
<b>B170 saline</b>	4.22 mg/ml HA	8.28 mg/ml HA	6.87 mg/ml HA
<b>B173 isopropanol*</b>	1.76 mg/ml HA	8.30 mg/ml HA	4.58 mg/ml HA

\* = visible evidence of incomplete solubilization

### 3.8. COMPRESSION TESTING OF HYLAN B167 AND B180

Compression testing of hylan B167 and B180 showed reproducible results as indicated by the standard deviations (Table 3-6) and the similarity of the curves for each of the three specimens taken from each sample (see Appendix). A general, but not absolute, trend of increasing modulus is seen as the amount of crosslinking reagent used increases, which can be seen in the graphs and the table (see Appendix and Table 3-6).

Table 3-6: Compressive modulus at 25% strain for hylan B167 & B180

<b>Compressive Modulus at 25% Strain</b>		
<b>Sample</b>	<b>Mean (kPa)</b>	<b>Std. Dev.</b>
B167-1.0	13.04	2.18
B180-1.0	10.57	0.84
B180-1.2	7.79	1.04
B180-1.4	4.04	0.15
B180-1.6	2.73	0.29
B180-1.8	1.94	0.22
B180-2.0	2.05	0.12
B167-2.0	2.05	0.05
B167-2.5	2.52	0.30
B167-3.0	2.25	0.42
B167-3.5	1.86	0.23
B167-4.0	0.83	0.09
B167-5.0	0.84	0.17

### 3.9. COMPRESSION TESTING OF A COLLAGEN GEL

Compression tests on a 2.2 mg/ml collagen gel did not reveal the sample to sample similarity as did hylan as shown in the curves (see Appendix). For the collagen gel, the mean compressive modulus at 25% strain was found to be 21.09 kPa, and the standard deviation was 6.7.

### 3.10. TENSILE TESTING OF HYLAN B173

Due to the isopropanol wash, this set of hylan samples had characteristics that allowed testing in tension, in addition to compression. The elastic modulus, failure stress, and failure strain were measured for three different crosslinking formulations (Table 3-7). A small amount of hysteresis is seen between the loading and unloading curves (see Appendix).

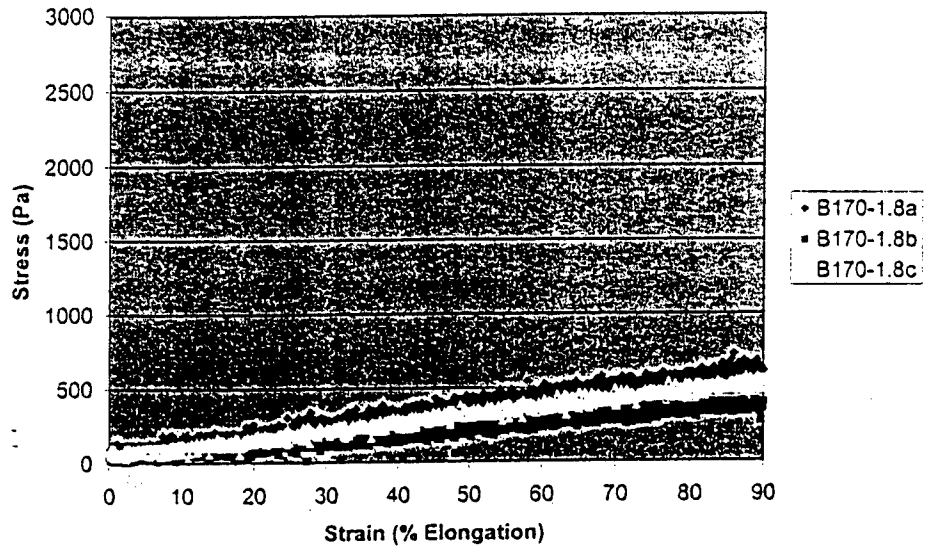
Table 3-7: Material parameters determined by tensile testing of hylan B173

<b>Hylan B173 Tensile Test</b> (isopropanol washed hylan)						
	<b>Modulus, 25% Strain</b> (kPa)		<b>Failure Strain</b> (% strain)		<b>Failure Stress</b> (kPa)	
	Mean	St. Dev.	Mean	St. Dev.	Mean	St. Dev.
<b>B173-R0.7P</b>	18.90	1.31	114.58	15.96	20.99	3.69
<b>B173-R1.4P</b>	5.23	3.10	154.80	16.45	21.65	2.42
<b>B173-R1.8P</b>	1.84	0.88	129.48	20.54	14.00	5.93

### 3.11. COMPARISON OF COMPRESSIVE AND TENSILE MODULI

It was found that the same hylan material tested in compression and in tension gave different moduli (Figure 3-6, 3-7, Table 3-8). For both the saline and isopropanol washed gels, the compression tests gave a modulus approximately one order of magnitude greater than the tension tests. Additionally, the isopropanol washed hylan has a modulus one order of magnitude greater than the same formulation of saline washed hylan, for both the tensile and compressive cases.

### B170-1.8 Tension Test



### B170-1.8 Compression Test

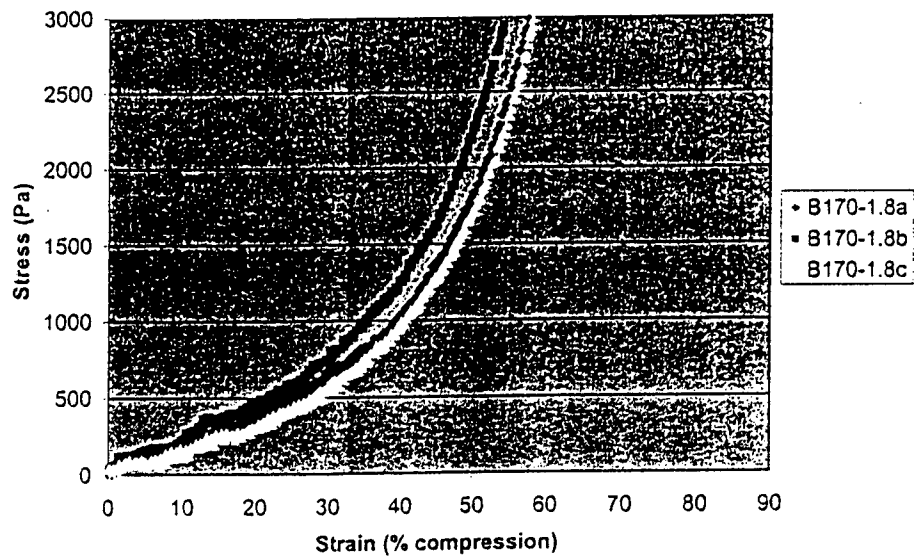
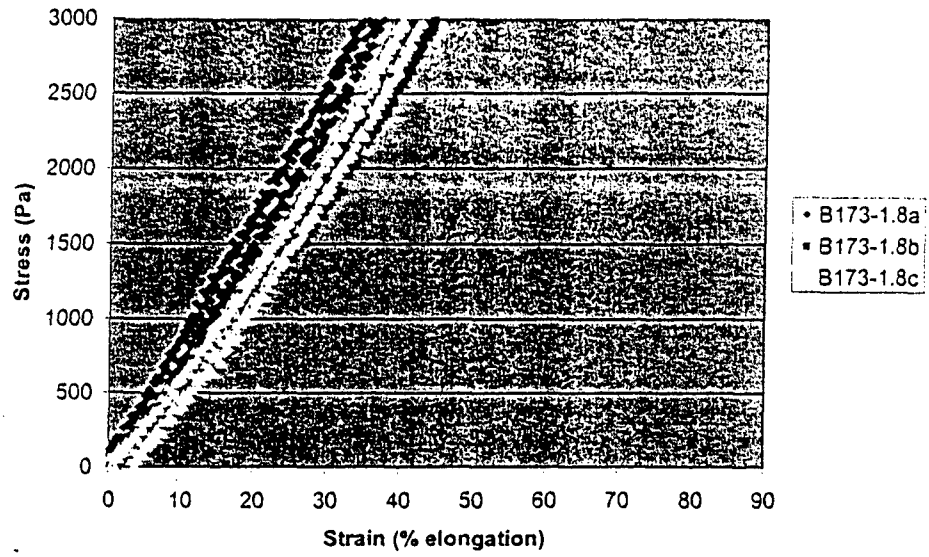


Figure 3-6: Tension and compression tests on hylan B170-1.8, saline washed



### B173-1.8 Tension Test



### B173-1.8 Compression Test

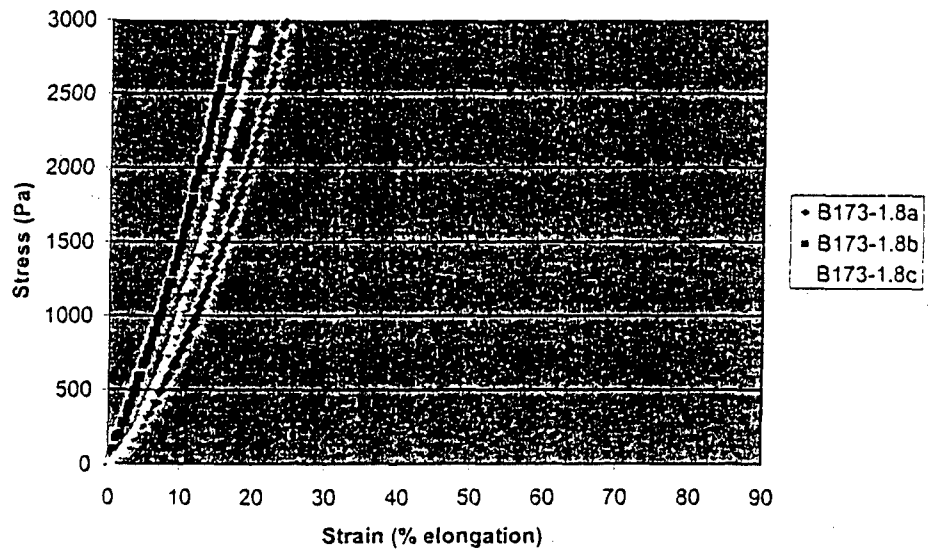


Figure 3-7: Tension and compression tests on hylan B173-1.8, isopropanol washed

Table 3-8: Comparison of testing methods for isopropanol and saline washed hylans

Sample	Testing Method	Modulus, 10% Strain		Modulus, 25% Strain	
		Mean(kPa)	Std. Dev.	Mean(kPa)	Std. Dev.
B170-1.8 Saline	Tension	0.40	0.32	0.54	0.23
B170-1.8 Saline	Compression	2.03	0.47	2.77	0.34
B173-1.8 Isoprop	Tension	7.13	0.93	8.15	0.69
B173-1.8 Isoprop	Compression	15.11	3.98	45.64	22.06

### 3.12. SWELLING EXPERIMENTS

Hylan B167 and B180 were measured as to the percent increase in weight when stored in water as opposed to saline, and is defined as the percent swell. The recorded percent swell is shown in Figure 3-8. The general trend is that hylan samples that had more crosslinking reagent added during manufacturing, have a smaller percent swell.

### % Swell in Water from Saline

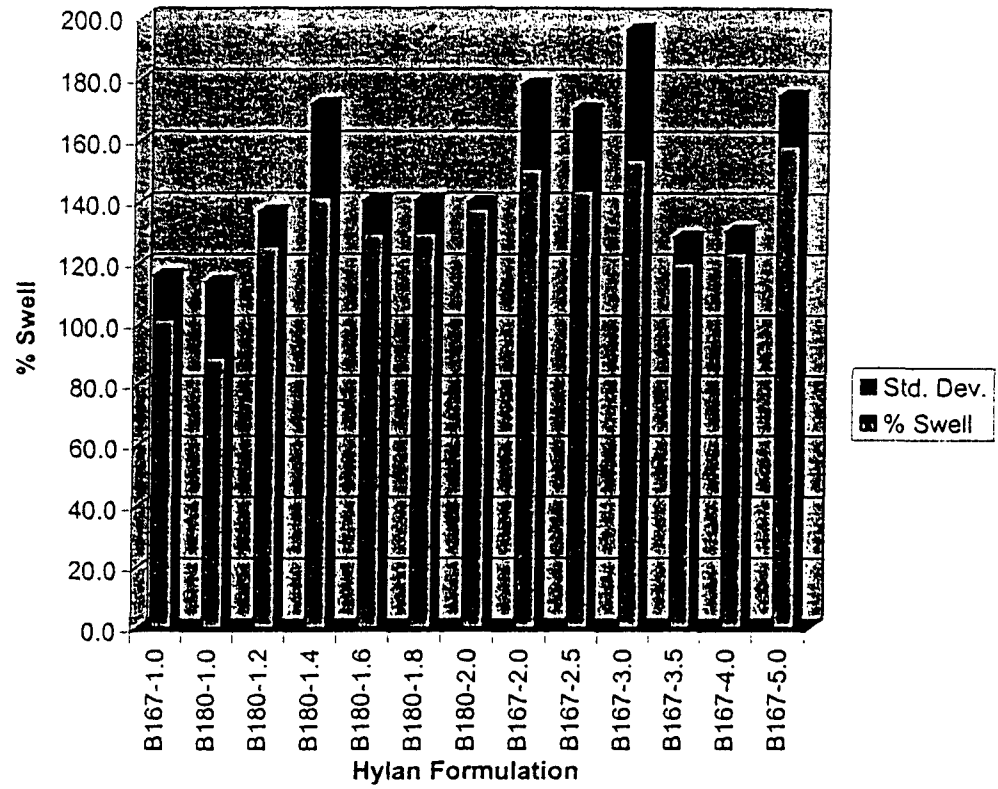


Figure 3-8: Percent hylan B167 and B180 swell when in water as compared to saline

## 4. DISCUSSION

### 4.1. FACE ANALYSIS OF HEALON AND HYLAN B

To identify which bands in the FACE gel are due to hyaluronan disaccharides and which are due to crosslinked hyaluronan, Healon, a purified hyaluronan containing no crosslinks, and hylan B, a crosslinked hyaluronan, were run on a FACE gel. Hyaluronidase SD cleaves pure hyaluronan completely into disaccharides, so it would be expected that only one band would be present. The lane containing Healon fits this description. It has only one band, which is the HA disaccharide band. It is completely free of any other bands, indicating that it does not contain any crosslinks. The lane containing hylan B shows several bands, which is also expected. The HA disaccharide band is the prominent band and there are several other bands which are bands containing crosslinked HA. The various bands are due to the different types of crosslinked HA pieces that can be created by the enzyme digest as discussed previously. The HA band overlaps the crosslink B band to some degree. This did not appear to be as great of a problem on other FACE gels. However, one way to solve this problem would be to treat the samples with mercuric ion prior to AMAC derivatization. This would shift the crosslinked bands to new places, while the HA band would stay in relatively in the same location (Calabro 2000). This would allow for easier and more accurate quantification of crosslink B, since it would no longer overlap with the HA band. Another possible solution to the problem of overlapping bands would be to load less material in the lane. If there is less total material present in the lane, the HA band will be smaller and should not overlap the crosslink B band.

#### 4.2. ANALYSIS OF RADIOLABELED HYLAN

The HA disaccharide band should contain no radioactive counts since it contains no crosslinking. A small number of counts are seen in the HA disaccharide band. This is most likely due to the fact that because it is such a broad band, it is concealing a small band that contains crosslinking. Alternatively, the radioactivity could be contributed to the HA band by crosslink band B, which lies directly above it, if these two bands overlapped at all. One way to solve this problem would be to treat the samples with mercuric ion prior to AMAC derivatization, as described previously.

All of the other bands evaluated contain a much higher ratio of radioactive counts to HA fluorescence, indicating that those bands are bands due to crosslinked HA. The five main bands analyzed contain 38% of the total counts loaded on the gel. When considering that only 46% of the total counts loaded were actually measured, it is evident that these are the major bands containing crosslink.

#### 4.3. FACE ANALYSIS OF HYLAN B167 AND HYLAN B180

The hylan B167-1.0, B180-1.0, and B1801.2 samples were not fully solubilized after 4 hours which is why the lanes containing these samples contain less material in all bands as compared with other lanes. The incomplete solubilization is due to the high degree of crosslinking present in these samples, which prevents the enzyme from fully solubilizing it. The general trend of both the hylan B167 and B180, when evaluating the releasable mg/ml HA, is that the releasable mg/ml HA increases with decreasing amount of starting crosslinking reagent. This is expected because the more highly crosslinked

hylans will have more pieces containing crosslink, leaving less material present in the HA disaccharide band. The ratio of HA to crosslink B follows the expected trend, with the exception of hylan B167-1.0, and B180-1.0, which are the formulations that could not be solubilized completely, so the numbers reported are not comparable with the other data. All other formulations show an increase in the ratio of HA to crosslink B with decreasing crosslinking reagent added.

#### 4.4. URONIC ACID ASSAY OF HYLAN B167 AND HYLAN B180

The results of the uronic acid assay indicate that with decreasing crosslinking there is also decreased HA content per wet weight of hylan material. This is reasonable considering that the materials with less crosslinking will be allowed to swell a greater amount during the wash step, so for the same wet weight of hylan the less crosslinked hylans will contain more water and less HA and crosslink. Because the assay is done only on the solubilized portion of the sample, both the hylan B167-1.0 and hylan B180-1.0 samples have a significantly decreased mg/ml HA because they were not fully digested. Although the samples do follow the expected trend, there is quite a large range of mg/ml HA as detected by this assay. It does not seem realistic that the values would span such a wide range.

#### 4.5. FACE ANALYSIS OF HYLAN B170 AND HYLAN B173

The FACE gel containing both hylan B170 and hylan B173 reveals the changes in the hylan material that the wash procedure can cause. For each formulation, 0.7, 1.4, 1.8, less than half the material shows up in the hylan B173 isopropanol washed lane as does in the hylan B170 saline washed lane. This is mainly due to the fact that the enzyme was not able to fully digest any of the isopropanol washed samples. The hylan B170-0.7 was not fully solubilized either, but it still produced over twice the mg/ml HA as the hylan B173-0.7 did. The isopropanol wash has an effect on the hylan that causes it to be insoluble by the enzyme, even though the hylan was crosslinked in the same manner as other hylan gels that are digestable. It is still unknown what role the isopropanol plays in changing the characteristics of hylan. The isopropanol washed hylan is opaque, rather than translucent like the saline washed gels. The isopropanol wash also has dramatic effects on the mechanical properties of hylan, as will be discussed.

#### 4.6. URONIC ACID ASSAY ON HYLAN B170 AND HYLAN B173

The results of the uronic acid assay on hylan B170 and hylan B173 correlate quite well with the results of the FACE analysis and the mechanical properties. However, they do not correlate with the ratios of starting HA to divinyl sulfone. For both B170 and B173 hylans the medium crosslinked hylan has the highest mg/ml HA. All of the isopropanol samples had incomplete solubilizations, and it is possible that the B170-0.7

sample was not fully solubilized either, making the values for all these numbers lower than they should be since only the solubilized portion is analyzed.

#### 4.7. COMPRESSION TESTING OF HYLAN B167, B180, AND A COLLAGEN GEL

Compression testing was performed and the compressive moduli at 25% strain of all samples was compared. The samples follow the general trend of increasing compressive modulus with increasing crosslinking reagent added. The middle group of samples, between B180-1.8 and B167-3.5, seem to all lay around the same value. The sample to sample variability was quite low, indicating that the hylan gels were uniformly made. A table (4-1) comparing the moduli of some familiar materials is presented below to give some indication of how hylan relates to other biomaterials and biological tissues. It was found that the compressive modulus and the modulus determined by tensile testing are not equivalent for hylan samples (Table 3-8), and therefore should not be compared directly. In compression, hylan shows non-linear behavior. However, in tension, hylan shows highly linear behavior. This is most likely the reason why the moduli measured in tension and compression do not give the same result. A collagen gel was tested in compression in the same manner as hylan for direct comparison with hylan results, both of which are recorded in the table (4-1).



Table 4-1: Moduli of Various Biomaterials and Biological Tissues

Specimen	Modulus (KPa)	Source of Information
Human Abdominal Skin	1-2	Bader & Bower 1983
Hylan (saline wash, high crosslink)*	10	Experimental Results
Hylan (isopropanol wash, high crosslink)	19	Experimental Results
Collagen Gel, 2.2 mg/ml*	20	Experimental Results
Collagen Gel, 3 mg/ml	40	Osborne 1998
Elastin	600	Fung 1993
Collagen (along fiber)	1,000,000	Fung 1993

\* = Tested in compression, all others tested in tension

By direct comparison with other materials, the applications of hylan in the world of biomaterials is defined. It has sufficient properties to serve as a substrate for growing cells, as an epidermal replacement, or other applications that do not require a high modulus of elasticity.

#### 4.8. TENSILE TESTING OF HYLAN B173

Tensile testing was performed on three different crosslinking formulations of isopropanol washed hylan. The isopropanol washed samples were sturdy enough to be able to perform pre-conditioning. The elastic modulus, failure stress, and failure strain were measured for each formulation and found to be quite similar. The modulus is the only parameter measured that directly relates to the amount of crosslinking reagent

added. The formulation with the highest modulus is the one that has the most crosslinker added to it, and the middle and lowest modulus correspond to the middle and lowest amount of crosslinker added, respectively. The isopropanol wash increases the modulus of hylan by an order of magnitude, making it comparable to the collagen gels tested by Osborne (1998) (Table 4-1).

#### 4.9. RELATION BETWEEN AMOUNT OF RELEASABLE HYALURONAN AND THE COMPRESSIVE MODULUS OF HYLAN SAMPLES

The compressive modulus was plotted against hylan formulation, which is the ratio of HA:crosslinker used in the manufacture of hylan (Figure 4-1). This suggests that even though a certain amount of crosslinking reagent is added, it can not be assumed that the resulting hylan actually contains a certain amount of crosslinking. Therefore, some type of analysis is needed to determine the degree of crosslinking, if the modulus is to be predicted. From the experiments performed here, it was found that the releasable mg/ml HA from FACE analysis indicates the degree of crosslinking and correlates much better with the compressive modulus than hylan formulation does (Figure 4-2). If the B167 set and the B180 set are evaluated individually, they both follow a smooth curve. However, when plotted together the curve is not nearly as smooth. This could be due to the variations in the production of the two hylan lots.

### Compressive Modulus at 25% Strain vs. Hylan Formulation

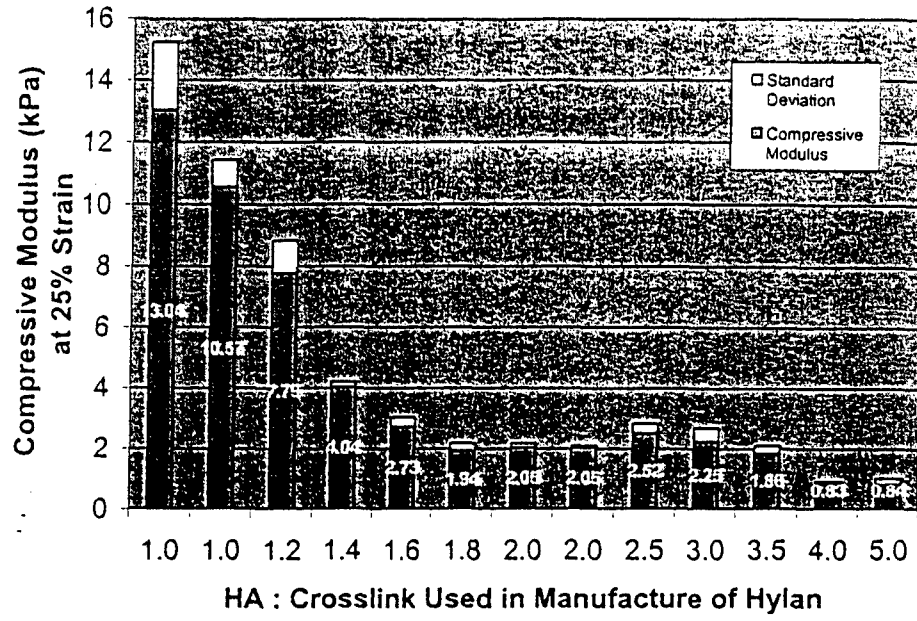


Figure 4-1: Compressive Modulus at 25% Strain vs. Hylan Formulation

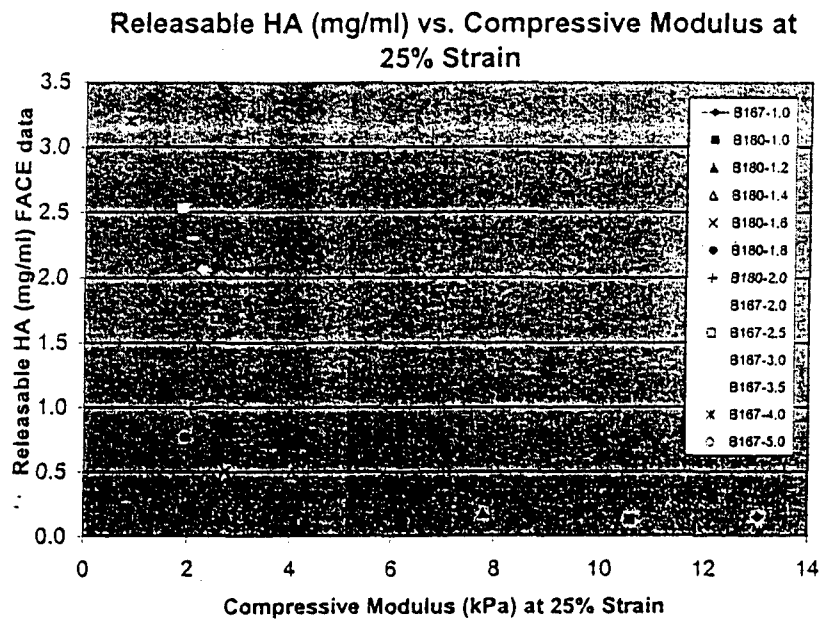


Figure 4-2: Releasable HA mg/ml determined by FACE analysis vs. compressive modulus at 25% strain

#### 4.10. SWELLING EXPERIMENTS

The general trend found is that hylan samples that had more crosslinking reagent added during manufacturing have a smaller percent swell. This is expected because a more highly crosslinked material will hold the HA molecules together more closely, and will not allow as much water to permeate the structure, resulting in less swelling. However, this trend is not followed by many of the samples. Additionally, many of the samples swell approximately the same percent. Only at the very extremes does the percent swell correlate well with the amount of crosslinker added. Again, this

demonstrates that the amount of crosslinking reagent added during manufacture does not always relate to the mechanical properties of the final product.

#### 4.11. OTHER EXPERIMENTS

##### 4.11.1. Conversion of Saline Washed Hylan to Isopropanol Washed Hylan

To investigate the effects of using an isopropanol wash, we tried to convert a saline washed hylan into an isopropanol washed hylan. The saline washed hylan, which was transparent, was taken back into 0.1 M NaOH as it would have existed during the crosslinking reaction. The NaOH was removed and the isopropanol washes were performed. Then they were washed in saline, as is typically done after the isopropanol wash. Upon visual inspection, the samples appeared to have decreased in size and were more opaque than translucent. This indicates that the process performed on the samples seems to have converted them, at least partially, to a formulation that more resembled an isopropanol washed hylan than a saline washed hylan. To further explore this subject, a more systematic experimental protocol needs to be developed and pursued.

##### 4.11.2. Seeding of Keratinocytes Upon Hylan

Several different experiments were performed involving keratinocyte seeding on hylan. Unfortunately, none of the experiments were successful. The keratinocytes preferred the tissue culture dish over the hylan substrate. They also preferred to ball up

and associate with other cells rather than stick to the hylan. Perhaps coating hylan with fibronectin, or collagen type I will help the keratinocytes to attach to hylan. These experiments were preliminary and more extensive studies should be performed.

#### 4.12. FUTURE DIRECTIONS

For future work on this project it would be best make the hylan gels in-house rather than obtaining them from an outside source. That would allow tight control of the way the hylan is prepared, hopefully resulting in less variation in the samples.

It will be very interesting to pursue the study of the isopropanol washed hylan samples. The mechanical properties of these materials are superior to the saline washed hylans in terms of handling which is important for clinical applications. However, until the differences between the isopropanol washed hylans and the saline washed hylans are defined, biocompatibility is a question. The isopropanol could be trapped in the hylan which would not be favorable in terms of biocompatibility.

The seeding of keratinocytes on hylan in hopes of creating an artificial epidermis is also an area that will be interesting to study. Perhaps through the use of coatings on the hylan the keratinocytes will be able to attach. Hylan would still be the component in contact with the body, so the coatings should not affect the biocompatibility of the hylan substrate.

## 5. WORKS CITED

- Balazs, E.A.; Band, P.A.; Denlinger, J.L.; et al. "Matrix Engineering," *Blood Coagulation and Fibrinolysis*, 2(1991) 173-178.
- Balazs, E.A.; Denlinger, J.L. "Clinical uses of hyaluronan," *The Biology of Hyaluronan*, John Wiley & Sons, New York, 1989.
- Balazs, E.A.; Leshchiner, E.; Larsen, N.E.; et al. "Hyaluronan Biomaterials: Medical Applications," *Encyclopedic Handbook of Biomaterials and Bioengineering*, Marcel Dekker, Inc., New York, 1995.
- Band, P.A. "Hyaluronan derivatives: chemistry and clinical applications," *The Chemistry, Biology and Medical Applications of Hyaluronan and its Derivatives*. Wenner-Gren Intl., 1996.
- Calabro, A.; Benavides, M.; Tammi, M.; et al. "Microanalysis of enzyme digests of hyaluronan and chondroitin/dermatan sulfate by fluorophore-assisted carbohydrate electrophoresis (FACE)," *Glycobiology*, 10 [3] (2000) 273-281.
- Calabro, A.; Hascall, V.C.; Midura, R.J. "Adaptation of FACE methodology for microanalysis of total hyaluronan and chondroitin sulfate composition from cartilage," *Glycobiology*, 10 [3] (2000) 283-293.
- Clark, J.A.; Cheng, J.C.; Leung, K.S. "Mechanical properties of normal skin and hypertrophic scars," *Burns*, 22[6] (1996) 443-446.
- Fraser, J.R.E.; Laurent, T.C. "Turnover and Metabolism of Hyaluronan," *The Biology of Hyaluronan. Wiley, Chichester (Ciba Foundation Symposium)* 143 (1989) 41-59.
- Fung, Y.C.; *Biomechanics, Mechanical Properties of Living Tissues*, Springer-Verlag, New York, 1993.
- Gallico, G.G.; O'Connor, N.E. "Engineering a Skin Replacement," *Tissue Engineering* 1 (1995) 231-240.
- Ghersetich, I.; Lotti, T.; Campanile, G.; et al. "Hyaluronic Acid in Cutaneous Intrinsic Aging," *Inter. J. Dermatol.*, 33 [2] (1994) 119-121.
- Hansbrough, J.F.; Morgan, J.; Greenleaf, G.; et al. "Development of a temporary living skin replacement composed of human neonatal fibroblasts cultured in Biobrane, a synthetic dressing material," *Surgery*, 115 (1994) 633-644.
- Hanthamrongwit, M.; Reid, W.H.; Grant, M.H. "Chondroitin-6-sulphate incorporated into collagen gels for the growth of human keratinocytes: the effect of cross-linking agents and diamines," *Biomaterials*, 17 [6] (1996) 775-780.

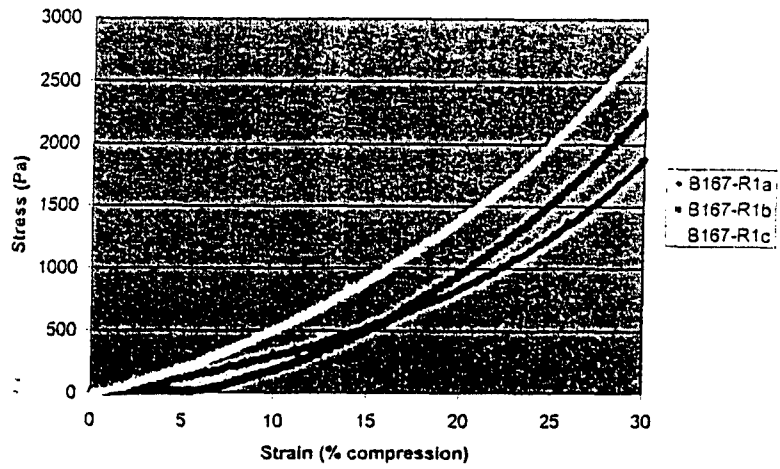
- Hascall, V.C.; Heinegard, D.K.; Wight, T.N. "Proteoglycans: Metabolism and Pathology," *Cell Biology of Extracellular Matrix, Second Edition*. Plenum Press, New York, 1991.
- Larsen, N.E.; Leshchiner, E.; Balazs, E.A. "Use of Hyaluronic Acid as a Biocompatible Interface in a Vascular Prosthesis," *1<sup>st</sup> Atlantic Congress of the Future of Collagen and Other Connective Tissue Compartments and Biomaterials*, Sept. 10-12, 1985, Lyon, France, Conference Trans. 1, 116-123.
- Larsen, N.E.; Leshchiner, E.; Balazs, E.A. "Biocompatibility of Hylan Polymers in Various Tissue Compartments," *Polymers in Medicine and Pharmacy* (Proceedings of the Materials Research Society, Spring Meeting, April 17-21, 1995, San Francisco, CA). Materials Research Society, Pittsburgh, PA, 149-153.
- Larsen, N.E.; Leshchiner, E.; Pollak, C.T.; et al. "Evaluation of Hylan B (Hylan Gel) as Soft Tissue Dermal Implants," *Polymers in Medicine and Pharmacy* (Proceedings of the Materials Research Society, Spring Meeting, April 17-21, 1995, San Francisco, CA). Materials:Research Society, Pittsburgh, PA: 193-197.
- Larsen, N.E.; Pollak, C.T.; Reiner, K.; et al. "Hylan gel biomaterial: Dermal and immunologic compatibility," *J Biomed Materials Research*, 27 (1993) 1129-1134.
- Larsen, N.E.; Pollak, C.T.; Reiner, K.; et al. "Hylan Gel for Soft Tissue Augmentation," *Biotechnology and Bioactive Polymers*, Plenum Press, New York, 1994.
- Laurent, T.C. *The Chemistry, Biology and Medical Applications of Hyaluronan and its Derivatives*, Portland Press Ltd, London, 1998.
- Lesley, J.; Hyman, R.; English, N.; et al. "CD44 in Inflammation and Metastasis," *Glycoconj. J.*, 14 (1997) 611-622.
- Ludger, J.M.; Meyer; Stern, R. "Age-Dependent Changes of Hyaluronan in Human Skin," *J. Invest. Dermatol.*, 102 (1994) 385-389.
- Oksala, O.; Salo, T.; Tammi, R.; et al. "Expression of Proteoglycans and Hyaluronan During Wound Healing," *J. Histochem. Cytochem.*, 43 (1995) 125-135.
- Osborne, C.S.; Barbenel, J.C.; Smith, D.; et al. "Investigation into the tensile properties of collagen/chondroitin-6-sulphate gels: the effect of crosslinking agents and diamines," *Med Biol Eng Comput*, 36[1] (1998) 129-134.
- Saphwan, A.A.; Phillips, G.O.; Deeble, D.J.; et al. "The Enhanced Stability of the Cross-Linked Hylan Structure to Hydroxyl (OH) Radicals Compared with the Uncross-Linked Hyaluronan," *Radiat Phys Chem*, 46[2] (1995) 207-217.
- Strange, C.J. "Second Skins," *FDA Consumer 1997*, 31 (1997) 12-17.



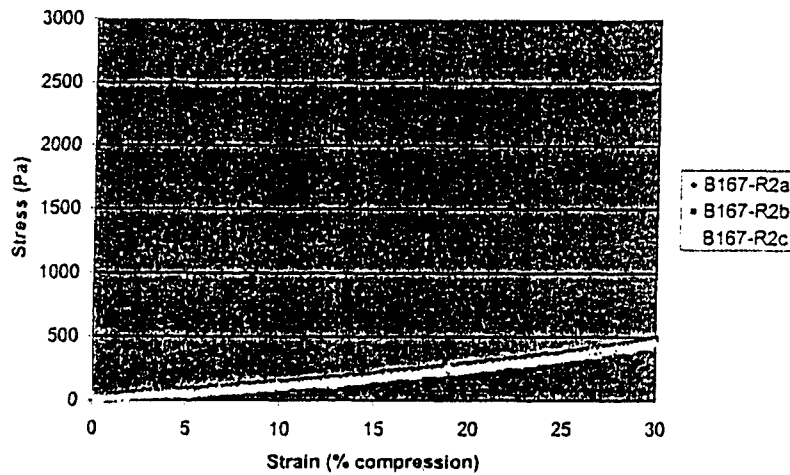
Wight, T.N.; Heinegard, D.K.; Hascall, V.C. "Proteoglycans: Structure and Function,"  
*Cell Biology of Extracellular Matrix, Second Edition*. Plenum Press, New York, 1991.

APPENDIX: Graphs of Mechanical Testing Data

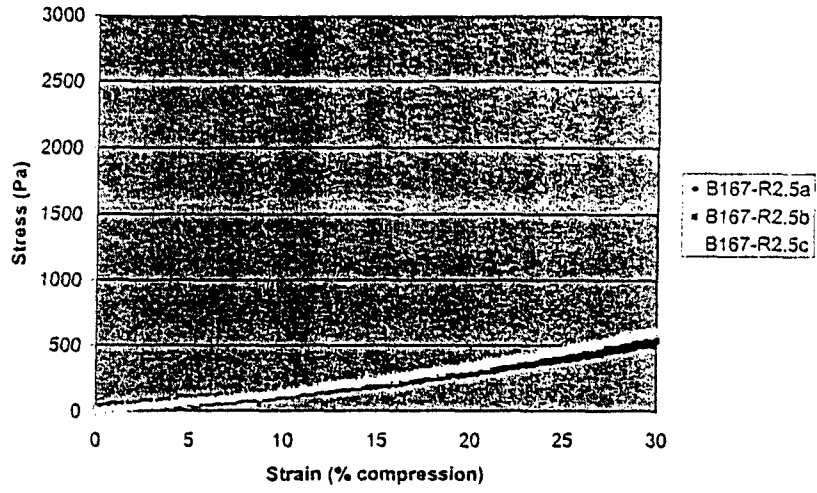
B167-1.0 Compression Test



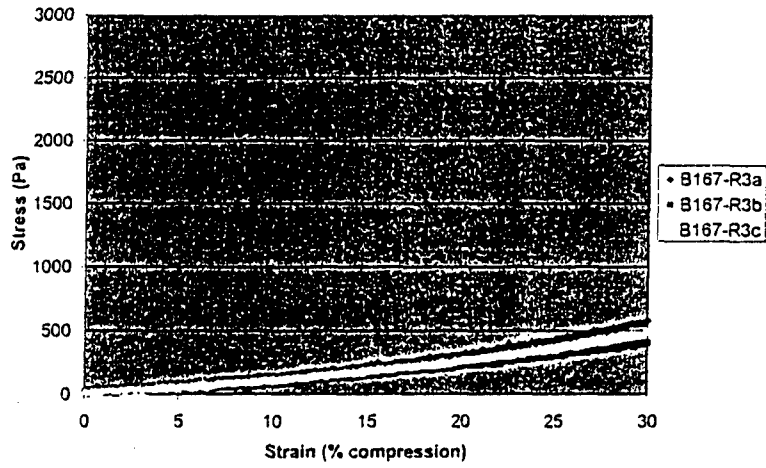
B167-2.0 Compression Test



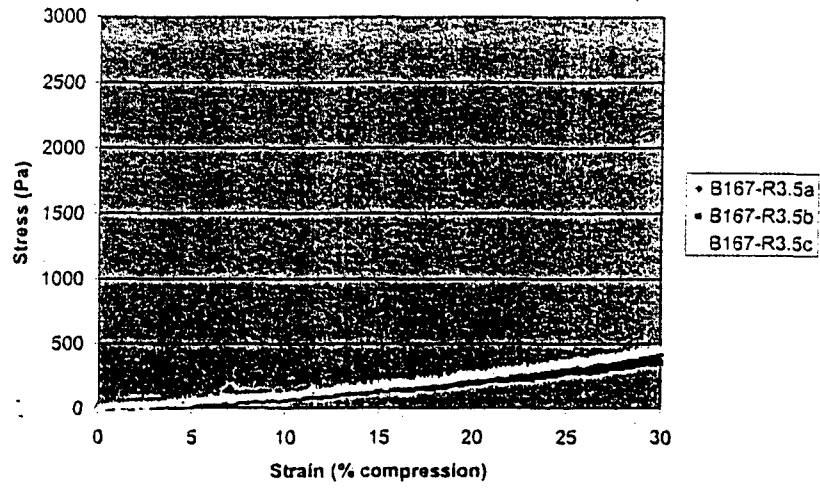
### B167-2.5 Compression Test



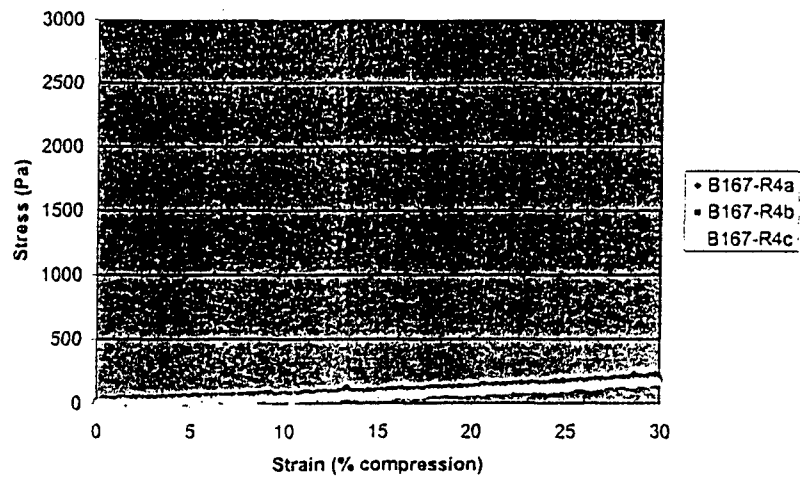
### B167-3.0 Compression Test



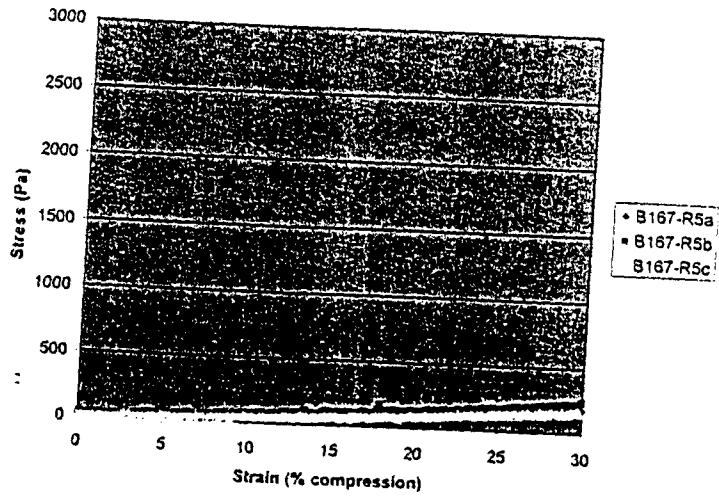
### B167-3.5 Compression Test



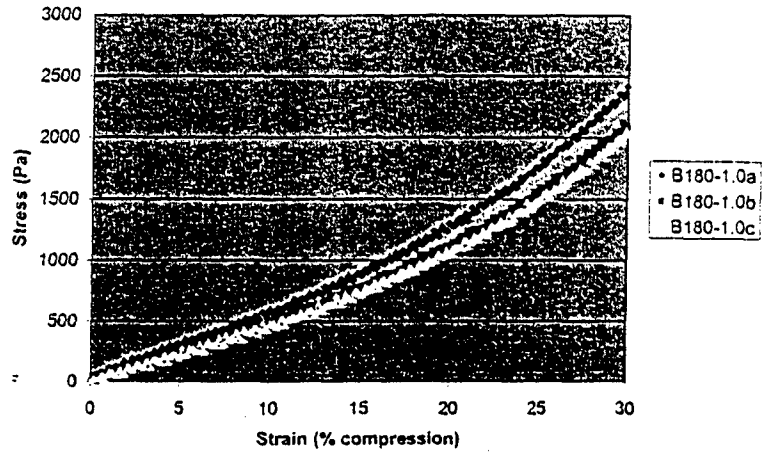
### B167-4.0 Compression Test



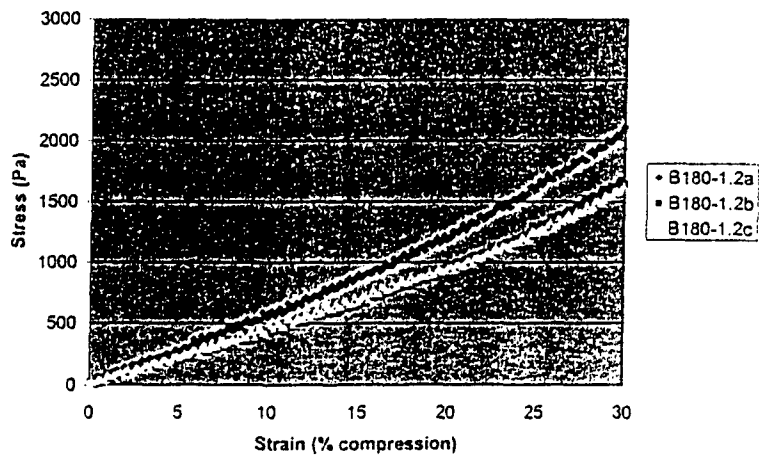
B167-5.0 Compression Test



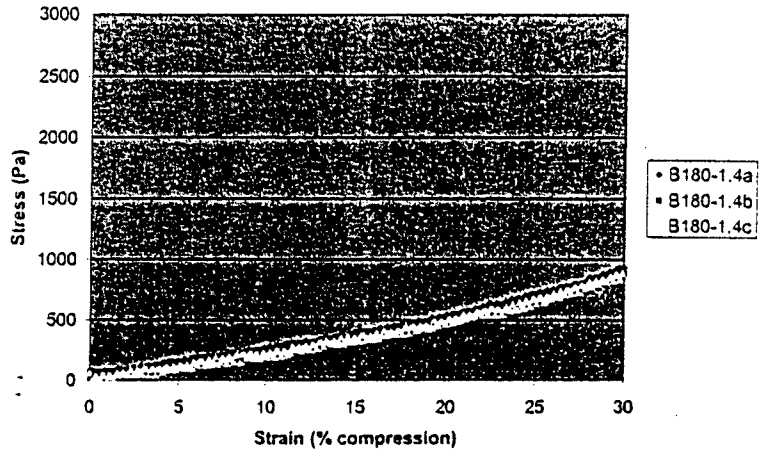
B180-1.0 Compression Test



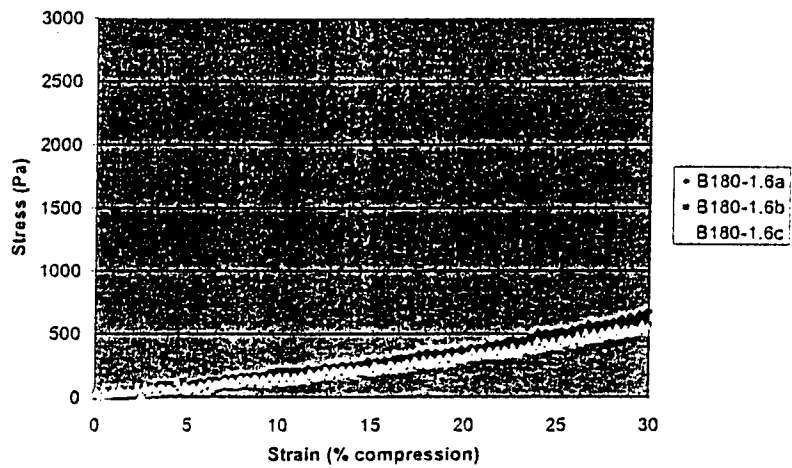
B180-1.2 Compression Test



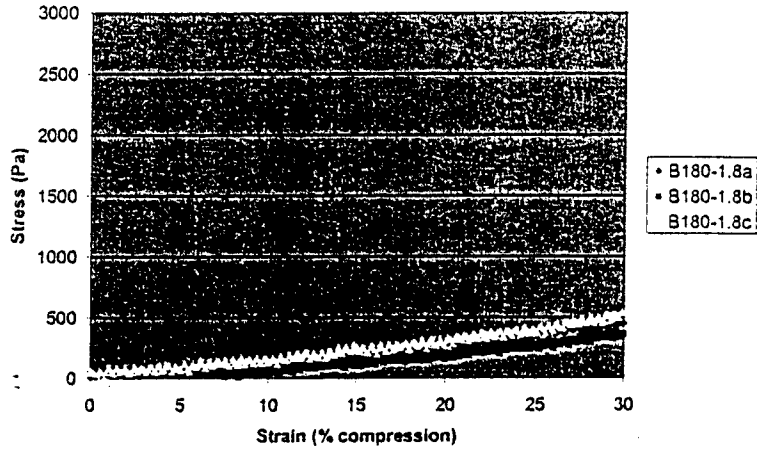
B180-1.4 Compression Test



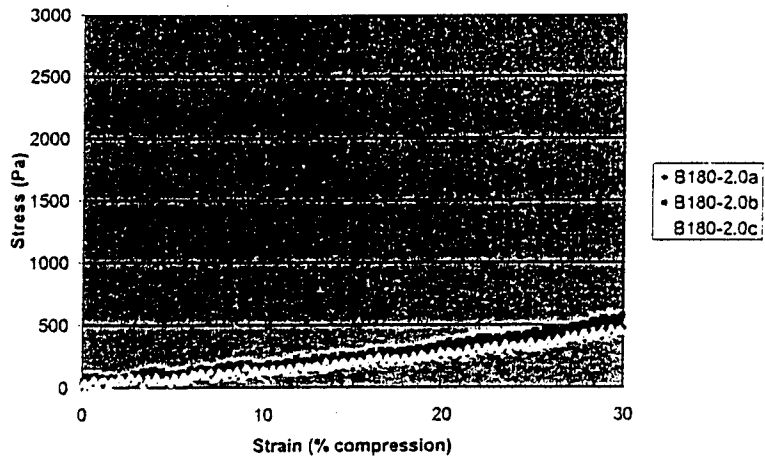
B180-1.6 Compression Test



### B180-1.8 Compression Test

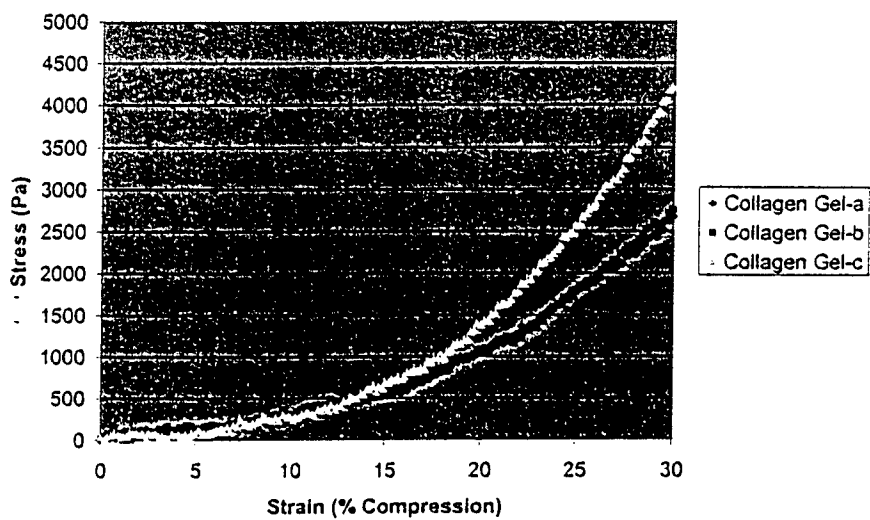


### B180-2.0 Compression Test

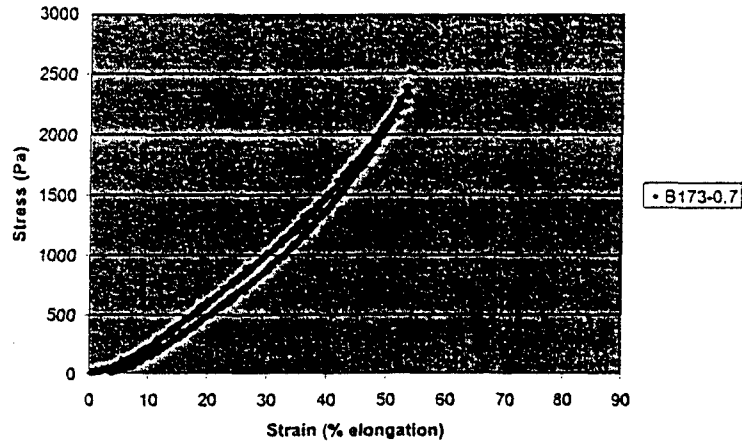




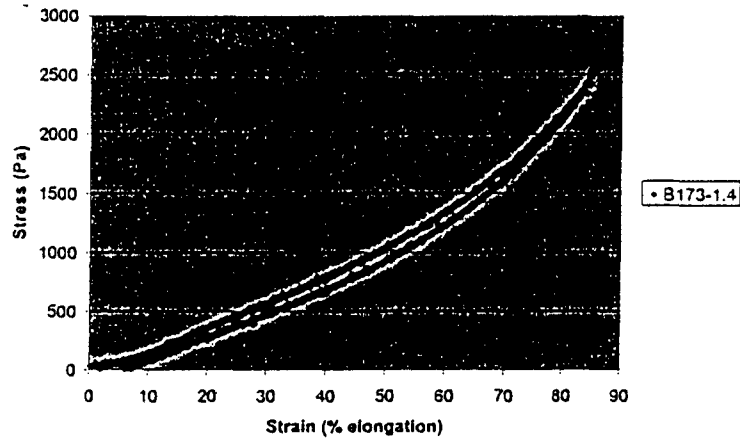
### Collagen Gel Compression Test



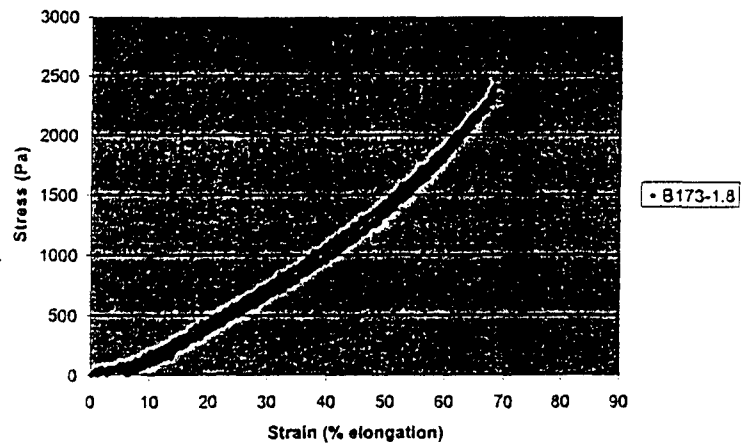
B173-0.7 Tensile Test



B173-1.4 Tensile Test



B173-1.8 Tensile Test



Raija H. Tammi · Markku I. Tammi  
Vincent C. Hascall · Michael Hogg · Sanna Pasonen  
Donald K. MacCallum

## A preformed basal lamina alters the metabolism and distribution of hyaluronan in epidermal keratinocyte “organotypic” cultures grown on collagen matrices

Accepted: 18 January 2000 / Published online: 7 March 2000  
© Springer-Verlag 2000

**Abstract** A rat epidermal keratinocyte (REK) line which exhibits histodifferentiation nearly identical to the native epidermis when cultured at an air–liquid interface was used to study the metabolism of hyaluronan, the major intercellular macromolecule present in basal and spinous cell layers. Two different support matrices were used: reconstituted collagen fibrils with and without a covering basal lamina previously deposited by canine kidney cells. REKs formed a stratified squamous, keratinized epithelium on both support matrices. Hyaluronan and its receptor, CD44, colocalized in the basal and spinous layers similar to their distribution in the native epidermis. Most (approximately 75%) of the hyaluronan was retained in the epithelium when a basal lamina was present while most (approximately 80%) diffused out of the epithelium in its absence. While REKs on the two matrices synthesized hyaluronan at essentially the same rate, catabolism of this macromolecule was much higher in the epithelium on the basal lamina (half-life approximately 1 day, similar to its half-life in native human epidermis). The formation of a true epidermal compartment in culture bounded by the cornified layer on the surface and the basal lamina subjacent to the basal cells provides a good model within which to study epidermal metabolism.

### Introduction

Hyaluronan (hyaluronic acid) is a macromolecule with a disaccharide repeat formed by the polymerization of alternating glucuronic acid and *N*-acetylglucosamine residues. A single hyaluronan molecule can have a molecular weight of 10 million daltons (approximately 25,000 repeat disaccharides). Because of the large number of carboxyl groups on the glucuronic acid residues, hyaluronan functions as a large polyanion in the body with its open random coil structure occupying large solvent domains (Wight et al. 1991; Laurent et al. 1996). Hyaluronan is generally regarded as a component of connective tissue extracellular matrices and, indeed, in embryonic connective tissue, it can be the major structural molecule in the extracellular matrix where it plays roles in cell proliferation and migration (Toole 1991).

Recent studies have emphasized that hyaluronan is not simply a component of connective tissue extracellular matrices, but that it is also present in restricted locations within the nervous system (Ripellino et al. 1988; Bignami et al. 1993) and in certain epithelial tissues (Mani et al. 1992; Tammi et al. 1994a,b; Yung et al. 1996; Usui et al. 1999) including its universal presence within stratified epithelia (Tammi et al. 1988, 1990; Laurent et al. 1995; Wang et al. 1996; Hirvikoski et al. 1999). We (R.T. and M.T.) have studied the distribution of hyaluronan in the epidermis, a stratified squamous keratinizing epithelium. Hyaluronan is present in exceedingly high concentrations in the small intercellular spaces between adjacent basal and spinous keratinocytes, among the highest concentrations of any place in the body (Tammi et al. 1994b, 1999). Additionally, studies of human skin organ cultures have demonstrated that hyaluronan within the epidermis is rapidly turned over, an observation that suggests that the epidermis possesses mechanisms to catabolize hyaluronan that are closely coordinated with its synthesis by keratinocytes (Tammi et al. 1991).

In skin, both epidermal keratinocytes and the cells present in the dermis (principally fibroblasts) synthesize

R.H. Tammi · M.I. Tammi · S. Pasonen  
Department of Anatomy, University of Kuopio, 70211 Kuopio,  
Finland

V.C. Hascall · M. Hogg  
Department of Biomedical Engineering, ND 20,  
Cleveland Clinic Foundation, 9500 Euclid Avenue, Cleveland,  
Ohio 44195, USA

D.K. MacCallum (✉)  
Department of Anatomy and Cell Biology,  
University of Michigan, Ann Arbor,  
Michigan 48109–0616, USA  
e-mail: dkmb@umich.edu  
Tel.: +1-734-7635032, Fax: +1-734-7631166

hyaluronan (Tammi et al. 1994b). Because both portions of the skin (epidermis and dermis) form and contain hyaluronan, it is frequently difficult to resolve the specific contribution of each component to the overall metabolism and content of this macromolecule in skin. To understand more completely the nature of hyaluronan synthesis and distribution in the epidermis, we have studied a rat epidermal cell line in culture. Our initial experiments utilized monolayer cultures to determine how hyaluronan is organized on the keratinocyte cell surface and its relationship to the cell surface hyaluronan-binding molecule, CD44 (Tammi et al. 1998).

We now extend these studies to the metabolism of hyaluronan in a reconstituted epidermis formed by the rat epidermal keratinocytes (REKs) when grown on collagen at the interface between the medium and gaseous phase of the culture (a "lifted" culture; Lillie et al. 1980). This culture conformation facilitates reformation of a stratified epithelium that more closely resembles the native epidermis than conventional "submerged" cultures and is often called an "organotypic" culture (Voigt and Fusenig 1979). Midway into our studies, it became apparent that while the REKs reformed an epidermis that closely resembled the native tissue, with basal cells dividing and moving through various cell strata ultimately to form a cornified ("keratinized") tissue surface, the epidermis remained "open" on its inferior aspect. In order to form a true epidermal compartment bounded superiorly by the stratum corneum and inferiorly by a basal lamina, we cultured the REKs on a collagen matrix that was covered by a basal lamina previously deposited by Maden Darby canine kidney (MDCK) cells which were then removed from the matrix prior to adding the keratinocytes. The presence of the basal lamina on the collagen matrix altered the metabolism and distribution of hyaluronan when compared to the "open" collagen matrix alone. A comparison of hyaluronan metabolism on the two different culture substrates and the barrier function of the basal lamina in altering the metabolism of hyaluronan are the subjects of this report.

## Materials and methods

### Keratinocyte culture

The REK cell line used in this study was derived from neonatal REKs (a gift of Howard Baden) originally isolated by Baden and Kubilus (1983). The keratinocytes stratify and terminally differentiate ("keratinize") in culture in the absence of "feeder" cells and exhibit a particularly high degree of tissue organization when cultured on collagen at the interface between the culture medium and culture gas phase (MacCallum and Lillie 1990). Stock cultures were grown in Dulbecco's modified minimal essential medium (1 g glucose/l), 10% fetal bovine serum, 50 µg/ml gentamicin sulfate ("complete medium") at 37°C in humidified 95% air/5% CO<sub>2</sub>. Keratinocytes were subcultured by incubating them for approximately 10 min at 37°C in 0.02% EDTA and 0.05% crystalline trypsin (Calbiochem, La Jolla, Calif., USA) in Ca<sup>2+</sup>, Mg<sup>2+</sup>-free Earle's balanced salt solution buffered to pH 7.4 with 20 mM HEPES.

### Collagen substrate

Commercially available rat tail collagen (Sigma, St. Louis, Mo., USA) was dissolved at a concentration of 2.2 mg/ml in 0.034 N acetic acid at 4°C overnight. The dissolved collagen was dialyzed at 4°C against 2x500 volumes 0.2 M NaCl in 50 mM TRIS-HCl, pH 7.6, over 24 h. The dissolved collagen, 800 µl, was added to individual 24.5-mm-diameter tissue culture inserts (Costar Transwell; 3.0 µm pore size). Collagen fibrils were formed by incubating the tissue culture inserts for 45 min at 37°C in a humidified atmosphere. The collagen gels thus formed were used directly without further treatment or, alternatively, were immersed in balanced salt solution at 4°C until needed.

### Preformed basal lamina

MDCK cells were obtained from the American Type Culture Collection (Bethesda, Md., USA) and were subcultivated onto collagen gels in the tissue culture inserts (200,000 cells/24.5-mm insert). The MDCK cells were fed 3 times per week for 18–22 days using the same medium as that used for the keratinocytes. MDCK cells were removed using a protocol slightly modified from that of Huber and Weiss (1989) and Kramer et al. (1985). This required exposing the cells for approximately 10 min to a sterile 10 mM TRIS-HCl hypotonic buffer that contained 0.1% bovine serum albumin (BSA) and 0.1 mM CaCl<sub>2</sub>, pH 7.5. The MDCK cells on the collagen were subsequently solubilized by incubating them in sterile 0.2% deoxycholate (Calbiochem) in the same buffer for 2x5 min at 37°C followed by incubation in sterile 0.5% Nonidet P-40 in the same buffer for 5 min at room temperature. After each incubation, the surface of the Transwell was gently washed using a Pasteur pipette and the detergent solution removed. When viewed with a phase microscope, there should be no morphological evidence of the MDCK cells after the second deoxycholate incubation. Following lysis of the cells, the Transwell culture surface was covered by a basal lamina, deposited by the MDCK cells, sitting on the surface of a collagen gel composed of reconstituted native collagen fibrils. The cleaned culture substrates are rinsed 3 times over 1 h in balanced salt solution followed by two changes of complete tissue culture medium over 0.5 h at 37°C. Alternatively, the basal lamina-covered collagen gels can be stored in balanced salt solution at 4°C for several months and subsequently treated with complete culture medium immediately prior to use.

### "Lifted" or "organotypic" keratinocyte cultures

Cultures of REKs just having reached confluence with little or no morphological evidence of stratification were subcultivated onto either collagen-covered (designated BL-) or basal lamina-coated/collagen-covered (designated BL+) Transwell culture inserts at a concentration of 150,000–200,000 REKs/24.5-mm insert. The subcultivated REKs were grown for 2 days with culture medium present both in the well beneath the Transwell insert as well as on the surface of the cells. The culture medium was subsequently removed from the surface of the cells and the level of the medium beneath the Transwell insert adjusted to the level of the REKs present on the BL- or BL+ collagen gels. The cultures for this study were grown for an additional 5 days at 37°C in humidified 95% air/5% CO<sub>2</sub> with the medium being changed 3 times per week.

### Electron microscopy

Culture substrates to be examined by scanning electron microscopy were fixed for 2 h at room temperature in 2.5% glutaraldehyde in pH 7.4, 0.1 M sodium cacodylate that contained 4% sucrose and 2 mM CaCl<sub>2</sub>. The substrates were then sequentially fixed in aqueous 1% OsO<sub>4</sub>, 1% tannic acid, 1% OsO<sub>4</sub> for 1 h each before being dehydrated through ascending concentrations of ethanol. The etha-

nol was exchanged by three changes of hexamethyldisilazane from which the substrates were subsequently air dried. The substrates were mounted on stubs and sputter coated with platinum/palladium prior to scanning.

Cultures examined as either epoxy-embedded 1- $\mu$ m-thick light microscopic sections or as conventional electron microscopic thin sections were fixed for 2 h at 4°C in a 50:50 mixture of buffered 2.5% glutaraldehyde and 2% aqueous OsO<sub>4</sub> with the final mixture containing 4% sucrose and 2 mM CaCl<sub>2</sub>. The samples were dehydrated in ethanol and propylene oxide and embedded in epoxy resin. Sections were stained with either toluidine blue (light microscope) or uranyl acetate and lead citrate (electron microscope).

#### Histochemical demonstration of hyaluronan

A hyaluronan-specific probe, biotinylated hyaluronan binding complex (bHABC), was prepared from a 4-M guanidine-HCl extract of bovine articular cartilage after dialysis and digestion with trypsin, as described previously (Tammi et al. 1994b). The bHABC probe exhibited the biotinylated G1 domain of aggrecan and biotinylated link protein as the only silver stained and biotinylated proteins present when analyzed by SDS-PAGE.

Eight-millimeter circular biopsies were cut from individual culture inserts and fixed in 2% paraformaldehyde, 2.5% glutaraldehyde, 0.5% cetylpyridinium chloride, and 30 mM NaCl in 0.1 M phosphate buffer, pH 7.4, overnight. The biopsies were washed with buffer, dehydrated, and embedded in paraffin. Three-micron-thick sections were cut, deparaffinized, and incubated in 1% BSA in phosphate buffer for 30 min. The sections were then incubated with bHABC (3–5  $\mu$ g/ml diluted in 1% BSA, 0.1 M sodium phosphate, pH 7.4) overnight at 4°C, washed with buffer 3 times (5 min each), and incubated with avidin-biotin-peroxidase (Vector Laboratories, Irvine, Calif., USA) for 1 h at room temperature. The sections were then incubated for 5 min in 0.05% 3,3'-diaminobenzidine (DAB) and 0.03% hydrogen peroxide in the phosphate buffer. After washes, the sections were counterstained with Mayer's hematoxylin for 2 min, washed, dehydrated, and mounted in DPX. The specificity of the staining was controlled by preincubating the sections with Streptomyces hyaluronidase (100 turbidity reducing units/ml) in 50 mM sodium acetate buffer, pH 5.0, containing protease inhibitors for 3 h at 37°C to remove hyaluronan from the tissue (Tammi et al. 1989). Other controls included sections reacted with the bHABC probe that was pretreated with hyaluronan oligosaccharides as described (Tammi et al. 1989) to block specifically the binding of the probe to endogenous hyaluronan in the sections.

#### CD44 localization

For the localization of CD44, the tissues were fixed in Histochoice (Amresco, Solon, Ohio, USA) for 2 h, washed, dehydrated in graded ethanol, and embedded in paraffin. The sections were first treated for 5 min with 1% H<sub>2</sub>O<sub>2</sub> to block endogenous peroxidase, and then incubated with 1% BSA in phosphate-buffered saline (PBS) for 30 min to block non-specific binding. Thereafter the sections were incubated with monoclonal anti-CD44 (OX50; Biosource, Camarillo, Calif., USA; 1:50 dilution in 1% BSA) overnight at 4°C, followed by sequential 1-h incubations with biotinylated anti-mouse antibody (Vector; dilution 1:50), and avidin-biotin-peroxidase (Vector; 1:200 dilution). The color was developed with DAB as described above. The controls included sections treated in the same way but omitting the primary antibody, or by replacing it with non-immune mouse IgG.

#### Metabolic labeling of REK cultures

Five days after the REK cultures were configured at the gas-liquid interface (7 days after subcultivation onto the respective matrices), cultures were metabolically labeled with 20  $\mu$ Ci/ml [<sup>3</sup>H]glucos-

amine and 100  $\mu$ Ci/ml <sup>35</sup>SO<sub>4</sub> (both compounds were from Amersham, Little Chalfont, UK) in complete tissue culture medium. Cultures were analyzed at 3, 6, 9, 12, 18, and 24 h after labeling. In separate cultures, fresh medium without radiolabeled precursors was added at time 0. At 15 or 24 h, the radiolabeled precursors were then added in a small aliquot from a concentrated stock solution to give final concentrations equivalent to the continuously labeled cultures. In each case, these cultures were incubated for an additional 3 h giving labeling windows of 15–18 h and 24–27 h. Addition of isotopes near the end of the experiment was done to ensure that any changes observed in metabolic labeling were not due to progressive dilution or exhaustion of the isotopes.

#### Culture compartments defined

Three "compartments" of the cultures (medium, epithelium, and matrix) were analyzed. As explained below, values for two of the compartments (medium and matrix) were combined and expressed as a single value. At the end of each labeling interval, the medium (2 ml) was collected and the culture inserts were washed once with 0.5 ml Dulbecco's PBS which was added to the medium (= medium compartment). Thereafter the cultures were immersed in 1 ml 0.04% sodium EDTA in PBS for 5 min at 37°C to separate the epithelium from the matrix (Tammi and Tammi 1986). The epithelial sheets were mechanically lifted off the matrices (BL+ and BL-) using a stereo microscope and fine needles to accomplish the separation. The epithelial sheets were analyzed separately (= epithelial compartment) and the EDTA separating solution was combined with the collagen or basal lamina + collagen matrix (= matrix compartment). All three compartments were analyzed for glycosaminoglycans. Some of the separated cultures were processed for light microscopy to ensure that the separation between the two compartments took place at the junction of the basal cells with the underlying matrix (data not shown). Data obtained from the "media" and "matrix" compartments have been combined and treated as a single value for each time point for the sake of simplicity in the presentation of graphs and to facilitate the comparison between the REKs cultured on the two different matrices (BL- or BL+).

#### Purification of the radiolabeled hyaluronan and glycosaminoglycans

Carrier hyaluronan (4  $\mu$ g in 40  $\mu$ l, Healon; Pharmacia, Uppsala, Sweden) and 4 volumes 100% ethanol saturated with NaCl were added to each medium, matrix, and epithelial sheet. After 1 h at -20°C, precipitates were centrifuged for 15 min at 2500 g. Each precipitate was suspended in 200  $\mu$ l 50 mM sodium acetate, pH 5.8, containing 5 mM cysteine-HCl and 5 mM sodium EDTA to which 50  $\mu$ g papain (Sigma) in 50  $\mu$ l water was added followed by incubation at 60°C for 4 h. The samples were heated at 100°C for 10 min, centrifuged at 13,000 g for 15 min, and supernatants containing hyaluronan and other glycosaminoglycans recovered. Cetylpyridinium chloride (1% in 20 mM NaCl, 4 volumes) was added to each supernatant followed by incubation for 1 h at room temperature. After centrifugation at 13,000 g for 15 min, each supernatant was carefully removed by aspiration. Each precipitate was washed with 1 ml H<sub>2</sub>O, centrifuged, and the supernatant discarded as above. Each cetylpyridinium chloride precipitate was dissolved in 50  $\mu$ l 4 M guanidine-HCl, and 900  $\mu$ l ethanol, saturated with NaCl, was added. After 1 h at -20°C, each sample was centrifuged and the precipitate retained.

Each purified sample was dissolved in 50  $\mu$ l 50 mM sodium acetate, pH 6.7, and digested for 3 h at 37°C with 25 mU chondroitinase ABC and 1 mU of Streptococcal hyaluronidase (both from Seikagaku Kogyo, Tokyo, Japan), and 10–45  $\mu$ l injected onto a 1 $\times$ 30 cm Superdex Peptide column (Pharmacia) and eluted at 0.5 ml/min with 0.1 M NH<sub>4</sub>HCO<sub>3</sub>. The eluent was monitored at 232 nm, and aliquots of the 250- $\mu$ l fractions were counted for <sup>3</sup>H and <sup>35</sup>S. The carrier hyaluronan produced a disaccharide peak at

232 nm which was used to monitor the recovery (about 80%) and correct for any losses in purification.

#### Ion-exchange chromatography

The radiolabeled disaccharide peaks from Superdex chromatography were dried, redissolved in water, and their identities confirmed by ion-exchange chromatography. The non-sulfated disaccharides and monosulfated chondroitin disaccharides were fractionated on 4×50 mm Carboapak MA1 and PA1 columns (Dionex, Sunnyvale, Calif., USA) eluted isocratically with 20 mM and 500 mM sodium phosphate, pH 7.0, respectively. The disulfated disaccharides were chromatographed on a 0.4–1.0 M LiCl gradient on the PA1 column. More than 85% of the radioactivity in the dried peaks coeluted with standards (Seikagaku Kogyo) in the expected positions.

#### Chemical quantitation of hyaluronan with double labeling

The specific activity of [<sup>35</sup>S]sulfate in the medium compartment is the same as that in 3'-phosphoadenosine-5'-phosphosulfate, the metabolic precursor of sulfate incorporation into sulfated glycosaminoglycans, after a short equilibration time between the medium and intracellular pools. Thus the <sup>35</sup>S activity in chondroitin sulfate is a measure of the mass of chondroitin sulfate synthesized during the labeling period. Conversely, the specific activity of [<sup>3</sup>H]glucosamine in the medium is much higher, often more than 100-fold, than the specific activity of the uridine diphosphate (UDP)-*N*-acetylhexosamine pool even after equilibration between the medium and intracellular compartments. This occurs because glucose is the primary source of glucosamine inside the cell, and therefore, metabolic conversion of glucose to glucosamine dilutes the specific activity of the exogenous, radiolabeled glucosamine. This dilution factor is generally unknown. However, we take advantage of the dual label in the chondroitin sulfate disaccharides to circumvent this problem.

From the known specific activity of the [<sup>35</sup>S]sulfate in the medium, the masses of the monosulfated disaccharides were determined for each sample. Since the UDP-*N*-acetylhexosamine pool is a common precursor for both chondroitin sulfate and hyaluronan synthesis, the ratio of <sup>3</sup>H activity for these two glycosaminoglycans is equivalent to their mass ratio. Thus, the product of the mass of chondroitin sulfate synthesized (derived from the <sup>35</sup>S activity) times the ratio of <sup>3</sup>H in hyaluronan to that in chondroitin sulfate is a measure of the mass of hyaluronan synthesized. The rationale and efficacy of this method is presented in greater detail in Yanagishita et al. (1989).

#### Determination of size distribution of hyaluronan using S1000 size-exclusion chromatography

Extracts of collagen were combined with the medium, and 0.5 ml of this sample was used for size distribution determination. The samples were injected into a 1×30 cm column of Sephacryl S1000 (Pharmacia), eluted with a flow rate of 20 ml/h with sodium acetate buffer (0.15 M, pH 6.8) containing 0.1% CHAPS. Half-milliliter fractions were collected and two samples of 100 µl were taken for the assay of hyaluronan using CPC precipitation on nitrocellulose membrane as previously described (Ågren et al. 1997). One of the samples was subjected to digestion with *Streptomyces* hyaluronidase (5 turbidity reducing units/sample) for 3 h at 37°C before CPC precipitation, while the other sample got an equal volume of buffer. The difference in DPMs between the undigested and digested sample was used to represent counts in hyaluronan.

## Results

### Culture substrates

The basal lamina deposited on the collagen gel by MDCK cells exhibited a clean, smooth, featureless surface when examined at low power by scanning electron microscopy (Fig. 1A). When the surface of the collagen gel was gently scraped by fine forceps, the basal lamina was torn and the underlying collagen fibrils could be visualized (Fig. 1B,C). When the surface of the basal lamina was examined at high power faint, linear profiles that sometimes overlapped were observed (Fig. 1D,E). These profiles represented collagen fibrils immediately subjacent to the basal lamina that apparently were firmly adherent to the basal lamina because in no case were we able to peel just the basal lamina from the surface of the gel without accompanying collagen fibrils.

Occasional (1–2/100 µm<sup>2</sup>), small (<1.0 µm) circular or oval defects in the lamina were evident at high magnification (Fig. 1F). These defects apparently result from MDCK cell cytoplasmic processes projecting through the formed basal lamina (Valentich 1982). Thus, while a basal lamina covers the entire surface of the collagen gel, it is evident that the lamina is not 100% intact. [Our experience is that one of each batch of basal lamina-covered collagen gels should be examined by scanning electron microscopy before using them as culture substrates because infrequent batches may exhibit many small holes (approximately 100/100 µm<sup>2</sup>)]. The arrangement and space occupied by the collagen fibrils exposed by peeling back the basal lamina (Fig. 1C) was characteristic of the collagen matrix without a basal lamina used in these culture experiments, and was conspicuously "open" when compared to the basal lamina-covered collagen gels.

### Morphology of REKs cultured on collagen or basal lamina-covered collagen at the air-medium interface (an "organotypic culture")

REKs subcultured onto either substrate grew to confluence, stratified, and exhibited the normal progression from basal cell to cornified surface cell (Fig. 2A,B). The number of cells in the viable cell strata remained relatively constant from 5 days of lifted culture onward; however, the cornified layer continued to increase in thickness as terminally differentiated cells were continually added for the duration of the culture period (not shown). The major morphological difference between REKs grown on collagen alone (BL-) and REKs grown on the basal lamina-covered collagen (BL+) was evident at the junction of the basal keratinocytes with the underlying matrix. Basal keratinocytes grown on collagen alone exhibited numerous, small cytoplasmic processes extending from the undersurface of the cell down into the meshwork of collagen fibrils. With extended culture, a sizable population of detached cytoplasmic fragments

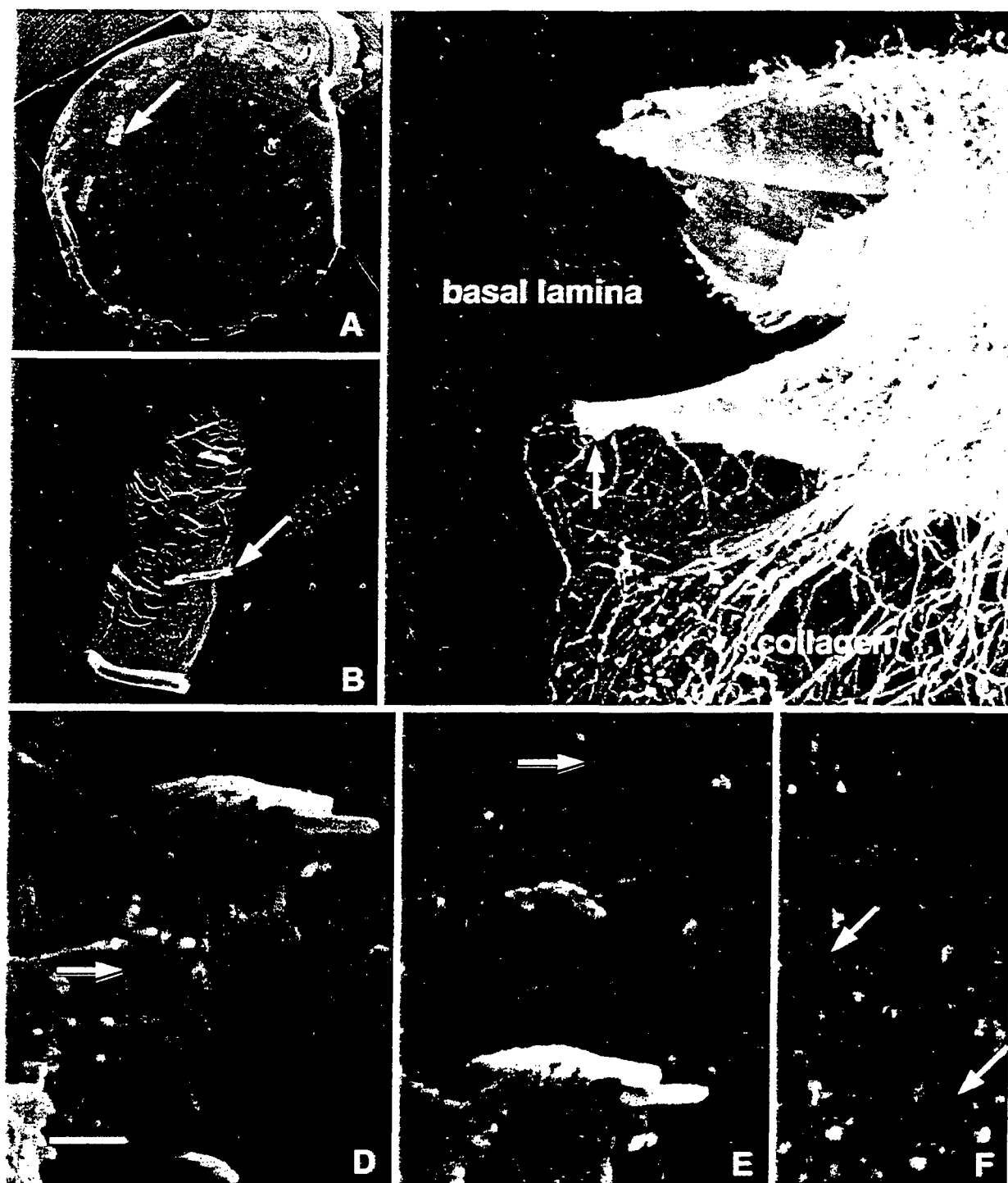


**Fig. 1A-F** Scanning electron micrographs of basal lamina-covered collagen support matrices. **A** Eight-millimeter diameter sample of the basal lamina-covered matrix. *Arrow* points to the region shown in **B**. **B** Surface defect made by dragging fine forceps across the basal lamina exposing the underlying collagen. The edge indicated by the *arrow* is shown at higher power in **C**. **C** Torn edge of the basal lamina (*arrow*). The solid surface of the basal lamina contrasts with the mesh work of collagen fibrils underlying it. Collagen fibrils always were torn away with the basal lamina when the surface was disturbed indicating that the basal lamina was firmly adherent to the collagen. The arrangement of

the collagen fibrils in the micrograph is identical to that of matrices used to culture keratinocytes in the absence of a basal lamina (BL-). **D,E** High power scanning electron micrographs of the basal lamina surface indicating a faint fibrillar texture (examples at *arrows*) due to the underlying collagen fibrils. Each micrograph includes a surface defect made to expose underlying collagen fibrils. **F** Two pores (50 and 80 nm; *arrows*) in the basal lamina due to processes of Maden Darby canine kidney cells extending through the basal lamina as it was being formed. *Bar* (in **D**) 1.7 mm in **A**; 600  $\mu$ m in **B**; 1.6  $\mu$ m in **C**; 1  $\mu$ m in **D-F**

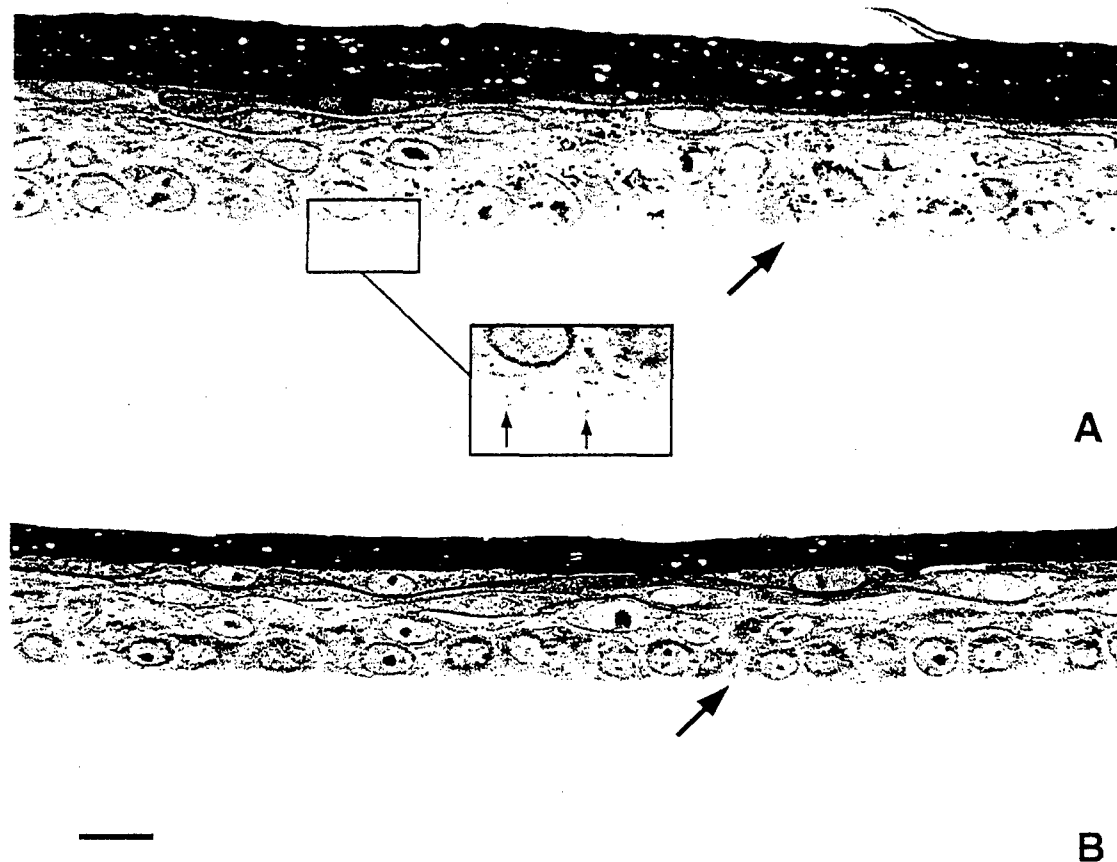


**Fig. 2** Light micrographs of rat epidermal keratinocytes (REKs) cultured on collagen alone (BL-; **A**) and on a basal lamina-covered collagen gel (BL+; **B**) after 5 days of growth at the air-liquid interface of the culture. *Arrows* mark the junction of the stratified epithelia with their support matrices. The upper part of the cornified layer was lost during processing of the BL+ culture (**B**) and thus appears thinner than that on the BL- culture. Basal keratinocytes cultured on collagen (BL-) often released cytoplasmic fragments (*arrows*) from their undersurface into the collagen matrix (*inset*, **A**). *Arrows* mark the junction of the epithelium with the support matrix. *Bar* 15  $\mu$ m

("blebs") accumulated immediately beneath the basal cells (Fig. 2A). Basal cells apposed to the basal lamina exhibited a smooth undersurface (Fig. 2B). Ultrastructural study of the REKs cultured on the two different substrata confirmed the light microscopic results. Basal cells on collagen alone exhibited cytoplasmic processes extending from the undersurface of the basal cells down among the collagen fibrils (Fig. 3A). Basal cells opposite the basal lamina appeared to have reestablished the normal basal keratinocyte relationship with the basal lamina and exhibited a smooth inferior plasma membrane surface with variable numbers of hemidesmosomes spaced along its length (Fig. 3B).

#### Hyaluronan and hyaluronan receptor (CD44) localization in organotypic cultures

Hyaluronan was identified in five 5-day organotypic cultures using a hyaluronan-specific bHABC purified from bovine articular cartilage. Hyaluronan was present between keratinocytes in either culture configuration (BL-, BL+) in the spinous and basal cell layers with the strongest signal present between suprabasal spinous cells (Fig. 4A,B). Hyaluronan was demonstrable in the subjacent collagenous matrix either in a beaded pattern (not shown) or as a diffusely stained zone (Fig. 4A) in cultures grown on collagen alone (BL-), but was absent in cultures grown on a basal lamina-covered collagen matrix (BL+; Fig. 4B). The hyaluronan-binding molecule, CD44, localized immunohistochemically, exhibited a distribution in the cell layers nearly identical to that of hyaluronan in REKs cultured on either support matrix (Fig. 4C). CD44 was present in the BL-collagen matrix in the form of small globular deposits, presumably localized on the cytoplasmic blebs cast off from the basal keratinocytes (not shown).

#### Biosynthesis of glycosaminoglycans by REK organotypic cultures

The biosynthetic data presented are from a single experiment with one sample for each time point in each group



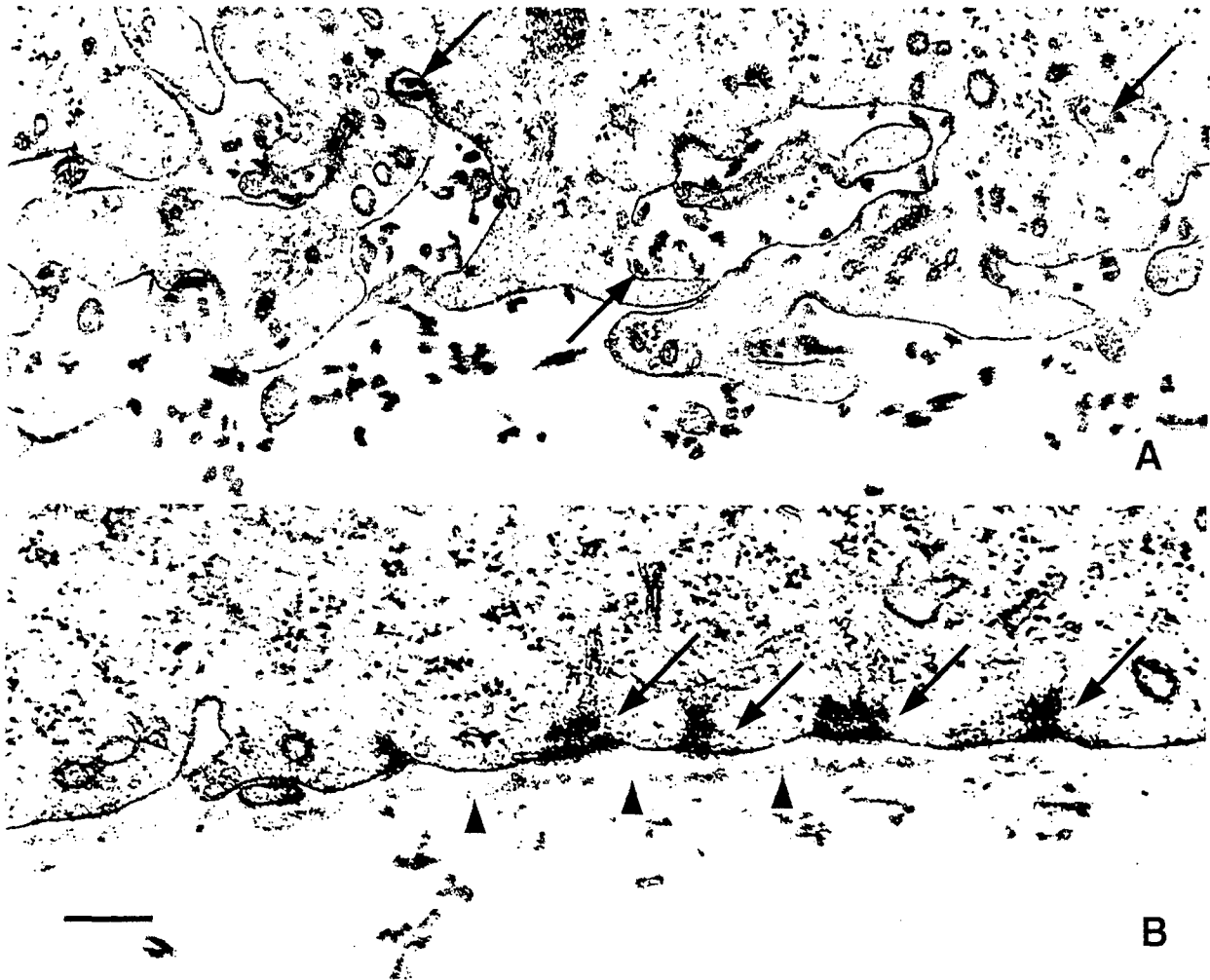


**Fig. 3A,B** The junction of basal keratinocytes with support matrices is illustrated. **A** Basal keratinocytes extend cell processes out into the underlying mesh of collagen fibrils, often enveloping groups of fibrils (*arrows*), when cultured on a collagen support matrix lacking a basal lamina. **B** The undersurface of a basal keratinocyte opposite a basal lamina (*arrowheads*) exhibits attachment specializations, hemidesmosomes (*arrows*), that are a normal feature of the native tissue. The "open" nature of the collagen support matrix (**A**: BL-) is evident when compared with boundary formed by the basal lamina (**B**: BL+). Bar 0.2  $\mu$ m

(BL+, BL-) together with cultures used in the labeling window experiments (16 total cultures, each of which yielded three components that were, in turn, then subjected to eight separate analyses). The data presented are consistent with two previous experiments that were conducted with fewer time points to establish labeling conditions and times.

Seven-day-old organotypic cultures of REKs were incubated for different times with [ $^{35}$ S]sulfate and [ $^3$ H]glucosamine as metabolic precursors for labeling glycosaminoglycans. The total incorporation of each precursor into purified glycosaminoglycans is shown in Fig. 5 as a function of labeling time and for individual 3-h labeling windows (0-3, 12-15, 24-27 h). Incorporation of  $^{35}$ S into sulfated glycosaminoglycans (chondroitin

in sulfate and heparan sulfate) decreased with labeling time, but showed no difference between cultures with (BL+) or without (BL-) an intervening basal lamina. While incorporation of  $^3$ H activity into glycosaminoglycans also decreased with labeling time, there was a distinct difference between the two culture configurations with significantly less label in the BL+ configuration at times greater than approximately 10 h.

The differences in  $^3$ H incorporation into the glycosaminoglycans at the 12- to 24-h time points do not reflect different incorporation rates during that time period of the experiment because  $^3$ H incorporation at each of the 3-h labeling windows was the same for both culture configurations. However, there was a gradual decrease in net incorporation from the first labeling window (0-3 h) to the final labeling window (24-27 h) in both culture configurations, most likely reflecting decreases in medium components, for example, glucose, necessary for glycosaminoglycan synthesis.

#### Quantitation of glycosaminoglycans

Portions of the purified glycosaminoglycans from each compartment (epithelium, matrix + medium) of each cul-

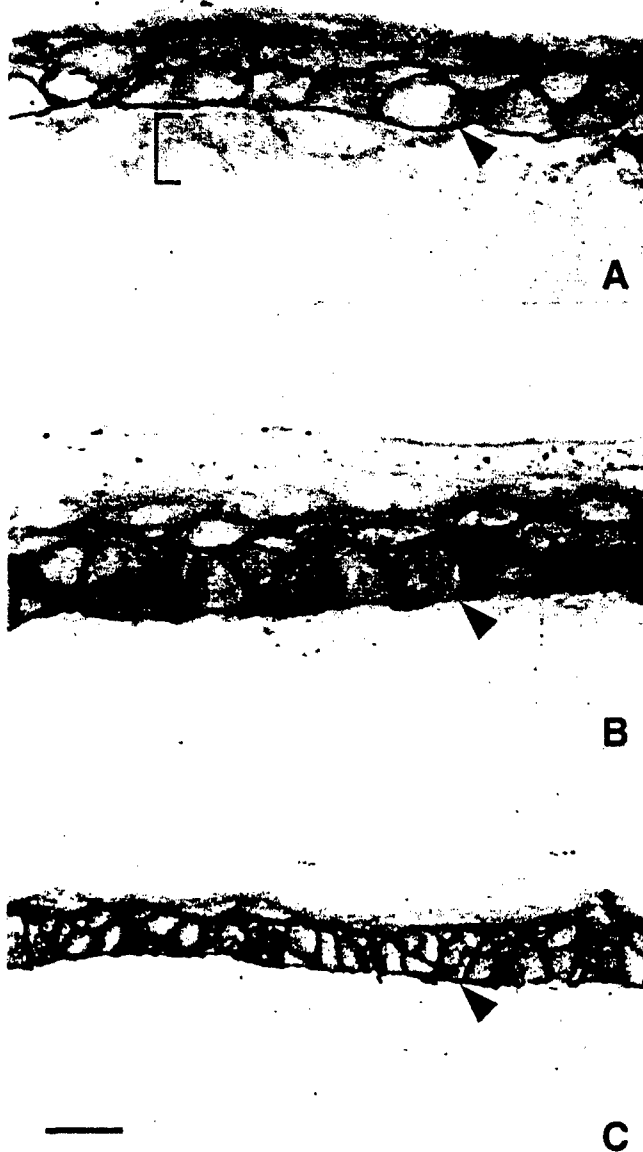


**Fig. 4** Hyaluronan in REK cultures lacking a basal lamina (BL-; **A**) and with a basal lamina (BL+; **B**). In cultures lacking a basal lamina hyaluronan diffused into the collagen matrix immediately subjacent to the epithelium (*bracket*) while no hyaluronan was observed in this location in the BL+ cultures. Panel **C** demonstrates the presence of the hyaluronan-binding molecule CD44 in the same regions in which hyaluronan is present in both culture configurations. *Arrowheads* mark the junction of the epithelium with the support matrix. *Bars* 14  $\mu\text{m}$  in **A,B**; 20  $\mu\text{m}$  in **C**

ture configuration (BL-, BL+) were digested with a combination of chondroitinase ABC and Streptococcal hyaluronidase. Each digest was eluted on a Superdex Peptide gel filtration column, an example of which is shown in Fig. 6. The three classes of glycosaminoglycans resolve as indicated, with intact heparan sulfate

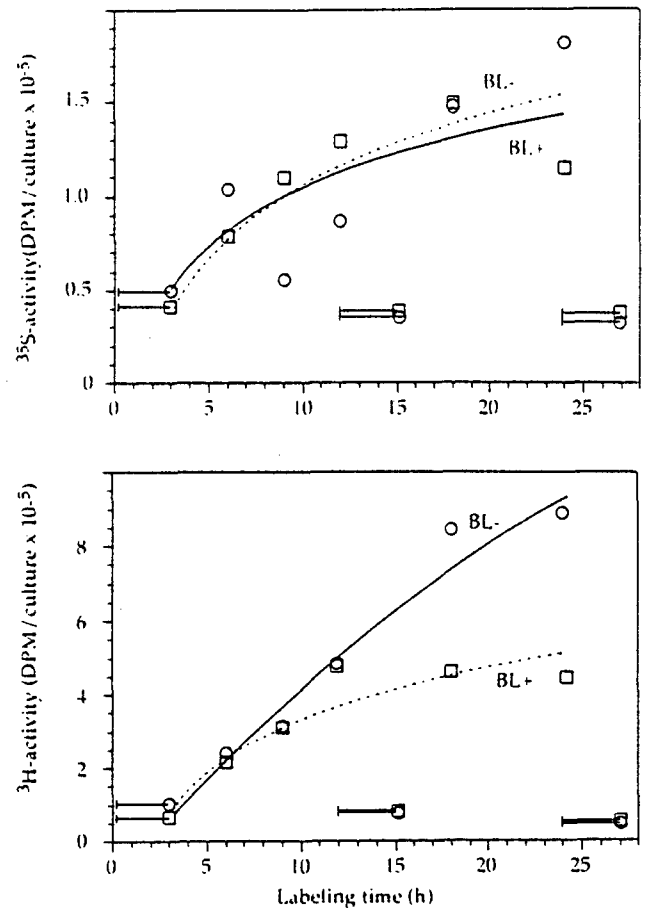


**Fig. 5** Incorporation of radioactive  $^{35}\text{SO}_4$  (*upper graph*) and  $^3\text{H}$  ( $^3\text{H}$ ]glucosamine as precursor; *lower graph*) as precursors into glycosaminoglycans synthesized in organotypic cultures of epidermal keratinocytes on collagen gels with (BL+ = *squares*) or without (BL- = *circles*) an intervening basal lamina. The curves show logarithmic fitting of the data points (*dotted line* = BL+; *solid line* = BL-) for the 3- to 24-h labeling periods. *Horizontal bars* indicate values obtained from separate 3-h labeling windows 0-3, 12-15, and 24-27 h after starting the continuous labeling

chains eluting in the void volume and the disaccharides derived from chondroitin sulfate eluting as two separate peaks immediately before the disaccharides derived from hyaluronan. The hyaluronan disaccharide peaks represented a high proportion of the total  $^3\text{H}$  activity (55-70%) indicating that hyaluronan is the predominant glycosaminoglycan synthesized by the REKs.

The ratio of  $^3\text{H}$  to the mass of monosulfated disaccharide (derived from  $^{35}\text{S}$  activity) is a measure of the specific activity of the galactosamine incorporated into chondroitin sulfate during the labeling period as described in Materials and Methods (Yanagishita et al. 1989). Values for this ratio are shown in Fig. 7 for the labeling experiment. For both culture configurations the values gradually increase approximately twofold during the 24 h of the experiment reflecting the slower equilibration of  $^3\text{H}$ ]glucosamine than of  $^{35}\text{S}$ ]sulfate between the medium and intracellular pools. Importantly, however, there is no significant difference in this parameter be-

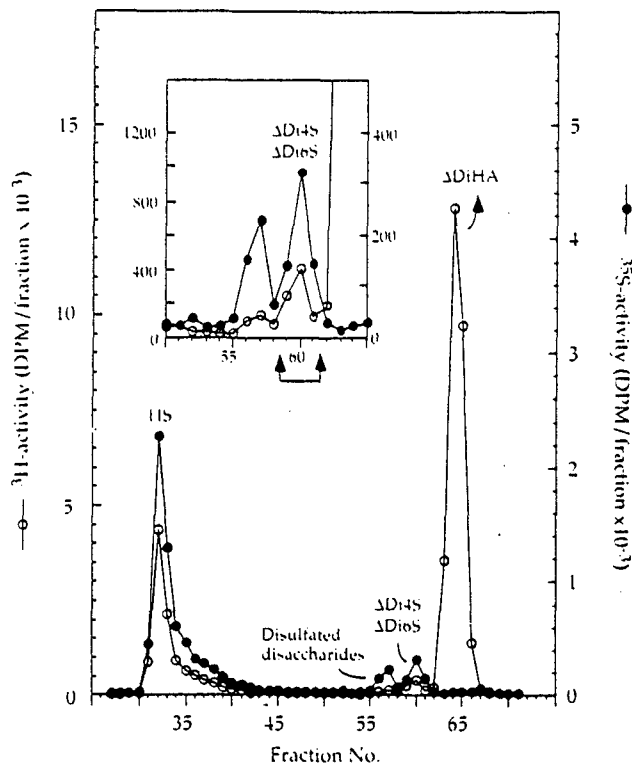


**Fig. 6** An example of a chromatographic analysis of glycosaminoglycans synthesized by keratinocytes in an organotypic culture. Purified  $^{35}\text{S}$ - and  $^3\text{H}$ -labeled glycosaminoglycans were digested with chondroitinase ABC and Streptococcal hyaluronidase and separated on a Superdex Peptide gel filtration column. Undigested material, mainly heparan sulfate (*HS*), appears in the void volume and disaccharides elute in the order of decreasing sulfation, as indicated in the figure. The  $^{35}\text{S}$  radioactivity in the monosulfated chondroitin sulfate disaccharides ( $\Delta\text{Di}4\text{S}$  and  $\Delta\text{Di}6\text{S}$ , fractions 59–61, see *inset*) were used to calculate the specific activity of the incorporated  $^3\text{H}$  and the chemical quantity of hyaluronan in the non-sulfated disaccharide peak ( $\Delta\text{DiHA}$ )

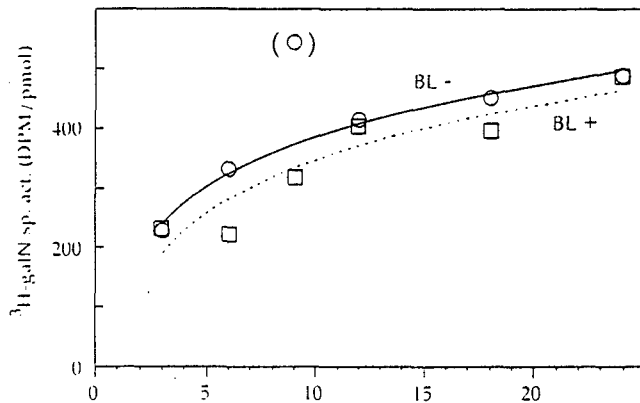


**Fig. 7** Specific activity of *N*-acetylgalactosamine incorporated into chondroitin sulfate in organotypic cultures of epidermal keratinocytes. The values were obtained from the epithelium of cultures labeled for 3–24 h, each chromatographed as demonstrated in Fig. 6. The curves represent logarithmic fitting of the data points (excluding the value in parenthesis). For symbols and labels, see Fig. 5

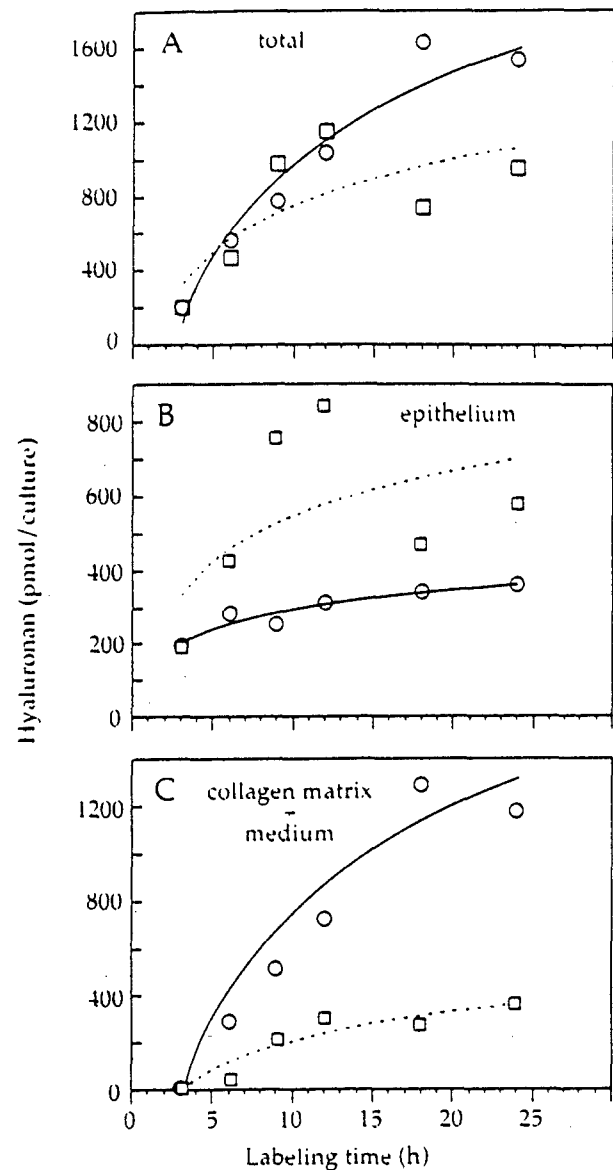


**Fig. 8** Newly synthesized hyaluronan (total; A), and amounts in the epithelium (B) and the subjacent matrix plus medium compartments of organotypic keratinocyte cultures (C). The curves show the data points fitted to logarithmic equations. For symbols and labels, see Fig. 5

tween the two culture configurations (BL–, BL+). This means that differences in the distribution of  $^3\text{H}$ -labeled hyaluronan in the two different culture configurations reflect real differences in the amounts of the  $^3\text{H}$ -labeled hyaluronan and are not due to differences in specific activities of the precursor pools.

#### Compartmentalization of hyaluronan

Figure 8A shows that the total  $^3\text{H}$  activity, hence the total mass, of hyaluronan that accumulates over 24 h is approximately 35% greater in REK cultures without a basal lamina (BL–) than in cultures with a basal lamina (BL+).

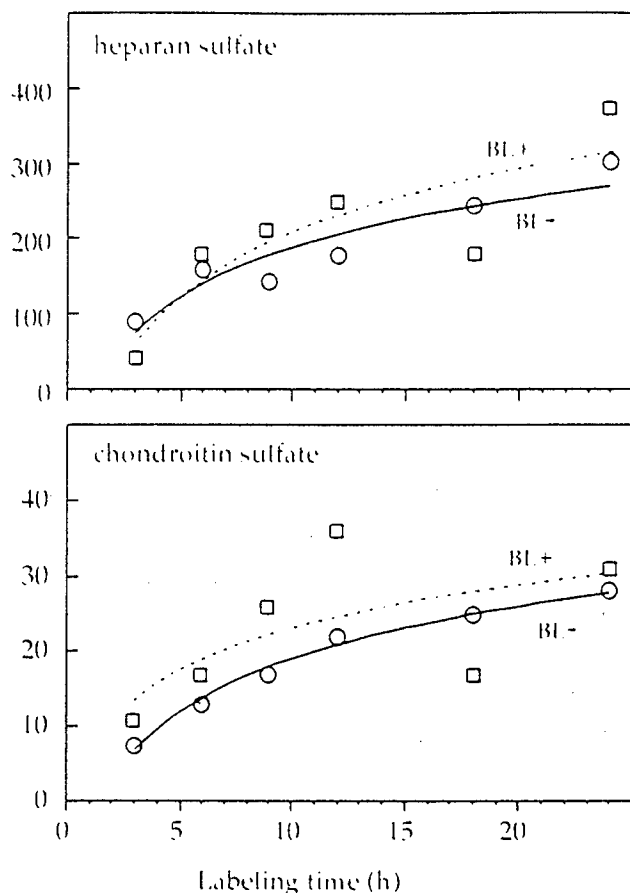


**Fig. 9** Newly synthesized heparan sulfate (*upper panel*) and chondroitin sulfate (*lower panel*) in the epithelium of organotypic keratinocyte cultures. The values were based on separation of the glycosaminoglycans as shown in Fig. 6, and the specific activities of incorporated  $^3\text{H}$  in Fig. 7. For symbols and labels, see Fig. 5

Inspection of the earliest time points (up to 6 h; Fig. 8A) as well as the data in Fig. 5 indicate that there is no significant difference between the rates of hyaluronan synthesis between the two culture configurations. Therefore the results in Fig. 8A indicate that cultures with a basal lamina are catabolizing significantly more of the hyaluronan that was synthesized during the labeling period. Importantly, the amount of hyaluronan that is retained in the epithelial compartment of cultures with a basal lamina at 24 h is much higher (Fig. 8B). In this case approximately 75% of the total labeled hyaluronan is in the epithelial compartment. Conversely, only approximately 20% of the total hyaluronan is retained in this compartment in the cultures lacking a basal lamina; most has diffused into the underlying collagen matrix and medium compartments (Fig. 8C).

#### Heparan sulfate and chondroitin sulfate in the epidermal compartment

In contrast to hyaluronan, there were no differences in the accumulation of labeled heparan sulfate and chon-

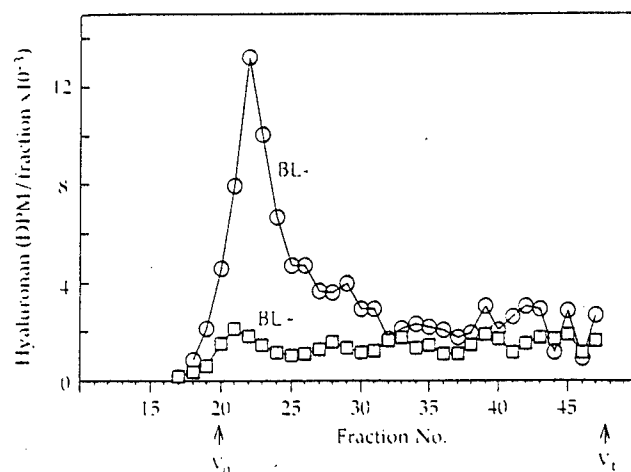


**Fig. 10** Size distribution of hyaluronan in the matrix plus medium compartments of epidermal keratinocyte organotypic cultures. Proportional aliquots of extracts of the collagen gel and medium were combined and injected onto a 1x30-cm Sephacryl S1000 column eluted with 150 mM sodium acetate, 0.1% CHAPS, pH 7.0. Each fraction was analyzed for hyaluronan, based on its susceptibility to *Streptomyces hyaluronidase*. Arrows indicate the void ( $V_0$ ) and total volume ( $V_t$ ) of the column. For symbols and labels, see Fig. 5

droitin sulfate within the epidermal compartment of the two culture configurations (Fig. 9). In each culture condition, the accumulation continued, but with a gradually decreasing rate. The curves suggest that some of these glycosaminoglycans are also being catabolized, but additional experiments would be required to confirm this and to define approximate half-lives. The results also indicate that the keratinocytes synthesize approximately ten-fold more heparan sulfate than chondroitin sulfate.

#### Barrier function of the basal lamina

Portions of extracts of the collagen matrix compartment were combined with equivalent portions of medium for cultures from the 24-h time points. Aliquots were then eluted from a Sephacryl S1000 column and fractions analyzed for content of hyaluronan. Figure 10 shows a major peak eluting near the void volume of the column for the sample from the cultures without a basal lamina (BL-), indicating the presence of high molecular weight hyaluronan. In contrast, very little high molecular weight hyaluronan was observed in the sample from the cultures with a basal lamina (BL+) although high molecular weight hyaluronan was present in the epithelium (data not shown). This demonstrates that the basal lamina deposited by the MDCK cells formed an effective barrier to high molecular weight hyaluronan.

#### Discussion

Growing epidermal keratinocytes on a support matrix at the interface between the gaseous and liquid phases of a

culture greatly facilitates reformation of a tissue that closely resembles an epidermis. There are many variations used in such "organotypic" cultures with respect to the supporting matrices employed and the inclusion of viable connective tissue cells (see Schoop et al. 1999 for an excellent current review of such culture methodologies). The inclusion of viable connective tissue cells in the support matrix generally seems necessary for the reliable formation of a basal lamina by the cultured keratinocytes (Fleischmajer et al. 1998; Shoop et al. 1999). However, because fibroblasts or fibroblast-like cells included in the matrix synthesize and catabolize hyaluronan, use of a support matrix with included fibroblasts to facilitate reformation of an epithelial basal lamina would have confounded our objective of studying hyaluronan metabolism within the epidermal compartment.

Since cultures lacking a basal lamina permitted diffusion of newly synthesized hyaluronan away from the reconstituted epidermis, and inclusion of supporting cells in the collagen matrix necessary for basal lamina formation would have partially masked hyaluronan synthesis by the keratinocytes, we employed the concept of culturing keratinocytes on a preformed basal lamina, a strategy previously employed by one of us (D.K.M.) in culturing oral keratinocytes (Lillie et al. 1988). In those previous studies, a basement membrane deposited on a supporting matrix of collagen fibrils by bovine corneal endothelial cells was employed (the *in vitro* equivalent of Desmet's membrane). However, the membrane deposited by the bovine corneal endothelial cells exhibited numerous pores caused by corneal endothelial processes that remained in place as the membrane was deposited. Since the porous nature of the bovine corneal endothelial-deposited membrane ruled out its use, we modified the experiments of Valentich (1982), who found that a basal lamina was deposited by MDCK cells when they were cultured on a supporting matrix of collagen fibrils. MDCK cells were subsequently shown to synthesize normal components of an epithelial basal lamina: type IV collagen, laminin, and heparan sulfate proteoglycan (perlecan) (Taub 1991; Patrone et al. 1992).

In our experiments, detergent lysis of the MDCK cells followed by scanning electron microscopic examination showed an essentially intact basal laminar surface interrupted by an occasional pore, a result of MDCK cell processes extending through the membrane as previously reported by Valentich (1982). These pores were occupied by cell processes of the cultured keratinocytes (not shown) in a manner identical to that described for cultured oral keratinocytes (Lillie et al. 1988) thus making the basal lamina an effective barrier to the diffusion of macromolecular hyaluronan out of the epithelium.

Culture of the REKs on a basal lamina-covered collagen fibrillar matrix markedly altered the manner in which hyaluronan was treated by the keratinocytes when compared to those cultured on a collagen support matrix without a basal lamina. In cultures lacking a basal lamina, abundant, large hyaluronan molecules were found in the supporting collagenous matrix and underlying medi-

um. In contrast, hyaluronan recovered from the basal lamina-covered matrix and underlying medium was reduced in amount and of smaller molecular mass suggesting that macromolecular hyaluronan was retained within the epithelium. Key observations from these experiments were that: (1) the total  $^3\text{H}$ -labeled hyaluronan accumulated in cultures without a basal lamina was greater than in cultures with a basal lamina and (2) conversely, the total amount retained in the epithelium was greater in cultures with a basal lamina. The first of these observations indicates that at least 35% of the hyaluronan synthesized during the labeling period, the difference between the two culture configurations at the end of the labeling period, was catabolized within the epithelium in cultures with a basal lamina. The actual amount is likely to be more because cultures without a basal lamina also catabolize some hyaluronan even though most diffuses out of the epithelium. We expect, then, that the half-life of a newly synthesized hyaluronan molecule in cultures with a basal lamina will be close to that observed for explants of human skin, approximately 1 day (Tammi et al. 1991). The second observation indicates that the retention of hyaluronan within the epithelial layer when a basal lamina is present increases the steady state concentration of hyaluronan around the cells in the basal and spinous cell layers. Besides demonstrating the effectiveness of the basal lamina in preventing the movement of macromolecules out of the epidermal compartment, experiments with the two different support matrices emphasize that not all hyaluronan synthesized by the keratinocytes is tethered to the cell surface and that some is free to move within the intercellular space. While the present experiment was not designed to study hyaluronan internalization, the results obtained emphasize the importance of high concentrations of hyaluronan proximate to the keratinocyte cell surface for efficient catabolism.

Our previous work with these REKs indicated that hyaluronan was tethered to the cell surface either by the enzymes responsible for its synthesis, hyaluronan synthases, or by the hyaluronan receptor CD44 (Tammi et al. 1998). Although the catabolic processes responsible for hyaluronan breakdown are not fully understood, there is evidence that the hyaluronan receptor is important in the binding and subsequent internalization of hyaluronan (Hua et al. 1993; Kaya et al. 1997).

Hyaluronan was the major glycosaminoglycan synthesized by the cultured REKs followed by heparan sulfate and chondroitin sulfate. The relative proportions of these glycosaminoglycans formed by the cultured keratinocytes are very similar to that formed by the epidermis in organ cultures of porcine (King 1981) and human skin (Tammi and Tammi 1986). This finding indicates the REKs may be an excellent model in which to study overall glycosaminoglycan/proteoglycan metabolism in the epidermis.

Although the functional roles of hyaluronan are not completely understood, it is now evident that it is not simply a large, passive, space-filling connective tissue molecule. Hyaluronan has been shown to be an impor-

tant cell surface component which, through interactions with other molecules, plays significant roles in morphogenesis, wound healing, immune function, and malignant behavior (Sherman et al. 1994; Entwistle et al. 1996; Knudson 1998; Zeng et al. 1998). The homeostatic roles of hyaluronan in epithelia are not understood. Certain secretory epithelia add hyaluronan to their secretions (Mani et al. 1992; see Tammi et al. 1994b; Yung et al. 1996; Usui et al. 1999). But such secretory epithelia together with most simple epithelia lack demonstrable intercellular hyaluronan. That finding contrasts with the universal presence of intercellular hyaluronan within the basal cell layer and proximate suprabasal layers of all stratified epithelia studied thus far (Tammi et al. 1988, 1990; Laurent et al. 1995; Wang et al. 1996; Hirvikoski et al. 1999). It is possible that the large hydrated domain produced by intercellular hyaluronan in these stratified epithelia facilitates diffusion of metabolites in and out of these avascular tissues as well as providing a hydrated pathway for cells of the immune system that traffic through these tissues. A further role for hyaluronan within these stratified epithelia may be one of regulating cell division. Transgenic mice expressing an antisense CD44 hyaluronan receptor also lacked demonstrable intercellular epidermal hyaluronan. These same mice did not exhibit a normal proliferative response following wounding or challenge with phorbol ester; observations which seem to implicate that hyaluronan is necessary for a normal proliferative response (Kaya et al. 1997). Hyaluronan may also, in some way, play a role in regulating the differentiation of keratinocytes as they move toward the surface of the tissue. This idea comes from the observation that dysplastic stratified epithelia that contain increased layers of immature basal-like and suprabasal cells exhibit intercellular hyaluronan throughout a much greater depth of the tissue than that seen in normal stratified squamous epithelium (Wang et al. 1996; Hirvikoski et al. 1999). Some experiments also indicate hyaluronan or its CD44 receptor may play a role in keratinocyte cell to cell adhesion but the mechanisms are not understood (Milstone et al. 1994; Hudson et al. 1995).

REKs cultured on collagen or basal lamina-covered collagen matrices grow, stratify, and differentiate in a manner similar to the native epidermal tissue. The distribution of hyaluronan and the hyaluronan receptor CD44 within the "epidermis" formed by the cultured keratinocytes is similar to that in native epidermis as is the exceptionally active synthesis and catabolism of hyaluronan by the keratinocytes. The addition of the basal lamina to the collagen matrix permits the formation of a true epidermal compartment bounded by the cornified layer on the surface and the basal lamina subjacent to the basal cells. The basal lamina forms a true barrier to the diffusion of macromolecular hyaluronan away from the keratinocytes and results in increased catabolism of the molecule within the epithelium. Surprisingly, this study appears to be the first to demonstrate that a basal lamina acts as a barrier to a naturally occurring tissue macromolecule either in vivo or in vitro, based on a review of

the literature concerned with the barrier functions of the basement membranes (Farquhar 1991; Williams 1994). REKs cultured on a basal lamina-covered collagen gel provide a good model within which to study epidermal metabolism isolated from the influence of dermal cells or other supporting cells included in a collagen matrix.

**Acknowledgements** The authors wish to thank Dr. Stephen J. Weiss, the E. Gifford and Love Barnett Upjohn Professor of Internal Medicine and Oncology, University of Michigan, for freely sharing his laboratory's experience in fabricating MDCK cell basal lamina-covered collagen gels. Dr. Weiss provided protocols and the MDCK cells used in this study, as well as the initial set of basal lamina-covered collagen gels in tissue culture inserts for which we are very grateful. Drs. Raija and Markku Tammi thank the Cleveland Clinic Foundation for support during their sabbatical in the Department of Biomedical Engineering, and acknowledge additional support from the Academy of Finland, the University of Kuopio Biotechnology funds, and the Technology Development Centre of Finland (TEKES). Ms Eija Rahunen and Mr. Kari Kotikumpu are acknowledged for skillful assistance in preparing the paraffin sections and doing the histochemical reactions.

## References

- Ågren UM, Tammi RH, Tammi MI (1997) Reactive oxygen species contribute to epidermal hyaluronan catabolism in human skin organ culture. *Free Radical Biol Med* 23:996-1001
- Baden HP, Kubilus J (1983) The growth and differentiation of newborn rat keratinocytes. *J Invest Dermatol* 80:124-130
- Bignami A, Hosley M, Dahl D (1993) Hyaluronic acid and hyaluronic acid-binding proteins in brain extracellular matrix. *Anat Embryol (Berl)* 188:419-433
- Entwistle J, Hall CL, Turley EA (1996) HA receptors: regulators of signaling to the cytoskeleton. *J Cell Biochem* 61:569-577
- Farquhar MG (1991) The glomerular basement membrane: a selective macromolecular filter. In: Hay ED (ed) *Cell biology of extracellular matrix*, 2nd edn. Plenum Press, New York, pp 365-417
- Fleischmajer R, Perlish JS, MacDonald ED, Schechter A, Murdoch AD, Iozzo RV, Yamada Y (1998) There is binding of collagen IV to beta 1 integrin during early skin basement membrane assembly. *Ann NY Acad Sci* 857:212-227
- Hirvikoski P, Tammi R, Kumpulainen E, Virtaniemi J, Parkkinen JJ, Tammi M, Johansson R, Ågren U, Karhunen J, Kosma VM (1999) Irregular expression of hyaluronan and its CD44 receptor is associated with metastatic phenotype in laryngeal squamous cell carcinoma. *Virchows Arch* 434:37-44
- Hua Q, Knudson CB, Knudson W (1993) Internalization of hyaluronan by chondrocytes occurs via receptor-mediated endocytosis. *J Cell Sci* 106:365-375
- Huber AR, Weiss SJ (1989). Disruption of the subendothelial basement membrane during diapycnosis in an in vitro construct of a blood vessel. *J Clin Invest* 83:1122-1136
- Hudson DL, Sleeman J, Watt FM (1995) CD44 is the major peanut lectin-binding glycoprotein of human epidermal keratinocytes and plays a role in intercellular adhesion. *J Cell Sci* 108:1959-1970
- Kaya G, Rodriguez I, Jorcano JL, Vassalli P, Stamenkovic I (1997) Selective suppression of CD44 in keratinocytes of mice bearing an antisense CD44 transgene driven by a tissue-specific promoter disrupts hyaluronate metabolism in skin and impairs keratinocyte proliferation. *Genes Dev* 11:996-1007
- King IA (1981) Characterization of epidermal glycosaminoglycans synthesized in organ culture. *Biochim Biophys Acta* 674:87-95
- Knudson W (1998) The role of CD44 as a cell surface hyaluronan receptor during tumor cell migration and metastasis. *Front Biosci* 3:604-615

- Kramer RH, Fuh GM, Bensch KG, Karasek MA (1985) Synthesis of extracellular matrix of glycoproteins by cultured microvascular endothelial cells isolated from the dermis of neonatal and adult skin. *J Cell Physiol* 123:1-9
- Laurent C, Hellström S, Engström-Laurent A, Wells AF, Bergh A (1995) Localization and quantity of hyaluronan in urogenital organs of male and female rats. *Cell Tissue Res* 292:241-248
- Laurent TC, Laurent UB, Fraser JR (1996) The structure and function of hyaluronan: an overview. *Immunol Cell Biol* 72:A1-A7
- Lillie JH, MacCallum DK, Jepsen A (1980) Fine structure of subcultured stratified squamous epithelium grown on collagen rafts. *Exp Cell Res* 125:153-165
- Lillie JH, MacCallum DK, Jepsen A (1988) Growth of stratified squamous epithelium on reconstituted extracellular matrices: long-term culture. *J Invest Dermatol* 90:100-109
- MacCallum DK, Lillie JH (1990) Evidence for autoregulation of cell division and cell transit in keratinocytes grown on collagen at an air-liquid interface. *Skin Pharmacol* 3:86-96
- Mani SK, Carson DD, Glasser SR (1992) Steroid hormones differentially modulate glycoconjugate synthesis and vectorial secretion by polarized uterine epithelial cells in vitro. *Endocrinology* 130:240-248
- Milstone LM, Hough-Monroe L, Kugelmann LC, Bender JR, Haggerty JG (1994) Epcan, a heparan/chondroitin sulfate proteoglycan form of CD44, mediates cell-cell adhesion. *J Cell Sci* 107:3183-3190
- Patrone LM, Cook JR, Crute BE, Van Buskirk RG (1992) Differentiation of epithelial cells on microporous membranes. *J Tissue Culture Methods* 14:225-234
- Ripellino JA, Bailo M, Margolis RU, Margolis RK (1988) Light and electron microscopic studies on the localization of hyaluronic acid in developing rat cerebellum. *J Cell Biol* 106:845-855
- Schoop VM, Mirancea N, Fusenig NE (1999) Epidermal organization and differentiation of HaCaT keratinocytes in organotypic coculture with human dermal fibroblasts. *J Invest Dermatol* 112:343-353
- Sherman L, Sleeman J, Herrlich P, Ponta H (1994) Hyaluronate receptors: key players in growth, differentiation, migration and tumor progression. *Curr Opin Cell Biol* 6:726-733
- Tammi R, Tammi M (1986) The influence of retinoic acid on the ultrastructure and hyaluronic acid synthesis of adult human epidermis in whole skin organ cultures. *J Cell Physiol* 126:389-398
- Tammi R, Ripellino JA, Margolis RU, Tammi M (1988) Localization of epidermal hyaluronic acid using the hyaluronate binding region of cartilage proteoglycan as a specific probe. *J Invest Dermatol* 90:412-414
- Tammi R, Ripellino JA, Margolis RU, Maibach HI, Tammi M (1989) Hyaluronate accumulation in human epidermis treated with retinoic acid in skin organ culture. *J Invest Dermatol* 92:326-332
- Tammi R, Tammi M, Häkkinen L, Larjava H (1990) Histochemical localization of hyaluronate in human oral epithelium using a specific hyaluronate-binding probe. *Arch Oral Biol* 35:219-224
- Tammi R, Säämänen A-M, Maibach HI, Tammi M (1991) Degradation of newly synthesized high molecular mass hyaluronan in the epidermal and dermal compartments of human skin in organ culture. *J Invest Dermatol* 97:126-130
- Tammi R, Rönkkö S, Ågren UM, Tammi M (1994a) Distribution of hyaluronan in bull reproductive organs. *J Histochem Cytochem* 42:1479-1486
- Tammi R, Ågren UM, Tuhkanen A-L, Tammi M (1994b) Hyaluronan metabolism in skin. In: Graumann W (ed) *Progress in histochemistry and cytochemistry*. Fischer, Stuttgart, 29:1-81
- Tammi R, MacCallum D, Hascall VC, Pienimäki JP, Hyttinen M, Tammi M (1998) Hyaluronan bound to CD44 on keratinocytes is displaced by hyaluronan decasaccharides but not hexasaccharides. *J Biol Chem* 273:28878-28888
- Tammi R, Tammi M, Hascall VC, Hunziker EB, MacCallum DK (1999) Does keratinocyte hyaluronan determine the volume of the extracellular space in the epidermis? In: Abatangelo G (ed) *New frontiers in medical science: redefining hyaluronan*. Elsevier Science Publishers, Amsterdam, (in press)
- Taub M (1991) Retinoic acid inhibits basement membrane protein biosynthesis while stimulating dome formation by Madin Darby canine kidney cells in hormonally defined serum-free medium. *J Cell Physiol* 148:211-219
- Toole BP (1991) Proteoglycans and hyaluronan in morphogenesis and differentiation. In: Hay ED (ed) *Cell biology of extracellular matrix*, 2nd edn. Plenum Press, New York, pp 305-334
- Usui T, Suzuki K, Kaji Y, Amano S, Miyata K, Heldin P, Yamashita H (1999) Hyaluronan synthase expression in bovine eyes. *Invest Ophthalmol Vis Sci* 40:563-567
- Valentich JD (1982) Basal lamina assembly by the dog kidney cell line MDCK. *Cold Spring Harbor Conf Cell Prolif* 9:567-579
- Voigt W-H, Fusenig NE (1979) Organotypic differentiation of mouse keratinocytes in cell culture: a light- and electron-microscopic study. *Biol Cell* 34:111-118
- Wang C, Tammi M, Guo H, Tammi R (1996) Hyaluronan distribution in the normal epithelium of the esophagus, stomach, and colon and their cancers. *Am J Pathol* 148:1861-1869
- Wight TN, Heinegård DK, Hascall VC (1991) Proteoglycans, structure and function. In: Hay ED (ed) *Cell biology of extracellular matrix*, 2nd edn. Plenum Press, New York, pp 45-78
- Williams JC (1994) Permeability of basement membranes to macromolecules. *Proc Soc Exp Biol Med* 207:13-19
- Yanagishita M, Salustri A, Hascall VC (1989) Determination of the specific activity of hexosamine precursors by analysis of double labeled disaccharides from chondroitinase digestion of chondroitin/dermatan sulfate. *Methods Enzymol* 179:435-455
- Yung S, Coles GA, Davies M (1996) IL-1 beta, a major stimulator of hyaluronan synthesis in vitro of human peritoneal mesothelial cells: relevance to peritonitis in CAPD. *Kidney Int* 50:1337-1343
- Zeng C, Toole BP, Kinney SD, Kuo JW, Stamenkovic I (1998) Inhibition of tumor growth in vivo by hyaluronan oligomers. *Int J Cancer* 77:396-401

## Cell Attachment on Surface-Treated Hylan Gels

Anand Ramamurthi and Ivan Vesely

Department of Biomedical Engineering,  
The Cleveland Clinic Foundation, Cleveland, OH 44195

Crosslinked hyaluronans (hylans) are attractive materials for biomedical applications owing to their high biocompatibility. Our objectives are to investigate the conditions necessary for cell attachment, proliferation, and matrix synthesis on solid and particulate hylan gel formulations, obtained from Biomatrix, Inc. Samples were equilibrated overnight with serum-free culture medium and surface-coated with collagen I or collagen IV, fibronectin, fibrinogen, reconstituted extracellular matrix gel or laminin from suspensions containing between 10 and 100  $\mu\text{g}$  of protein /100  $\mu\text{l}$ . Neonatal rat aortic smooth muscle cells were seeded on the gel surface and cultured for up to 21 days. Cells on particulate gels appeared either rounded or irregularly shaped (ECM, fibronectin and laminin), and rounded or highly spread (collagen I, IV). Gel surfaces were confluent in some regions. Cells did not attach to hylans treated with fibrinogen, nor to untreated controls. Cells attached on solid gels were mostly rounded although spread cells were also observed on gels treated with collagen type I or ECM gel. Cell attachment, as quantified with the MTT assay, depended on bulk protein concentration and the type of adhesion protein. At two weeks, cell attachment on particulate gels coated with Collagen type I, ECM, laminin, and fibronectin was enhanced by 4.8, 3.3, 4.3, and 3.6 times respectively over attachment at one week [ $n=3$ ]. On solid gels, cell counts were similar at one and two weeks for all pretreatments except with ECM where cell attachment was enhanced to 1.7 times. The results obtained are useful towards the development of bioengineered materials based on cell-hylan composites.



## Cell Attachment on Surface-Treated Hylan Gels

Anand Ramamurthi and Ivan Vesely

Department of Biomedical Engineering,  
The Cleveland Clinic Foundation, Cleveland, OH 44195

Because of their high biocompatibility, crosslinked hyaluronans (hylans) are materials attractive for biomedical applications. We investigated the conditions necessary for cell attachment, proliferation, and extracellular matrix synthesis, on solid and particulate hylan gel formulations, obtained from Biomatrix, Inc. Samples were equilibrated overnight with serum-free culture medium and surface-coated with collagen types I or IV, fibronectin, fibrinogen, reconstituted ECM gel, or laminin from suspensions containing between 10 and 1000  $\mu\text{g/ml}$  of protein. Neonatal rat aortic smooth muscle cells were seeded on the gel surface and cultured for up to 21 days. At ten days, cells on particulate gels appeared irregularly shaped (ECM), needle-like (fibronectin), or were highly spread (collagen I, IV). Cells did not attach to hylans treated with fibrinogen, nor to untreated controls. Cells attached on solid gels were rounded, regardless of pretreatment. Cell attachment, as quantified with the MTT assay, depended on bulk protein concentration and not on the protein type. Cell attachment on solid gels was enhanced by 46% (fibronectin), depleted by 33% (collagen I and IV), or remained unchanged (ECM) for a threefold increase in coating concentration (30 to 100  $\mu\text{g/ml}$ ) [ $n=6$ ]. The results obtained are useful towards the development of bioengineered materials based on cell-hylan composites.

THE CLEVELAND CLINIC  
FOUNDATION   
LENER RESEARCH INSTITUTE

Daniel R. Beyer, M.S., M.H.A.  
Administrator, Research Division / NB21  
Office: 216/444-5848  
Fax: 216/444-3279  
E-mail: beyerd@ccrf.org

July 28, 2000

Sacelia L. Heller, Contract Specialist  
Department of the Army  
US Army Medical Research Acquisition Activity  
820 Chandler Street  
Fort Detrick MD 21702-5014

Dear Ms. Heller:

We want to thank Dr Calvin B. Carpenter for the May 25th site visit he conducted of our facilities and for the recommendations he gave us in your letter of June 12/00. There are some clarifications we would like to make regarding his comments and recommendations.

*Finding A): "Animals are housed on coated wire mesh floors which have a gap on the side that is large enough for the animal's foot and leg to become entrapped. Additionally, the runs do not have a solid resting surface."*

Reply: Years ago we installed plastisol covered floors to prevent the animals from resting directly on cement. The thickness of the plastisol covered surface goes from 1" to 2" and there are no wires or cutting edges. In some pens there is a gap on the side but this gap is over 4" and so it provides enough space for the paw and lower leg to go in and out without getting entrapped. In more than 10 years that we have had these floors, there was never a dog that got its paw caught in that gap. As to the solid surface resting area we had all the dog pens equipped with resting boards in the past. We opted to eliminate them because contrary to what it may be perceived, the kind of dogs we work with rarely used them and most of the time defecated and urinated on them, the dogs chose instead to rest directly on the cement. After many site visits by the USDA and AAALAC-INTERNATIONAL, we never had any problem with our floors. It should be pointed out the Animal Welfare Act mandates solid resting boards only for cats. They are recommended for dogs but only when the ambient temperature is below 50.0F. Our dogs are housed in temperature controlled rooms.

*Finding B): "Although there is evidence that the animals are provided with the opportunity for exercise, the facility does not have a written exercise plan for dogs."*

Reply: During the site visit we discussed the issue of socialization to which I commented to Dr. Carpenter that while we socialize the dogs we do not keep records of it. It was not clear to me Dr. Carpenter was referring to exercise. Yes we do have a written plan for exercise. This plan has been in place for years and was discussed in several IACUC meetings. Its description is found in pages 51 and 52 of the manual entitled "Information on the Care and Use of Research Animals at the Cleveland Clinic Foundation" This manual is distributed to all the investigators of the Institution. Copy of the exercise plan is attached.

*Finding C): "Animals are currently being procured from a Class B Dealer ....recommend that the institution inspect the vendor's premises for compliance".*

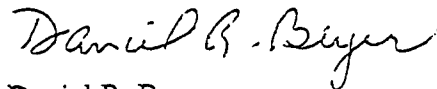
Reply: Prior to our dealing with any dog supplier, we contact the USDA to verify that the person indeed has the proper license and is in good standing. In addition, we require the dog dealer to provide us with copy of recent unannounced USDA inspections. In effect then we rely on the USDA to make sure the Dealer is complying with federal regulations. Were we to make a site visit, it would have to be announced and so we may have less opportunity than a USDA inspector to verify compliance. Still, we will be happy to send a member of our Animal Care Group to visit the Dealer's premises.

*Finding D): "Corridors used for the passage of personnel or equipment are also used for the storage of equipment".*

Reply: Dr. Carpenter is right about this. This problem originated when a new building we were to have was put on hold. The institution is now working diligently to solve this problem. To this end, the services of a well known consultant, Dr. Rozmiarek has been retained to develop plans for a state of the art Animal Facilities. It is anticipated that this new building will provide 60,000 sq.ft. of space and will be completed in 18 months.

Please let us know if you have any further questions or concerns.

Sincerely,



Daniel R. Beyer  
Administrator, Research Institute

cc Hector Munoz-Ramirez DVM, Ph.D.  
Vincent Hascall, PhD

It is evident that implementation of the surcharge will result in better communication between investigators and Biological Resources Unit personnel. The goal is to use animals and space in the most efficient manner. Monitoring the need to keep animals at different stages in the breeding programs will be done according to what was specified in the protocols approved by the Animal Research Committee.

#### Guidelines for Exercise and Housing of Dogs

On February 15, 1991 the final regulations (9 CFR Part 3) related to amendments of the Animal Welfare Act (enacted December 23, 1985) were published in the Federal Register. These regulations are enforced by the Animal and Plant Health Inspection Service (APHIS) of the USDA. In part, these final regulations stipulate new guidelines for housing and exercise of dogs, cats, and nonhuman primates. The final rule became effective March 18, 1991 and institutions such as The Cleveland Clinic Foundation had until August 14, 1991 to implement plans for the exercise of dogs. Based upon the published guidelines the Animal Research Committee and the Veterinarian of the Biological Resources Unit offer the following guidelines for exercise and housing of dogs. In particular, these recommendations apply to dogs involved in long-term studies.

#### A. Guidelines for Exercise

1. Under our present housing conditions, all dogs greater than 34" long (from tip of the nose to base of the tail) will be exercised.
2. Dogs less than 30" long (from tip of the nose to base of the tail) will have the required space for exercise when housed in our standard size pen (18 sq.ft.).
3. Dogs from 30" to 34" long (from tip of the nose to base of the tail) will have the required space for exercise when housed in Ecker-Shane in the pens equipped with the elevated platform.
4. Dogs will be released for a period of 10 minutes per day during the weekdays.
5. The exercise periods will be spread throughout the day.
6. On the 6th floor, dogs can be released from their pens (18 sq.ft.) to move about. The space in the aisle around the pens is at least 84 sq.ft. This space plus the pen space (total 102 sq.ft.) gives more than 100% of the space required by law to exercise the size of dog we house in this institution.
7. In Ecker-Shane, dogs will be released from their pens (18 sq.ft.) to move about in the aisle (141.8 sq.ft.). This space plus the pen space (159.8 sq.ft.) gives more than 100% of the space required by law to exercise dogs.

8. Recommendation of investigators will be taken into account in providing exercise opportunities for their animals.

B. Restrictions on Exercise

1. Dogs that undergo surgical procedures will be allowed to recover (i.e., left in their primary enclosure) for at least 3 days. Thereafter, the animals will be evaluated periodically to see whether they can be released for exercise.
2. Dogs with arterial or venous catheter, flow probes, or infusion pumps, will not be allowed out of their primary enclosures, except as specified by the protocol. A notation to this effect must be made in the chart.
3. Dogs used in fluid balance studies and/or urine collections will not be released for exercise during the time needed to conduct those studies. A notation to this effect must be made in the chart.
4. Dogs impaired with alcohol or experimental drugs will not be released for exercise. A notation to this effect must be made in the chart.

Hazardous Agents in the Biological Resources Unit

The only hazardous agents currently permitted are radioisotopes, and any use of these must be approved by the Radiation Safety Office. New investigators planning to use isotopes must obtain authorization from the Radiation Safety Office. In order for animals, which have received a radioisotope to be housed in the Biological Resources Unit, approval must be obtained from the Radioisotope Committee, the Radiation Safety Officer, and the Animal Research Committee.

Each authorized user of radioisotopes is responsible for recording radioactive waste disposal of an animal and its excreta. Each authorized user is responsible for wipe tests of animal cages and animal areas. These surveys will be supplemented by surveys performed by the Radiation Safety Office.

The following are the regulations issued by the Radiation Safety Office for radioactive waste disposal by incineration.

1. At this time, radioactive waste for incineration must be incinerated in the incinerator located on FF6 of the Research Building, not in the West Clinic incinerator.
2. Any radioactive waste for incineration must be delivered to the sixth floor in a plastic bag that has been secured with a "Caution Radioactive Material" tag that has been properly filled out. Call the Manager of the Biological Resources Unit to arrange for incineration (45860).

DESIGN AND TEST OF AN EXTENSOMETER  
FOR GLOBAL MEASUREMENT OF BONE STRAIN  
SUITABLE FOR USE *IN VIVO* IN HUMANS

by

GAIL PATRICIA PERUSEK

Submitted in partial fulfillment of the requirements  
For the degree of Master of Mechanical Engineering

Thesis Advisers: Dr. Clare M. Rimnac, Dr. Brian L. Davis

Department of Mechanical and Aerospace Engineering  
CASE WESTERN RESERVE UNIVERSITY

May, 2000

CASE WESTERN RESERVE UNIVERSITY  
SCHOOL OF GRADUATE STUDIES

We hereby approve the thesis/dissertation of

GAIL P. PERUSEK

candidate for the MASTER OF SCIENCE degree \*.

(signed) Clare M Rinnac  
(chair of the committee)

D. Saur

Joseph M. Mansour

(date) APRIL 14, 2000

\*We also certify that written approval has been obtained for any proprietary material contained therein.

I grant to Case Western Reserve University the right to use this work, irrespective of any copyright, for the University's own purposes without cost to the University or to its students, agents and employees. I further agree that the University may reproduce and provide single copies of the work, in any format other than in or from microforms, to the public for the cost of reproduction.

A handwritten signature in cursive script, appearing to read "Carl Peruch", written over a horizontal line.

(sign)



## Table of Contents

	Page
<b>1. Introduction</b>	
1.1 Statement of the Problem	1
1.2 Evaluating Bone Strain <i>In Vivo</i>	1
1.3 Bonded Strain Gage Limitations	2
1.3.1 Compatibility of Bonding Agents with Biological Environments	3
1.3.2 Reliability	3
1.3.3 Invasiveness	4
1.4 A Novel Approach to Bone Strain Measurement	5
1.5 Purpose	6
1.6 Specific Aims	7
<b>2. Background</b>	
2.1 Measurement of Strain	8
2.1.1 Strain Averaging and Gage Length	9
2.2 Capacitors	11
2.2.1 How a Capacitor Works	12
2.2.2 Capacitive-Based Sensors	14
2.2.3 Transverse Sensitivity Considerations	14
2.3 Bone Gross Anatomy	16
2.4 The Mechanical Properties of Bone	17
2.5 Mechanotransduction in Bone	18

## Table of Contents, continued

2.5.1	Mechanical Parameters Associated with Osteogenesis	19
2.5.2	The Calcaneus and Bone Loss	21
2.6	Measurement of Bone Strain <i>In Vivo</i> in Humans	22
2.7	Measurement of Bending in Bone <i>In Vivo</i>	25
2.8	Design Process for a New Method of Strain Measurement	26
2.8.1	Cadaver Tests with Commercially Available Extensometers	26
2.8.2	Capacitive-Based Sensors in a New Extensometer Design	27
2.8.3	Requirement for Bending Measurement Capability	30
2.8.4	Pilot Studies with Axial Capacitive Extensometer	32
2.8.4.1	Cantilevered Bending Measured in an Acrylic Specimen	33
2.8.4.2	Axial Strain Measurement in Cadaver Foot Specimen	34
2.9	Delta Extensometer Design Considerations	35
<b>3.</b>	<b>Methodology</b>	
3.1	Overview of Extensometer Design	38
3.1.1	Axial Extensometer Design Features	39
3.1.2	Delta Extensometer Design Features	41
3.2	Experimental Design for Four-Point Bending Validation Tests	45
3.2.1	Specimen Material Selection	45
3.2.2	Strain Magnitude, Frequency and Rate Determination	46
3.2.3	Four-Point Bending Test – Axial Extensometer	50

## Table of Contents, continued

4.3.2	Dynamic Characterization of Axial Extensometer	90
4.3.3	Probe Angle Sensitivity	91
4.4	<i>In Vivo</i> Test Results	93
4.4.1	<i>In Vivo</i> Geometry	94
4.4.2	<i>In Vivo</i> Principal Strain for Standing and Walking in a Human	98
4.5	Summary	105
<b>5. Experimental Uncertainty and Error</b>		
5.1	Overview	106
5.2	Uncertainty Analysis	106
5.2.1	Determination of Uncertainty in Individual Measured Variables	109
5.2.2	Sensitivity of Overall Uncertainty Calculation to Measured Variables	111
5.3	Effective Resolution of Extensometers	112
5.4	Sources of Error in the <i>In Vivo</i> Study	115
5.5	Summary	120
<b>6. Discussion</b>		
6.1	Overview	121
6.2	Four-Point Bending Tests	121
6.3	<i>In Vivo</i> Strain Data in Human Calcaneus	124

## Table of Contents, continued

6.3.1	Comparison of Strain Measurements in Potoroos	125
6.4	Probe Angle Determination is Not a Function of Pooling Error	128
6.5	Conclusions and Recommendations	131
6.5.1	Effect of Cortical Shell	131
6.5.2	Effect of Pin Misalignment and Geometric Errors	132
6.5.3	Design and Implementation Enhancements	132
6.5.4	Advantages of Capacitive Extensometer Design	134
6.5.5	Limitations of Capacitive Extensometer Design	135
6.6	Potential Applications	135
 <b>Appendices</b>		
Appendix A	Supplemental Data	137
Appendix B	Procedures	148
Appendix C	Original Drawings	155
Appendix D	Mohr's Circle for Strain	159

## List of Tables

Table	Description	Page
3.1	Young's Modulus (E) for selected materials	45
3.2	Extensometer/signal conditioner specifications	57
4.1	Summary of statistical results from delta extensometer	88
4.2	<i>In vivo</i> system geometry – measured values	96
A.1	Test conditions and statistical summary – axial extensometer	138
A.2	Test cond's. and stat. summary – delta extensometer, sinusoids	141
A.3	Test cond's. and stat. Summary – delta extensometer, square waves	143

## List of Figures

Fig.	Description	Page
2.1	Definition of gage length	9
2.2	Peak strain and average strain underneath a strain gage	10
2.3	Elements of a capacitor	12
2.4	Flow of electrons in a capacitor	13
2.5	Overlapping / underlapping capacitive plates	15
2.6	Gross structure of a long bone	16
2.7	SEM of trabecular bone	18
2.8	Fluid shear stress near a wall	20

## List of Figures, continued

2.9	Normal vs. osteoporotic bone	22
2.10	Cadaver foot with commercially-available extensometers	27
2.11	Prototype extensometer in live subject	28
2.12	Representative <i>in vivo</i> calcaneal strain time history	30
2.13	Two-probe axial extensometer in cadaver foot	35
2.14	60-degree delta rosette strain gage configurations	36
2.15	60-degree grid orientations	37
3.1	Capacitive "button" probe	39
3.2	Capacitive axial extensometer components	40
3.3	Delta extensometer assembly and components	42
3.4	Orientation of "grid" directions on delta extensometer	44
3.5	Delta rosette and delta extensometer grid layouts are the same	44
3.6	Strain magnitudes and rates encountered <i>in vivo</i>	49
3.7	Expanded view of Fig. 3.6 showing strain rate similarity	50
3.8	Axial extensometer in four-point bending apparatus	51
3.9	Delta extensometer in four-point bending apparatus	52
3.10	Original and revised extensometer orientations	53
3.11	Delta extensometer shown mounted in acrylic specimen	54
3.12	Schematic of data acquisition and wiring scheme	58
3.13	Schematic of delta extensometer coordinate system	61
3.14	Definition of planes used for calculation of strain	63

## List of Figures, continued

3.15	Renshape™ specimen photograph	71
3.16	Schematic of Renshape™ specimen used to test the $\phi$ calculations	72
3.17	Single moving anvil test schematic	74
3.18	Centerline shift from capacitive “pooling”	75
3.19	Probe angle sensitivity test configuration	76
3.20	Close-up photograph of rotary table, adapter plug, probe, target	78
3.21	Surgical implantation of stainless steel pins	79
3.22	Definition of grid orientations in the calcaneus <i>in vivo</i>	80
3.23	<i>In vivo</i> study instrumentation and channel configuration	81
3.24	Subject demonstrates the zero load position	82
4.1	Representative output from axial extensometer for 1 Hz loading	85
4.2	Correlation coeff. as a fcn. of loading freq. – axial extensometer	85
4.3	Correlation coeff. as a fcn. of loading freq. – delta extensometer	87
4.4	Mean and maximum differences plotted for the delta extensometer	87
4.5	Representative time histories from Renshape™ specimen	90
4.6	Probe angle sensitivity test results	93
4.7	Fluoroscopic image of calcaneus used to establish system geometry	95
4.8	Schematic of measured values on human subject	97
4.9	Photograph of model of delta extensometer in calcaneus	98
4.10	Principal strain angle in calcaneus schematic and radiographic image	99

## List of Figures, continued

4.11	Range of principal compressive strain angle during walking	100
4.12	<i>In vivo</i> principal strain magnitude overlaid on vertical force time history	101
4.13	Step by step principal compressive strain during stance phase	102
4.14	MRI images of subject at four months post-test	104
5.1	Spreadsheet used to determine uncertainty in strain calculation	108
5.2	Uncertainty sensitivity to error in gage length measurement	111
5.3	Coordinate system used for calculating effective resolution	113
5.4	Intraosseus pin installation introducing measurement error	118
6.1	<i>In vivo</i> principal strain magnitude comparison with potoroo	126
6.2	<i>In vivo</i> principal strain angle in potoroo calcaneus	127
6.3	“Stress-lines” in human foot and calcaneus schematic	128
6.4	Pooling error does not affect knowledge of angle schematic	130
A.1	Sample time histories for axial extensometer	140
A.2	Sample data output from delta extensometer	144
A.3	Sample time histories for delta extensometer	145
A.4	Pin angles for walking	146
A.5	<i>In vivo</i> principal minimum strain angle time history	147
C.1	Original concept sketch for delta extensometer	156
C.2	Delta extensometer acrylic body detail drawings	157
C.3	Connector diagram showing pin-out designations	158
D.1	Delta rosette and delta extensometer installed on part	160



**List of Figures, continued**

D.2	Rosette grid axes superimposed on Mohr's circle for strain	163
-----	--	-----

## Acknowledgements

I would like to thank my thesis committee, Dr. Clare M. Rimnac, Dr. Joseph M. Mansour, and Dr. Brian L. Davis, for their input and guidance throughout the process of developing this experiment and writing the thesis. I also thank Ralph J. Pawlik of NASA Glenn Research Center, for welcoming me into his laboratory and offering generous technical assistance during the four-point bending evaluations; John Miller at NASA Glenn for providing his machining talents; Brian L. Davis, Ph.D., Julie E. Perry, M.S., and James Sferra, M.D., of the Cleveland Clinic Foundation, for their support throughout the development process and testing of the extensometers. Stephen P. Wnuk of NASA Glenn Research Center is acknowledged for introducing me to capacitive sensors. My former supervisor at NASA, Wayne Thomas and current supervisor, Osvaldo Rivera, are acknowledged for granting me time to complete this project, and supporting my graduate program at the Mechanical and Aerospace Engineering Department at Case Western Reserve University. Acknowledgement is given for NASA Grant NAGW-5008, which financially supported purchase of data acquisition equipment, and NASA Space Act Agreement FA-131 under which this research collaboration between NASA Glenn Research Center and the Cleveland Clinic Foundation was conducted.

Special thanks go to Linda D. White for looking after me; my Mother, Patricia A. Perusek for proof-reading the manuscript; and my Father, Wesley Perusek, Ed.D., for always encouraging me and explaining how things work.

Finally, a sincere thank you is given to the subject who offered me the generous opportunity to obtain strain data *in vivo*, and who underwent surgery for implantation of pins in his calcaneus. His personal dedication to the field of biomechanics is an inspiration.



*Figure 0.0. Subject and Julie Perry prior to surgery at the Cleveland Clinic Foundation.*

## List of Abbreviations

<u>Symbol</u>	<u>Definition</u>
$\varepsilon$	Engineering strain, defined as change in length ( $\delta$ ) divided by original length ( $L$ ). Here, it is defined as change in air gap divided by the gage length of extensometer.
$\varepsilon_p$ , or $\varepsilon_P$	Maximum principal strain magnitude. Oriented along the maximum principal strain axis. Calculated via strain transformation relationships (Mohr's circle for strain).
$\varepsilon_q$ , or $\varepsilon_Q$	Minimum principal strain magnitude. Oriented along the minimum principal strain axis. Calculated via strain transformation relationships (Mohr's circle for strain).
$\phi_p$ , or $\phi_P$	Angle measured <b>from</b> reference grid (grid 1) on strain gage or sensor pair 1 on extensometer <b>to</b> principal maximum strain axis. $\phi = -\theta$ . Also called "principal maximum strain angle".
$\phi_q$ , or $\phi_Q$	Angle measured <b>from</b> reference grid (grid 1) on strain gage or sensor pair 1 on extensometer <b>to</b> principal minimum strain axis. $\phi = -\theta$ . Also called "principal minimum strain angle".
$\theta$	Angle measured <b>from</b> principal axis <b>to</b> reference grid.  Also used in development of strain calculations for capacitive extensometers, defined as the angle the pin makes with the x-axis.
$\gamma$	shear strain ( $\gamma_{\max} = \varepsilon_p - \varepsilon_q$ )
C	capacitance (Farads, F)
x	displacement of the plates of capacitor
A	area of capacitor
$\varepsilon_r$	relative dielectric constant of insulator (=1.0 for air)
$\varepsilon_0$	dielectric constant of free space ( $8.85 \times 10E-4$ F/cm)

### List of Abbreviations, continued

<u>Symbol</u>	<u>Definition</u>
A	location of inboard sensor plane, as measured from the surface of the specimen, or measurement plane of interest, to the centerline of the sensors
B	location of outboard sensor plane, as measured from the surface of the specimen, or measurement plane of interest, to the centerline of the sensors
S	location of the surface plane, or measurement plane of interest, lying transverse to the long axis of intracortical pins
GL	gage length of the extensometer
AB	distance measured between capacitive sensor centerlines
SB	distance measured from outboard capacitive sensor centerline to the measurement plane of interest, e.g., the surface of the specimen
L	original length of the deformed specimen, used in definition of engineering strain
$\delta$	amount of linear deformation in a specimen, used in definition of engineering strain
$y_{A0}, y_{Ai}$	elevation of pin at location A, from the x-axis, at time=0, or time=i
$y_{B0}, y_{Bi}$	elevation of pin at location B, from the x-axis, at time=0, or time=i
$y_{S0}, y_{Si}$	elevation of pin at location S, at time=0, or time=i
$E_t, E_c$	maximum (tensile) and minimum (compressive) principal strains, respectively; same as $\epsilon_p$ and $\epsilon_Q$

Design and Test of an Extensometer for Global Measurement of Bone Strain  
Suitable for Use *In Vivo* in Humans

Abstract

by

GAIL PATRICIA PERUSEK

The purpose was to design, validate, and test a novel extensometer concept for measuring *in vivo* bone strains at physiological magnitudes and rates. Two extensometers are described (an axial, and a multi-axial, or "delta" design) which use coupled non-contact capacitive linear displacement sensors mounted to intraosseus pins. Both extensometers are able to discern axial from bending strains, and the delta extensometer has the added capability of measuring principal strains and their direction, and maximum shear strain. The extensometers were validated in four-point bending with sinusoidal and square wave loading inputs up to 20 Hz and 90,000  $\mu\epsilon/\text{sec}$ . Strain magnitudes reached 5,000  $\mu\epsilon$ . Pilot data from an *in vivo* study in a human calcaneus are presented, and principal strains are shown for a human subject during walking for the first time. Other potential applications include strain measurement in porous materials, materials that have rough surfaces, or in destructive or explosive testing.

# CHAPTER 1

## INTRODUCTION

### 1.1 Statement of the Problem

Astronauts in space and bed-rest patients on Earth share the problem of loss of bone and muscle mass due to a reduced demand on their musculoskeletal system to perform daily activities. Bone loss as a result of unloading the skeletal system, or disuse osteoporosis, can increase the risk of fracture and possibly lead to other physiological problems, such as developing kidney stones (Rambaut, et. al., 1975). NASA has a special interest in developing ways to understand these physiological effects of spaceflight and in devising countermeasures to ameliorate these changes. One of the most promising countermeasures to spaceflight-induced bone loss is exercise, but no exercise regime has yet been fully successful. Understanding how bone adapts to its functional environment is essential for the development of effective exercise-based countermeasures. Further, bone loss associated with the aging process parallels that experienced by astronauts, and a thorough understanding of the mechanisms which may help to diminish bone loss has broader implications for the general population.

### 1.2 Evaluating Bone Strain *In Vivo*

Researchers have focused on the measurement of strain in bone to more fully understand the adaptation of bone to its functional environment. To obtain strain measurements in physiological environments, or *in vivo*, bonded metal foil strain gages have been the standard measurement method. Bonded metal foil strain gages are commonly used for

measuring strain in engineering materials, and many different materials have been gaged, including wood, cement, glass, plastics, rubber, ceramics, stone, aggregates, and bone. Bonded gages are also commonly bonded to spring-members in sensor applications for measurement of mechanical parameters such as pressure, load, and deflection. Various gage lengths and configurations are available for different applications. As its name implies, the bonded strain gage must be in intimate contact with the substrate, or spring member, to which it is bonded. In fact, the most critical component of the strain gage and spring member system is the medium that shear-couples these two elements (Pierson, 1999), or bonding adhesive. The bonding adhesive must be chemically compatible with the substrate to which the strain gage is bonded. Also critical to the success of the strain gage application is proper surface preparation so that a good bond may be achieved.

### **1.3 Bonded Strain Gage Limitations**

Although bonded strain gages have been used *in vivo* in humans, (e.g., Lanyon, et. al., 1975, Burr, et. al., 1996), and is considered the gold standard for strain measurements in bone, the bonded gage method has certain limitations for use in humans, which has motivated the development of new methods. These limitations include i.) compatibility of bonding agents with the biological environment, ii.) reliability, iii.) surface preparation and quality and, iv.) level of invasiveness.



### ***1.3.1 Compatibility of Bonding Agents with Biological Environments***

Alternative bonding agents for use with bonded strain gages have been sought (e.g., Szivek, *et. al.*, 1997; Hoshaw, *et. al.*, 1997) to overcome the problems associated with cyanoacrylate-based adhesives *in vivo*. Cyanoacrylate, the standard bonding agent for strain gages, is not approved by the FDA and is a potential carcinogen. The bone-gage bond also deteriorates with time and is at its best as soon as the adhesive has polymerized, limiting the length of time that reliable measurements may be made. Szivek, *et. al.* (1997) used calcium phosphate ceramic coated strain gages to allow consistent longer-term *in vivo* strain measurements to be made with characterizable accuracy. Hoshaw *et. al.* (1998) developed a strain gage bonding technique as an alternative to cyanoacrylate-based adhesives using polymethyl methacrylate (PMMA), an FDA approved substance, for use in humans and animals for up to several days following gage application. The existence of such techniques highlights the necessity for alternatives to existing standard strain gage methods for *in vivo* use.

### ***1.3.2 Reliability***

The second limitation of bonded strain gages on bone *in vivo* is reliability. Proper surface preparation is essential for obtaining reliable measurements, but often difficult to achieve *in vivo*. Examples are common where bonded gages fail and test data cannot be used, for example, Burr, *et. al.*, (1996) where one of the two subjects' gages became unaffixed, or Biewener, *et. al.* (1996) where 3 out of 6 animals strain gaged were eliminated from the study for the same reason. To improve measurement reliability, bonded strain gages attached to surgical staples have been used both in humans (Rolf, *et. al.*, 1997), and

animals (Buttermann, *et. al.*, 1994), where the strain in the specimen to which the surgical staple is attached tends to deform the staple, producing a change in resistance in the strain gage bonded to it. A measure of axial deflection can be obtained in a gaged surgical staple system that has been calibrated. Strain measurements have also been made *in vivo* using bonded gages adapted to intracortical pins that protrude from the skin. Milgrom, *et. al.* (1997) used two threaded K-wires ("Kirschner wires", or K-wires are normally used by the orthopedic surgeon for fixation of bone fractures) inserted in the antero-medial tibial midshaft, drill and wire placement guides, and a custom displacement transducer attached between the two K-wires. The transducer consisted of a phosphor bronze beam with two pairs of uniaxial metal foil strain gages. This technique is attractive because the sensor is not exposed to the biological environment, and the bone surface does not require special preparation.

### *1.3.3 Invasiveness*

Proper surface preparation leads to a further limitation to bonded strain gages when used *in vivo*, which is the associated surgical trauma, or invasiveness. Bonded strain gages require that the bony surface to which the gage is mounted have the periosteum (a thin layer of connective tissue covering the bone) removed where the gage is to be bonded, and the bone be sanded, degreased, dried, and cleaned. Also, bonded strain gages require that the surface be relatively smooth. Where the measurement surface is rough or porous, the surface must be sanded or filled to allow for a proper bond. The procedure involves disruption of the tissue surrounding the bonding site, as well as disruption to the bone surface, as mentioned. Additionally, depending on the type of filler used and the

associated stiffness, a "reinforcing effect" might occur where the relatively soft substrate is restricted from movement, which can negatively affect the accuracy of strain measurements.

#### 1.4 A Novel Approach to Bone Strain Measurement

In the interest of mitigating these limiting factors in strain measurement *in vivo*, a novel device will be described. The device is classified as an extensometer, which has the inherent advantages of not requiring special surface preparation or requiring that the sensing elements be exposed to the biological environment. Both the extensometer design described here and staple-type gages eliminate the need for degreasing agents, chemical bonding agents, or surface preparation such as drying, sanding, and filling associated with resistance-type bonded strain gages; an advantage for *in vivo* applications. Although, as with staple-type gages, the intraosseous pins (K-wires) used by this extensometer design are implanted into the bone, no incisions or suturing are necessary, and invasiveness is minimal. Thus the limitations of compatibility of bonding agents, reliability, surface preparation, and invasiveness associated with bonded strain gages are alleviated. A further advantage offered by the extensometer that will be described here is the ability to distinguish axial strains from strains due to inhomogeneous deformations (e.g., bending), and provide information on the magnitude and sense of the bend (tensile or compressive) without requiring access to the opposing side of the specimen. Bending loads are thought to better represent normal *in vivo* loading regimens (e.g., Scott and Winter, 1990; Qin, et. al. 1998) than purely axial or torsional loads. Calculation of strains due to bending

require that strain gage instrumentation, including staple-type gages, be mounted to opposing faces of the specimen, which is not always feasible *in vivo*.

Two extensometer designs are presented: an axial design, capable of discerning axial from bending strains, and a multi-axial or "delta" design, which has the additional benefit of providing principal strain magnitudes and their direction, as well as maximum shear strain in the specimen.

### 1.5 Purpose

The purpose of this study is to i.) design, ii.) validate and iii.) test a novel method for measurement of strain in bone *in vivo* in human subjects, using a capacitive based extensometer. Design requirements dictate that the extensometer be able to measure physiologic levels and rates of strain in bone and therefore be useful up to and beyond 4,000  $\mu\epsilon$  in a given direction (tension or compression) at rates up to and exceeding 40,000  $\mu\epsilon/\text{sec}$  (e.g., Rubin and Lanyon, 1985). The calcaneus, or heel bone, was selected as the site of interest because of its relatively high susceptibility to bone loss from disuse, such as in long-duration space flight. The unique loading environment in the calcaneus requires that the extensometer be able to resolve principal strains, as the loading direction, and hence direction of strain, is not known *a priori*.

## 1.6 Specific Aims

- Design an extensometer suitable for measuring global bone strain *in vivo* that is;
  - 1.) able to measure strain due to inhomogeneous deformation (i.e., bending),
  - 2.) capable of measuring strains up to and exceeding 4,000  $\mu\epsilon$  (in tension or compression),
  - 3.) capable of measuring dynamic strains up to and exceeding 40,000  $\mu\epsilon/\text{sec}$ , and,
  - 4.) able to measure principal strain magnitudes and their direction.
  
- Test the extensometers in dynamic four-point bending in a test material and compare the output to a "standard" method of strain measurement.
  
- Determine system characteristics and limitations;
  - 1.) Quantify the sensitivity of the probes to angle.
  - 2.) Determine range of frequencies over which device can operate without introducing artifacts.
  
- Test the multi-axial extensometer design *in vivo* in a human subject.

## CHAPTER 2

### BACKGROUND

#### 2.1 Measurement of Strain

Strain is a dimensionless unit, and engineering strain is defined as a change in length, delta ( $\delta$ ) divided by original length ( $L$ ) of a specimen. Strain is represented as epsilon ( $\epsilon$ ) and, since it is usually very small, is typically expressed in terms of microstrain ( $1 \times 10^{-6}$ ) or  $\mu\epsilon$ . The strain relationship used as a basis for the equations developed in this study (engineering strain) is thus:

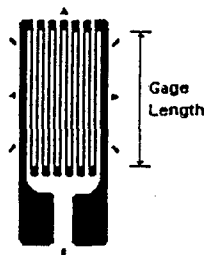
$$\epsilon = \frac{\delta}{L}$$

Engineering strain can be expressed in terms of a percent. For example, 0.5 % strain is equivalent to 5,000  $\mu\epsilon$ . Tensile strain is taken as positive and compressive strain as negative. When strain is measured with a device such as a bonded strain gage or extensometer, the original length is taken as the gage length of the device. For a bonded, metal foil strain gage, the gage length is the length of the active grid (Fig. 2.1a). For an extensometer, the gage length is the distance between arms, defined as where the contact points (knife-edges, for example) interface with the specimen (Fig. 2.1b).

Contact extensometers are conventionally used to develop stress-strain relationships and failure criteria by measuring strain directly in the material under an applied load. These extensometers typically clamp onto the specimen with knife-edges as contact points and provide highly accurate strain measurements. Commercially available contact

extensometers cover a broad range of configurations for measuring axial, biaxial, diametral, and torsional strains, for example. An advantage of using extensometers over strain gages is that the extensometer need not be exposed to the material test environment. For example, with high temperature testing, the sensing component of the extensometer is mounted external to the oven surrounding the test material, and high-temperature arms protrude from their engagement with the specimen to the extensometer sensing component through the wall of the oven. This advantage is realized with the extensometer design described in this study, where the sensing elements of the device are not exposed to the biological environment.

a.)



b.)

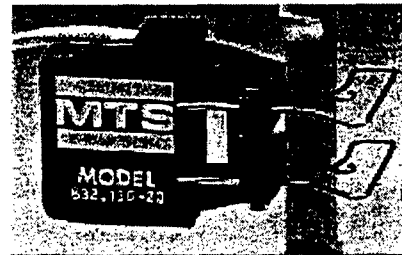


*Figure 2.1. a.) Definition of gage length for a uniaxial strain gage (Adapted from Measurements Group, Inc. website, [measurementsgroup.com](http://measurementsgroup.com)) (b.) For an extensometer, gage length is the distance between arms (Adapted from MTS Systems Corporation website, [mts.com](http://mts.com)).*

### **2.1.1 Strain Averaging and Gage Length**

When mounted in a nonuniform strain field, a strain gage will always under-report the peak strain magnitude (Fig. 2.2). Since the net resistance change of the gage is produced

by the average strain acting over the grid area, in non-uniform strain fields this value will always be less than the peak strain that exists under the strain gage (Pierson, 1999). When attempting to measure strain gradients, it is desirable to have a smaller gage length, since strain gradients tend to be averaged over the gage length of the strain gage (Fig 2.2).

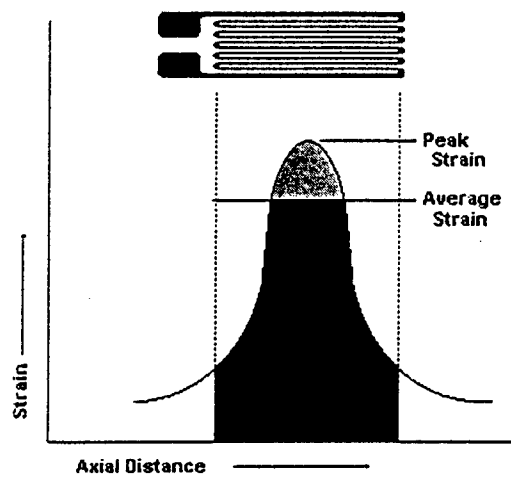


Figure 2.2. Gage length is a consideration when dealing with strain gradients. (Adapted from Measurements Group, Inc. website, [www.measurementsgroup.com](http://www.measurementsgroup.com).)

Conversely, an application of large strain gages, or gages with large gage lengths, is with strain measurement on inhomogeneous materials. When measuring strain in concrete, for example, which is a mixture of aggregate (usually stone) and cement, it is ordinarily desirable to use a strain gage of sufficient gage length to span several pieces of aggregate to measure the representative strain in the structure. In other words, it is usually the average strain that is sought in such instances, not the local fluctuations in strain that



occur at the interfaces between the aggregate particles and the cement. In general, when measuring strains on structures made of composite materials of any kind, including bone, the gage length should normally be large with respect to the dimensions of the inhomogeneities in the material (Measurements Group, Strain Gage Selection Procedures, Tech Note 505).

## 2.2 Capacitors

In contrast to resistive-type strain gages, where the resistance of the metal grid changes when the substrate to which the gage is bonded is deformed, the strain-sensing device described in this study, classified as an extensometer, employs capacitance as the measurement principle. Capacitive sensors are used in many different types of sensing and measurement applications; for example, rotary and linear position encoding, liquid level sensing, proximity detection, flow and pressure measurement, digital levels and stud-sensing devices (Baxter, 1997).

In general, the capacitance (C) between two parallel plates of area (A) separated by distance (x) is:

$$C = \epsilon_0 \epsilon_r \frac{A}{x}$$

where  $\epsilon_0$  (not to be confused with  $\epsilon$  denoting strain) is the dielectric constant of free space ( $\epsilon_0 = 8.85 \times 10^{-4}$  Farads / cm) and  $\epsilon_r$  is the relative dielectric constant of the insulator (air) which is 1 (Webster, ed. 1985).

Displacement can be monitored by changing any one of the parameters:  $\epsilon_r$ ,  $A$ , or  $x$ . The simplest and most commonly used method is to change  $x$ , the separation between plates, which is the method used in this thesis (Fig. 2.3).

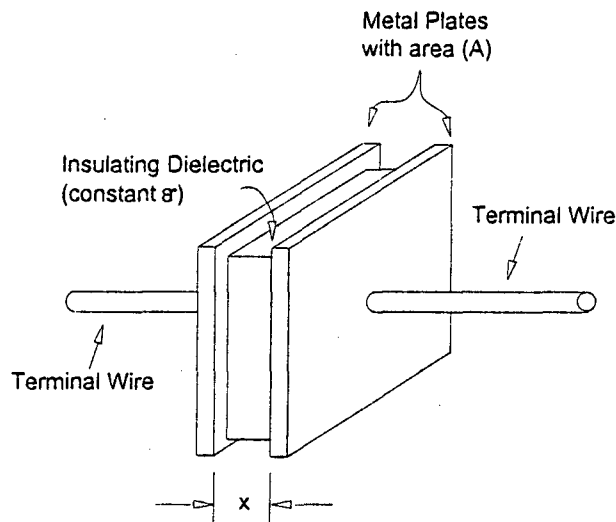


Figure 2.3. Elements of a capacitor. (Adapted from Bishop, 1995.)

### 2.2.1 How a Capacitor Works

If a capacitor is connected across the terminals of a power source (cell), electrons will flow from the negative terminal of the cell and enter the plate connected to that terminal (Fig. 2.4). The negative charge on that plate will repel the free electrons that are in the conductor (e.g., metal) of the opposing plate. These are electrons associated with the outer orbits of the metal atoms, but which tend to wander around inside the lattice. The electrons will flow away from the plate, attracted toward the positive terminal of the cell.

The atoms they leave behind are now positively charged. This flow of electrons into one plate and out of the other will continue until the potential difference between the two plates is equal to the potential difference of the cell (Bishop, 1995).

Note that, although electrons flow into one plate and out of the other plate, there is no flow of electrons *from* one plate to another. Such a flow across the dielectric is not possible, because the plates do not touch one another and the dielectric is an insulator. If the terminals of the cell are disconnected from the capacitor, the plates will remain charged. Capacitors are commonly used in this way to store charge.

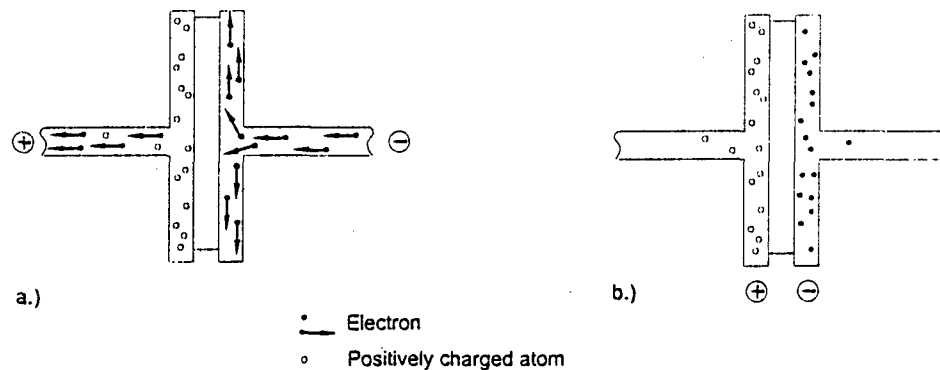


Figure 2.4. Flow of electrons in capacitor that is a.) charging and b.) charged. (Adapted from Bishop, 1995.)

### *2.2.2 Capacitive-Based Sensors*

In contrast to applying and removing a DC power cell across the plates of a capacitor for the purpose of storing a charge as described above, capacitive-based sensors require a dynamic excitation. All capacitive signal conditioning designs contain an internal oscillator and signal demodulator to provide static capable outputs (Pierson, 1999).

Sensors that are based upon the capacitive sensing technique are strain-based sensors. For example, pressure sensors and accelerometers, which use capacitors as the sensing method, rely on the deflection or deformation of a spring element within the sensor to register a change in capacitance. A geometry which uses two parallel plates with air as the dielectric is useful for measuring motion where either the spacing between plates is changed, or the common area is changed by transverse motion of one of the plates. The two plates comprising a capacitance sensor can be termed the "probe" and the "target." Typically, the probe is driven with an AC current at a particular frequency and peak-to-peak voltage. The signal conditioner through which the signal passes has demodulating circuitry for converting the sensor output to a DC voltage. This voltage is proportional to the distance between probe and target.

### *2.2.3 Transverse Sensitivity Considerations*

Although changing the distance between plates is the most common way to effect a change in capacitance, changing the common area of the plates will also effect a change. This transverse sensitivity occurs when a portion of one plate has no opposing surface, as when plates slide transversely to one another. To eliminate undesired sensitivity to

motion in unwanted axes (Fig. 2.5), the edges can be overlapped or underlapped such that only displacement in the desired axis will effect a change in capacitance (Baxter, 1997).

This principle is employed in the capacitive extensometers designed for this study, where the targets are oversized compared to the probes. Each sensing unit is sensitive only to the motion of the probe toward and away from the target in a direction normal to the probe. This is analogous to a bonded strain gage with no transverse sensitivity, or where transverse sensitivity is ignored. In this study, if capacitance were to be affected by transverse motion, there would be no way to decouple the signal due to transverse motion from that due to axial motion. Therefore oversizing the target relative to the probe is a necessary design feature in the extensometer concepts because it is necessary to obtain the perpendicular distance between plates, an assumption made in the processing of the data from the extensometer system.

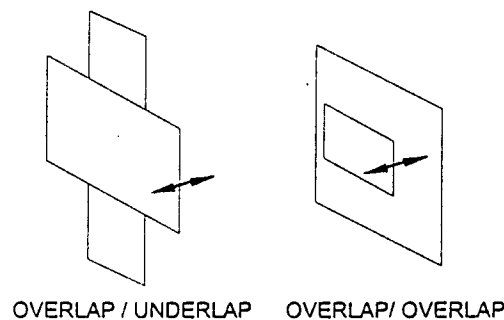


*Figure 2.5. Relative sizing of capacitive plates can eliminate sensitivity to motion in certain axes. (Adapted from Baxter, 1997.)*

### 2.3 Bone Gross Anatomy

The bones in an adult skeleton can be classified into two distinct types of arrangements according to their porosity. Cortical bone is a relatively dense structure, which forms the hard, outer shell, and provides strength and resistance to bending (Fig. 2.6). Trabecular bone (also called cancellous or spongy bone) is present at the ends of long bones, in the vertebral bones and in the heel bone, or calcaneus. Trabecular bone is relatively porous and composed of an interconnected lattice of strut-like structures called trabeculae. Like cortical bone, trabecular bone contains networks of bone cells called osteocytes which are thought to be involved in the transduction of mechanical signals in the process of osteogenesis (*osteo* = bone, *genesis* = forming). The periosteum is a thin layer of connective tissue that surrounds the outer surface of all bones, except at articulating surfaces. The calcaneus is composed primarily of cancellous, or trabecular bone, with a thin cortical shell.

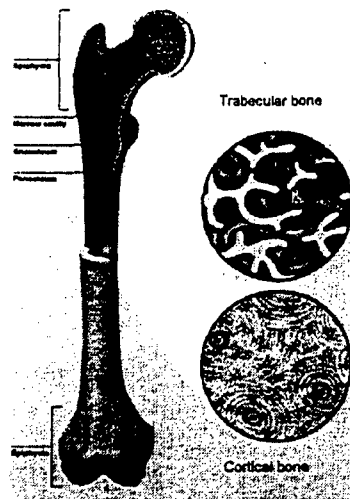


Figure 2.6. The gross structure of a long bone. Cortical vs. trabecular structure.

(Adapted from Abbott Laboratories Online, [abbottrenalcare.com](http://abbottrenalcare.com)).

## 2.4 The Mechanical Properties of Bone

Both cortical and trabecular bone contribute to the overall properties of whole bone structures; however, their respective material properties vary greatly due to differences in density and architecture. Cortical bone has been classified as an anisotropic or transversely isotropic material. For normal compressive or tensile loading, Young's modulus is approximately 17.0 GPa in the longitudinal direction, 11.5 GPa in the transverse direction, and 3.3 GPa in shear (Reilly and Burstein, 1975). The yield strain for cortical bone is approximately 7,000  $\mu\epsilon$  (0.7% change in length) with the ultimate strain up to 15,000  $\mu\epsilon$  (Carter et. al., 1981).

Yield strains for human trabecular bone have rarely been reported. Bovine trabecular bone from the distal femur has been shown to yield at approximately 0.74% (Turner, 1989). Chang, et. al. (1999), reported yielding in bovine trabecular bone to be isotropic, i.e., independent of loading direction. They found yield strains to be similar in tension (up to 0.85%) and compression (up to 0.97%, or approximately 10,000  $\mu\epsilon$ ). Keaveny et. al. (1999) reported loading trabecular bone from human lumbar vertebrae to failure up to 3.0% (30,000  $\mu\epsilon$ ) at 5,000  $\mu\epsilon$ /second. These variations in reported yield strains for trabecular bone are not surprising, considering the variety of morphologies trabecular bone can assume, not only from species to species but within a single organism (Fig. 2.7).

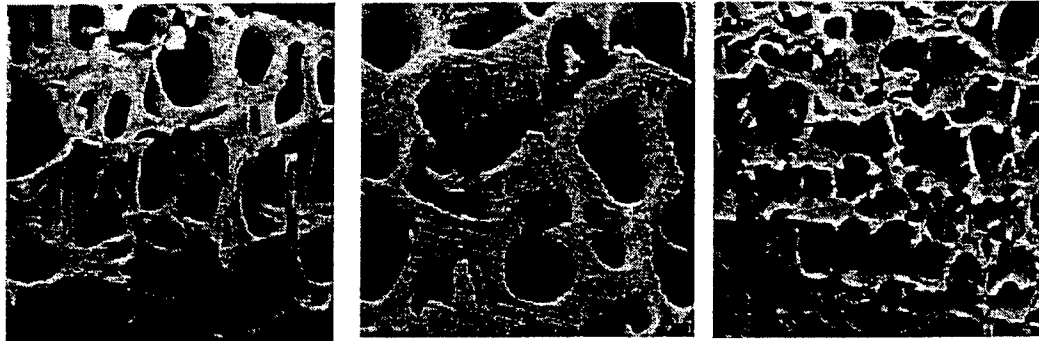


*Figure 2.7. Scanning electron micrographs showing different trabecular bone architectures found within the human skeleton. (Adapted from Keaveny and Hayes, 1993.)*

### **2.5 Mechanotransduction in Bone**

The ability of bone to regulate its mass and architecture according to perceived structural demands is a source of continued research interest, and has implications for the study of osteoporosis, including that experienced by astronauts in long-duration spaceflights.

Simply stated, decreased activity precipitates a loss of bone mass, and increased activity stimulates skeletal hypertrophy. The concept that “form follows function” articulated by Jeffries Wyman (1849), Hermann Meyer (1867) and later in greater detail by Julius Wolff in his monograph *Das Gesetz der Transformation bei Knochen (The Law of Bone Remodeling, 1892)*, is the basis for this concept. Wolff theorized that the balance of bone remodeling can be affected by mechanical function and that bone tissue has the capacity to adapt to its functional environment such that its form is optimized for the mechanical



demands to which it is subjected. Although numerous investigators have provided evidence that functional adaptation occurs in the skeleton, little is known about the cellular mechanisms that perceive and transduce mechanical stimuli into the biochemical events eliciting adaptive change at the level of the bone cell (Gross and Bain, 1993).

### *2.5.1 Mechanical Parameters Associated with Osteogenesis*

Several mechanical parameters, including strain magnitude, strain rate, strain gradients, and fluid shear stresses within the bone, have been proposed to be involved in remodeling. Rubin and Lanyon (1985) found that the extent of the osteogenic response correlated with the peak strain (magnitude) encountered during daily loading regimens. Peak strains of 1,000  $\mu\epsilon$  maintained bone, and peak strains of 2,000, 3,000 and 4,000  $\mu\epsilon$  effected increasingly osteogenic responses. McLeod, Bain, and Rubin (1990) found that high-frequency mechanical stimuli were more osteogenic than low-frequency stimuli of identical amplitude, suggesting that strain rate is an important factor in the mechanosensory system of bone. More recently, fluid shear stress acting on the surfaces of bone cells has been shown to stimulate osteoblastic activity (e.g., Ichiro, et. al., 1997) and has been proposed as a mechanical parameter responsible for osteogenesis (Weinbaum, et. al., 1994).

The variety of types of stimuli postulated as being osteogenic in nature including strain magnitude, rate, and fluid shear stress, highlights the need for investigators to design experiments where osteogenic parameters may be isolated and studied independently. For example, fluid shear stress is not dependent upon strain magnitude, but rather the time

rate of strain. As an illustration, the shear stress of a fluid near a wall is given by the equation in Figure 2.8:

$$\tau = \mu \frac{dV}{dy}$$

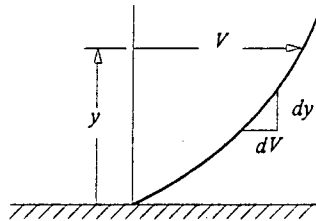


*Figure 2.8. Fluid shear stress near a wall is not a function of strain magnitude. Fluid shear stress is a proposed osteogenic stimulus to certain bone cells.*

In the equation in Figure 2.8,  $\tau$  is the shear stress,  $\mu$  is the dynamic viscosity, and  $dV/dy$  is the time rate of strain, which is also the velocity gradient normal to the wall. Fluid shear stress is not a function of strain magnitude, unlike shear stress in a solid. An observation, which directly supports the theory that fluid forces affect bone remodeling, is that dynamic loading, which enhances fluid flow, induces an osteogenic response, whereas static loading, which has little effect on flow, does not (Hert, et. al., 1971; Turner, et. al., 1994). Lanyon, et. al. (1984), showed the response to functional isolation in avian ulna preparations with a superimposed static strain was no different from the response to functional isolation alone; static loading did not effect an osteogenic response. For this reason, strain rate, as well as strain magnitude, was a parameter of interest in this study,

and strain rate and frequency response were considered during validation tests of the extensometers.

### *2.5.2 The Calcaneus and Bone Loss*

The human calcaneus, the largest of the tarsal bones, is subject to age-related decreases in density and strength, and is particularly affected by disuse such as that which occurs during bed rest, reduced loading, or zero gravity conditions (LeBlanc et. al., 1990) due in part to its high content of cancellous bone. The increased surface area of the trabeculae that comprise cancellous bone makes them particularly sensitive to the cellular events responsible for removing bone (Gross and Bain, 1993). In spaceflight, the calcaneus has been reported to lose as much as 17% of its preflight mass after only twenty-four days (Kakurin, 1972). In general, once bone mass is lost after disuse, trends in animal studies suggest that mineral recovery can be at least partially restored, and that the rate of restoration is slow compared to the rate of loss (Sessions, et. al., 1989; Jaworski and Uthoff, 1986; Rubin, et. al., 1987).

Weight-bearing bones, including the calcaneus, are more severely affected by bone loss in microgravity environments. Based on calcium balance studies, it has been predicted that a 5% loss in total body calcium after one year in space reflects a 25% decrease in mineralization of the lower extremities (Whedon, 1984). This is roughly equivalent to the loss experienced during forty years of aging in post-menopausal women (Courtney, et. al., 1995). Researchers have suggested that high loading rates and impact forces are critical for reducing spaceflight-induced osteoporosis (Cavanagh, et. al., 1992). In the

interest of combating the problem of bone loss in space (Fig. 2.9), determining the relationship between external loading and internal bone strains experienced during physiological activity would help in the design of more effective exercise-based countermeasures. While some mechanical properties of calcaneal trabecular bone specimens have been measured, there are almost no data regarding physiologic strains in the human calcaneus (D'Andrea, 1998). Because of the unique challenge measuring physiologic strains in the calcaneus presents, a new method of bone strain measurement was sought.

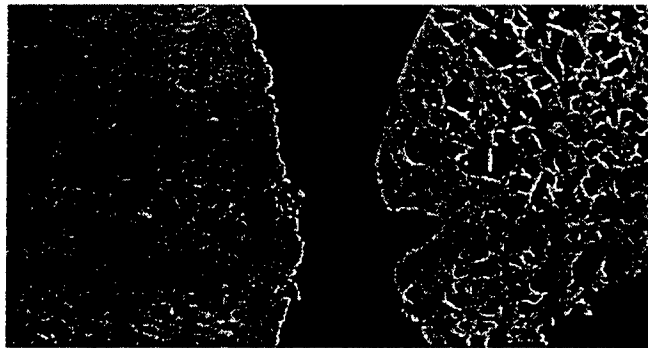


*Figure 2.9. Normal (at left) versus osteoporotic bone (at right) showing effect of loss of bone mass*

### **2.6 Measurement of Bone Strain *in Vivo* in Humans**

Very few investigators to date have attempted to measure human bone strains *in vivo*; therefore, understanding of the mechanical influences in regulation of bone remodeling has been derived almost completely from animal models. Peak principal compressive strains are generally acknowledged to be on the order of  $-2,000$  to  $-3,000 \mu\epsilon$  in most

animals (Rubin and Lanyon, 1982), although strains as high as  $-5,670 \mu\epsilon$  have been measured in young racehorses (Nunamaker, et. al., 1990).

The first study to measure *in vivo* human bone strains was Lanyon et. al. (1975), where a 35 year old male was instrumented with a rosette strain gage on the antero-medial aspect of the tibial midshaft. The subject performed walking and running trials on a treadmill and on the floor, with and without shoes for each condition, while strain traces were recorded. The investigators found that a distinct four-phase pattern of strain was present for walking; two during swing phase and two during stance phase. During treadmill walking, strain magnitudes reached their highest range in Phase 3, heel off to toe off, where values ranged from  $-368 \mu\epsilon$  to  $434 \mu\epsilon$ . Strains during treadmill running reached  $847 \mu\epsilon$ . Strain rates ranged from  $-2,300 \mu\epsilon/\text{sec}$  for walking to  $13,000 \mu\epsilon/\text{sec}$  for treadmill running.

This study by Lanyon et. al. (1975) was significant in many respects. First, it demonstrated that bonding a strain gage rosette *in vivo* to human cortical bone and obtaining a record of strain output from the gage during activity was technically feasible. Second, it showed that strain angle can change throughout the gait cycle without visibly noticeable changes in gait. Finally, this study established that the strain time histories measured from the tibia during gait are comprised of a series of discrete events in which bone is deformed, unloaded, and then deformed in the opposite direction.

In a more recent study, Burr, et. al. (1996) implanted rosette strain gages in two subjects on the medial tibial cortex at midshaft. Subjects performed activities similar to military field training exercises often associated with stress fractures in military recruits. Compressive, tensile, and shear strains were recorded during (a) walking, jogging, and sprinting on a level surface, (b) walking carrying a 17 kg pack, (c) walking and running uphill and downhill, and (d) zigzag running uphill and downhill. Results showed principal compressive strains ranging from  $-414 \mu\epsilon$  to  $-1,226 \mu\epsilon$  in downhill walking and uphill zigzag running, respectively. The most vigorous activities resulted in strain magnitudes and rates two to three times higher than walking on a level surface, in accordance with the findings of Lanyon, et. al., (1975).

Rolf, et. al. (1997) used an instrumented surgical staple to measure local bone deformation in the tibia in seven human subjects. The subjects performed two types of jumps in the study; (a) a forward jump from a horizontal position 0.3 m away from a force plate, landing on the forefoot with the foot in the neutral position, and (b) similar to (a) but with heel landing. Although the authors reported no absolute strain values pending further studies of reliability and validity, they did find that peak deformation, or strain, in the tibia occurred at 20 to 42 ms (median) after ground contact, and was up to eight times higher during stance phase loading compared to standing still on one leg.

Milgrom et. al. (1998) used instrumented surgical staples in "three staple modified 30 degree rosette" arrangements in the mid-diaphysis of the medial aspect of the tibia in four human subjects. They found that during jumping, average tibial compressive strains were

-1,872  $\mu\epsilon$ , compared to 912  $\mu\epsilon$  in tension. Peak compressive and tensile strains in the tibia during landing from a jump were not significantly different from those recorded during vigorous military training activities (Burr et. al., 1996). Shear strains during jumping, however averaged 5,429  $\mu\epsilon$ , and were generally three to six times greater than compressive or tensile strains, indicating a risk of stress fractures for this type of activity.

### **2.7 Measurement of Bending in Bone *In Vivo***

Rubin and Lanyon (1982) concluded that bending moments are responsible for over 80% of the strain at the bone surface. Bending loads are thought to better represent normal *in vivo* loading regimens (e.g., Scott and Winter, 1990; Qin, et. al. 1998) than purely axial or torsional loads. Although bending moments will always be present within the structure of bones, these moments can be significantly reduced by alteration of the longitudinal curvature. However, the orientation of bone does not appear to be directed toward this neutral bending axis and in some cases is directed to increase bending (Rubin, 1984), suggesting that bone curvature acts to accentuate strain rather than limit it.

To determine the strain distribution across a section of the bone and thus obtain a measure of bending, it is necessary to have at least three strain gage rosettes placed around the circumference of the specimen. Rubin and Lanyon (1985) describe this technique as applied to turkey ulnae, whereby principal strains are computed for each strain gage location around the bone circumference. By knowing the location of each gage around the bone circumference, it is possible to determine the longitudinal strain at any point throughout the bone cross section. Two assumptions are made in this analysis: material properties are assumed to be homogeneous, and strain distribution is assumed to

be uniform. Using this technique, they determined the changing location of the neutral axis in bending turkey ulnae specimens *in vivo* during wing flapping and *in situ* during artificial loading.

## **2.8 Design Process For a New Method of Strain Measurement**

The design process for developing an extensometer as an alternative method to bonded strain gages, or to commercially available extensometers, occurred in stages. It was desired that whole bone strain (i.e., global strain) be measured, so that inferences could be made about the amount of compression or extension experienced by the trabecular bone within the calcaneus. The calcaneus was targeted as the bone to study because it is a site that is particularly prone to disuse osteoporosis, such as that experienced by astronauts during long-duration space flights, or patients subjected to prolonged bed rest.

### ***2.8.1 Cadaver Tests with Commercially Available Extensometers***

The first approach to measuring strain in the calcaneus was to mount a commercially available axial extensometer to two intraosseus pins (K-wire, 1.98 mm diameter), which were inserted into the bone of cadaveric lower limbs and which protruded beyond the bone cortex through the soft tissue. An MTS model 632.13E-20 was used initially. The instrumented limbs were potted in aluminum tubes with polymethyl methacrylate (PMMA), mounted in a drop test apparatus, and dropped onto a force plate as a way to generate and measure impact loading regimes that would be encountered during jumping exercises (Fig. 2.10). This extensometer, a strain-gage-based instrument, weighs 27 grams and has a maximum operating frequency of 40 Hz, which is possible only at small



displacements. An artifactual strain was encountered during these tests, which was attributed to the relatively large mass of the extensometer, causing a relative displacement of the extensometer upon its grips, and/or causing deformation of the cantilevered intraosseus pins. This error was on the order of the magnitude of signal measured. Stabilizing mounts and changing the grip design did not decrease the errors.



*Figure 2.10. One of the cadaver feet used in drop test experiments where bone strain was measured using commercially available axial extensometers.*

### ***2.8.2 Capacitive -Based Sensors in a New Extensometer Design***

A new solution to the problems encountered with commercially available axial extensometers was sought, and capacitive sensors were investigated for their non-contact properties, small size and weight, high resolution and dynamic range. The capacitive sensors could be mounted to the protruding ends of the intraosseus pins such that a

change in pin position could be detected by the change in air gap between the capacitive sensor and its target. The prototype version of the capacitance-based extensometer utilized a single capacitive sensor. This design was used in cadaver drop tests (Courtney, *et. al.*, 1997), and in human subjects (Fig. 2.11) who performed jumping exercises in 1g and simulated zero gravity (D'Andrea, 1998). Subjects gave written informed consent to participate in the protocol, which was approved by the Internal Review Board of the Cleveland Clinic Foundation.



*Figure 2.11. Prototype capacitive axial extensometer utilizing a single capacitive probe shown implanted into the lateral aspect of the right calcaneus in a live human subject.*

The average peak magnitudes of the compressive strain measured during jumping exercises in a custom zero gravity simulator ranged between 0.34 and 0.57 % strain (3,400 to 5,700  $\mu\epsilon$ ) with individual strains as high as 1.36% (D'Andrea, 1998). One of the results that was considered surprising at the time was the presence of substantial

tensile strains in the data (Fig. 2.12, where tensile strains are indicated as a positive VDC probe output). Initially, it was believed that the impact force as the subject came in contact with the ground would cause compressive loading in the bone. At times, the tensile strain was greater than the compressive strain, and there were noticeable tensile strains recorded during the push-off phase of the countermovement during the jumping exercises. This was evident in all of the subjects and at times was greater than the strain during landing (D'Andrea, 1998). During jumping exercises, tensile peaks were on average 1.5 times the compressive peak. Tests were performed to ensure that the tensile strains were not an artifact in the data but were indeed being measured, and to obtain conclusive evidence that the bone was in fact experiencing tension.

Although a major aim of the jumping study was to determine the relationship between externally applied force and internal bone strains, peak correlations between these two variables did not exceed 0.53, with most values below 0.3 (D'Andrea, 1998). Several reasons for this were postulated, including excessive vibration of pins upon impact (although by the use of Castigliano's Theorem, this was shown to have little or no effect on the resultant strain), variation in bone stiffness between cortical and trabecular bone, causing the pins to possibly "teeter totter" about the stiff cortical shell, and finally, the possibility that the calcaneus does not simply compress with loading, but experiences complex deformation, including bending.

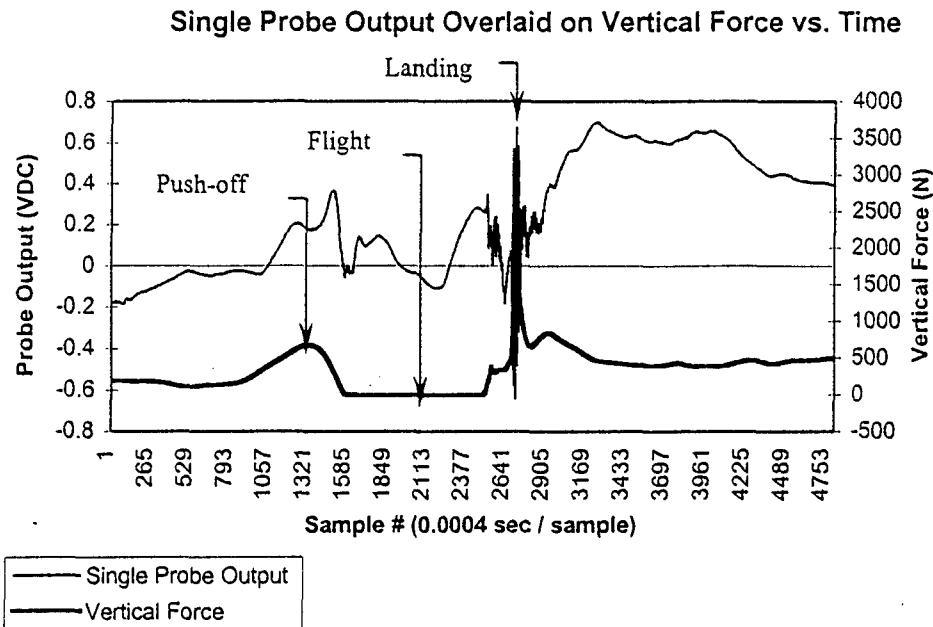


*Figure 2.12. Representative in vivo calcaneal strain time history plotted with vertical force during jumping movement in human subject. Data obtained with capacitive extensometer outfitted with a single sensor.*

### **2.8.3 Requirement for Bending Measurement Capability**

Of the possible reasons for a lack of a relationship between external force and internal bone strains, the most apparent was that in a specimen undergoing bending, a single sensor would not be adequate to measure pin displacement. Given the irregular geometry of the bone and irregular loading directions imposed upon it, the calcaneus most certainly does not deform solely in a uniaxial fashion. Due to its angulation with the ground and

the concavity of its medial surface, for example, it is conceivable that bending occurs in both the coronal and sagittal planes during normal loading. In general, loading on bone occurs from both external loading i.e., ground reaction force, and internal loading, e.g., bone-on-bone contact forces, forces imposed via tendons due to muscle activity, and forces from ligaments. For example, the force in the Achilles tendon, an internal load, can reach magnitudes of up to 2,000 N during jumping (Fukashiro, et. al., 1995).

Because the capacitive sensor is a non-contact device, the intraosseus pins may move independently, and, within a given plane, may become non-parallel, or may move out of plane with one another. This is not necessarily a disadvantage, however, as this observation led to the conclusion that for a single sensor mounted external to the measurement site of interest, strain magnitude will be independent of sensor position along the pins only if the pins remain parallel to one another, i.e., if the specimen experiences pure axial deformation. In bending, the intraosseus pins may become non-parallel and strain magnitude becomes a function of sensor position. Therefore, to account for bending, the single-sensor design evolved into one that incorporates two identical sensors mounted at some distance apart, along the exposed length of the pins. Using geometric variables measured from the extensometer, i.e., distance between sensors and distance from sensors to bone, and displacement data from each of the two sensors, it is possible to calculate strain at a plane that does not contain the sensors, such as the bone surface, or within the bone.

With the capacitive extensometers described in this study, bending strains are measured by means of the differential output from a sensor pair mounted to pins that project from the specimen. This gives a measure of both axial pin position and pin angle. When pin angle is used with other geometric parameters of the device, surface strain in a bending specimen can be calculated. The sense of the pin angle allows one to reconstruct whether the bend is compressive or tensile. A benefit is realized when this measurement can be obtained from a single site, as this means a less invasive measurement process.

Coupling linear displacement transducers to track pin movement and compute strain is the basis for the extensometer designs. The design requires that the pins be allowed to move freely, so in this way, this design is distinguished from other devices that use pins (such as external fixators) or screws (such as pedicle screws) implanted into the bone where external loading is applied. The extensometer designs require non-contact displacement sensors, which is an important consideration when choosing capacitance sensors as the displacement-measuring technique.

#### *2.8.4 Pilot Studies with the Axial Capacitive Extensometer*

To test the feasibility of the capacitive extensometer concept, two pilot studies were performed with the axial extensometer design utilizing two capacitive sensors. The first study, a.) explored the ability to predict strains within a specimen in bending. The second study, b.) estimated the actual global strain in a cadaveric calcaneus undergoing non-uniaxial deformation due to external impact loading. These studies were designed to illustrate not only the magnitude of error encountered by using a single sensor

arrangement, but also to demonstrate that an extensometer that incorporates sensor-pairs is a viable method of strain measurement for this medium.

#### 2.8.4.1 Cantilevered Bending Measured in an Acrylic Specimen

Study a.) used an acrylic bar measuring 19 x 19 x 152 mm long, instrumented with the axial extensometer and with a single uniaxial strain gage mounted to the specimen surface within the gage length of the extensometer as a comparison measurement. The instrumented bar was subjected to cantilevered bending over a series of loads. The maximum strain was extracted from the time histories of the axial extensometer, and the surface mounted strain gage. At one load condition, for example, the analysis predicted a maximum surface strain of 1,230.77  $\mu\epsilon$ . The actual measured strain from the surface mounted gage was 1,222  $\mu\epsilon$ . Pearson's correlation coefficient ( $r$ ) between measured and calculated strain at the surface was  $r = 0.989$  ( $n = 16$  trials). This preliminary analysis demonstrated the ability to predict surface strains from an extensometer outfitted with a sensor pair. One problem with the design of this experiment was that cantilevered bending produces a non-uniform strain along the beam, so that if the comparison strain gage mounted to the surface of the beam is not precisely located between the pins at their midpoint, the strain measured from the strain gage and the strain calculated from the extensometer will be different. This was remedied by the use of four-point bending, described later in Chapter 3, Methods, which produces uniform strain between the loading points (load span) where the measurement is made.

#### 2.8.4.2 Axial Strain Measurement in Cadaver Foot Specimen

Study b.) involved instrumenting the lateral aspect of the calcaneus of a fresh frozen cadaver foot specimen with the axial extensometer using two capacitive sensors, and loading the cadaver foot with an external impact to the heel. The author planned to use a uniaxial strain gage as a comparison measurement as in study a.), however, difficulty was encountered with bonding the gage to the surface of the calcaneus, so this measurement was abandoned. The difficulty stemmed primarily from the roughness of the bone surface, but keeping the surface dry was also difficult because of several seeping pores within the mounting area after the periosteum was removed and the area was sanded and degreased with alcohol. Figure 2.13 shows the extensometer mounted within the lateral aspect of the calcaneus, and results from a data set where the maximum strain value was extracted from time histories of each of the two sensors during external impact loading of the foot and used to calculate strain at the bone midline (halfway into the bone). Note that not only does the strain magnitude vary between sensors #2 and #3, indicating that the pins became non-parallel, but also that the sense of the measured strains (positive) was different from the sense of the predicted strain within the region of the bone (negative). This is indicative of there being present a "crossing over point" of the path taken by each pin where, conceivably, strain would be measured as zero. The analysis assumed that each pin displaced symmetrically, and that the final pin location could be described as a translation plus a rotation. The analysis was performed in 2D due to limitations of the extensometer. Of note is the fact that both the sense and magnitude of the predicted strain are reasonable for this loading condition and within the expected physiological range. This pilot study also showed that, in the calcaneus undergoing external "axial" loading, a



tensile bend (causing the lateral surface of the calcaneus to experience more tension than the medial side) was present, causing the outboard sensor (#3) to measure higher strain than the inboard sensor (#2).

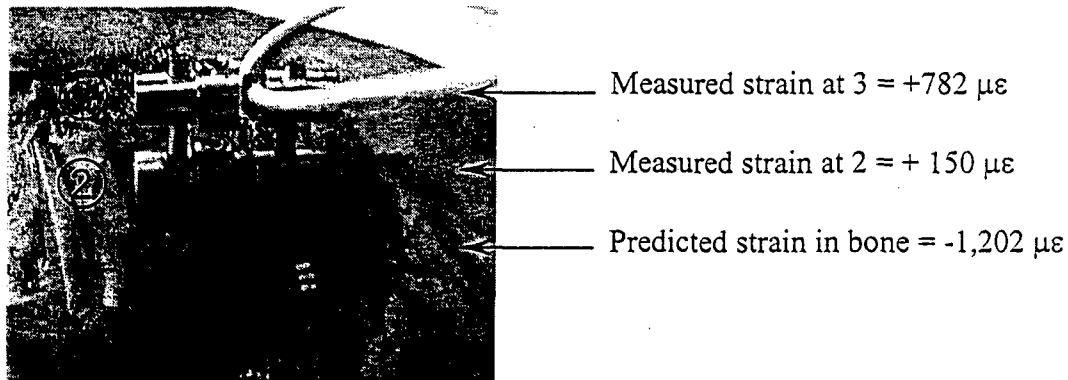


*Figure 2.13. Axial extensometer utilizing two capacitive probes (labeled 2 and 3) mounted in calcaneus of cadaver foot. The measured values from sensors 2 and 3 are used to calculate strain (predicted strain) at a third plane, within the bone. Differences in strain sense and magnitude at the three sites indicate that the bone experiences tensile bending.*

### **2.9 Delta Extensometer Design Considerations**

The axial extensometer utilizing two sensors (and targets) and two pins was found to be a feasible device, capable of measuring strains at a plane of interest lying outside the measurement planes. The axial extensometer measures strains in only one direction and should only be used where the direction of strain is known.

When the strain state of a specimen is unknown, it is possible to determine both the magnitude and direction of principal strains by using a rosette, or three-element gage (Fig. 2.14).

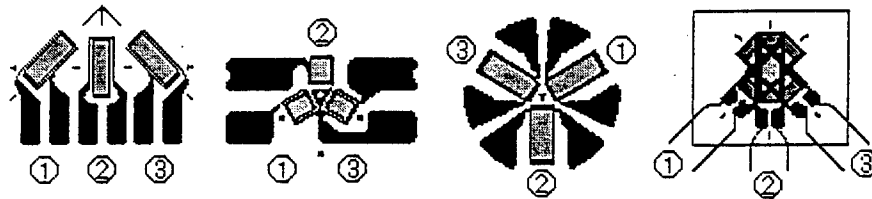
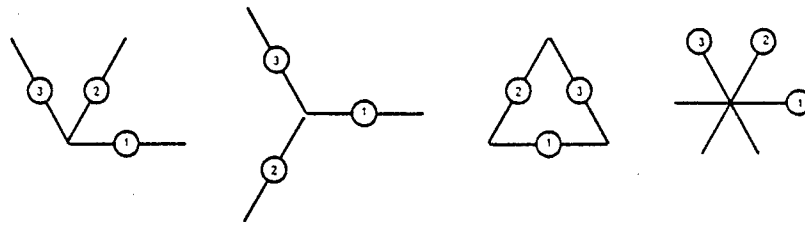


Figure 2.14. Representative three-element 60-degree delta rosette strain gages. (Adapted from Measurements Group, Inc. website, [measurementsgroup.com](http://measurementsgroup.com)).

Each element within the rosette is termed a “grid” and each has a “grid direction.” Strain gage rosettes are typically available in 45 (rectangular) or 60 (delta) degree styles, which refers to the angle between grids. Looking more closely at the delta rosette grid directions, it can be seen that it is possible to have geometrically different but functionally equivalent grid orientations (Fig. 2.15).

The functionality of a delta rosette was designed into the capacitive extensometer design by the addition of a third pin and additional sensors. If pin and sensor pairs are coupled together in a 60-degree orientation, it is possible to measure principal strain



*Figure 2.15. Geometrically different but functionally equivalent grid orientations for a delta rosette.*

magnitudes and their direction, and maximum shear strain, as would a strain gage rosette. This device is termed a capacitive “delta extensometer” (“delta” since sensor pairs are oriented 60 degrees apart, as in a delta rosette). The delta extensometer, described further in Chapter 3, Methods, incorporates three intraosseus pins; each positioned at an apex of an equilateral triangle, and not two, but six capacitive probes. Each of the six capacitive probes in this design measures axial displacement only, as do the individual gage elements in a rosette. Strain transformation relationships (Mohr’s circle for strain) are used to calculate principal strain magnitude and their direction, and maximum shear strain in the specimen.

## CHAPTER 3

### METHODOLOGY

#### 3.1 Overview of Extensometer Design

The extensometers designed in this study use capacitance as the sensing technique. The designs use at least two pins inserted into a specimen, and at least two non-contact capacitive displacement probes with targets. These probes and targets are mounted across the pins, and provide a variable capacitance whose output is varied by the displacement between the pins. The pin displacement is proportional to the global strain experienced by the specimen within the gage length. The sensors are mounted to machined bases, which are insulated from the sensors, and provide a means to mount the sensor to its pin.

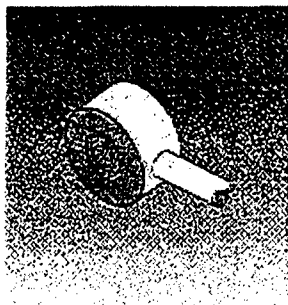
Targets are required to be machined flat, be made of a conductive material, and be grounded. Target surfaces were slightly oversized with reference to the sensing area to minimize or eliminate a change in capacitance due to transverse motion. The distance between pin centerlines defines the gage length, which is allowed to change, depending on the user's needs. For example, if the user is interested in capturing more accurate strains, or the strain field beneath the gage is expected to have high strain gradients, the gage length should be reduced. If the user expects high strain values within the site of interest, or wishes to capture average, or global, strains within a structure such as cancellous bone, or an aggregate such as concrete, larger gage lengths may be used. The user may also select different sensors or linear ranges, depending on the application.

The capacitive delta extensometer has the benefits of an extensometer that is used to measure axial strain, as well as the benefits of providing principal strain magnitudes and their direction, maximum shear strain, and a measure of bending in the specimen.

### 3.1.1 Axial Extensometer Design Features

The axial extensometer incorporates two intraosseus pins and paired capacitive sensors (HPB-75/156B-A-I3-15-B-D probe, Capacitec Inc., Ayer, MA). A capacitive "button" sensor (Fig. 3.1), which is a non-contact device, was chosen for its small size and weight, resolution, and dynamic range. Specifically, the sensor body measures 5.59 mm in diameter, and is 2 mm thick. The entire extensometer weighs less than 8 grams. The sensors have a resolution of  $\pm 0.0001$  mm (or  $\pm 0.1$   $\mu\text{m}$ ).

a.)



b.)

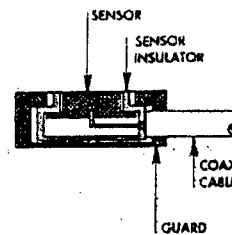


Figure 3.1. a.) Capacitive "button" probe. b.) cutaway view of same. Adapted from Capacitec Product Manual (Capacitec, Inc., Ayer, MA).

The capacitive button probes are mounted to insulated aluminum bases with cyanoacrylate adhesive. The bases attach to an intraosseus pin (K-wire, Trochar tip, 1.98

mm dia.) with setscrews. Each sensor faces a target surface mounted via an aluminum base to a second pin (Fig. 3.2). The target is a machined cap that mounts to and slides along its base. This target cap allows a linear adjustment of the air gap of approximately 0.25 mm, to allow the air gap to be set to a nominal 0.5 mm. This linear adjustment is a desirable feature because pins are not completely parallel upon insertion even with the use of a drilling jig, because of tolerances in the jig and manual drilling imposes some inevitable side loading on the pins, causing them to have a slight spring load which, upon removal of the jig, causes small deviations from parallel. The target body accepts a grounding clip which is attached to a cable running to the signal conditioner chassis ground.

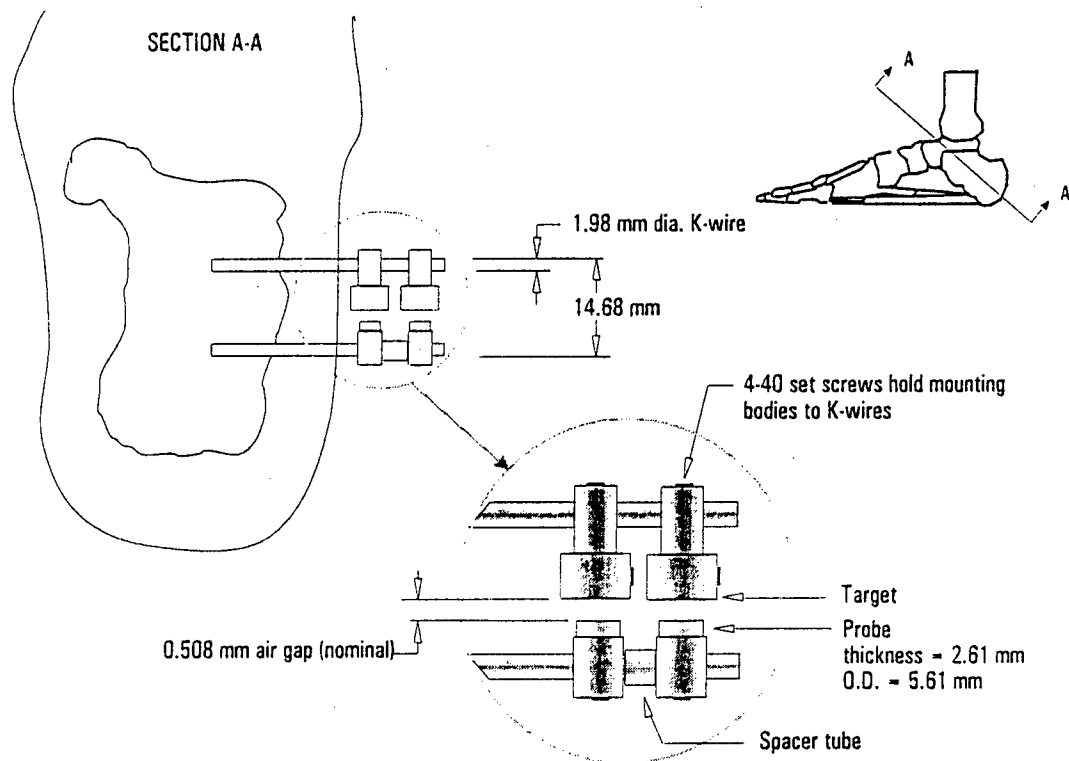


Figure 3.2. Capacitive axial extensometer components. Shown mounted into the lateral aspect of the right calcaneus in a human.

### *3.1.2 Delta Extensometer Design Features*

The delta extensometer (Fig. 3.3) utilizes six sensors (HPS-1X4C-A-200-FX, Capacitec, Inc.) and three pins (K-wire, Trochar tip, and 1.57 mm dia.). The sensors are mounted to acrylic bodies (five-sided, although there is no requirement for five sides). Each acrylic body is identical and has two internal faces; a sensor face, and a target face. The sensor face carries a pair of capacitive sensors spaced apart from each other by some distance, and oriented with respect to each other by a value of 60 degrees. The target face, acting as the target to the sensor-pair mounted to the adjacent acrylic body, is machined flat, and as the conductive surface, has aluminum tape affixed to it. The tape is cut so that a tab extends from the target area, and a thin grounding wire is fastened to the tab with conductive epoxy. Each grounding wire is routed to a custom connector to a grounding cable, which is attached to the signal conditioner chassis ground. The five-sided mounting bases provide for the proper alignment of the sensors, and also provides for the proper air gaps within the linear range of the sensors. The acrylic bodies mount to the pins via setscrews.

The HPS series of sensors are thinner and lighter in weight than the button probes used in the axial extensometer design. These features made the HPS sensors attractive for the delta extensometer design. In addition, the probe areas, which, as opposed to being circular as with the axial extensometer, were rectangular in shape (measuring 1 by 4 mm by 0.25 mm thick). The probes were oriented with their short dimension (1 mm) positioned transversely to the pin long axes, and were mounted as far apart as possible on the acrylic bodies to improve the effective resolution of the extensometer. A quantitative

relationship between the effective resolution as a function of sensor area, sensor spacing, and other system parameters was developed, and is presented in Section 5.3 of this thesis.

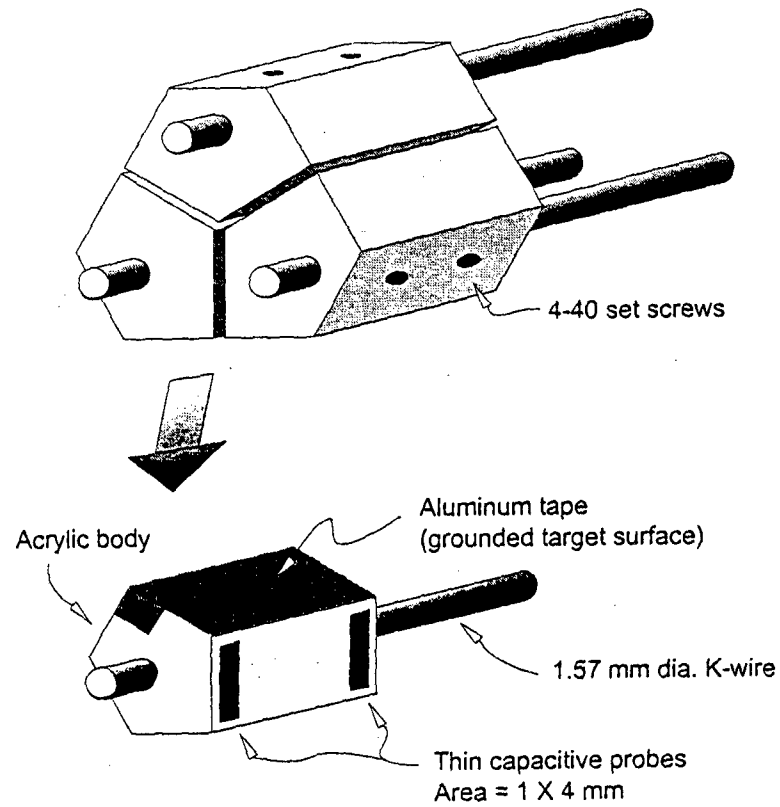


*Figure 3.3. Delta extensometer assembly (top) and the components associated with each intraosseus pin, or K-wire (bottom).*



The smaller pin diameter used with the delta extensometer (1.57 mm as opposed to 1.98 mm diameter for the axial extensometer) allows linear adjustment of the air gap, analogous to the adjustable target cap in the axial design. Since the acrylic bodies were not designed to adjust, a slightly smaller pin (therefore slightly oversized through-hole) allows the linear adjustment required enabling the nominal air gap of 0.5 mm to be realized in practice. The linear adjustments are made with copper shims placed adjacent to the pins but within the through-holes.

The delta extensometer extends the capability of axial extensometers by providing a measure of principal strain direction and magnitude. Since each sensor pair is oriented at 60 degrees (Fig. 3.4), strain transformation relationships (Mohr's circle for strain) can be used to calculate principal strain magnitudes and their direction. The numbering convention for grid directions on a strain gage rosette is identical to the convention used for the delta extensometer (Fig. 3.5). The terminology "grid direction" is kept for the delta extensometer, even though no actual resistive grids are present in the design.

Proper spacing and alignment of the pins is accomplished with a drilling jig designed to ensure that the pins are parallel and positioned correctly, and that the sensor bed assembly is properly aligned and provides air gaps within the linear range of the sensors.

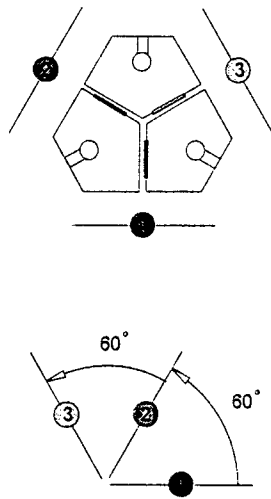


Figure 3.4. Delta extensometer in cross section shows orientation of "grid" directions, or sensor pair separation at 60 degrees.

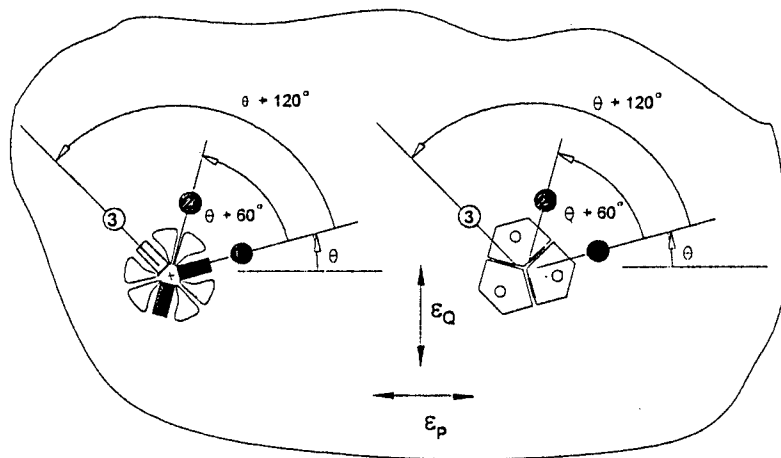


Figure 3.5. Delta rosette bonded strain gage grid layout (at left) and delta extensometer layout (at right) are the same. Shown with both strain gage and extensometer oriented at some arbitrary angle,  $\theta$ , as measured from the principal maximum strain axis,  $\epsilon_p$ , on a generic specimen.

## 3.2 Experimental Design for Four-Point Bending Validation Tests

### 3.2.1 Specimen Material Selection

Dynamic four-point bending tests were performed to validate the performance of the axial and delta extensometers against a known standard, and it was desired that the validation specimen have a modulus on the order of that of trabecular bone, such that the validation test could be run over a range of strain magnitudes that might be realistically encountered *in vivo*. The measurement site of interest, the calcaneus, is composed primarily of trabecular bone with a thin cortical shell. Trabecular bone has a Young's Modulus of 1 GPa. For comparisons, the moduli of trabecular bone and other selected materials are listed below in Table 3.1.

Table 3.1 Young's Modulus for trabecular bone and other selected materials.

Material	Young's Modulus (E) (typical)
Trabecular (cancellous) bone	1 GPa
Acrylic	3 GPa
Oak	12 GPa
Cortical bone	17 GPa
Aluminum alloy	76 GPa
Brass, annealed	103 GPa
Stainless steel	200 GPa

The yield strain of cortical bone has been reported to be on the order of 7,400  $\mu\epsilon$  (Turner, 1989). Typical *in vivo* cortical bone strains reach 4,000  $\mu\epsilon$  (Rubin and Lanyon, 1987). Thus, a relatively low modulus material was needed to be able to reach or exceed these magnitudes in the four-point bending apparatus for the validation study. Acrylic was chosen as the test material, both for its availability and its relatively low modulus (3 GPa) on the order of that of trabecular bone. The acrylic bar has a yield stress  $\sigma_y$  of 73.5 MPa, giving a yield strain ( $\epsilon_y$ ) of:

$$\epsilon_y = \frac{\sigma_y}{E} = \frac{73.5 \times 10^6 \text{ Pa}}{3.1 \times 10^9 \text{ Pa}} = 23,740 \mu\epsilon$$

indicating that the material would not fail over the planned test regime.

### **3.2.2 Strain Magnitude, Frequency, and Rate Determination**

To show that the extensometers would be useful for measuring physiologically relevant strain magnitudes, frequencies, and rates, the range of values reported in the literature for these parameters was used to develop the four-point bending test envelope.

Consideration for the test equipment limitations was involved in developing the test envelope. For example, the materials test machine was not able to exceed 20 Hz operating frequency, but it was desired that the extensometer be shown to be useful in situations where 30 Hz fluctuations in strain might be present. Further, *in vivo* strains may pass through zero (e.g., Lanyon, et. al., 1976, Swartz, et. al., 1992) which is not desirable to do in the materials test machine during high frequency tests. Considering these variables, the parameter of strain rate was used to develop a test envelope that

would validate the usefulness of the extensometer over the range of strain magnitudes, frequencies, and rates encountered in physiological settings while not exceeding the limits of the test equipment (Fig. 3.6).

A LabVIEW virtual instrument (VI) was written to allow calculation of maximum strain rate for any sinusoidal input, so that the limitations of the test equipment could be incorporated into the development of the test regime, while maintaining the desired strain magnitudes and rates. Specifically: (i) a preload was kept on the specimen so a zero load condition did not occur; (ii) the materials test machine could not exceed a 20 Hz load input, and; (iii) the yield strain of the strain gage instrumentation could not be exceeded. With the VI, the user input the desired magnitude and frequency of the sinusoidal waveform, and the program calculated the maximum strain rate by fitting a linear regression through the first 5 samples of the generated sinusoidal waveform sampled at 1,000 Hz. In this way, the strain rates encountered physiologically could be achieved while not exceeding the limits of both the test equipment and the test specimen. This exercise was simply a way of establishing a meaningful test envelope.

For example, Rubin and Lanyon (1985) reported that 1 to 2 Hz events during locomotion produce levels of strain on the order of 1,000 to 3,000  $\mu\epsilon$  and are osteogenic in nature. These ranges of strain magnitudes and frequencies were plotted as two sinusoidal events, with the zero to peak values reaching 1,000 and 3,000  $\mu\epsilon$ . Maximum strain rates were calculated for each sinusoid, that is;

Regime 1: (Rubin and Lanyon, 1985)

3,000  $\mu\epsilon$  at 2 Hz gives a max. strain rate = 37,676  $\mu\epsilon$  /sec

1,000  $\mu\epsilon$  at 1 Hz gives a max. strain rate = 6,282  $\mu\epsilon$  / sec

With the range of strain rates known, the curves may be shifted such that they do not pass through zero, and a new frequency can be found while matching the strain rate and magnitude, or if desired, a new magnitude can be found while matching the strain rate and frequency. This is especially important when one encounters parameter values that are not attainable on the materials test equipment.

Cowin (1997) reported that higher frequency events of 15 to 25 Hz on the order of 100 to 250  $\mu\epsilon$  magnitude, possibly associated with muscular contractions to maintain posture, are of importance in maintaining bone mass. Calculating the strain rates for these events;

Regime 2: (Cowin, 1997)

250  $\mu\epsilon$  at 25 Hz gives a max. strain rate = 35,533  $\mu\epsilon$  /sec

100  $\mu\epsilon$  at 15 Hz gives a max. strain rate = 9,096  $\mu\epsilon$  /sec

Of note is the fact that, although the regimes reported by both Rubin and Lanyon (1985) and Cowin (1997) are very different both in terms of magnitude, frequency, and the daily activities from which they are derived, the range of strain rates encompassed by these regimes are very similar (Fig. 3.7), which seems to lend support to the fact that strain rate

may be an important mechanical parameter related to osteogenesis (mechanical parameters related to osteogenesis were discussed earlier in Chapter 2, Background). The maximum target strain magnitude and rate for this study were chosen to be 4,000  $\mu\epsilon$  and 40,000  $\mu\epsilon/\text{sec}$ , respectively, in order to encompass the physiological regimes discussed above.

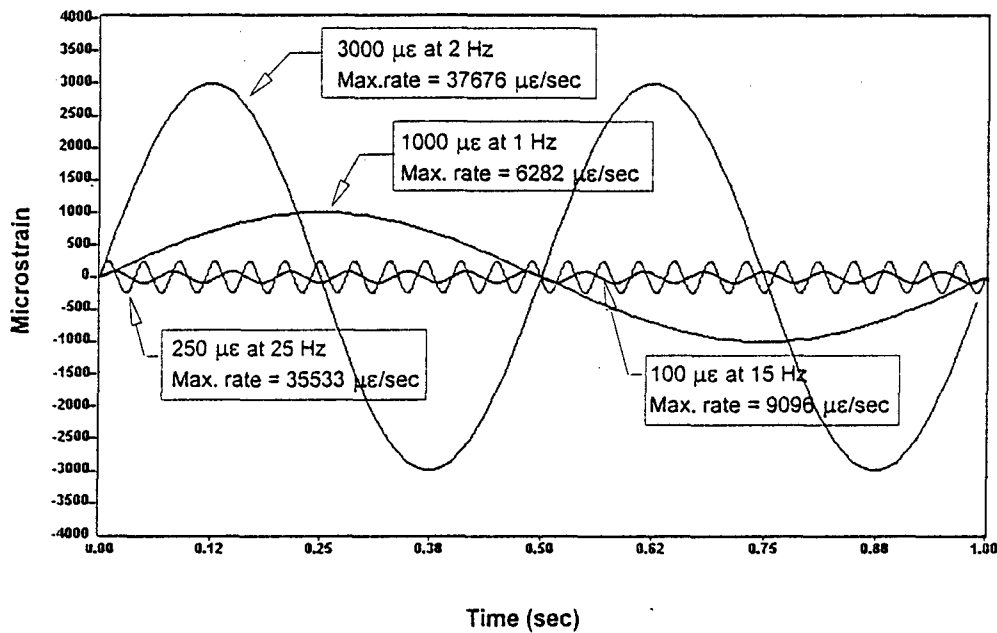


*Figure 3.6. The range of strain magnitudes and rates encountered from physiological activity from two separate investigations (Regimes 1 and 2 indicated in the text), associated with osteogenesis were used to establish the four-point bend test envelope.*

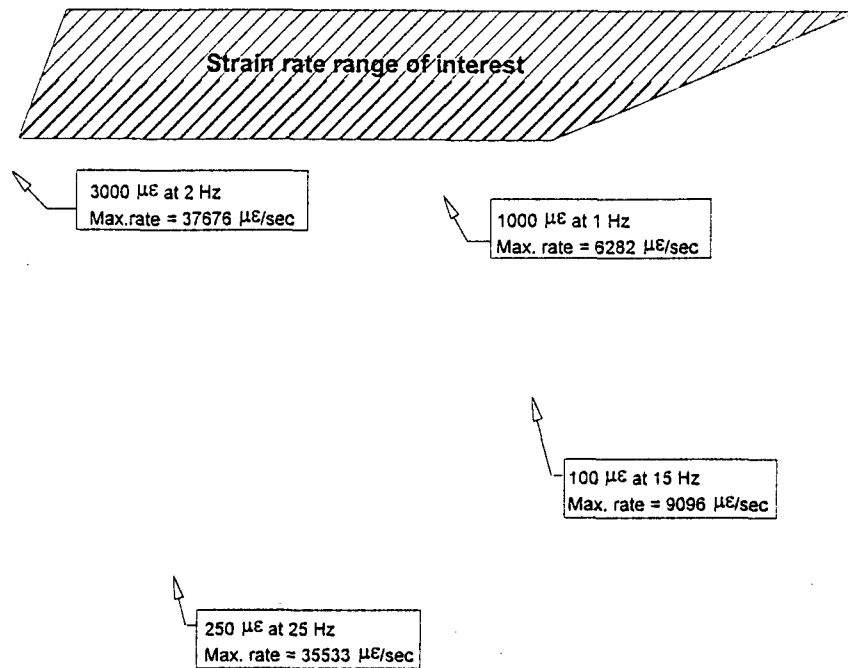


Figure 3.7. Expanded view of Figure 3.6, whereby the two different test regimes are shown to have a similar range of strain rates associated with osteogenesis. This range of strain rates was included in the four-point bend test regime.

### 3.2.3 Four-Point Bending Test – Axial Extensometer

The four-point bending test for the axial extensometer used an acrylic bar measuring 19 x 19 x 152 mm long, instrumented with the capacitive extensometer and, as a comparison strain measurement, a single uniaxial strain gage (Measurements Group, CEA-00-062UW-350, gage length = 1.57 mm) mounted to the specimen surface between the pins and aligned with the extensometer axis (Fig.3.8).



Maximum strain rates reported in the literature for *in vivo* studies were used to create the validation test envelope from low levels of strain (down to the resolution of the extensometers) up to and exceeding 4,000  $\mu\epsilon$ . The rate of 40,000  $\mu\epsilon/\text{sec}$  was targeted as the maximum desired strain rate for the validation tests. The materials test equipment was operated up to its maximum operating frequency of 20 Hz (for more see section 3.3.4 Four-Point Bending Test Procedure).

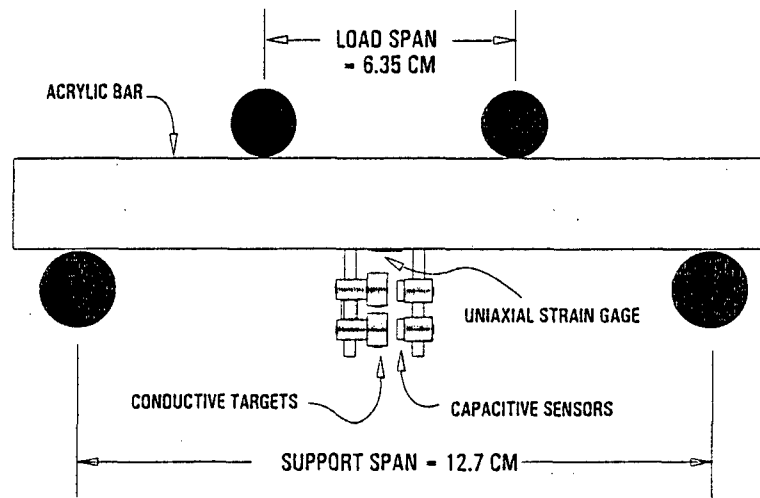
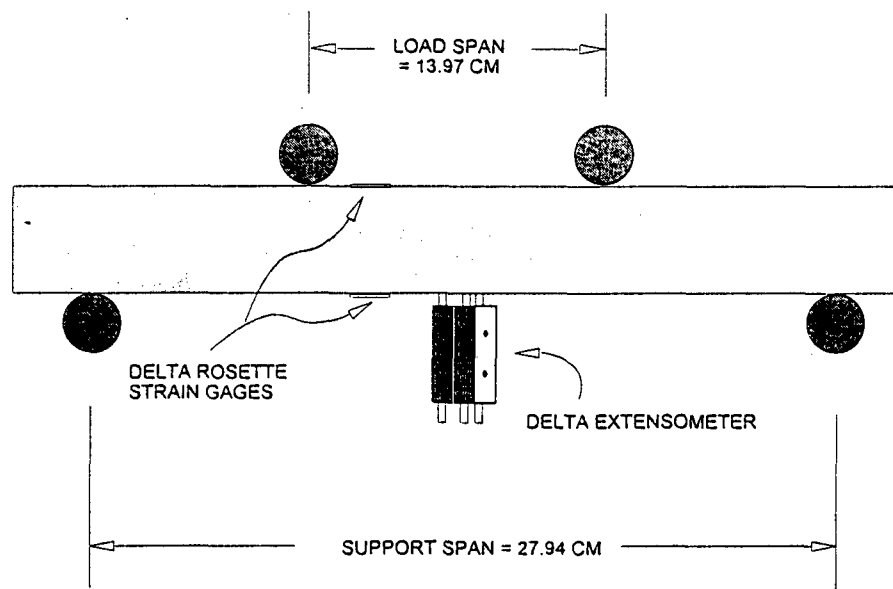


Figure 3.8. Axial extensometer shown mounted in four-point bending specimen.

### 3.2.4 Four-Point Bending Test – Delta Extensometer

The four-point bending test for the delta extensometer used an acrylic bar measuring 25.4 x 25.4 x 304.8 mm long. The bar was instrumented with the capacitive extensometer and, as a comparison strain measurement, delta rosette strain gages (Measurements Group,

WA-03-030WY-120). The rosette strain gages were mounted to the specimen surface next to the extensometer insertion site within the load span (Fig. 3.9). The delta rosette strain gages were bonded to the specimen outside the area enclosed by the pins due to size of the gage and associated solder tabs, and to minimize the possibility of stress concentrations from the mounting holes from interfering with the strain gage output.



*Figure 3.9. Four-point bend set up for delta extensometer test in acrylic specimen. The load is applied at top (roller contact points define the load span), and is supported by the rollers at bottom.*

The extensometer alignment was changed from having the reference grid (grid 1) aligned with the long axis of the specimen, to having the reference grid rotated 22.5-degrees off-axis. This was done to maximize the signal from the three grid directions, as the

Poisson's ratio of approximately 0.3 for acrylic brings grids 2 and 3 very close to zero for the specimen in bending when grid 1 is aligned with the long axis. This can be readily seen from constructing Mohr's circles for strain, drawn for the original and the revised orientations (Fig. 3.10). The delta extensometer is shown mounted in the acrylic test specimen (in revised orientation) in Figure 3.11.

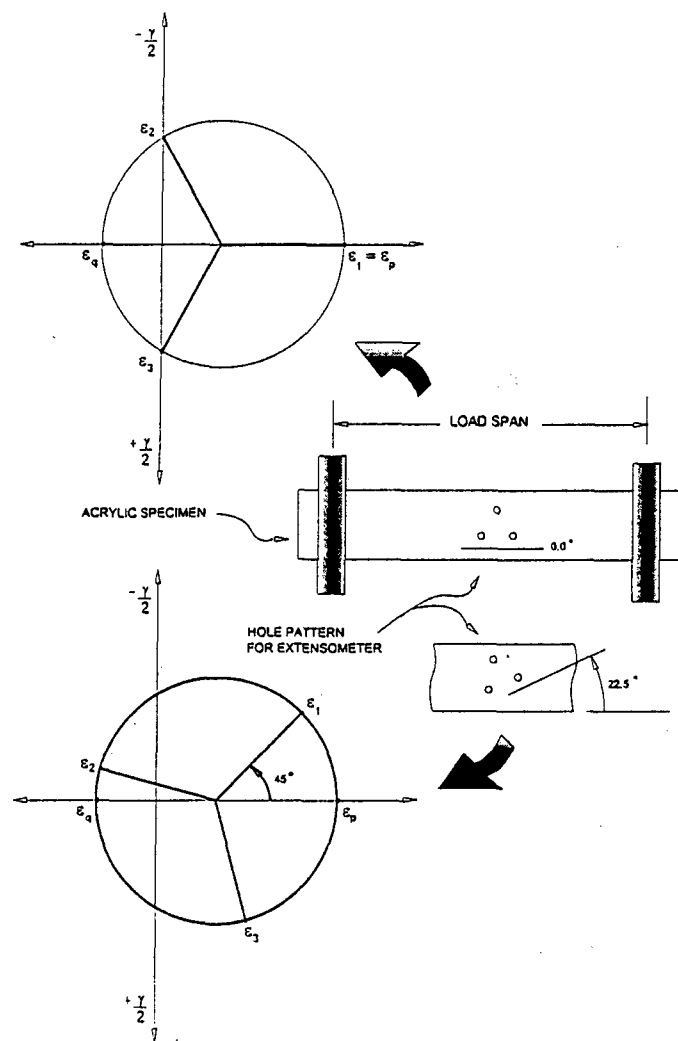
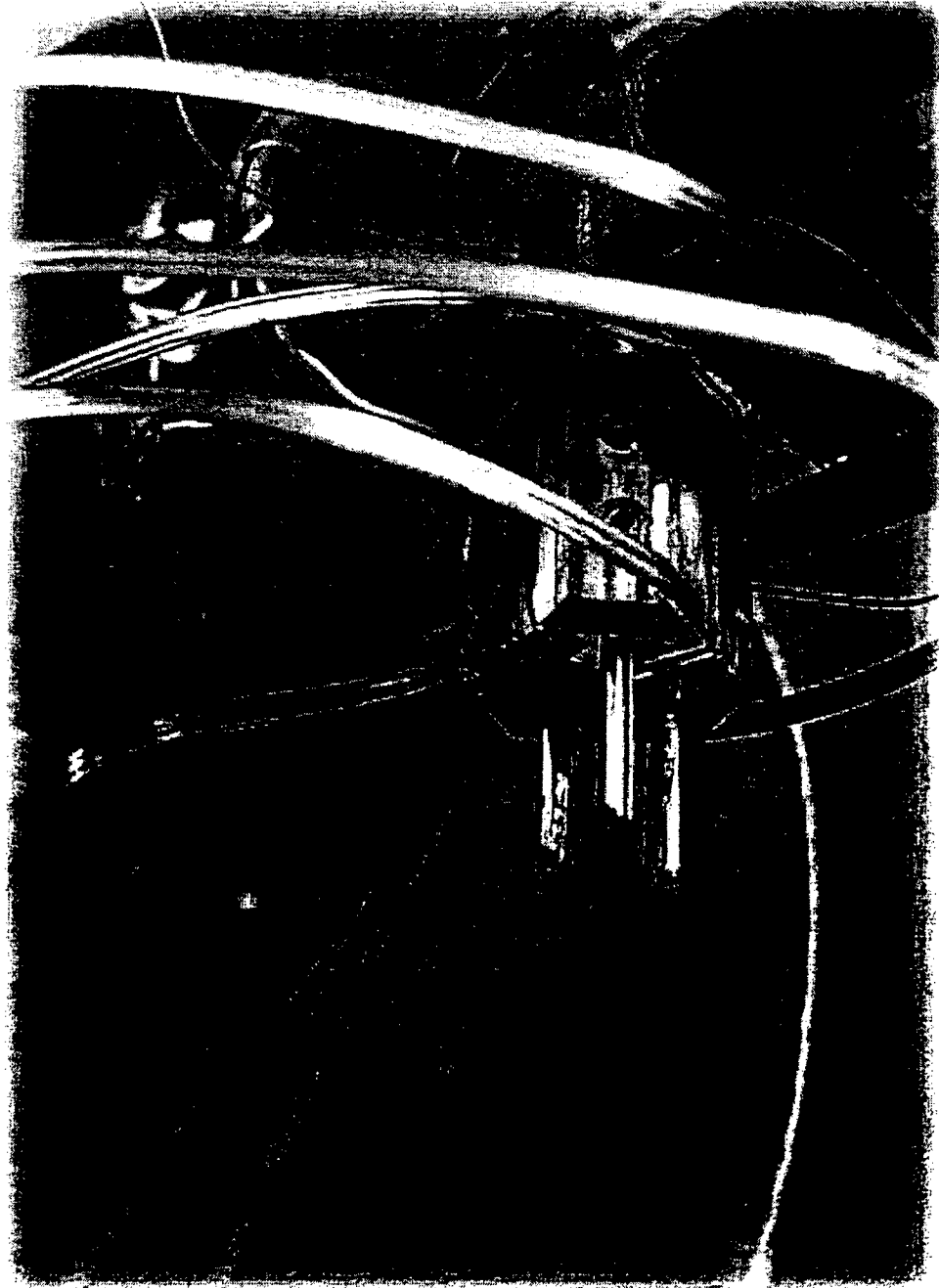


Figure 3.10. Original (top) and revised extensometer orientation (bottom) and associated Mohr's circles for strain for four-point bending tests with the delta extensometer.



*Figure 3.11. Delta extensometer shown mounted in acrylic specimen during four-point bending tests. The strain gage rosette used for comparison measurements is visible at left.*

### *3.2.5 Instrumentation and Wiring*

The capacitive probes used in the extensometer designs were calibrated at the factory (Capacitec, Inc., Ayer, MA) over an air gap of 0 to 1.016 mm, corresponding to -5 to +5VDC, or a linear range of +/- 40,000  $\mu\epsilon$  with a 12.7 mm gage length (axial extensometer), or +/- 71,000  $\mu\epsilon$  with a 7.1 mm gage length (delta extensometer). The amplifier resolution (Capacitec) is +/-0.01% of full scale, or +/- 1 mV over a 10 V full-scale range. The engineering unit conversion for both extensometers is  $1.016 \times 10^{-4}$  mm/mV. Each probe therefore has a resolution of +/-  $1.016 \times 10^{-4}$  mm, or +/- 8  $\mu\epsilon$  for the axial extensometer, and +/- 14.3  $\mu\epsilon$  for the delta extensometer. However, this resolution is associated with each probe in the extensometer system, and when probes are coupled together to allow calculation of displacement (or strain) at a third location, this resolution decreases. The term "effective resolution" is given to the resolution of the calculated strain, and the equations for this are developed in Chapter 5 (Section 5.3, "Effective Resolution of Extensometers"). The extensometer and signal conditioning specifications are summarized in Table 3.2. Probe frequency responses up to 200 kHz are possible (Foster, 1989).

Data were collected with a 16-bit A/D board (AT-MI0-16E-10, National Instruments, Austin, TX) in a personal computer, and processed through a custom LabVIEW data acquisition and analysis program (National Instruments). Data were oversampled at 5,000 Hz, and plotted as 10 sample averages, giving an effective sampling rate of 500 Hz. Resolution can be improved by oversampling due to the oscillatory nature of the modulation /demodulation circuitry (carrier frequency =15 kHz) used by the amplifiers.

Oversampling improved the effective resolution of the extensometers by approximately 50%. A gain stage and anti-aliasing filter (8300 XWB, Preston Scientific, Anaheim, CA) with cutoff frequency of 100 Hz was used prior to digitizing (Fig. 3.12).

### *3.2.6 Filtering and Sampling Rate Considerations*

An anti-alias filter was used prior to digitizing with (8300 XWB, Preston Scientific, Anaheim, CA). Loading inputs to the acrylic specimen did not exceed 20 Hz in the four-point bending test regime. To determine the frequency range of interest for the validation test, and to ensure that valuable frequency content in the sampled signal was not attenuated by the lowpass filter, the analog load signal from the Instron machine was sampled at 5000 Hz for 2 conditions expected to have the highest frequency content: a 20 Hz sinusoidal load input and a 2 Hz square wave input. Frequency spectra of the load signals were generated, and the frequency above which energy content in the signal was attenuated to less than 0.1 % of the maximum was chosen as the frequency range of interest, and found to be 50 Hz. Based on this value (50 Hz) a filter cutoff frequency ( $F_c$ ) = 100 Hz and sampling rate ( $F_s$ ) = 5000 Hz were chosen, giving a sampling ratio  $F_s/F_c$  of 50 to 1. In general, a  $F_s/F_c$  ratio of 10 is a rule of thumb, but a higher ratio was used in this case because of the relatively slow roll-off characteristics of the 2<sup>nd</sup> order filter in the Preston amplifier. Aliasing occurs when false low-frequency components appear in the sampled data due to undersampling. The anti-alias filter ensures that frequency content in the digitized signal does not exceed the Nyquist frequency ( $F_s/2$ ), such that undersampling does not occur.

Table 3.2. Extensometer/Signal Conditioner Specifications:

Extensometer Type

Parameter	Axial	Delta
Probe model (Capacitec)	HPB-75/156B-A-13-15-B-D	HPS-1X4C-A-200-FX
Probe size	1.91 mm sensor O.D. 5.59 mm guard O.D.	1X4 mm sensor area (rectangular)
Probe linear range	1.270 mm	1.270 mm
Extensometer size	2 X 2 X 1 cm	2 cm <sup>3</sup>
Extensometer weight	8 grams	8 grams
Gage length	12.70 mm	7.1 mm
No. of sensors used	two (2)	six (6)
Extensometer linear range	1.016 mm	1.016 mm
Extensometer strain range	+/- 40,000 $\mu\epsilon$ (or +/- 4%)	+/- 71,000 $\mu\epsilon$ (or +/- 7%)
Input connector	BNC	Microdot 10-32 miniature coaxial
Amplifier model used	4100-SL	4100-S
Low-pass filter Fc used	-3 dB at 3.5 kHz	-3dB at 200 Hz
Linearity	0.2% of full scale	
Resolution	+/-0.01% F.S., or +/- 1 mV	
Analog Output	-5.000 to +5.000 volts DC signal, proportional to gap	
Probe Excitation: Voltage Frequency	AC proportional to gap 3 V P-P max. 15.562 kHz +/- 0.01 %	
Engineering unit conv.	1.016 X 10 <sup>-4</sup> mm/mV	

### INSTRUMENTATION AND WIRING SCHEMATIC

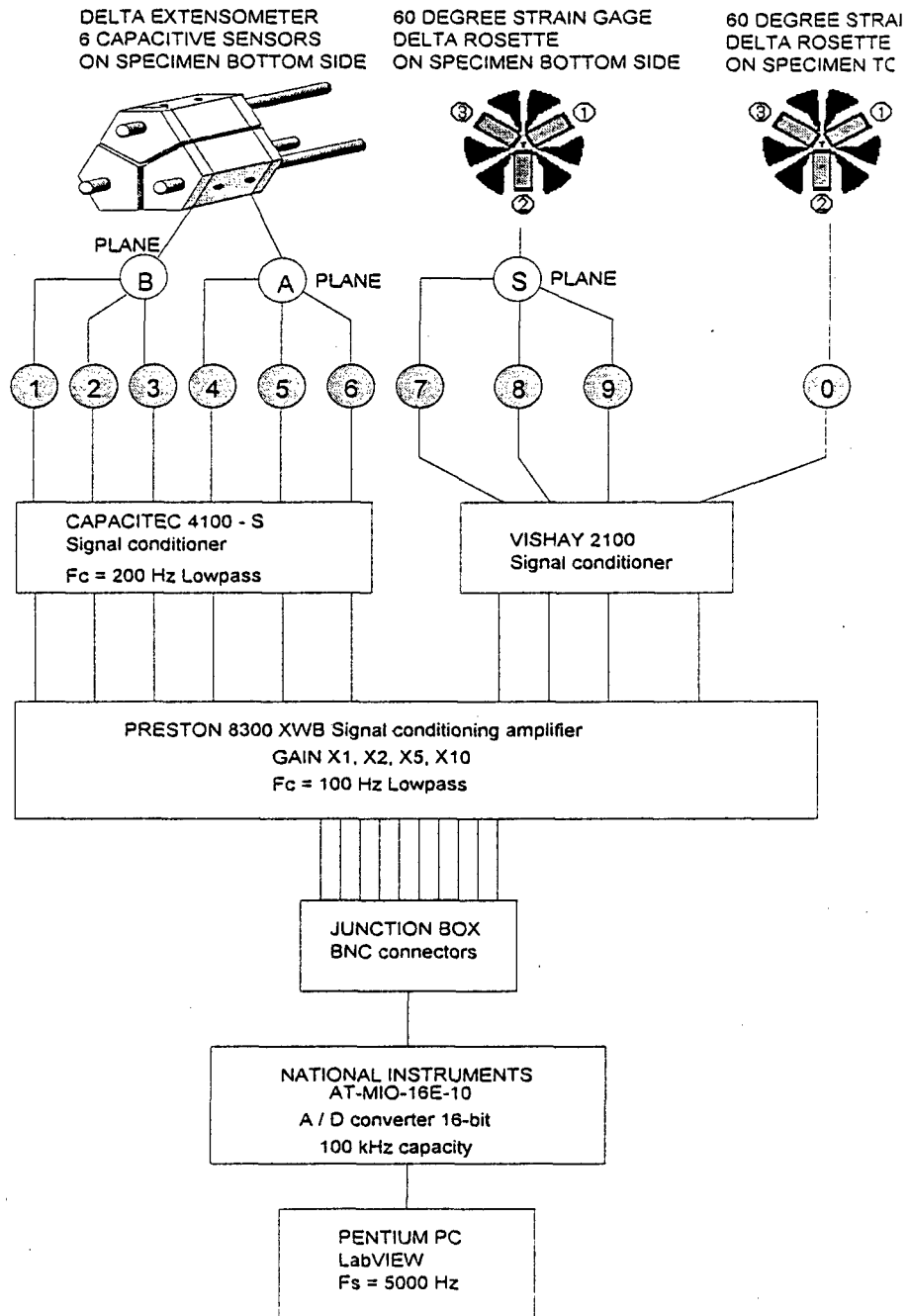


Figure 3.12. Schematic of data acquisition and wiring scheme for delta extensometer. A similar scheme was used for the axial extensometer, with a uniaxial strain gage used in place of the delta rosettes.



### 3.3 Experimental Procedure

#### *3.3.1 Strain Calculation Equation Development*

Strain in the specimen is calculated from measurements obtained from sensor pairs that lie outside of the plane of interest (e.g., the surface). The basic concept is that a line can be defined in two-dimensional space by two points. In this case, there are three lines, each corresponding to a pin. Each pair of lines is contained within a two dimensional coordinate system, and if we assume the pins displace symmetrically with respect to each other in the 2D system, can be analyzed for displacement from an imaginary X-axis which lies centrally located between them (Fig. 3.13). Three coordinate systems exist, each oriented from the other by 60 degrees. At the plane where each pair of pins intersects the surface of the specimen, three distances can be obtained through trigonometric relationships, which represent the change in distance between pin pairs ( $\Delta L$ ), which can be converted to engineering strain by dividing by gage length. Stated in other words, strain is calculated using the measured outputs from the two sensors lying at known points along each pair of pins, and geometry variables which are measured manually beforehand and entered into the data reduction program. The data reduction program calculates strain at any desired location, as measured from the outer sensor (SB). Based on strain-time histories in three directions, each 60 degrees apart, strain-transformation relationships are used to calculate principal strain magnitudes and their direction, and maximum shear strain in the specimen. The measured variables were:

- AB (measured length) = centerline distance between sensor pairs
- SB (measured length) = distance from measurement plane of interest (e.g., surface) and the centerline of the outboard sensor
- $y_{Bi}$  (obtained from sensor output) = outboard sensor output
- $y_{Ai}$  (obtained from sensor output) = inboard sensor output
- $y_{Si} = f(y_{Bi}, SB, \theta) = y$  location of pin where it intersects measurement plane
- $y_{S0} = f(GL) =$  half of the gage length
- GL = (measured length) = centerline distance between pins
- $\theta = f(y_{Bi}, y_{Ai}, AB) =$  half angle of any pair of pins

The procedure was:

- Measure lengths AB ( $= x_{B0} - x_{A0}$ ), SB ( $= x_{B0}$ ), and GL (gage length),  $y_{S0} = GL / 2$  (Fig. 3.13).
- Record zero (unstrained) sensor voltage outputs; convert to engineering units (mm)
  - gives initial pin position from x-axis at A and B;  $y_{A0}, y_{B0}$
- Deform specimen, record sensor outputs (for "i" number of samples); convert to engineering units
  - gives new pin position at A and B;  $y_{Ai}, y_{Bi}$ , assume  $x_{Ai} = x_{A0}, x_{Bi} = x_{B0}$
- Subtract zero readings to obtain change in air gaps;  $\Delta y_{Ai} = y_{Ai} - y_{A0}; \Delta y_{Bi} = y_{Bi} - y_{B0}$
- Define  $\theta = \sin^{-1} ((y_{Bi} - y_{Ai}) / AB)$  (eqn. 3.1)
- By similarity,  $y_{Bi} - y_{Si} = (SB)(\sin \theta)$
- Rearranging,  $y_{Si} = y_{Bi} - (SB)(\sin \theta)$  (eqn. 3.2)

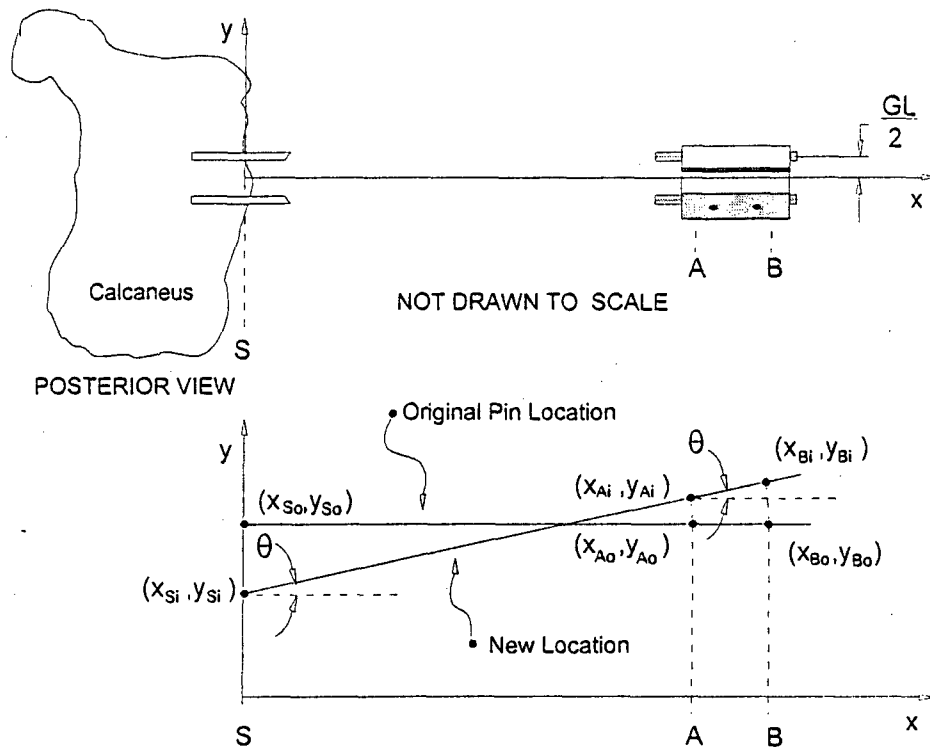


Figure 3.13. Schematic of extensometer (top) and coordinate system (bottom).

- $y_{Si} - y_{S0} = \Delta y_{Si}$  = change in pin location at surface (eqn. 3.3)

- Then, strain at surface is;  $\epsilon_S = (2 \Delta y_{Si}) / GL$  (eqn. 3.4)

- And,  $y_{S0} = GL / 2$  (eqn. 3.5)

- Substituting eqn. (3.3) into (3.4)

$$\epsilon_S = 2 (y_{Si} - y_{S0}) / GL \quad \text{(eqn. 3.6)}$$

- Substituting eqn. (3.5) into (3.6)

$$\varepsilon_S = \frac{2(y_{si} - \frac{GL}{2})}{GL} \quad (\text{eqn. 3.7})$$

- Substituting eqn. (3.2) into (3.7)

$$\varepsilon_S = \frac{2 \left[ (y_{Bi} - SB(\sin \theta) - \frac{GL}{2}) \right]}{GL} \quad (\text{eqn. 3.8})$$

- Substituting eqn. (3.1) into eqn. (3.8)

$$\varepsilon_S = \frac{2 \left[ y_{Bi} - SB \left( \frac{y_{Bi} - y_{Ai}}{AB} \right) - \frac{GL}{2} \right]}{GL}$$

- Simplifying,

$$\varepsilon_S = \frac{2y_{Bi}}{GL} - \frac{2(SB)y_{Bi}}{(AB)GL} + \frac{2(SB)y_{Ai}}{(AB)GL} - 1 \quad (\text{eqn. 3.9})$$

Which can be partially differentiated with respect to variables AB, SB,  $y_{Bi}$ ,  $y_{Ai}$ , and GL for the uncertainty analysis presented in Chapter 5, Experimental Uncertainty and Error.

### 3.3.2 Data Acquisition and Processing

The virtual instruments (VIs) in LabVIEW were used to collect, process, and display information related to the extensometer and the surface-mounted comparison strain gages. The overall goal of the programs was to perform data acquisition and analysis for 10 separate channels of data, and provide a user interface for data collection and storage.

For the delta extensometer, six of the channels were associated with the 6 capacitive

sensors used. Three channels were from the individual grid elements on a 3-element delta rosette strain gage, used as a comparison measurement to validate the device. One channel was left available for a single grid measurement from a strain gage mounted to the underside of the validation specimen. The VI hierarchy and purposes of each VI are:

1.) Setup: Input raw and processed filenames, define geometric parameters of system; gage length, distances SB, AB (Fig. 3.14), input gain settings, establish sampling rate, establish number of samples to average, input comments for data file.

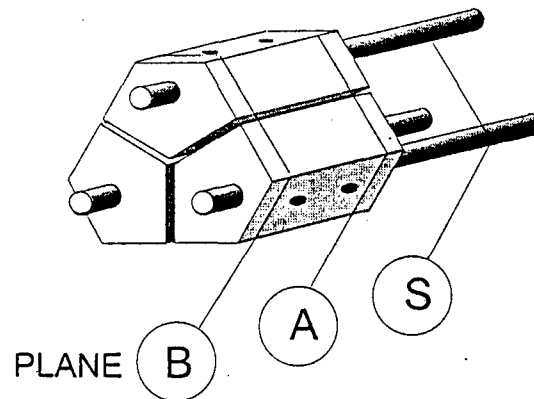


*Figure 3.14. Definition of planes used for calculations of strain with the delta extensometer.*

2.) Acquire Zero: Record initial displacements in unstrained specimen (baseline). Zero data are sampled and stored for later use as a baseline for subsequent strain measurements.

- Apply 2<sup>nd</sup> order polynomial calibration fits to convert voltage to displacement.

Calculate initial air gaps.

### 3.) Collect, Process, Display, and Save Data:

- Apply 2<sup>nd</sup> order polynomial calibration fits to convert voltage to displacement for capacitive sensors.
- Acquire “n” number of scans as specified by the user and save to a two dimensional array. Record measured values on strained specimen throughout sample period as change from baseline. Record from capacitive sensors and strain gages.
- Take an average of every “n” points as specified by the user and pass through as single point averages of every “n” data points for further processing. Pass through unaveraged measured values to raw data file.
- Calculate strain at extensometer planes A and B (obtain  $\epsilon_{1A}$ ,  $\epsilon_{2A}$ ,  $\epsilon_{3A}$ ;  $\epsilon_{1B}$ ,  $\epsilon_{2B}$ ,  $\epsilon_{3B}$ ).
- For each sensor pair (e.g., 1A and 1B, or sensor channel numbers 1 and 4) calculate  $\theta$  = half angle between pins associated with sensor pairs and their target, or angle between pin and the x-axis.
- Calculate three strains at new plane (S) using geometric parameters and  $\theta$ ; ( $\epsilon_{1A}$  and  $\epsilon_{1B}$  give  $\epsilon_1$ ;  $\epsilon_{2A}$  and  $\epsilon_{2B}$  give  $\epsilon_2$ ;  $\epsilon_{3A}$  and  $\epsilon_{3B}$  give  $\epsilon_3$ .)
- Apply Strain Transformation Relationships (Mohr’s circle for strain) using  $\epsilon_1$ ,  $\epsilon_2$ , and  $\epsilon_3$  for both extensometer and strain gage rosette.

Calculate principal strains and their direction from:

$$\varepsilon_{p,q} = \frac{\varepsilon_1 + \varepsilon_2 + \varepsilon_3}{3} \pm \frac{\sqrt{2}}{3} \sqrt{(\varepsilon_1 - \varepsilon_2)^2 + (\varepsilon_2 - \varepsilon_3)^2 + (\varepsilon_3 - \varepsilon_1)^2}$$

$$\theta = \frac{1}{2} \tan^{-1} \left[ \frac{\sqrt{3}(\varepsilon_3 - \varepsilon_2)}{2\varepsilon_1 - \varepsilon_2 - \varepsilon_3} \right]$$

Where:  $\theta$  is measured from the principal axis to the reference grid (grid 1). (Note this is a new symbol from the above  $\theta$  which defines angle pin makes with x-axis. This new symbol is kept for convention with the strain transformation relationships, but is not actually used, as it gets replaced with  $\phi$  for subsequent calculations.)

- Calculate maximum shear strain from:

$$\gamma_{\max} = \varepsilon_p - \varepsilon_q$$

- Check for several conditions in order to determine whether the angle  $\phi$  is to the principal maximum or minimum axis (P or Q). The principal strain angle,  $\phi$ , is measured **from** the reference grid on the strain gage rosette or the extensometer to the principal strain axis. The principal strain angle  $\phi$  is equal to  $-\theta$ .

The conditions checked are:

- (a) if  $\varepsilon_1 > (\varepsilon_2 + \varepsilon_3) / 2$ , then  $\phi_{P,Q} = \phi_P$
- (b) if  $\varepsilon_1 < (\varepsilon_2 + \varepsilon_3) / 2$ , then  $\phi_{P,Q} = \phi_Q$

- (c) if  $\epsilon_1 = (\epsilon_2 + \epsilon_3) / 2$ , and  $\epsilon_2 < \epsilon_1$ , then  $\phi_{P,Q} = \phi_P = -45$  degrees
- (d) if  $\epsilon_1 = (\epsilon_2 + \epsilon_3) / 2$ , and  $\epsilon_2 > \epsilon_1$ , then  $\phi_{P,Q} = \phi_P = +45$  degrees
- (e) if  $\epsilon_1 = \epsilon_2 = \epsilon_3$ , then  $\phi_{P,Q}$  is indeterminate (equal biaxial strain)

- Display data on front panel. Three waveform graphs display time history direct comparisons of extensometer and rosette grid strains (one graph for each grid). Display of principal strain magnitudes and their direction is also done with waveform graphs.
- Save processed data to file for subsequent processing with header information.
- Save raw voltage (pre-processed) data to separate file for subsequent processing if necessary.

### *3.3.3 Assumptions in Data Analysis*

The assumptions made in the data reduction algorithms for the capacitive extensometer designs are:

- 1.) The pins do not deform. They can move (translate and rotate) but remain rigid.
- 2.) When calculating strain at some plane within the specimen, the strain gradients along the pin axis are assumed to be linear.
- 3.) The displacement measured from the capacitive probe is a result of a change in plate separation (probe from target), not transverse motion.
- 4.) The strain transformation relationships used for a 60-degree rosette assume a planar state of strain.



5.) The material is assumed to be isotropic and homogeneous.

The first assumption, that the pins do not deform, is reasonable given that they are not restrained externally – a benefit of using non-contact sensors in the design. This assumption, along with assumption #2, is necessary to allow estimation of strain *within* the bone. Considering the absence of any external loading, it is not likely that the pins would deform within the body of the specimen. If there were some external loading on the pins, this assumption would not be valid. For example, experience with instrumented pedicle screws in the spine has shown that bending moments are present within the screw when the spine is loaded axially. Bending moments are at a maximum near the screw hub, and decrease non-linearly toward the screw tip (Yerby, *et. al.*, 1997). These bending moments would tend to cause the pedicle screw to deform. However, pedicle screws are designed to carry loads applied externally through a fixation rod, which is not the case here, where the ends of the pins making up the extensometer are allowed to move about freely, and no external loading is applied.

Strain gradients in the specimen are assumed to be linear. Gradients within the gage length of the device tend to be averaged, which is not different from the principle of operation of commercially available extensometers or strain gages. Strain gradients that may occur along the pin axis direction are assumed to be linear, since sensor pairs are used to calculate strain at a new plane not contained within the measurement planes.

Assumption #3 relates to sensitivity to transverse movement of the sensor relative to its target, which, as mentioned previously, is minimized by making the target diameter

oversized relative to the sensor. As such, only displacements perpendicular to the probe face are sensed. This design feature is analogous to a uniaxial strain gage measurement where transverse sensitivity of the gage is neglected. Assumptions #4 and 5 are simplifying assumptions.

#### *3.3.4 Four-Point Bending Test Procedure*

The experimental procedures for four-point bending tests of the axial and delta extensometers were very similar, although different specimen sizes and four-point bending jigs were used, due to differences in the size of the extensometers. For both extensometer designs, the test objectives were to perform static and dynamic tests in four-point bending, and compare the output of the extensometers to a "standard" measurement obtained from bonded resistance type strain gages mounted to the specimen surface. The setup checklist involved recording geometric constants of the system; gage length (GL) measured between pin centerlines, distance between probe centerlines (AB) and distance from outboard sensor centerline to specimen surface (SB). For the delta extensometer tests, three gage lengths and three AB distances were measured, one for each "grid" direction. Measurement of these geometric parameters was accomplished via an Olympus microscope with an X-Y stage. The geometric parameters were input manually into the data acquisition program, used by the program data reduction routines, and stored as part of the processed data file headers.

Next, with the specimen unloaded but placed within the four-point bending jig, the strain gage amplifier bridges were balanced and the gain was set to the appropriate value

corresponding to the gage factor of the strain gage grid elements (see Appendix B for the bridge balancing / gain adjust procedure). The signal gain on the amplifiers (8300 XWB, Preston Scientific, Anaheim, CA) was set to 10 initially to maximize signal in the A/D converter voltage range, and the lowpass filters were set to cutoff frequency of 100 Hz for the strain gage and extensometer channels. For the high strain ranges (approximately 3,000  $\mu\epsilon$  and above, the gain setting was decreased to 5).

Prior to loading the specimen, zero readings were recorded. The specimen was then loaded statically in increments up to a nominal strain range (approximately 1,000  $\mu\epsilon$ ) to check agreement between strain gage and extensometer outputs. These static evaluations were useful for checking proper function of the data acquisition and reduction program. An additional value was realized in discovering that the gage length as measured between pin centerlines provided better agreement between extensometer and strain gage signals than gage length as measured from pin outside surface to outside surface.

Between each loading trial (both for static and dynamic trials) the strain gage bridge was balanced. Prior to loading the specimen, the data acquisition program also captured zero readings from the extensometer, which were used later in the strain calculation algorithms.

Sinusoidal and square wave dynamic loading profiles were performed over a range of preloads and peak to peak loads (or displacements) at a range of frequencies covering 1, 5, 10, 15, 19, and 20 Hz. Several of the test conditions were repeated for later comparison.

Of interest was not the stress/strain characteristics of the acrylic specimen, deflections, or input loads (loads and deflections were not recorded for the delta extensometer four-point bending tests because of available channels), but rather the strain output (magnitudes, rates, and frequencies) measured by the strain gage as compared to the extensometer calculated strain. Summaries of all test conditions performed are presented in tabular form in Appendix A.

### **3.4 Supporting Experiments**

Three experiments were conducted in addition to the dynamic four-point bending tests to further evaluate extensometer performance; i.) experimental verification of principal strain angle,  $\phi$ ; ii.) dynamic characterization of axial extensometer; and iii.) probe angle sensitivity. These tests were separate from the four-point bending evaluations, but were necessary to augment the understanding of the performance characteristics of the extensometers.

#### ***3.4.1 Experimental Verification of Principal Strain Angle, $\phi$***

For the delta extensometer, an important and unique capability is measurement of  $\phi$ , principal strain angle. The four-point bending tests allowed a comparison to be made of strain magnitudes and rates in the test specimen, but  $\phi$  was kept constant at  $-22.5$  degrees. As such, this part of the data reduction algorithms was not able to be rigorously tested. To verify that the delta extensometer could be used to determine  $\phi$  properly prior to being used in a complex strain environment such as the calcaneus, an additional test specimen (Fig 3.15) was made which would allow the principal strain angle to be input at

varying, but known, directions. The test specimen was made of Renshape™, a manmade material that machines similar to wood but which has no grain, and allowed the delta extensometer to be exposed to three arbitrary bending directions.

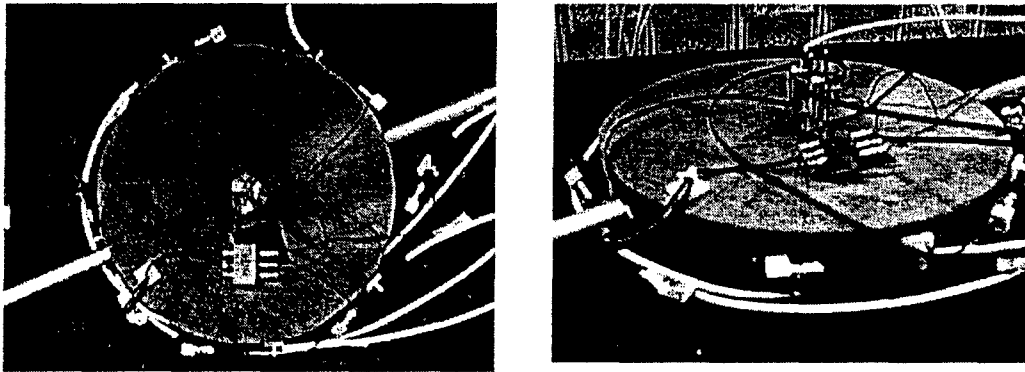


*Figure 3.15. Renshape™ specimen photographs. Test specimen was built to test proper data acquisition and reduction program calculation of principal strain angle,  $\phi$ .*

The Renshape™ specimen had three slots cut into the bottom surface at 50, 90 and 120 degrees (Fig. 3.16). To bend the specimen, three corresponding pockets offset at +/-90 degrees from each slot were drilled into the sides of the specimen such that rods could be inserted into opposing pockets and the specimen deformed along each of the specified angles as determined by the slots. The bending rods helped to increase the bending moment applied to the specimen such that the assembly could be deformed manually in tension or compression. The specimen also allowed a qualitative check of pin angle calculations (magnitude and sense).

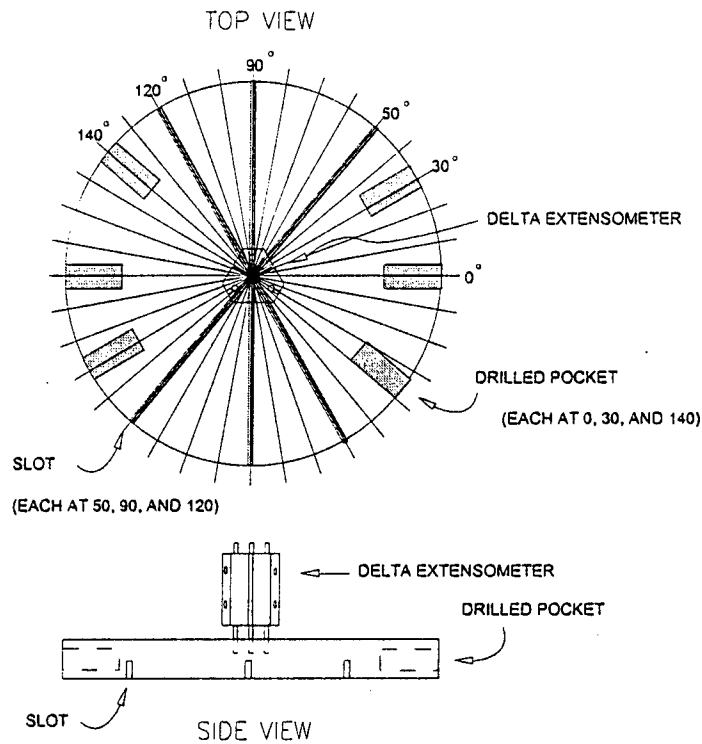


Figure 3.16. Schematic of Renshape™ specimen built to test proper data acquisition and reduction program calculation of principal strain angle,  $\phi$ .

### 3.4.2 Dynamic Characterization of Axial Extensometer

One of the obstacles to using an extensometer in a system that is not only undergoing deformation but is translating through space, as with the end of a moving limb, is that artifacts might be introduced into the strain measurement because the sensor itself has a certain mass. As such, the extensometer designs were kept as small and lightweight as possible. To make a fair comparison between the extensometers designed in this study and commercially available devices, such as the MTS extensometer described earlier and used in the cadaver foot studies, the dynamic performance of the capacitive extensometer

system was evaluated as described in ASTM E-83, 1996. A "single moving anvil" test was conducted (Fig. 3.17), which, as stated in the ASTM standard should be performed for new extensometer designs. In this test, the extensometer is mounted to a specimen, or single moving anvil, that has a frequency and amplitude input, but is not itself strained. The ideal outcome of this test is zero device output over the performance range of interest.

For this test, the acrylic specimen with axial extensometer was fitted with a stud at one end and mounted to the materials test machine actuator (Instron Corp., Canton, MA, with up to 500 Hz actuation capability), and frequency and amplitude input were varied over a range from 5 Hz up to 500 Hz and 0.076 mm displacement (actual) peak-to-peak. The displacement of 0.076 mm corresponds to approximately 6000  $\mu\epsilon$ , which would be a typical upper limit of strain measurement for the device. A frequency of 500 Hz was the upper limit of the materials test equipment. The specimen itself was not loaded. Signal conditioning amplifiers provided filtering with cutoff frequency ( $F_c = 3.5$  kHz). The sampling rate was increased to 10 kHz. In Figure 3.17, the extensometer was configured as the capacitive axial extensometer, and the single moving anvil was the acrylic specimen, fastened to the materials test machine actuator.

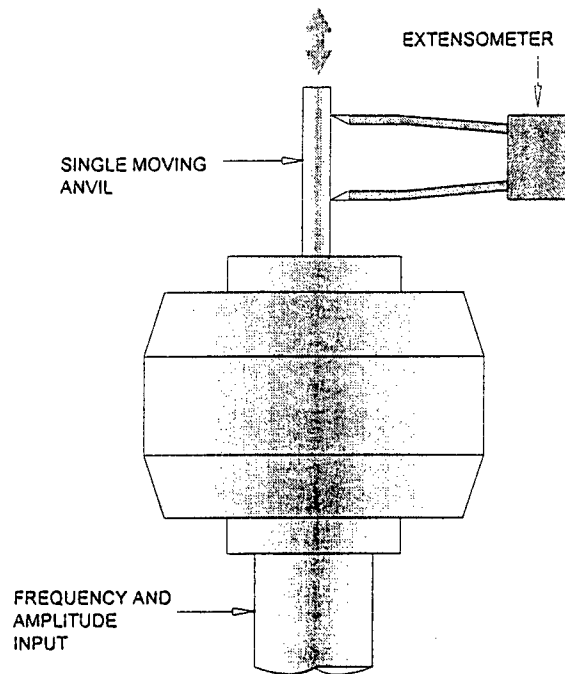


Figure 3.17. Extensometer on a single moving anvil. (Adapted from ASTM E-83).

### 3.4.3 Probe Angle Sensitivity

Because the operation of the capacitive extensometers in a bending specimen necessarily involves pins to become non-parallel, as would result in a bending specimen, an additional test was designed to determine if error was introduced into the strain measurement as a result of the plates of the capacitor becoming non parallel, and possibly reporting a false displacement. The probe angle sensitivity test was performed to quantify the effect of “pooling” of the electrostatic field within the dielectric volume between the plates of the capacitor that occurs when the probe and target become non-parallel. Pooling is a function of probe angle, and will effectively shift the measured centerline



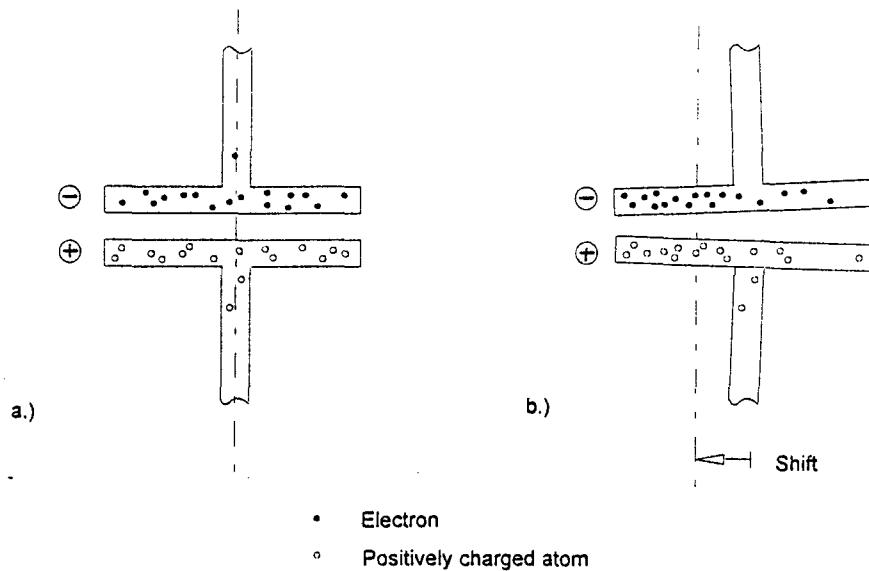


Figure 3.18. The separation of capacitive plates as measured at the probe centerline will shift as a result of "pooling" of the electrostatic field when plates of a capacitor that are (a.) initially parallel become (b.) non-parallel.

distance between sensor and target towards their closer edges (Fig. 3.18). It is important that *centerline* distance between probe and target is measured, as this distance is assumed in the strain calculations (distance AB). If the probe and target become non-parallel, the distance measured between them may be offset from the centerline, which would in turn affect the measured strain, possibly significantly. It can be shown that from the differential output from two probes mounted firmly to pins that do not themselves

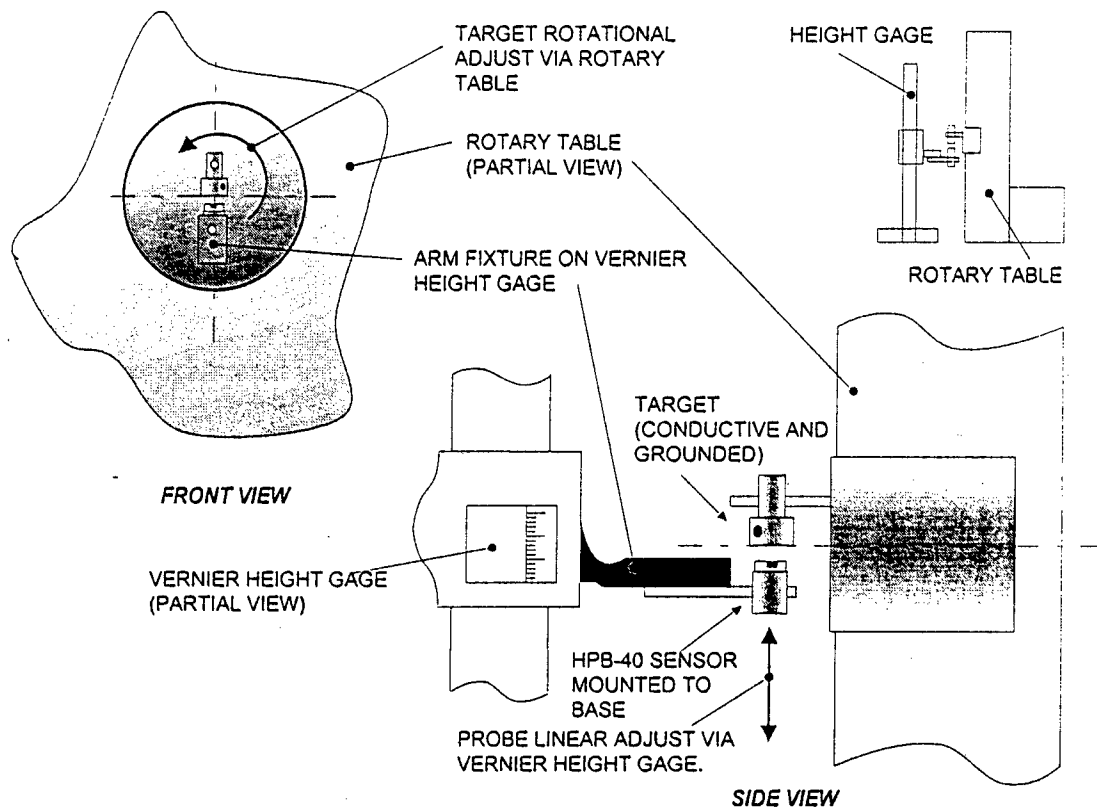


Figure 3.19. Probe angle sensitivity test configuration. The HPB-40 button probe shown in the sketch was used in the axial extensometer.

undergo deformation, that pin angle will always be known (this argument is developed in Section 6.4 of this thesis). It is assumed that the amount of offset is a function of angle only, that is, the offset due to pooling is not unique to each probe, which is a reasonable assumption.

To conduct the test, the target side of the extensometer was mounted to a rotary table with Vernier scale (Model U-9, Troyke Manufacturing, Cincinnati, OH), and the sensor side (HPB-40 sensor, Capacitec, Inc.) to a height gage with Vernier scale (Fig. 3.19). The rotary table was adapted with a machined plug, which accepted the pin, and allowed the target to mount in the exact center of rotation of the rotary table (Fig. 3.20).

The test was conducted in the inspection laboratory at NASA Glenn which is a temperature controlled environment and ideal for conducting such a test where data are recorded over a period of hours, such that thermal expansion of target or probe base will not affect the measurements. On a level surface, the air gap was set at a nominal distance with the height gage, and the target rotated incrementally through a series of angles, from  $-5$  to  $5$  degrees in  $0.33$ -degree increments. Since the plane of the target face was aligned with the center of rotation of the table, any output from the probe was due to probe angle only. Isolation of rotary motion from linear was a crucial aspect of the test, as measurements obtained from changes in probe linear displacement combined with changes in angle would not be able to be decomposed later. Steady-state probe output was measured on a precision voltmeter (34401A Hewlett-Packard, Loveland, CO). After an equipment warm up period of 2 hours, three trials were performed and voltmeter output recorded. Since the probe sensitivity is assumed to be a function of angle only, and not unique to each probe, the characteristic output was applied to both the axial and delta extensometer.

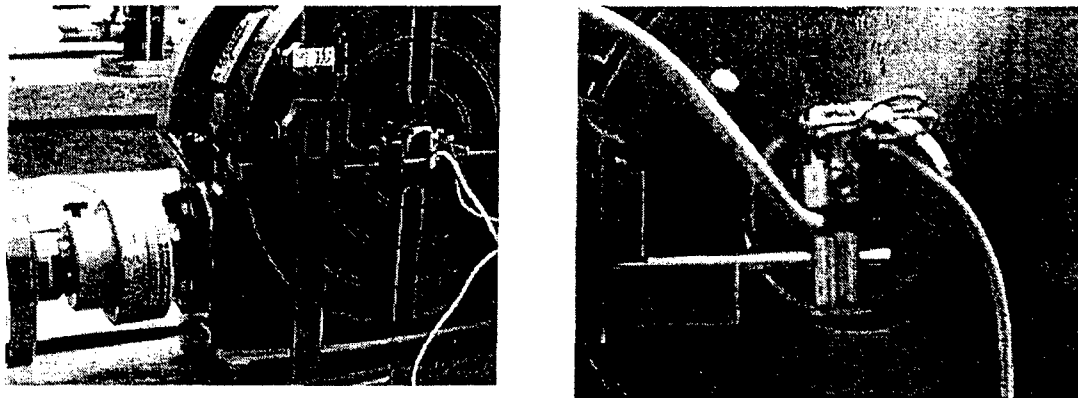


Figure 3.20. (a) Rotary table and Vernier height gage, (b) close-up of probe and target

### 3.5 *In Vivo* Strain Measurement with the Delta Extensometer

The author was given the opportunity to test the delta extensometer *in vivo* in a human subject, conditional upon the four-point bending tests and subsequent data processing proving the extensometer able to measure strain accurately at the surface of the acrylic specimen in four-point bending. The *in vivo* test was not an original objective of this study, however, and only selected data are presented here (see Chapter 4. Results, and Appendix A for additional data).

#### 3.5.1 *In Vivo* Test Procedure

For the *in vivo* test, one male subject (age = 39 yrs., height = 184 cm, weight = 82 kg) gave written informed consent to participate in the experimental protocol, which was approved by the Internal Review Board at the Cleveland Clinic Foundation. An orthopedic surgeon implanted three stainless steel intraosseus pins (K-wire, trochar tip,

and 1.57 mm diameter) approximately halfway through the lateral side of the left calcaneus under sterile conditions, local anesthesia, and prophylactic oral antibiotic therapy (Fig. 3.21). A custom drill and placement jig was used along with fluoroscopy to guide the placement of the pins to a centerline distance of 7.1 mm gage length.



*Figure 3.21. Orthopedic surgeon shown implanting stainless steel pin (K-wire) into lateral aspect of left calcaneus under local anesthesia and sterile conditions. Drilling jig is shown in surgeon's left hand.*

Two of the pins (forming the grid 1, or reference grid, direction) were aligned along the primary trajectory of the calcaneal trabeculae (Fig. 3.22). After implantation, the subject walked back to the laboratory where the acrylic bodies with capacitive sensors and target

surfaces were attached to the protruding ends of the pins. One pin required a slight bend to bring pins to parallel, and air gaps were set to nominal by use of copper shims between the pins and placed within the through holes in the acrylic bodies of the extensometer.

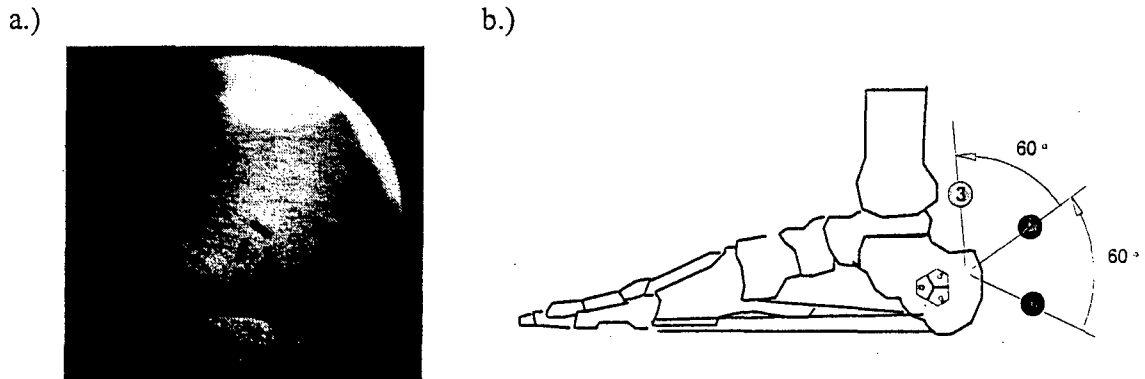


*Figure 3.22. Fluoroscopic image a.) of left calcaneus (lateral view) of subject with three intraosseous pins implanted. The two lower pins form the grid 1 direction (reference grid), which were aligned with the principal orientation of the trabeculae with the aid of a fluoroscope. Pins protrude toward the observer (out of the page). The three grid directions are defined in b.), with grid 1 oriented at 25 degrees from horizontal with subject standing quietly with weight on both feet.*

EMG electrodes were placed on the gastrocnemius and anterior tibialis. Force plate data, which provided a measure of the vertical force component beneath the treadmill belt,

were also collected. Figure 3.23 shows the instrumentation and channel configuration.

Video recordings at 30 frames per second were made of the activities for later use.

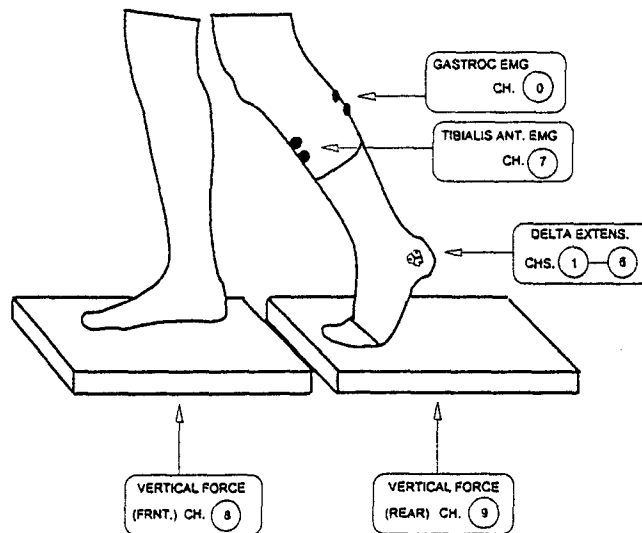


*Figure 3.23. Instrumentation and channel configuration for the in vivo study. The force plates were mounted underneath the treadmill belt.*

After the lead connectors were attached to the subject and strain relief provided with athletic tape, the subject was asked to load the left foot by standing and performing various movements, while raw voltage signals from the extensometer were continuously monitored. The voltages recorded were large enough in magnitude to require a reduction in the gain settings on the amplifiers to a gain of one (1). The "zero" position was defined as the foot suspended in a neutral position with the subject sitting quietly. Data for the

zero position were captured prior to data collection for each trial (Fig. 3.24). After zero readings were recorded, the subject performed non-weightbearing and weightbearing activities, including quiet standing, standing up on toes, walking at 5 km/hr on a treadmill, bouncing on one foot, jumping, and running at 11 km/hr on a treadmill.

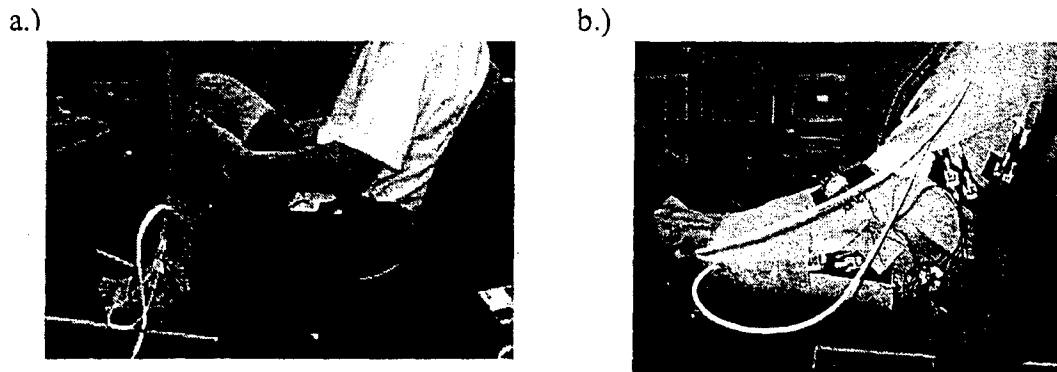


*Figure 3.24. a.) Subject demonstrates the "zero" position with foot unloaded. Subject held leg up with hands underneath left knee to support the weight of the leg, and b.) close-up view of same.*

### **3.6 Summary**

This chapter described the experiments that were devised to test the unique capabilities and limitations of two new extensometer designs. Dynamic four-point bending tests, with bonded metal foil strain gages mounted to the test specimens as comparisons, were chosen as the best evaluation of the extensometers capabilities to measure physiological levels and rates of strain. Consideration was given for the modulus of bone, the physiological strain environment associated with osteogenesis, and the type of loading that bone experiences (i.e., bending) prior to the conducting the experiments. The data



collection and analysis routines required for conversion of probe output to meaningful strain time histories were summarized in this chapter. Consideration was also given to the unique characteristics of the extensometers which might affect measurement accuracy; principal strain angle determination, how the extensometer responds to high frequency perturbations, and the sensitivity of the capacitive probes to angle between probe face and target. Finally, after confidence was gained with the extensometer system operation, the delta extensometer was used to collect *in vivo* strain data; a first-ever attempt at measuring principal strain magnitude and direction in the complex strain environment of the human calcaneus.

## CHAPTER 4

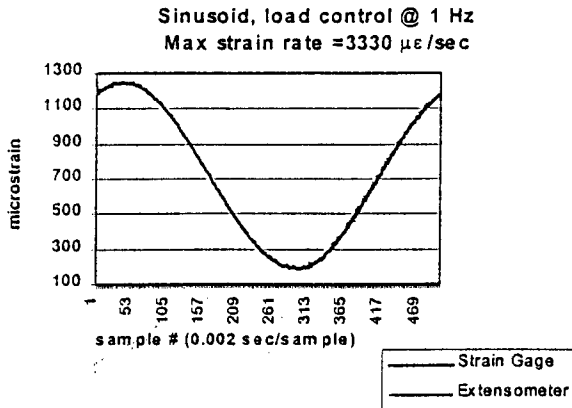
### RESULTS

#### 4.1 Four-Point Bending Test with the Axial Extensometer

Comparisons were made between the axial extensometer calculated strain and measured strain obtained from an axial strain gage bonded to the surface of the four-point bend specimen. The axial extensometer calculated strain at the surface tracked strain gage response to sinusoidal and square wave inputs up to 20 Hz and a maximum strain rate of 90,900  $\mu\epsilon$ /sec in four-point bending with mean differences between strain gage and extensometer output ranging to -15.3  $\mu\epsilon$ , corresponding to a 2.6 % mean error for that condition which was a 20 Hz sinusoid, with input strain range from 294 to 585  $\mu\epsilon$ . Pearson's correlation coefficient ( $r$ ) ranged between 0.966 (for a 20 Hz sinusoidal condition) to 0.999 (for a 1 Hz sinusoidal condition). Figure 4.1 shows a representative time history for the 1 Hz loading condition. A summary of the correlation coefficient as a function of loading frequency is presented in Figure 4.2. Maximum absolute strains ranged up to 1,500  $\mu\epsilon$ . The compiled test data and statistical summary are presented in their entirety in Appendix A.

The effective resolution of the extensometer (as determined at the specimen surface) was improved by about 50% by oversampling the signal and averaging. The sampling frequency was 5,000 Hz, and averages of every 10 points were taken and plotted as single points.

a.)



b.)

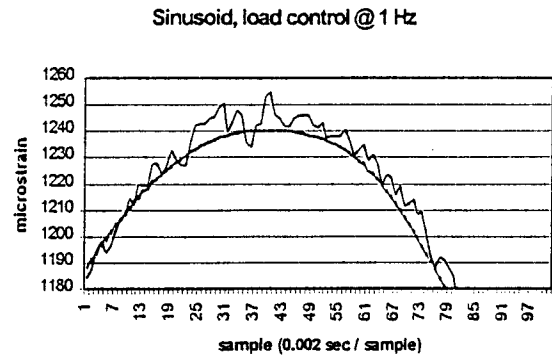


Figure 4.1. a.) Example sinusoidal strain time history shows comparison between measured strain gage output and calculated extensometer output in four-point bending. Sinusoidal load input at 1 Hz, sample time is 1 second; and b.) first 100 samples of same.

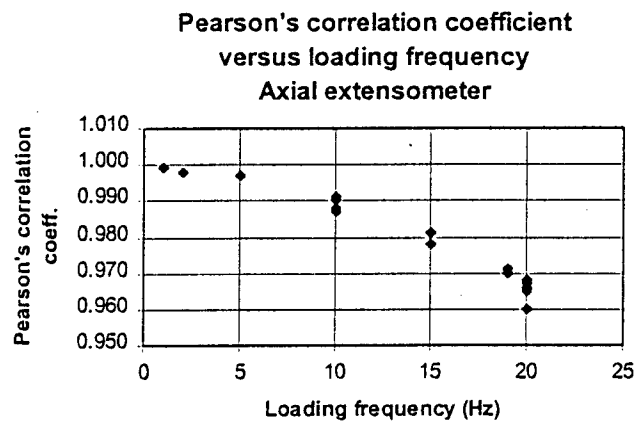


Figure 4.2. Pearson's correlation coefficient ( $r$ ) decreases as loading frequency input to the acrylic specimen increases, but remains above 0.96 for the entire test regime performed. Plotted for the axial extensometer.

One of the characteristics of testing with an acrylic specimen was the tendency for the specimen to not return to a state of zero strain for several minutes after being unloaded – a viscoelastic phenomenon. As a result, the strain gage bridge was balanced between trials. This was not done for the extensometer signal conditioner (offset adjust), as the extensometer initial output with no load was captured in the data acquisition program prior to each trial.

#### **4.2 Four-Point Bending Test with the Delta Extensometer**

For the delta extensometer, the calculated strain at the surface of the acrylic validation specimen tracked strain gage response to sinusoidal and square wave inputs up to 20 Hz and a maximum strain rate of 50,000  $\mu\epsilon/\text{sec}$  in four-point bending with the maximum mean percent error between extensometer and strain gage output ranging up to 15.1 % (measured as a % of maximum strain for that trial, not as a % of full scale), or 434  $\mu\epsilon$  out of 2,868  $\mu\epsilon$ . This error was experienced by grid 3 during a sinusoidal loading input, with strain for that grid ranging from 1,165 to 2,868  $\mu\epsilon$ . The correlation coefficient ( $r$ ) ranged between 0.711 (for a 20 Hz sinusoidal condition) to 0.9996 (for a 1 Hz sinusoidal condition.) Square wave loading inputs produced correlation coefficients ranging from 0.990 to 0.999. Figure 4.3 summarizes the range of correlation coefficients as a function of loading frequency. The statistical summary is presented in its entirety in tabular form in Appendix A.

The mean and maximum errors (in  $\mu\epsilon$ ) encountered between any grid on the strain gage rosette and the delta extensometer were tabulated and plotted in Figure 4.4.

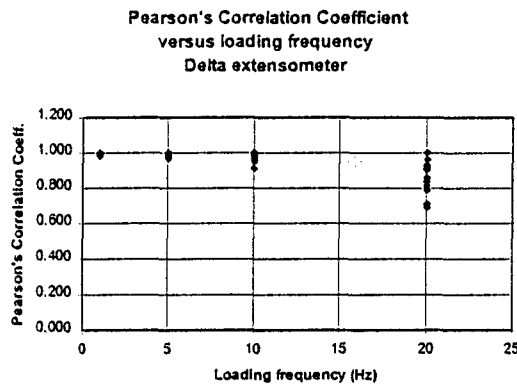
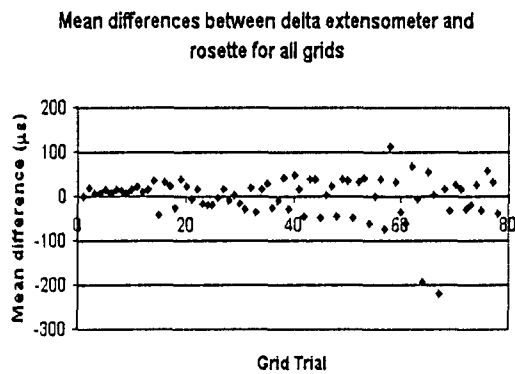


Figure 4.3. Pearson's correlation coefficient ( $r$ ) versus loading frequency input to the acrylic specimen. Plotted for all grid directions for the delta extensometer.

a.)



b.)

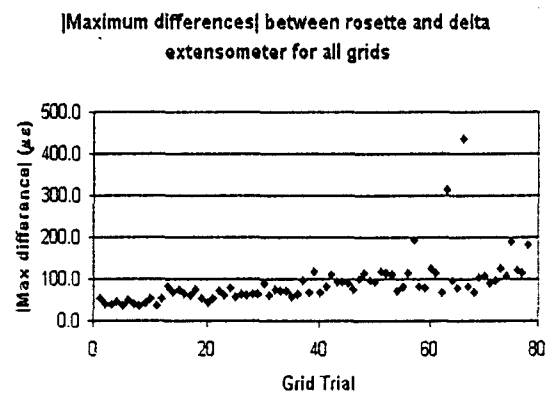


Figure 4.4. a.) Mean differences between rosette and delta extensometer during all trials of dynamic four-point bending tests, and b.) absolute values of maximum differences for same.

Of note is the fact that, if these errors are considered as a percentage of the full-scale (F.S.) range of the extensometer (+/- 71,000  $\mu\epsilon$ ), an error range of 112.0 - (-220.1) = 332.1  $\mu\epsilon$  (see Table 4.1) is approximately 0.002% F.S. error. A statistical summary for the output of each grid direction for all of the loading trials is presented in Appendix A. The range of statistical values are summarized and presented in Table 4.1.

*Table 4.1. Summary of statistical results from the delta extensometer four-point bending tests showing maximum and minimum values for the statistical variables considered.*

	Mean Diff. ( $\mu\epsilon$ )	Mean % Error (% max strain)	Pearson's $r$	Max Diff. ( $\mu\epsilon$ )	Max % Error (% max strain)	Std. Dev.
Max	112.0	11.6	1.0	434.2	19.5	95.8
Min	-220.1	-7.7	0.7	34.2	-14.5	9.6

### 4.3 Supporting Experiments Results

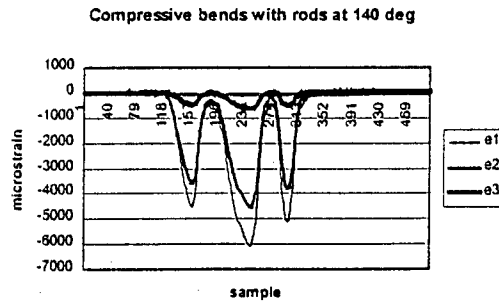
#### 4.3.1 Experimental Verification of Principal Strain Angle, $\phi$

The Renshape™ specimen provided valuable information regarding the calculation of the principal strain angle,  $\phi$ , and its relationship to the physical specimen and bending directions. With this specimen, the bending directions were known and could be

compared to the calculated output. Since there are several conditions checked for determining whether  $\phi$  is measured to the principal maximum ( $\phi_P$ ) or minimum ( $\phi_Q$ ) strain axis, this test allowed confidence to be gained in the data reduction program routines.

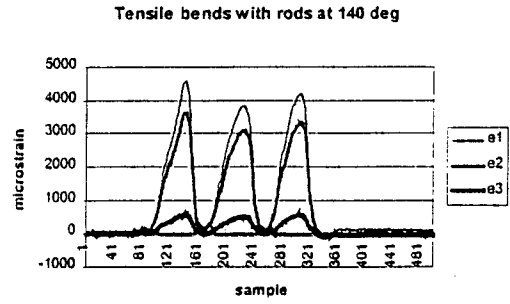
For a 50-degree bend orientation (bending rods placed in the 140-degree pockets, refer to Figure 3.16), for example, Figure 4.5 shows the results where the specimen was deformed in compression three times during the data collection period (Fig. 4.5a), then in tension (Fig. 4.5b). The reference grid direction (grid 1) was approximately aligned with the 120 degree axis, and the  $\phi$  calculation indicated  $\phi_Q$  was + 22 degrees (measured from grid 1 to the principal axis), which is a 2 degree variation from the expected value, due to the delta extensometer not being perfectly aligned. This value of +22 degrees could be readily verified from the physical specimen configuration. Likewise, during tensile bends, the  $\phi_P$  was calculated to be + 24 degrees, again agreeing with the physical setup. Of note is that the principal axis changes from min ( $\phi_Q$ ) to max ( $\phi_P$ ) when the sense of bend (tensile or compressive) changes, even though bend direction (a function of the position of rods in the specimen) has remained the same. This exercise was repeated for all three bending directions for which the specimen was designed.

a.)



e1	-6089.25
e2	-4588.07
e3	-641.657
ep	-523.925
eq	-7022.06
phi(p)	-68
phi(q)	22.26436

b.)



e1	1903.918
e2	1541.657
e3	241.5664
ep	2238.435
eq	219.6599
phi(p)	24.02065

Figure 4.5. Representative time histories for manual deformation of Renshape™ specimen, and associated calculations of principal strains and their direction for a single sample obtained from delta extensometer output.

#### 4.3.2 Dynamic Characterization of Axial Extensometer

The frequency response test yielded zero extensometer output within the resolution of the sensors over the range of frequency and amplitude inputs, up to 500 Hz, demonstrating its ability to measure strains at high frequencies without introducing experimental artifact.

Caution must be taken in interpreting these results, however, as this is valid for a specimen undergoing displacements on the order of the deformation expected in a loaded specimen. If the specimen is not fixed in a loading apparatus, artifact may be introduced



due to the inertial properties of the extensometer. This should be a concern when measuring especially “jerky” motions, as in jumping. This frequency response characterization is aimed more at making a fair comparison between the capacitive extensometers described and commercially available extensometers, which generally weigh more and are useable over a lower range of frequencies. For example, an MTS model 632.13E-20 which weighs 27 grams (compared to 8 grams for the axial extensometer) and has a maximum operating frequency of 40 Hz, which is possible only at small displacements (MTS Systems Corporation Product Manual, 1994).

#### *4.3.3 Probe Angle Sensitivity Test*

The probe angle sensitivity test was performed with a button probe to quantify the amount of error that could be encountered in determining displacement when the probe and target become non-parallel. Data were fit with a second order polynomial fit, yielding a general equation in the form  $y = f(x)$  in the shape of a parabola, shifted from the origin by some amount  $(x,y)$ . The equation  $dy/dx = 0$  was found to solve for the amount of  $x$  shift, then solved for  $y$ , to bring the point of zero slope back to the origin. This step was necessary because the probe and target were not initially parallel, due to slight variations in the thickness of cyanoacrylate adhesive underneath the probe. Problems were not encountered however, because the range of angles from +/- 5 degrees was able to be evaluated by including angles slightly beyond this range in the test procedure. After performing this shift in the parabola, the following relationship (Fig. 4.6) between probe output and angle was obtained ( $R^2 = 0.9971$ );

$$output = -0.0022(angle)^2 + (0.00006)(angle) \quad (4.1)$$

where:

*output* = probe voltage output (VDC) due to pooling error

*angle* = angle measured between probe face and target face (degrees)

The actual probe half angles measured during the dynamic 4-point bending tests ranged up to 0.1 degree. Substituting 2 times the half angle, or 0.2 into equation (1), the output becomes -0.032 mV and yields a maximum pooling error of  $-3.2 \times 10^{-6}$  mm, corresponding to  $0.26 \mu\epsilon$  over a 12.7 mm gage length (axial extensometer), or  $0.45 \mu\epsilon$  over a 7.1 mm gage length (delta extensometer). An error of this magnitude is well within the resolution of the device (by two orders of magnitude), and considered negligible.

During the *in vivo* study, a maximum pin half angle of 0.65 degree was measured (in the grid 1 direction, during running), which yields a pooling error of  $25.4 \mu\epsilon$ . This error is still within the resolution of the sensors ( $\pm 14.3 \mu\epsilon$ , or  $28.6 \mu\epsilon$ ). The relationship expressed in equation (4.1) could be used to make corrections in strain calculations if probe angle were to become large.

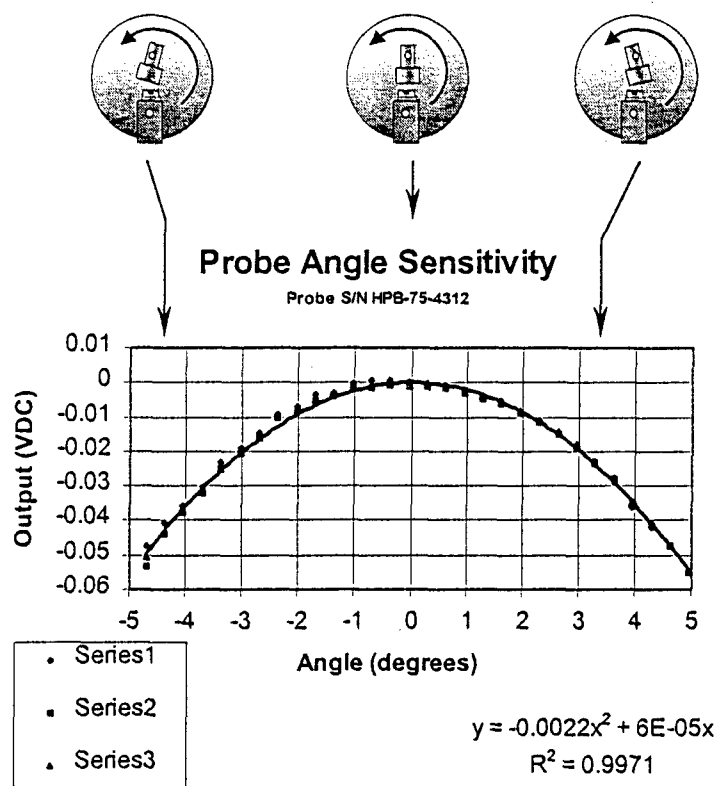


Figure 4.6. Probe angle sensitivity test results. Probe output in VDC is plotted versus angle between probe and target. Three series, or test trials are shown, and curve fit with a polynomial.

#### 4.4 In Vivo Test Results

The *in vivo* data collected with the delta extensometer provided unique insights into the strain environment in the calcaneus during weightbearing activities. In addition to the strain data from the extensometer, providing three “grid” directions of strain measurements at the bone surface, EMG data from the tibialis anterior and gastrocnemius

muscles were recorded, as well as vertical force data. Videotape at 30 frames per second from selected trials was digitized for later comparison with the recorded data time histories. The purpose of the video was to provide a qualitative record of the movement throughout the activities performed. A LED was programmed to illuminate during the data acquisition so as to be able to provide a time marker in the video, however the LED malfunctioned after approximately the first quarter of the trials were collected.

#### *4.4.1 In Vivo Geometry*

What became immediately apparent during set up of the instrumentation prior to data collection was that the DC voltage signal recorded from the extensometer was very strong, and voltages were much higher than those recorded in either of the four-point bending tests. The gain on the signal conditioners was set back to 1 (gain for four-point bending tests had been at 10 and 5 for the high strain conditions, up to 5,000  $\mu\epsilon$ ). There could be two reasons for this: a.) the deformation in the calcaneus during weightbearing was greater than the deformations encountered in the acrylic specimens; and b.) the geometry of the system (i.e., the distance from outboard sensor centerline to bone surface, SB) was different, which was indeed the case. During data collection, a "best guess" distance SB was used in the data acquisition program, as this information was obtained later from examination of the fluoroscopic images captured in the operating room. One fluoroscopic image was used to determine the distance from outboard sensor centerlines to bone surface, SB. This image is reproduced in Figure 4.7.

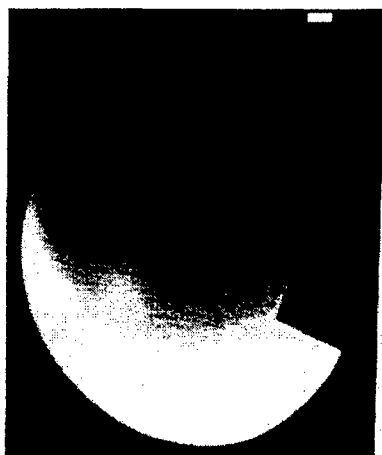


*Figure 4.7. Fluoroscopic image of calcaneus (posterior view) used to determine distance from the outside of the foot to the surface of the bone. The intraosseous pins and drilling jig are visible to the right of the image.*

To establish an image scale, landmarks of known size were needed in the image. The drilling jig would have been an ideal landmark because of its relatively large size, but the image unfortunately did not include an entire side of the jig to use for scale, nor was there assurance that the jig would be square with the image plane, thus eliminating parallax. Therefore, the pins were selected as landmarks, and more specifically, their diameter.

The pin diameter as measured on the image was 1.9 mm, and in actuality the pins measure 1.57 mm in diameter. This scaling ratio from fluoroscopic image to actual size,  $1.9 / 1.57 = 1.21$ , or 121 %, was used to determine the length of the pin inserted into the

calcaneus, which was 9.9 mm. The distance from skin surface to pin ends was measured with hand held calipers placed next to the extensometer while it was mounted in the subject's calcaneus (the average value was determined to be 33.9 mm). The pin lengths were measured with hand held calipers after removal from the subject (average pin length = 60.2 mm). Table 4.2 presents the measured values for the delta extensometer geometric parameters.

*Table 4.2. Measured values (mm) relating to system geometry for delta extensometer in human subject. Hand held calipers used to obtain measurements.*

Description	Pin# 1	2	3	Average
Pin lengths, from exposed tip to skin surface	33.9	33.6	34.2	33.9
Distance from exposed tip to top of acrylic	13.8	13.4	13.8	13.7
Actual pin length (after removal)	61.0	60.2	59.4	60.2
* Distance between probe centerlines (AB)	16.3	16.3	15.9	N/A

\* Measured prior to experiment with Olympus microscope with x-y stage.

From the measured values obtained from the fluoroscopic image and hand held calipers on the subject, the value for SB was determined to be 35.8 mm (Fig. 4.8). A value of 27.9 was used in the data acquisition and reduction program during data collection. The data reduction program provided presentations of strain time histories during data collection,

however, in general, the strain magnitudes displayed were larger than expected. After post-processing the data with new values for SB, the strain magnitudes were still larger than expected (up to 50,000  $\mu\epsilon$  for one running trial), and the strain magnitudes are therefore not presented here. More discussion regarding the results and sources of error for the *in vivo* experiment can be found in Chapter 5, Discussion. Figure 4.9 shows a model of the extensometer in a calcaneus in the approximate configuration as was used in the *in vivo* study.

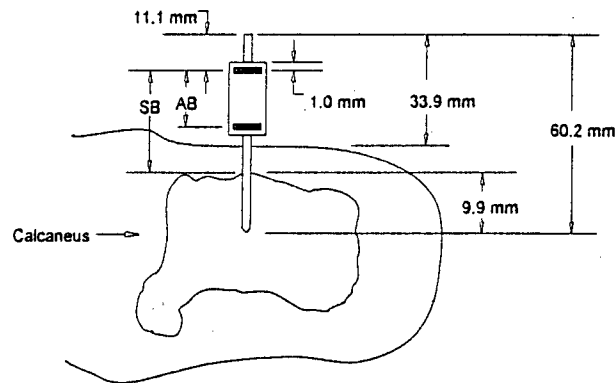


Figure 4.8. Schematic of values measured on human subject. Calcaneus is shown in posterior view, with subject lying on side. One acrylic body with a sensor pair, separated by distance AB is shown on one pin. Values shown are the average of the 3 assemblies that make up the delta extensometer system.

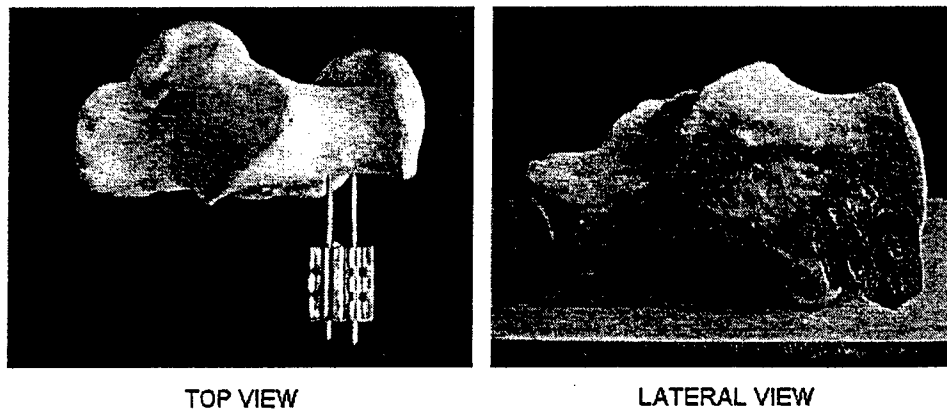


Figure 4.9. A model of the calcaneus with a model of the delta extensometer, mounted in the approximate position as was done for the *in vivo* study.

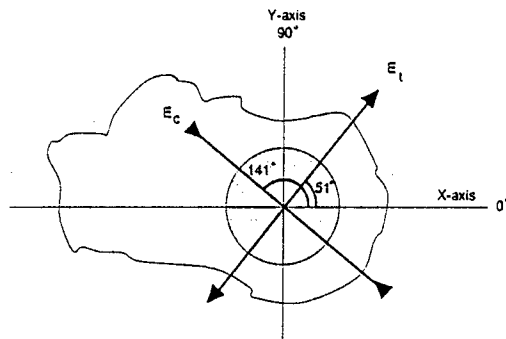
#### 4.4.2 *In Vivo* Principal Strain for Standing and Walking in a Human

If the absolute strain magnitudes in the *in vivo* data were suspect, the relative contributions of strain measured in the three grid directions can still be considered valid. The value of  $\phi$ , principal strain angle, does not depend on absolute magnitudes of strain values  $\epsilon_1$ ,  $\epsilon_2$ , and  $\epsilon_3$ , (which are directly correlated with the distances SB, and GL) but rather their relative values, making the parameter  $\phi$  a reportable value. From the *in vivo* data, two trials were selected for processing and determination of  $\phi$ ; standing quietly with weight on both feet, because of the relative simplicity of the loading, and walking on a treadmill at 5 km/hr, because of the fact that a weight bearing phase exists that might be compared with the standing trial. For standing with weight on both feet, principal compressive strain angle,  $\phi_0$ , at the surface of the lateral aspect of the calcaneus was



measured as  $141.6 \pm 0.8$  degrees (n of trials = 1, duration = 1 second) from the horizontal or X-axis (Fig. 4.12a).

a.)



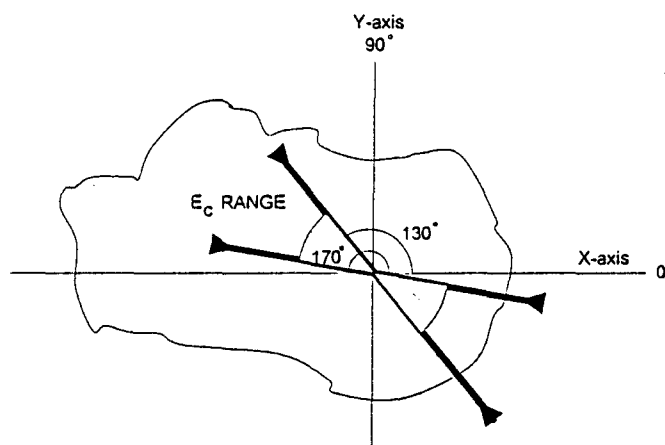
b.)



Figure 4.10. a.) Schematic drawing of the left calcaneus (lateral view) of human subject showing the definition of principal compressive ( $E_c$ ) and tensile ( $E_t$ ) strain angles (bold arrows) for subject standing quietly with weight on both feet. Radiographic image b.) of a human calcaneus showing the orientation of trabeculae in sagittal view.

In Figure 4.10 a.), the X-axis is defined as parallel with the floor when the subject was standing quietly with weight on both feet. The principal strain angle,  $\phi_Q$ , determines the orientation of the  $E_c$  (principal compressive) axis ( $141.6 \pm 0.8$  degrees) and the  $E_t$  (principal tensile) axis is orthogonal with  $E_c$ . This diagram was modeled after Biewener, et. al., (1996).

For the human subject instrumented with the delta extensometer, walking at 5 km/hr on a treadmill produced a range of principal compressive strain angles (n of trials = 1, duration = 3 seconds) from 130 to 170 degrees from the X-axis (Figure 4.11). The stance phase of this gait cycle produced a range of angles from 142 to 149 degrees. Pin angles during walking for the grid 1 pair ranged from 0 to + 0.01 degree, indicating that a tensile bend along this direction occurred during loading. The grid 1 pair was oriented in the calcaneus at 155 degrees from the positive X-axis.



*Figure 4.11. The stance and swing phases of walking on a treadmill at 5 km/hr produced a range of principal compressive strain angles from 130 to 170 degrees.*

Figure 4.12 presents the principal maximum and minimum strain magnitude data during walking on a treadmill at 5 km/hr on a time history plot of the vertical force for a comparison of “loading” (stance) and “unloading” (swing) phases of gait.

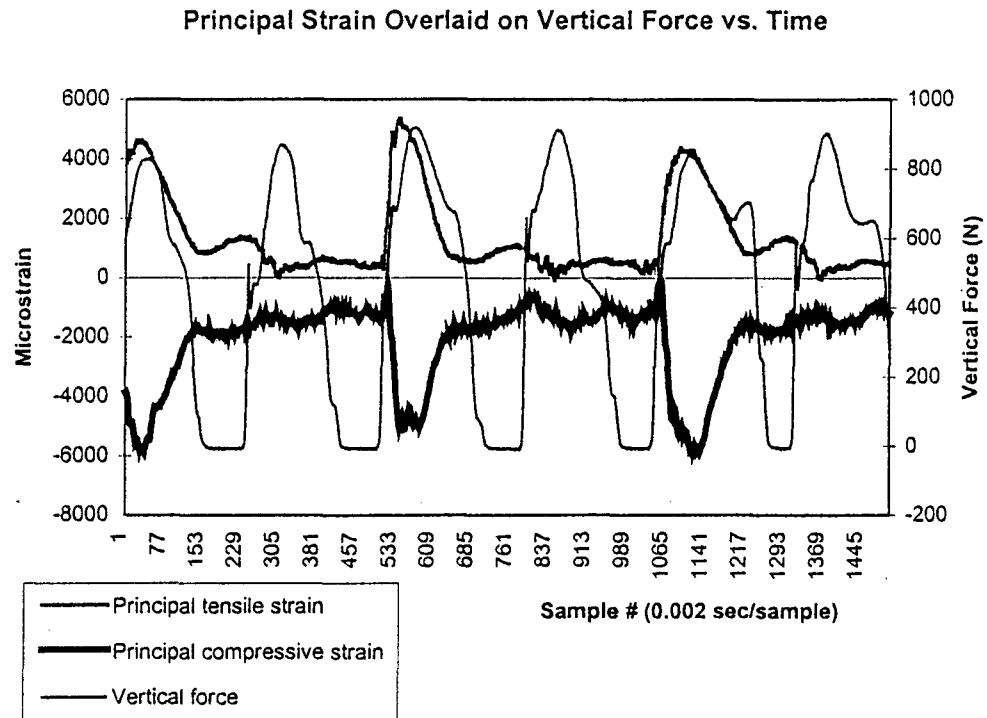


*Figure 4.12. In vivo principal strain magnitude in the calcaneus of a human walking on a treadmill at 5 km/hr overlaid on vertical force. Trial duration is 3 seconds. Note that only the left foot is instrumented with the delta extensometer, and as such the principal strain pattern follows every other peak in vertical force. Vertical force was captured for both left and right foot.*

From the principal strain angle and relative magnitude time histories obtained with the delta extensometer in the human subject *in vivo*, a composite drawing of stance phase of

gait during walking, presented with still images from the video (every third frame is shown, spaced at 0.1 second intervals), was produced and is presented in Figure 4.13.

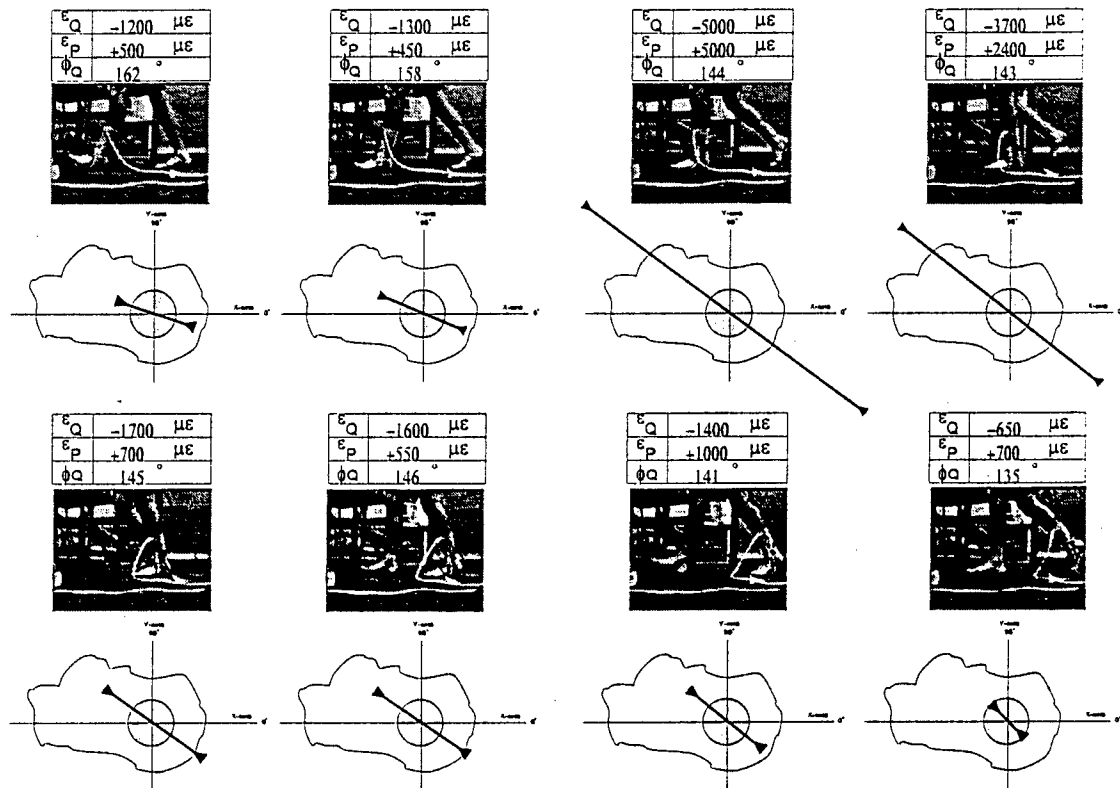
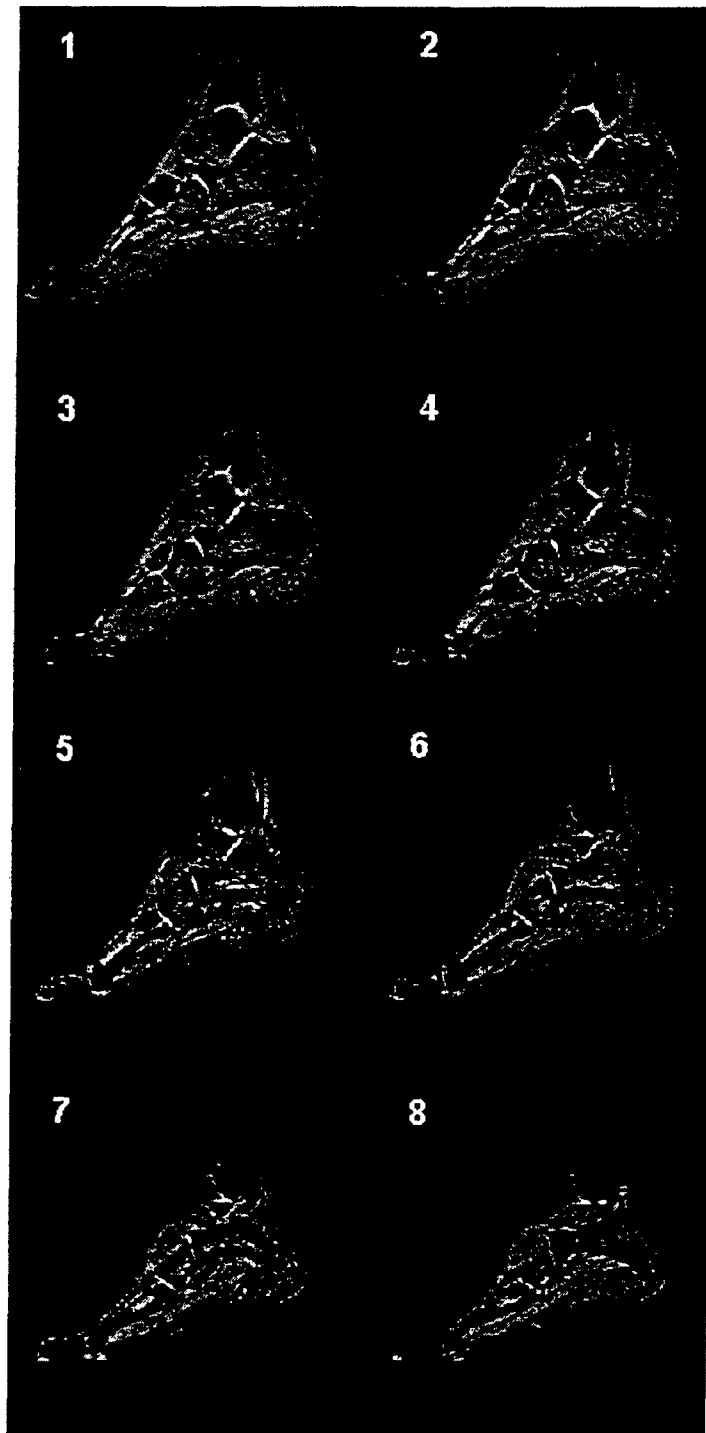


Figure 4.13. Principal strain magnitude and direction as it changes throughout the stance phase of gait. Video frames are taken at every 0.1 second during walking at 5 km/hr on a treadmill.

In Figure 4.13, the principal compressive strain axis is shown as a vector consisting of both magnitude and angle information obtained from the *in vivo* data. The principal compressive strain vector is overlaid on a drawing of the calcaneus in side view (obtained from a generic anatomy text, not an image of the subject), with the minimum strain magnitude during this period, at toe off which occurs in the last frame, defining the diameter of a circle upon which the data in the rest of the frames are referenced for a relative comparison of magnitude. The principal compressive and tensile strain magnitude and principal angle ( $\phi_0$ ) for each frame in the sequence is presented above the video still images.

Approximately four months after the *in vivo* study, a series of MRI images were taken of the subjects left foot, reproduced in Figure 4.14. The individual images represent sagittal cuts through the foot at 2 mm intervals. The areas where intraosseus pins were implanted for the study are still clearly visible, especially in frames 3, 4, and 5. One of the reasons for obtaining MRI images was to have a direct comparison of pin orientation with trabecular orientation in the subject. However, as can be seen in Figure 4.14, the trabeculae are not readily discernable in the image because the relative size of the trabeculae are on the order of the resolution of the image (1 mm).



*Figure 4.14 Sagittal MRI views of subject taken at approximately four months post-test. Each image separated by 2 mm; moving laterally from images 1 through 8 (image 1 is most medial).*

#### 4.5 Summary

This chapter presented results for validation tests performed with the extensometer designs mounted in acrylic specimens in four-point bending, supporting experiments results, and results from an *in vivo* study whereby strain was measured in a human calcaneus. The dynamic four-point bending tests compared the extensometer outputs to bonded strain gages for a direct validation of the extensometers' measurement accuracy. Pearson's correlation coefficient was used as a measure of how well the data compared, along with the maximum and mean differences between the two strain measurement techniques. The supporting experiments augmented the validation tests in terms of providing data useful for practical use of the extensometers, and for gaining confidence in the data reduction routines necessary for calculating principal strain angle. Finally, selected results from the *in vivo* study performed in a human calcaneus were presented, with emphasis placed on data from standing quietly with weight on both feet, and walking on a treadmill.

## CHAPTER 5

### EXPERIMENTAL UNCERTAINTY AND ERROR

#### 5.1 Overview

An uncertainty analysis was performed to establish the level of uncertainty in the strain calculations made with the extensometers as a function of the individual uncertainties of the measured parameters that are used in the extensometer strain calculation equation.

The uncertainty analysis did not include uncertainties in all signal conditioning equipment, digitizing errors in the data acquisition equipment, or errors associated with particular simplifying assumptions. An advantage of performing the uncertainty analysis is that the relative sensitivity of the strain calculation to individual uncertainties could be explored. Experimental error is discussed primarily in terms of the *in vivo* data, as these data were unique and were not able to be compared directly with strain gage output as was possible with the dynamic four-point bending tests.

#### 5.2 Uncertainty Analysis

In general, if a set of measurements has been made and these measurements are then used to calculate some desired result of the experiments, the uncertainty in the calculated result can be estimated on the basis of the uncertainties in the primary measurements. The result

$R$  is a given function of the independent variables  $x_1, x_2, x_3, \dots, x_n$ . Then,

$$R = R(x_1, x_2, x_3, \dots, x_n)$$



Equation (5.1) was derived as this R or "result" for calculation of surface strain in

Chapter 3: Methods (eqn. 3.9):

$$R = \epsilon_S = \frac{2y_{Bi}}{GL} - \frac{2(SB)y_{Bi}}{(AB)GL} + \frac{2(SB)y_{Ai}}{(AB)GL} - 1 \quad (\text{eqn. 5.1})$$

Let  $w_R$  be the uncertainty in the result and  $w_1, w_2, \dots, w_n$  be the uncertainties in the independent variables. If the uncertainties in the independent variables are all given with the same odds, as is assumed here, then the uncertainty in the result is (Holman, 1976) :

$$w_R = \left[ \left( \frac{\partial R}{\partial x_1} w_1 \right)^2 + \left( \frac{\partial R}{\partial x_2} w_2 \right)^2 + \dots + \left( \frac{\partial R}{\partial x_n} w_n \right)^2 \right]^{1/2} \quad (\text{eqn. 5.2})$$

Finding the partial differentials of equation (5.1), we see that;

$$\frac{\partial R}{\partial AB} = \frac{2(SB)}{(AB)^2 GL} (y_{Bi} - y_{Ai}) \quad (\text{eqn. 5.3})$$

$$\frac{\partial R}{\partial SB} = \frac{2}{(AB) GL} (y_{Ai} - y_{Bi}) \quad (\text{eqn. 5.4})$$

$$\frac{\partial R}{\partial y_{Bi}} = \frac{2}{GL} \left[ 1 - \frac{(SB)}{(AB)} \right] \quad (\text{eqn. 5.5})$$

$$\frac{\partial R}{\partial y_{Ai}} = \frac{2(SB)}{(AB)GL} \quad (\text{eqn. 5.6})$$

$$\frac{\partial R}{\partial GL} = -\frac{2y_{Bi}}{(GL)^2} + \frac{2(SB)y_{Bi}}{AB(GL)^2} - \frac{2(SB)y_{Ai}}{AB(GL)^2} \quad (\text{eqn. 5.7})$$

A spreadsheet was written to calculate uncertainty in the strain calculation. The program accepts input for the individual geometric constants (AB, SB, and GL), measured geometric values ( $y_{Ai}$ ,  $y_{Bi}$ ), and their associated uncertainties (Fig. 5.1).

**UNCERTAINTY ANALYSIS**

Strain equation for paired capacitors:

$$es = R = \frac{2y_{Bi}}{GL} - \frac{2SB y_{Bi}}{(AB)GL} + \frac{2SB y_{Ai}}{(AB)GL} - 1$$

**Uncertainty Analysis Parameters**

Geometric Constants			Uncertainties in measured values			Partial Derivatives	
Name	inch		Name	mm	inch	Name	(is really)
AB		0.643	wAB	0.1	0.003937	RAB	0.03628 dR/dAB
SB		0.7	wSB	1	0.03937	RSB	-0.033326 dR/dSB
ybi		0.028	wybi	0.000203	0.000008	Rybi	-0.633193 dR/dybi
yai		0.025	wyai	0.000203	0.000008	Ryai	7.77605 dR/dyai
GL		0.28	wGL	0.15	0.005906	RGL	-0.714286 dR/dGL

Uncertainty in strain calculation:

wR	9.76958E-06
strain	3.48914E-05
$\mu\epsilon =$	34.89

← uncertainty

Use either Axial or Delta Extensometer Constants in the "Geometric Constants" field

Axial Extensometer Constants			Delta Extensometer Constants		
Name	in		Name	in	
AB		0.3269	AB		0.643
SB		0.505	SB		0.7
ybi		0.028	ybi		0.028
yai		0.025	yai		0.025
GL		0.5	GL		0.28

Figure 5.1. Spreadsheet used to determine uncertainty in strain calculation and sensitivity of uncertainty to individual measured variables.

The spreadsheet allowed for computation of the overall uncertainty in the calculated strain, as well as quantification of how sensitive the computation was to errors in particular measurements. With typical geometric values and associated uncertainties, the uncertainty in the strain calculation for the delta extensometer configuration was approximately 35  $\mu\epsilon$ .

### *5.2.1 Determination of Uncertainties in Individual Measured Variables*

In the example above (Fig. 5.1), the geometric constants are entered for the delta extensometer as it would be mounted in the acrylic specimen. The uncertainty in measured values is derived (estimated) from the device or method used in making the various measurements of geometric constants. The first measured uncertainty  $w_{AB}$ , or distance between sensors, is given as 0.1 mm. This measurement is made with a microscope with X-Y stage, which is calibrated by using hand held calipers. During the calibration process of the X-Y stage, each measurement as viewed through the eyepiece crosshairs must fall within a tolerance of  $\pm 0.01$  mm from the actual distance given by the caliper. An uncertainty of the caliper calibration and user error in aligning the crosshairs with the feature of interest on the part, are combined to give an estimated uncertainty for this measurement of 0.1 mm, which is an order of magnitude greater than the value to which the X-Y stage is calibrated, and is a conservative estimate.

The second measured uncertainty,  $w_{SB}$ , or distance from the outboard sensor to the surface, is determined to be 1 mm. This measurement was also able to be made by using the microscope with X-Y stage for the validation tests, because the specimen was small

and could be manipulated under the microscope. However, because the specimen is not always small, and in the case of the *in vivo* study can only be determined by the use of MRI, fluoroscope, or other imaging technique, a larger uncertainty was assigned to this particular measured variable. One millimeter is a typical resolution (pixel size) for a MRI image.

The measured uncertainties associated with  $w_{y_{A_i}}$  and  $w_{y_{B_i}}$  are determined directly from the capacitor signal conditioning equipment. The resolution of the signal conditioners is  $\pm 1$  mV, which corresponds to a 0.0002032 mm error band ( $\pm 0.0001016$  mm). This resolution is presented as  $\pm 0.01\%$  of full scale in the signal conditioning equipment specifications from the manufacturer (Capacitec, Inc., Ayer, MA), and converted to distance by using the engineering unit conversion for the linear calibration for the particular sensors used in this experiment.

The uncertainty in gage length, or  $w_{GL}$ , is given in the above example as 0.15 mm. This is a conservative estimate for measurement with hand held calipers, given that there are no bends placed in the intraosseus pins prior to assembly of the sensor bodies onto the pins. In the case of the *in vivo* study, this uncertainty was determined to be more on the order of 3 mm, as determined by inspection of the intraosseus pins upon removal from the calcaneus.

### 5.2.2 Sensitivity of Overall Uncertainty Calculation to Measured Variables

The overall uncertainty will change when the uncertainties of individual measured variables change, with varying degrees of sensitivity. For example, the overall uncertainty is not very sensitive to changes in uncertainty of measured distance SB giving only approximately 90  $\mu\epsilon$  uncertainty for a 5 mm measurement error in SB, the distance from outboard sensor to the surface plane. However, the uncertainty calculation is very sensitive to gage length (GL), giving uncertainties on the order of 12,500  $\mu\epsilon$  for a 3 mm error in gage length measurement (Fig. 5.2).

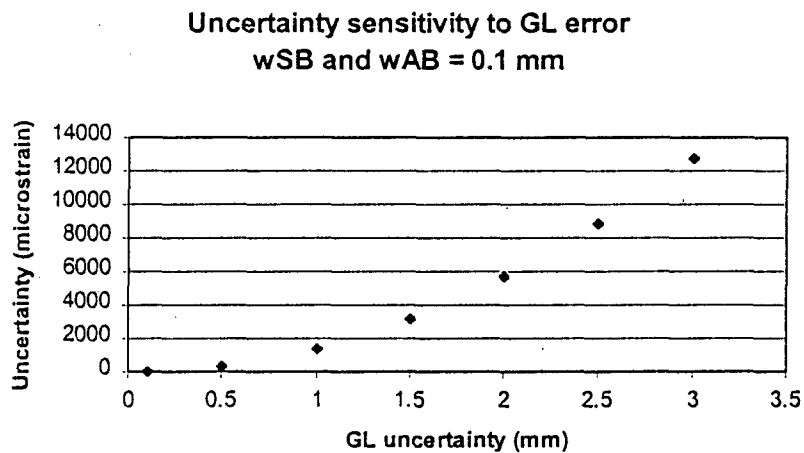


*Figure 5.2. Uncertainty in gage length affects the calculated microstrain ( $\mu\epsilon$ ) more dramatically than other parameters.*

This is useful information when considering how much effort should be placed on accurate determination of the different measured variables used in the calculation of

strain, and in weighing the costs associated with using various measuring devices versus the desired uncertainty in the calculations.

### 5.3 Effective Resolution of Extensometers

The probes (or sensors) used in the extensometer designs have a resolution associated with them which is a function of the amplifier resolution and the full scale voltage corresponding to the linear range over which they are calibrated. The amplifiers used (4100-S, and 4100-SL, Capacitec, Inc.) specify a resolution of  $\pm 0.001$  V ( $0.002$  V "step size", number of steps = 5,000), and full-scale range is 10 V. The linear range used was 1.016 mm, and the sensors, therefore, boast a resolution of  $R = \text{linear range} / \text{\#steps in amplifier} = 1.016 \text{ mm} / 5,000 = 0.0002032 \text{ mm}$  error band, or  $\pm 1 \times 10^{-4}$  mm. Over a gage length of 12.7 mm, the smallest strain the sensor can resolve is  $\pm 8 \mu\epsilon$  (for the axial extensometer, that is,  $0.0001 \text{ mm} / 12.7 \text{ mm}$ ). The best resolution the delta extensometer can have is  $\pm 13.6 \mu\epsilon$  with gage length of 7.37 mm. When we consider that two sensors are used to calculate strain at a third location, the resolution at that third location is less than that associated with a single sensor. This "effective resolution" or  $R_{\text{eff}}$ , is a function of the sensor resolution, sensor size, how far apart the sensors are placed, and how far the third location is from the sensors. Because the effective resolution is the "bottom line" for these extensometers, and effective resolution is dependent upon several factors which are under the control of the designer, a quantitative relationship was determined from which effective resolution can be calculated from these various design factors.

In general;

$R$  = the sensor resolution or "error band". See Figure 5.3.

$A$  and  $B$  = inboard and outboard sensor centerline location, respectively, as measured from the specimen surface

$SB$  = distance from outboard sensor centerline to surface

$AB$  = distance between sensor centerlines

$D$  = diameter of sensors (or, in the case of a rectangular sensor, width as measured along pin axis).

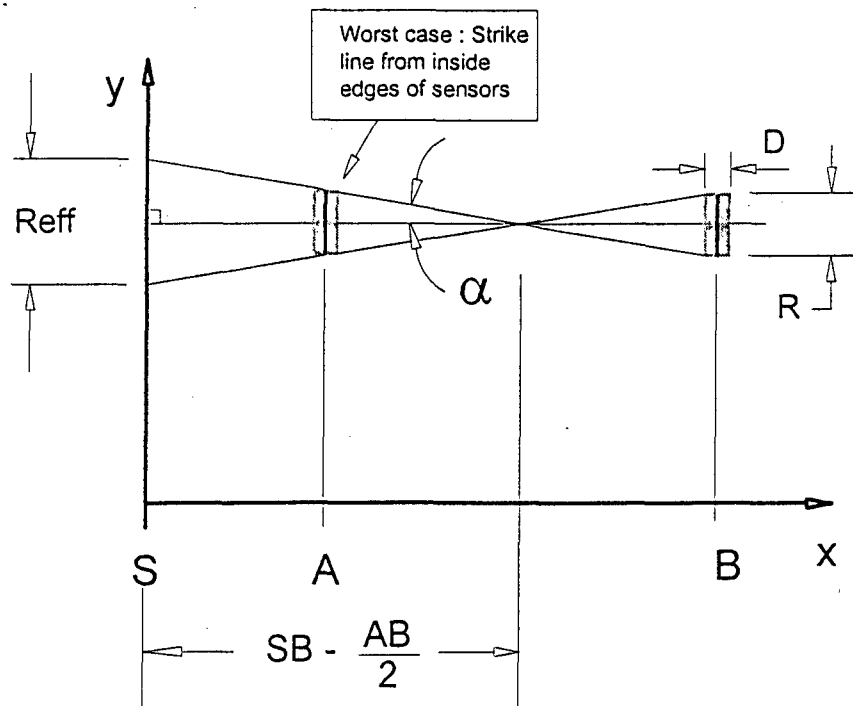


Figure 5.3. Coordinate system used for calculating effective resolution ( $R_{eff}$ ), which is affected by sensor spacing, resolution, and size.

From the diagram in Figure 5.3, we see that;

$$\alpha = \tan^{-1} \left[ \frac{R}{(AB - D)} \right] \quad \text{eqn. (5.8)}$$

$$R_{\text{eff}} = 2 \left[ SB - \frac{(AB - D)}{2} (\tan \alpha) \right] \quad \text{eqn. (5.9)}$$

$$\text{Effective strain resolution} = \frac{R_{\text{eff}}}{GL} \quad \text{eqn. (5.10)}$$

For the axial extensometer,

Resolution of amplifier is +/- 0.001 V (0.002 V "step size"), and full-scale range is 10 V.

This gives  $10/0.002 = 5,000$  steps,

$R = \text{linear range} / \# \text{steps in amplifier} = 1.016 \text{ mm} / 5,000 = 0.0002032 \text{ mm error band}$

$SB = 12.95 \text{ mm}$ ,  $AB = 8.30 \text{ mm}$ ,  $D = 1.91 \text{ mm}$

$\alpha = \tan^{-1}(0.000232/(8.30-1.91)) = 0.00208 \text{ degree}$

Entering these values into equation 5.9:

$R_{\text{eff}} = 2[(12.95 - ((8.30 - 1.91)/2))(\tan 0.00208)] = 0.0007079 \text{ mm}$

This  $R_{\text{eff}}$  over a gage length of 12.7 mm (eqn. 5.10);

Gives effective strain resolution  $R_{\text{eff}} = .0000557$  or +/- 28  $\mu\epsilon$  (axial extensometer)



For the delta extensometer (in acrylic specimen), the  $R_{eff}$  is  $\pm 22 \mu\epsilon$

For the delta extensometer in the *in vivo* study, the  $R_{eff}$  is  $\pm 60 \mu\epsilon$ .

The results of the effective resolution analysis for the axial and delta extensometers as they were configured in this study are summarized in Table 5.1. The parameter SB, or distance from outboard sensor to specimen surface, is readily altered in different measurement applications. Other parameters, i.e., distance between sensors (AB) and gage length (GL) can be altered only through redesign of the devices.

*Table 5.1 Summary of effective resolutions,  $R_{eff}$ , for the axial and delta extensometers.*

Device	Axial (in acrylic)	Delta (in acrylic)	Delta ( <i>in vivo</i> )
$R_{eff}$	$\pm 28 \mu\epsilon$	$\pm 22 \mu\epsilon$	$\pm 60 \mu\epsilon$

#### **5.4 Sources of Error in the *In Vivo* Study**

The data collected *in vivo* with the delta extensometer provided a unique insight into the strain in the human calcaneus during various weight bearing activities. Other than the data obtained with the prototype capacitive extensometer designed by the author, no data exist for strain in the calcaneus of a human *in vivo*, and, having no data to compare to in the literature other than for tibial strains, the data were considered to be “one shot”

measurements, which, until more data are available against which to compare, must stand alone. However, data from the literature regarding tibial strain magnitudes encountered *in vivo* (see section 2.6 in Chapter 2: Background) as well as bone yield data, can be of use in making comparisons.

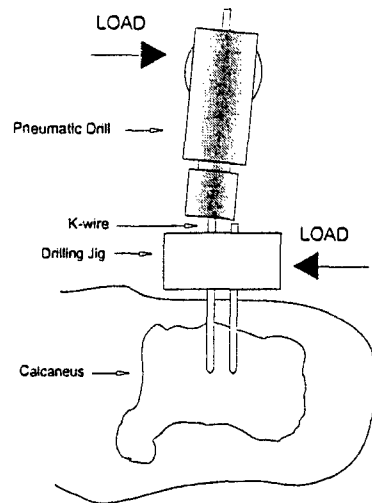
The data reduction algorithms require that the geometric parameters of the system be known. Since the sensors are assembled to the acrylic bodies beforehand, the distance between sensors, AB is readily obtained by use of hand held calipers or microscope with an X- Y stage, for example, which was the method used here. However, the other two sets of measured parameters, gage length (GL) and distance from outboard sensor to specimen plane of interest, which was taken as the surface of the calcaneus (SB), are determined only as part of the field installation during assembly of the acrylic body onto the intraosseus pins, and are not as straightforward. It was shown that strain calculations are extremely sensitive to changes in gage length. For example, if the uncertainties for distance SB and distance AB are both 0.1 mm, which is reasonable in a laboratory situation, the calculated strain uncertainty can exceed 12,000  $\mu\epsilon$  when gage length is over or underestimated by 3 mm.

The gage lengths (GL) were not measured during the experiment, and were each assumed to be 7.1 mm based on the drilling jig geometry. It was necessary to bend one of the pins (pin #3) slightly to allow for the nominal air gaps to be obtained, and copper shims were used as planned to bring the air gaps to very close to 0.5 mm, or midway through the sensor linear range. The shims changed the gage length slightly, and were not accounted for in the constants used in the data acquisition and reduction program. The bend placed

in one pin was necessary to establish the air gap within the linear range of the sensors and allow them to function. The pins became out of parallel most likely as a result of small unavoidable side loads placed on the pin during installation, either by the pneumatic drill used in surgery, or by the drilling jig itself, as it is held in place against the installed pin(s) as the next pin is installed. The orthopedic surgeon was consulted regarding this tendency, which was first discovered during the cadaver tests with the prototype extensometer, and had practiced the installation process with various jigs previously. The handle originally welded to the drilling jig used in the *in vivo* axial extensometer tests, provided for convenience during the surgical procedure, was purposely left off the new design for this reason, so that significant torque could not be developed as the jig was held in place, and spring loads in the pins would be minimized. However, this design change did not adequately address the side and rotational loads imposed on the pins during installation (Fig. 5.4a). Additionally, the surface of the foot under the drilling jig is relatively soft and uneven, and the jig will tend to shift and rotate on this surface, as it is only held in place by hand.

The jig design might be modified to help restrict this side loading, and also to prevent it from rocking against the relatively soft and uneven surface of the subject's limb such that it is not hand held, but perhaps mounted in a device similar to a drill press which holds the foot, drilling jig, and drill in place during pin installation to ensure pins are indeed parallel.

a.)



b.)

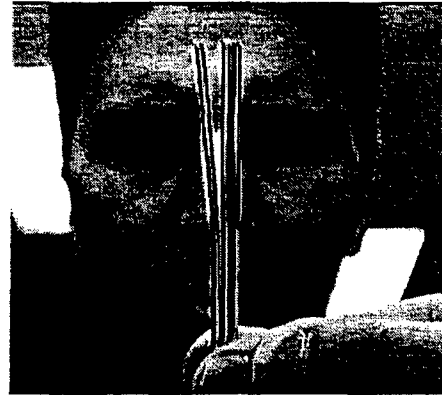


Figure 5.4. a.) Unavoidable side loads during installation of the intraosseous pins with drilling jig and/or drilling jig rocking against the relatively soft surface of the foot may have contributed to pins becoming non-parallel. b.) Author holds intraosseous pins after removal from subject; pin #3 was bent approximately 3 mm to bring the pins back to parallel to obtain a nominal air gap between probe and target.

Another source of error for the *in vivo* study was that the distance SB, measured from outboard sensor centerline to the specimen surface, was not obtainable *in vivo* without the use of some form of imaging technology, such as MRI or fluoroscope. The fluoroscopic image used to determine the SB distance for the *in vivo* study was difficult to measure directly from, and a ratio between pin diameter in the image and actual pin diameter was the only landmark that could be used to establish an image scale. From this image scale, the distance from bone surface to skin was determined, and this value was added to the

distance measured between skin and outboard sensor with hand held calipers after the extensometer was attached to the subject. These methods were developed for the most part during the test, and in future studies, might be improved upon. One possible method would be to obtain an MRI image of the assembly; pins, acrylic bodies with sensors, as implanted in the specimen, so that the values for distances GL and SB may be measured more directly.

From the measured values obtained from the fluoroscopic image and hand held calipers on the subject, the value for SB was determined to be 35.8 mm. A value of 27.9 was used in the data acquisition and reduction program during data collection. The effect this difference makes in the data varies depending on pin angle. For running, which had the most severe pin angles (maximum of 0.65-degree half angle), the difference in SB of 7.9 mm accounts for approximately 25,000  $\mu\epsilon$ . However, at this point in the time history, the strain value reached approximately 50,000  $\mu\epsilon$ . Considering previous values reported in the literature for *in vivo* bone strain in the tibia (on the order of 1,200  $\mu\epsilon$ , Burr, et. al., 1996), and yield strain values of trabecular bone (on the order of 10,000  $\mu\epsilon$ , Chang, et. al., 1999), the correction in SB did not bring the strain magnitude back to this range of values. It is likely that other experimental errors causing the absolute strain magnitudes were present, although, until more data are available against which these values may be compared, these data must stand alone. Since time histories of pin angles were recorded, and raw data stored, it is feasible that with additional post-processing, the absolute values of strain may be recalculated.

## 5.5 Summary

This chapter discussed the uncertainty associated with the capacitive extensometers, the sensitivity to the strain calculation to individual measured variables, the development of an effective resolution of the devices, and the possible sources of error in making strain measurements and associated calculations, particularly in the context of the *in vivo* measurements made in this study. Consideration of uncertainty and effective resolution hopefully gives the reader a sense of what accuracy is possible under ideal circumstances. Consideration of sources of experimental error hopefully leave the reader with a sense of the practical aspects of capturing “real world” data under circumstances where certain aspects of the experiment, i.e., system geometry, which was shown to have large effects on absolute strain magnitudes, are under less control than in the ideal laboratory setting. These sources of error were difficult to foresee. However, with careful analysis of the sources of error in the experiment, areas of improvement also surfaced, and possible enhancements to future studies were highlighted.

## CHAPTER 6

### DISCUSSION

#### 6.1 Overview

The overall purpose of the current study was to design, validate, and test a novel extensometer concept capable of measuring *in vivo* bone strains occurring at physiological magnitudes and rates, and to test in system *in vivo* in a human subject. The motivation for undertaking this study is that bone strain is thought to be an important parameter in maintaining bone mass, and investigators who are involved in the development of exercise regimes designed to maintain bone mass might benefit from information about *in vivo* bone strains during physiological activity. Further benefits are realized from the unique capabilities of the capacitive extensometers themselves, and with their potential application to materials other than bone.

#### 6.2 Four-Point Bending Tests

The dynamic four-point bending tests allowed for a direct comparison between extensometer calculated output and strain gage measured output on an acrylic specimen. The physiological range of strains and strain rates were used to develop the testing envelope (strain magnitude inputs up to and exceeding 4,000  $\mu\epsilon$ , and strain rate inputs up to and exceeding 40,000  $\mu\epsilon/\text{sec}$ ). These goals were met for the delta extensometer, where strain magnitudes up to 5,000  $\mu\epsilon$  were obtained in the test specimen, and strain rates up to 50,000  $\mu\epsilon/\text{sec}$  were measured. For the axial extensometer, strain rates exceeded 90,000  $\mu\epsilon/\text{sec}$  with a square wave loading input, indicating that the design concept is capable of

following strain rates well in excess of those required in a physiological setting. This difference in loading rates between the two test specimens was due to the difference in geometry of the four-point bending jigs – the axial four-point jig was smaller with a shorter load span. Thus strain rates were higher for a given input displacement to the materials test machine. The point-by-point differences between the two outputs calculated throughout the time histories for each extensometer design allowed computation of the maximum errors encountered with the capacitive extensometers under the conditions tested. ASTM E83 contains a table for “Classification of Extensometer Systems”, whereby the error of strain is not to exceed the greater of various fixed and relative strain levels for classification into different categories. Class C allows fixed errors up to 1,000  $\mu\epsilon$ . A class B-2 extensometer allows fixed errors up to 200  $\mu\epsilon$ , which might be a target class for this technology (refer to Figure 4.4b).

In addition, the oscillatory output measured from the capacitive sensor and signal conditioning system when sampled at high frequencies (i.e., 5,000 Hz), allowed a deeper understanding of the oscillatory nature of capacitive sensor systems (refer to Figure 4.1b), and refinement of the sampling algorithms for such a system, namely oversampling and averaging. This was originally troubleshot as a noise problem, until representatives from the supplier of the capacitive probes and signal conditioning equipment (Capacitec, Inc.) were consulted, and suggested oversampling and averaging to help to lessen the magnitude of oscillations in the data. In practice, the effective resolution was able to be improved over the calculated values presented in Table 5.1 by approximately 50%. With different oversampling algorithms, this value could conceivably be further improved.



The development of equations describing the effective resolution of the extensometers also originated from the experience gained in these validation tests. It can be seen that the effective resolution of the capacitive extensometers does not approach that of strain gages for this application. Metal foil strain gage systems like the one used in this experiment can resolve strain to perhaps  $\pm 1$  to  $2 \mu\epsilon$ . In contrast, the capacitive extensometer, because it uses paired values from sensors whose resolution is less than strain gages to calculate strain, has an inherently lower resolution. Resolutions on the order of  $\pm 15 \mu\epsilon$  were realized in the four-point bending phase of this experiment after the data were oversampled and run through averaging routines. The extensometer as described would not be particularly suited for measuring small strains, and the regime described by Cowin (1997) where strains on the order of 100 to  $250 \mu\epsilon$  of interest would not be able to be measured with the capacitive extensometers without introducing significant error. However, it is possible to change the linear range and associated resolution by using different sensor models and calibrations depending on the application. Effective resolution is also dependent upon extensometer geometry, and can be readily changed by altering gage length (GL), distance between sensors (AB), and distance from sensors to specimen (SB). These are variations on the design described that are all under control of the designer. The relationships developed between sensor spacing, resolution, and size, were presented to aid in the design process.

### 6.3 *In Vivo* Strain Data in Human Calcaneus

The main challenge to analyzing the strain data captured *in vivo* was that these data were unique – no data currently exist with which direct comparisons may be made. Data do exist, however, for *in vivo* strain in the human tibia. These studies and their results were presented in Section 2.6 of this thesis. The morphology of the tibia, and the loading it experiences, is different from the calcaneus, however. Although no data exist in the literature of strain in a human calcaneus, data do exist for strain measurements made *in vivo* in the calcanei of animals (e.g., Lanyon, et. al. 1976-b (sheep), and Biewener, et. al., 1996 (potoroos)), discussed further below in Section 6.3.1.

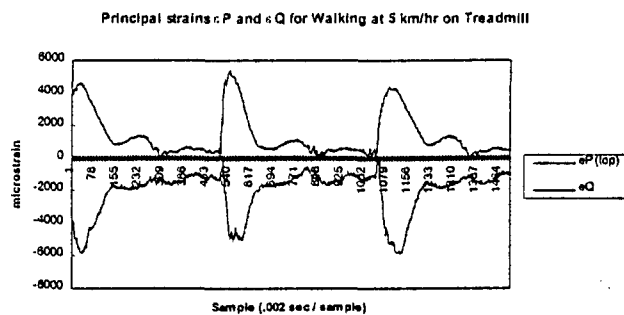
Comparisons may also be made between the strain data measured in this study with the yield strain for trabecular bone reported in the literature. The calcaneus, composed primarily of trabecular bone, obviously did not yield during the loading experienced with normal locomotion in the *in vivo* data collection trials. Therefore, it would be reasonable to assume that the strain magnitudes measured in this study would remain below this yield value. Chang, et. al. (1999) reported that the yield strain of bovine trabecular bone is on the order of 10,000  $\mu\epsilon$ . The absolute values of strain magnitudes measured in this study were variable and ranged between zero and 50,000  $\mu\epsilon$  for running. For this reason, the strain magnitude data for the *in vivo* study are suspect. Potential sources for error were discussed in Chapter 5.

### 6.3.1 Comparison with Strain Measurements in Potoroos

Not all magnitudes measured in the *in vivo* study were unreasonable, however, and one trial in particular was selected for comparison with an *in vivo* strain time history published in the literature. The strain time history for the walking trial selected (Fig. 6.1a) was similar in shape to that published in a study by Biewener et. al., (1996), where *in vivo* principal strains from the calcaneus of potoroos (a small marsupial, reproduced in Figure 6.1b) were measured. In terms of qualitative shape of the time histories, both show the principal tensile and compressive strains oriented symmetrically about the zero strain axis, or X-axis, with maximal strain peaks occurring during the weightbearing phase of gait. Of interest is that in both time histories during the swing phase, when the limb is “unloaded”, measurable strains are still recorded. These non-zero strains during swing phase occur in cyclic manner, indicating that strains are imposed on the calcaneus during swing phase by internal forces, for example, via tendons, but not due to external ground reaction force.

Another interesting aspect of the shapes of these curves is that the highest strain during swing phase occurs at different points in the gait cycle; for the human it is at push off, and for the potoroo it is just prior to “toe strike”. The locomotion of the potoroo is described as digitigrade, unlike humans, who walk in a plantigrade manner. A possible source of this strain is via the action of the achilles tendon in both species, causing strain in the calcaneus at different points in the gait cycle.

a.)



b.)

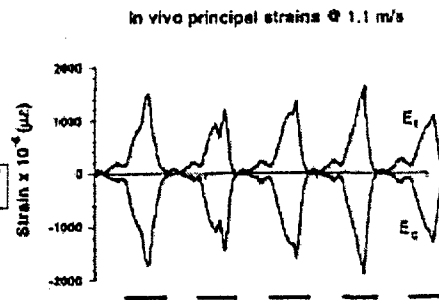


Figure 6.1. a.) In vivo principal strains from this study, measured in the calcaneus of a human subject during walking at 5 km/hr on a treadmill. Duration of trial is 3 seconds and for comparison; b.) in vivo principal strains measured in the calcaneus of a potoroo (a small marsupial) during walking (4 km/hr), adapted from Biewener, et. al. (1996).

Biewener, et. al., also found a quantitative agreement between principal strain angle recorded during walking and the trabecular orientation in the calcaneus ( $161 \pm 7$  degrees, measured from the longitudinal axis in the calcaneus) in potoroos (Fig. 6.2). This was described in the study as providing a quantitative verification of Wolff's Law, named for Julius Wolff who, in his monograph *The Law of Bone Remodeling*, 1892, observed that bone tissue has the capacity to adapt to its functional environment such that its form is optimized for the mechanical demands to which it is subjected. One concept to come from the observations of Hermann Meyer (1867) and later of Wolff, is that trabeculae tend to be aligned along the principal stress trajectories in bone, and in

directions orthogonal to these principal trajectories in a manner that tends to support the trabecular struts (Figure 6.3a).

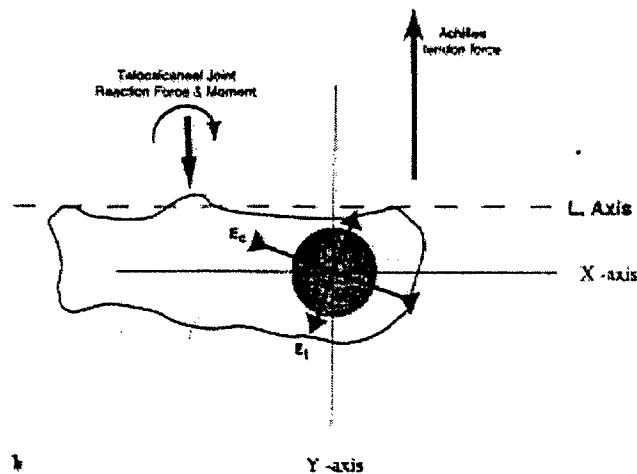
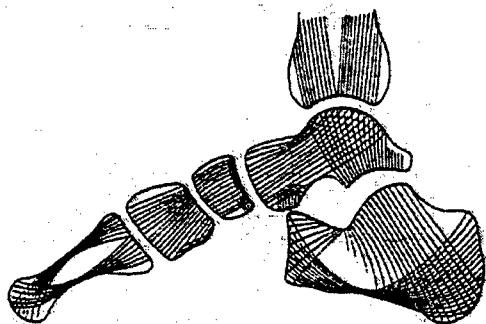


Figure 6.2. *In vivo* principal strain angle measured in the calcaneus of a potoroo (a small marsupial) during walking (4 km/hr) produced a range of angles of  $161 \pm 7$  degrees. Adapted from Biewener, et. al. (1996).

Although trabecular orientation was not measured in this study, principal strain angles in the calcaneus were measured via the delta extensometer, and they provided qualitative agreement with trabecular orientation as seen from radiographic images of the calcaneus (refer to Figure 4.10).

a.)



b.)

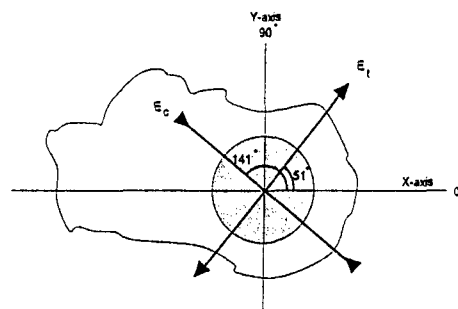


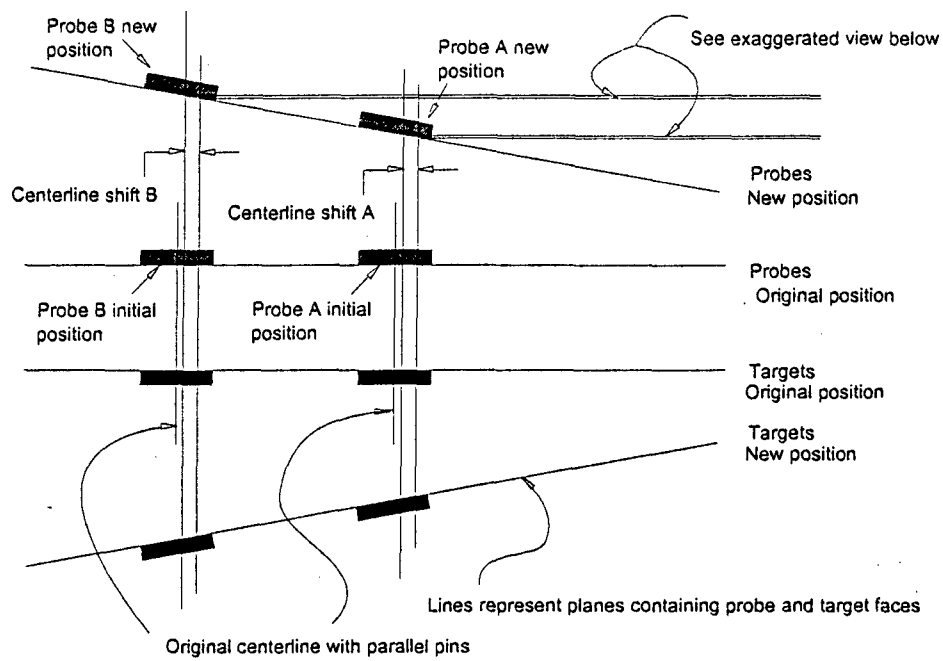
Figure 6.3. a.) Diagram of "stress-lines" in the human foot. Adapted from D'Arcy Wentworth Thompson (1942), after H. Meyer (1867), and b.) principal strain directions from the *in vivo* study described in this thesis for a human standing quietly (from Figure 4.10a.).

It should be noted that the diagram shown in Figure 6.3a has been scrutinized and modified somewhat from the original version shown through modern computer modelling and imaging techniques (e.g., Bacon, et. al., (1979), Yettram, et. al. (1993)), but the concept conveyed by the figure shown is basically correct and still relevant for this discussion.

#### 6.4 Probe Angle Determination is Not a Function of Pooling Error

In the determination of any pooling error encountered between probe and target as a result of the faces of these elements being non-parallel, it is necessary to know the angle

the probe face makes with the target face. One might think that it is not possible to know the angle, because of the error due to pooling, which seems to make the situation unresolvable. It can be shown that the pooling error discussed previously, quantified in the "probe angle sensitivity test", does not affect the determination of probe angle, as long as the pins remain rigid and do not deform. It is necessary to know probe angle prior to determining the error due to this angle, but this is not a problem. Figure 6.4 shows this idea, where a pair of capacitive probes and their respective targets are mounted to pins, and the specimen to which this system is mounted is deformed such that the pins become non-parallel. Any centerline shift at probes A and B caused by pooling will necessarily be the same, because the probes are both at the same angle, by virtue of the fact that they are mounted to the same pin, which does itself not bend or deform.



Exaggerated View:

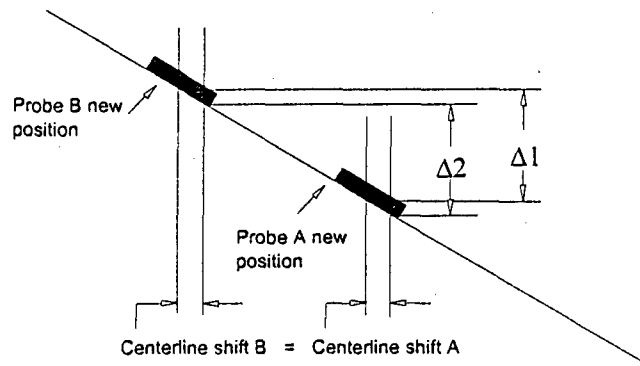


Figure 6.4. If pooling is a function of angle only, the centerline shift due to pooling at probes A and B (top) is necessarily the same for both probes, allowing angle to always be known.



## 6.5 Conclusions and Recommendations

### 6.5.1 *Effect of cortical shell*

One of the shortcomings of the study was that the extensometers were validated only in acrylic specimens. Bone is a complex structure, and there have been suggestions that complicating factors, such as micromotion of the pins within the trabecular bone, or the effect that the inhomogeneity of the structure might have on the strain measurement, should be evaluated. The calcaneus is composed primarily of trabecular bone with a thin cortical shell. Cortical and trabecular bone have very different Young's moduli – approximately 17 GPa and 1 GPa, respectively, for relatively stiff trabecular bone. As a comparison, stainless steel has a Young's modulus of 200 GPa, and oak has a modulus of 12 GPa. One question that can be addressed is how the presence of a cortex in the specimen affects pin displacement. Is it possible that the pins “teeter-totter” about this stiff cortical shell and are restricted by the strain occurring in the bone cortex? To investigate the effect of the cortical shell, the cortex surrounding the pins could be removed by counter boring past this layer such that the pins are isolated from the cortex and make contact only with trabecular bone. A compression test or four-point bending experiment could be performed before and after this counter-boring step and results compared. Likewise, a validation test set-up like the four-point bending tests described could be performed on cadaveric bone specimens with bonded gages as comparison measurements.

### ***6.5.2 Effect of Pin Misalignment and Geometric Errors***

The errors introduced during the *in vivo* study were primarily attributed to pin misalignment, causing errors to be made in the estimation of gage length, and in errors associated with defining the system geometry. These errors were not as apparent during the four-point bending tests because the acrylic specimen was able to be fixtured in a drill press for implantation of intraosseus pins, and the system geometry was able to be directly measured with a microscope and X-Y stage. The errors estimated by the uncertainty analysis, however, did not account for the relatively large strain magnitudes encountered during the *in vivo* study. A study could be designed where the effects of pin misalignment, gage length estimation error, pins entering the specimen plane at various angles (as opposed to orthogonally with the specimen plane as intended), could be investigated. This study might involve the use of bonded strain gages as comparisons.

### ***6.5.3 Design and Implementation Enhancements***

The axial extensometer described incorporated an adjustable target cap so that the air gap between sensor and target could be adjusted to some nominal spacing after pin installation. The delta extensometer as described does not have this feature. Linear gap adjustment was accomplished by using oversized through-holes (1.60 mm) in the acrylic bodies relative to pin diameter (1.58 mm), and placing copper shims between the pin and acrylic where needed to take up the extra space around the pin prior to tightening the set screws. Other methods of linear adjustment are possible, including an eccentric cam that would be able to rotate about the pin within the acrylic body, and be locked in place on

the pin when the desired gap is established. The setscrews in the acrylic bodies would then be used to lock the assembly in place. This adjustment in linear spacing between target and probe would be desirable to account for changes in distance from pin centerlines.

Design improvements might also be realized with the drilling jig, which ensures that the pins are properly spaced (establishing gage length) and are implanted parallel to one another. In practice, because the drilling jig and drill are both hand held, relative movement between the drilling jig and drill are unavoidable, which, in this experiment during the *in vivo* study, caused the intraosseus pins to become non-parallel enough to require an approximately 3 mm bend in one pin (as measured between the original and revised pin centerlines, see Figure 5.3b) to bring the air gap of the sensor pair associated with that pin into a nominal range. Design improvements might involve mounting the drilling jig and foot in a custom drill press type arrangement, where the drill may be translated in a precise fashion along a linear guide. This problem becomes less important where the specimen can be clamped and held in a drill press, or a drill press may be mounted to the substrate.

Because of the sensitivity of the strain calculations made from probe output to extensometer geometry, some form of imaging technology, such as fluoroscope or MRI, is necessary to obtain accurate strain measurements *in vivo*. Ideally, the imaging technology would be high resolution, and be able to measure the entire extensometer system after the probe and target bodies are assembled onto the pins. The use of hand

held calipers to make measurements on the as-installed device introduces errors which may not be correctable after the data are collected. Specifically, the distance from sensor plane B (the outboard sensor plane) to the surface of the specimen, and the as-installed gage length of the device, are crucial measurements input into the strain calculation algorithms.

#### ***6.5.4 Advantages of the Capacitive Extensometer Design***

The advantages of the capacitive extensometer design can be summarized as follows:

- The device is reusable
- Non-contact probe means no reinforcing effect. The stiffness of bonding agent relative to substrate is not a concern, because no bonding agents are necessary with this design.
- Can measure degree and sense of bending in plane normal to pin axis
- Can measure principal strain magnitudes and their directions (delta extensometer)
- Less invasive than bonded resistive strain gages when used *in vivo*, less complicated surgical procedure
- No bonding agents required
- No special surface preparation required (possibly more reliable on difficult surfaces)
- Lightweight compared to other extensometers
- Higher frequency response compared to other extensometers

### 6.5.5 Limitations of the Capacitive Extensometer Design

Along with the benefits these extensometer designs have brought to the current application, limitations exist which have been quantified as far as possible. Important limitations were realized in the resolution of the extensometers, making the physiological strain magnitudes of 100 to 250  $\mu\epsilon$  not practical to measure with this technology without significant error. Accuracy of the measurement depends greatly upon the ability to precisely measure the system geometry. Finally, the technique of using intraosseus pins, although less invasive than bonded strain gages when used *in vivo*, is still invasive, and specimens must be able to tolerate the implantation of pins used in the extensometer designs, and the associated stress concentrations developed from the resulting holes required. A summary of the limitations is as follows:

- Must implant pins into specimen – is an invasive method
- Resolution lower than bonded resistive strain gage and other extensometers for physiologic levels of strain
- More expensive than bonded resistive strain gages
- Method requires some form of medical imaging (MRI or fluoroscopy) when used *in vivo*
- Method is very sensitive to errors in geometric measurements of the device used as parameters in the strain calculation.

### 6.6 Potential Applications

An extensometer that can be used *in vivo* to discern axial from bending strains, and provide a measure of principal strain magnitude and direction has potential uses to the

biomechanics and orthopedics communities, and to materials testing applications in general. Example applications include finite element code validation and design of prosthetic devices, where experimental data are of value to the development and design process, or in bone studies where the bone surface cannot be prepared for application of bonded strain gages. The extensometers described were designed with the measurement of bone strain in mind, however they may be applied to other materials. For example, porous materials such as porous metals, plastics, or ceramics; materials that have rough, wet, or inaccessible surfaces, are potential applications for the capacitive extensometer designs. Because the sensors are non-contacting and each assembly in the extensometer design can move independently, application might be found in materials testing environments where fragmentation of the specimen occurs, such as with destructive or explosive testing. Further, a wide range of gage lengths is possible without changing sensor type or size, making these extensometers potentially useful in a broad range of materials testing and evaluation environments.

**Appendix A: Supplemental Data**

Table A.1. Test conditions and statistical summary for the axial extensometer validation tests in dynamic four-point bending.

AXIAL EXTENSOMETER									
Test Condition				Statistical Summary					
Preload strain ( $\mu\epsilon$ )	maximum ( $\mu\epsilon$ )	minimum ( $\mu\epsilon$ )	Frequency (Hz)	Mean Difference ( $\mu\epsilon$ )	Mean % Error (% of max strain)	Pearson's Correlation Coeff. r	Maximum Difference ( $\mu\epsilon$ )	Max % Error (% of max strain)	Standard Deviation ( $\mu\epsilon$ )
318	383	251	10	-8.57	-2.24	0.987	24.71	6.45	7.98
318	370	265	20	-11.50	-3.11	0.960	33.86	9.15	10.56
629	704	554	10	7.12	1.01	0.988	20.81	2.96	4.55
629	755	502	10	11.15	1.48	0.991	28.76	3.81	6.79
656	762	548	15	-10.87	-1.43	0.978	19.10	2.51	16.12
650	732	568	20	-2.81	-0.38	0.966	36.96	5.05	15.73
637	728	546	20	-6.94	-0.95	0.965	44.21	6.07	17.58
433	639	227	5	-14.49	-2.27	0.997	39.97	6.26	11.42
431	624	241	10	-13.15	-2.11	0.991	51.07	8.18	18.99
426	610	245	10	-14.09	-2.31	0.990	48.79	8.00	18.51
431	594	269	15	-10.53	-1.77	0.981	52.39	8.82	22.78
442	585	294	20	-15.27	-2.61	0.967	66.07	11.29	27.23
422	554	289	20	-14.76	-2.66	0.968	61.71	11.14	24.45
722	1240	189	1	-0.12	-0.01	0.999	23.31	1.88	9.44
726	1246	194	1	0.56	0.05	0.999	21.48	1.72	9.36
865	1087	636	19	-3.36	-0.31	0.971	67.73	6.23	39.27
834	1057	605	19	1.43	0.14	0.970	70.22	6.64	40.27
842	1189	495	2	-2.37	-0.20	0.998	78.49	6.60	16.51

Position control +/- 0.005" displacement, Square wave input at 2 Hz;

845	1501	207	2	1.13	0.08	0.998	214.38	14.28	40.18
829	1483	189	2	9.06	0.61	0.998	216.68	14.61	39.3



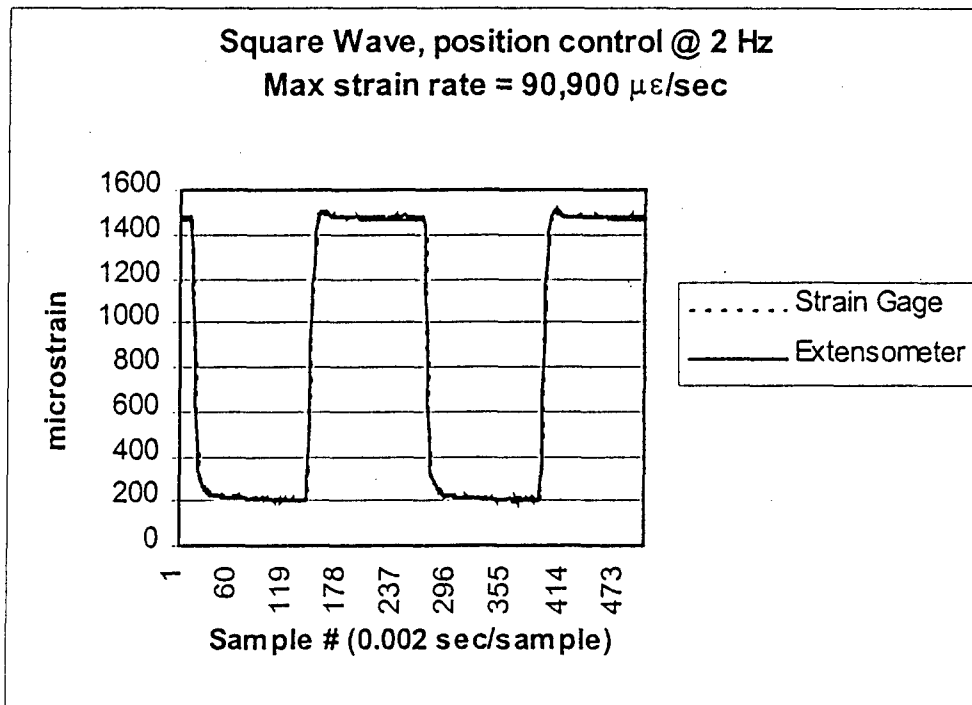
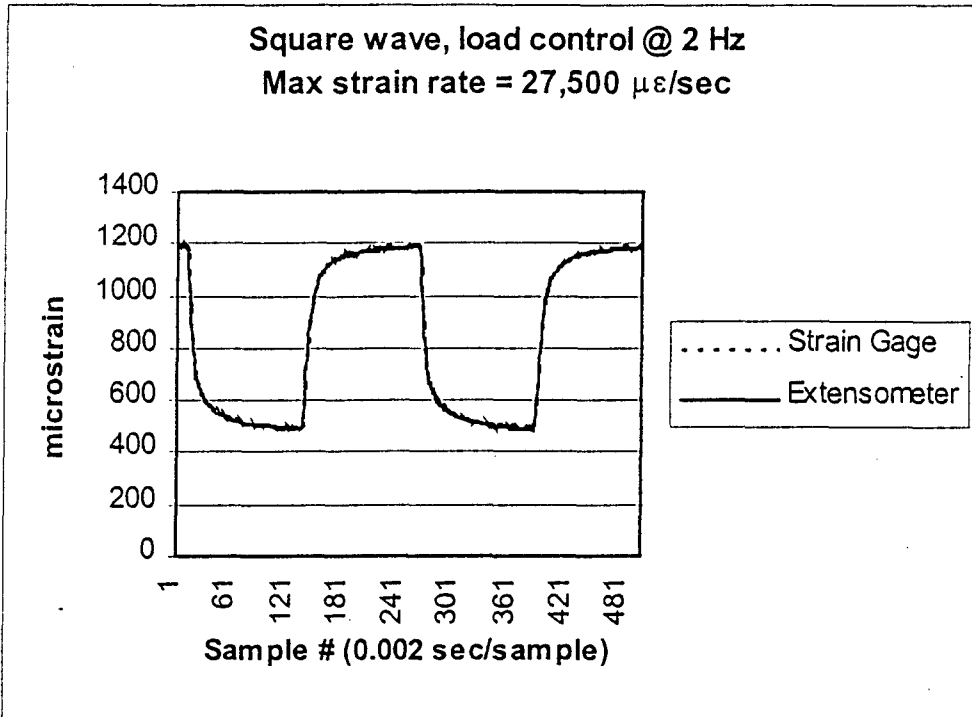


Figure A.1. Representative time histories for axial extensometer four-point bending test.

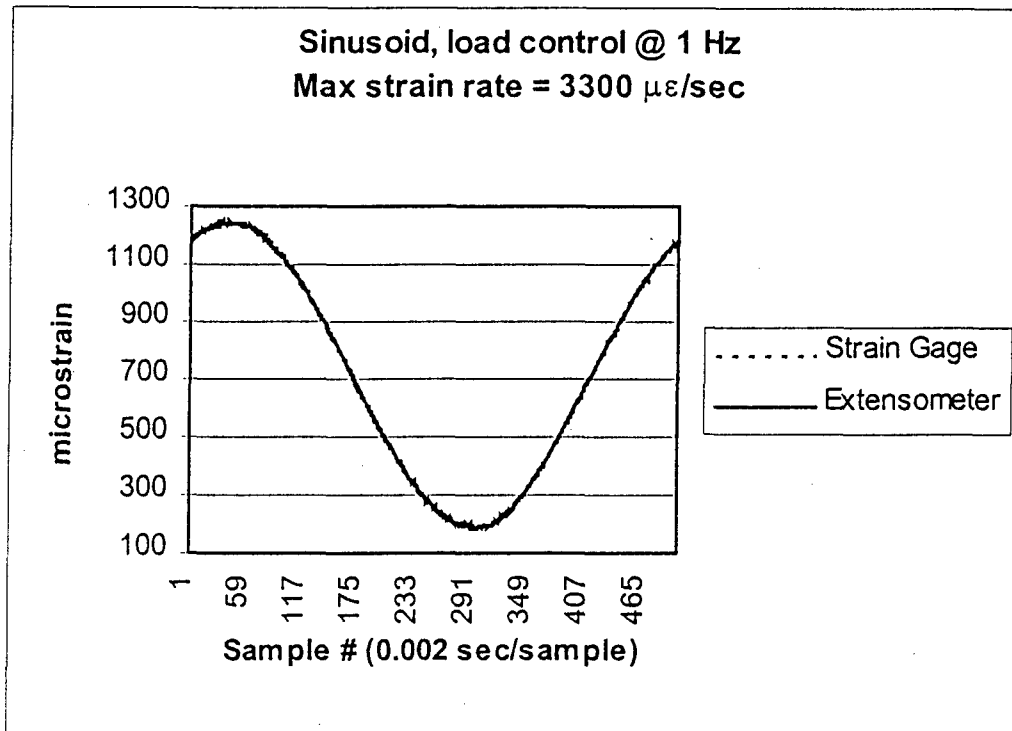
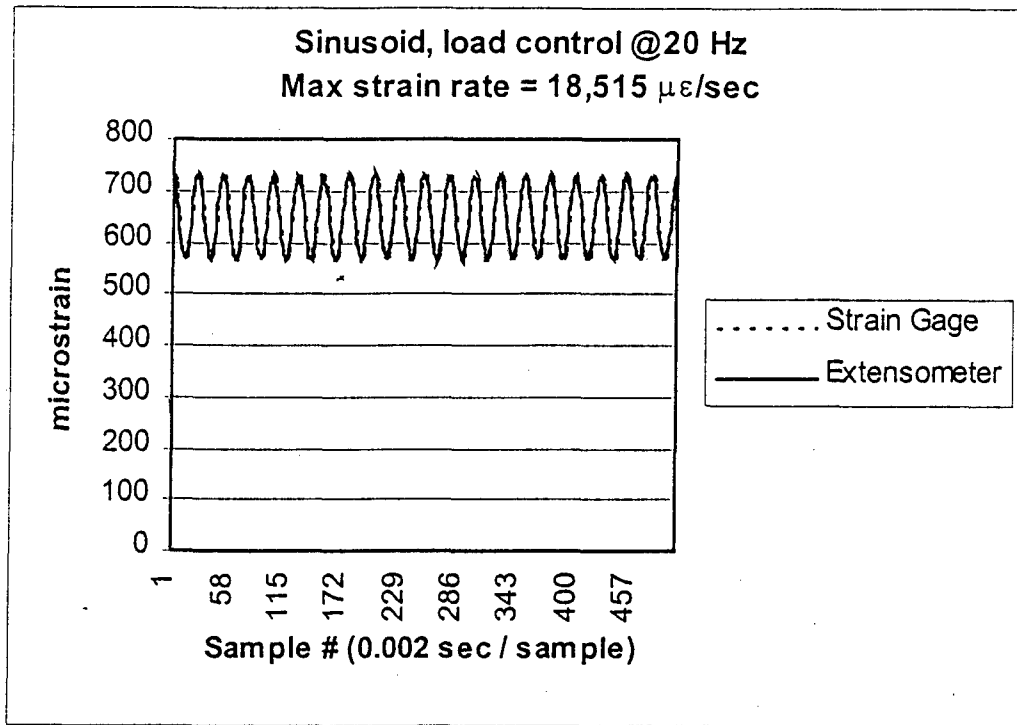


Figure A.1. con't. Representative time histories for axial extensometer four-point bending test.

Table A.2. Test results for delta extensometer in 4-point bending. Sinusoidal inputs.

Delta Extensometer -- Sinusoidal Loading Inputs											
File	Gnd. #	Test Condition			Statistical Summary						
		Strain range ( $\mu\epsilon$ )		Frequency (Hz)	Mean Diff. ( $\mu\epsilon$ )	Mean % Error (% max strain)	Pearson's	Max. Diff. ( $\mu\epsilon$ )	Max % Error (% max strain)	Std. Dev.	
		min.	max.								
a2	1	307.6	541.8	5	20.5	3.8	0.993	53.0	9.8	10.1	
	2	-290.0	-170.9	5	6.8	-2.3	0.970	39.3	-13.6	10.5	
	3	228.5	407.2	5	5.8	1.4	0.980	40.7	10.0	13.1	
a3	1	360.4	491.2	10	16.4	3.3	0.976	46.7	9.5	10.3	
	2	-264.6	-198.2	10	5.5	-2.1	0.912	34.2	-12.9	9.8	
	3	268.6	368.2	10	17.3	4.7	0.949	51.1	13.9	11.2	
a4	1	391.2	456.7	20	11.3	2.5	0.918	40.1	8.8	9.6	
	2	-245.1	-211.9	20	6.6	-2.7	0.711	35.4	-14.4	10.3	
	3	295.9	343.8	20	14.9	4.3	0.789	42.9	12.5	10.9	
a5	1	520.5	1208.0	1	22.9	1.9	0.999	54.8	4.5	9.7	
	2	-639.6	-289.1	1	9.8	-1.5	0.997	37.1	-5.8	10.3	
	3	395.9	915.6	1	16.2	1.8	0.998	53.7	5.9	13.2	
a6	1	675.8	1061.5	5	36.2	3.4	0.996	82.1	7.7	12.7	
	2	-548.8	-353.5	5	-42.5	7.7	0.988	67.6	-12.3	10.9	
	3	511.9	805.5	5	33.0	4.1	0.990	76.0	9.4	14.7	
a7	1	750.5	980.3	10	22.2	2.3	0.987	63.1	6.4	13.4	
	2	-509.8	-395.2	10	-25.9	5.1	0.949	59.9	-11.7	13.0	
	3	565.3	737.8	10	38.4	5.2	0.978	74.1	10.0	12.9	
a8	1	790.0	909.5	20	23.8	2.6	0.963	54.7	6.0	11.2	
	2	-480.5	-420.9	20	-5.7	1.2	0.836	41.2	-8.6	11.9	
	3	603.9	694.3	20	17.5	2.5	0.902	52.3	7.5	13.6	
a20	1	827.6	1999.5	1	-16.2	-0.8	0.999	70.4	3.5	23.7	
	2	-1049.6	-451.7	1	-19.5	1.9	0.997	60.7	-5.8	15.6	
	3	625.0	1506.3	1	-20.7	-1.4	0.998	79.6	5.3	25.0	
a21	1	1062.0	1742.2	5	-4.6	-0.3	0.996	58.0	3.3	25.2	
	2	-922.1	-578.6	5	16.2	-1.8	0.990	62.9	-6.8	17.6	
	3	800.8	1313.7	5	-9.5	-0.7	0.993	59.1	4.5	23.6	
a22	1	1198.7	1596.7	10	3.7	0.2	0.986	65.9	4.1	24.2	
	2	-817.9	-622.6	10	-17.1	2.1	0.965	63.0	-7.7	18.1	
	3	908.2	1208.7	10	-30.0	-2.5	0.979	89.0	7.4	22.0	

Table A.2., con't. Test results for delta extensometer in 4-point bending. Sinusoidal inputs.

Delta Extensometer - Sinusoidal Loading Inputs, continued										
File	Grid #	Test Condition			Statistical Summary					
		Strain range ( $\mu\epsilon$ )		Frequency	Mean Diff.	Mean % Error	Pearson's	Max. Diff.	Max. % Error	Std. Dev.
		min.	max.	(Hz)	( $\mu\epsilon$ )	(% max strain)	r	( $\mu\epsilon$ )	(% max strain)	
a34	1	505.4	1191.4	1	18.4	1.5	0.999	60.9	5.1	15.5
	2	-620.1	-273.4	1	-35.0	5.6	0.993	75.5	-12.2	14.4
	3	375.5	888.7	1	17.0	1.9	0.993	70.9	8.0	22.9
a35	1	730.6	965.8	10	28.0	2.9	0.983	70.3	7.3	15.2
	2	-503.9	-387.1	10	-25.8	5.1	0.969	58.3	-11.6	11.0
	3	544.0	719.7	10	-10.1	-1.4	0.911	64.1	8.9	26.1
a37	1	815.7	1977.5	1	42.5	2.1	0.999	97.2	4.9	17.7
	2	-1035.2	-446.8	1	-29.1	2.8	0.998	67.7	-6.5	14.6
	3	1474.6	605.5	1	48.9	8.1	0.996	117.9	19.5	29.6
a38	1	1198.7	1601.6	10	16	1.0	0.987	67.5	4.2	23.1
	2	-824.2	-622.6	10	-45.1	5.5	0.976	81.8	-9.9	15.5
	3	887.7	1191.4	10	39.2	3.3	0.948	111.7	9.4	33.9
a39	1	1302.2	1509	20	37.8	2.5	0.960	92.6	6.1	20.2
	2	-786.1	-685.8	20	-49.6	6.3	0.929	92.2	-11.7	13.2
	3	973.4	1130.4	20	4.4	0.4	0.815	88.5	7.8	39.1
a31	1	532.2	2285.2	1	21.2	0.9	0.999	75.0	3.3	20.4
	2	-1174.3	-290.5	1	-46.5	4.0	0.999	99.3	-8.5	15.5
	3	392.8	1696.8	1	38.2	2.3	0.997	115.0	6.8	37.3
a32	1	-878.9	1911.6	5	35	1.8	0.997	97.6	5.1	29.8
	2	-981.4	-469.7	5	-47.3	4.8	0.996	93.5	-9.5	17.2
	3	656.7	1425.8	5	31	2.2	0.991	116.2	8.1	37.0
a33	1	1064.5	1672.4	10	42.3	2.5	0.989	113.4	6.8	30.9
	2	-864.3	-563.9	10	-61.9	7.2	0.985	110.3	-12.8	18.3
	3	791	1245.6	10	-1.6	-0.1	0.971	72.2	5.8	37.6
a45	1	1240.2	2988.3	1	38.4	1.3	0.999	80.9	2.7	17.3
	2	-1540.5	-664.1	1	-74.3	4.8	0.998	113.2	-7.3	17.4
	3	925.3	2224.1	1	112	5.0	0.997	194.3	8.7	39.5
a46	1	947.3	3295.9	1	33.2	1.0	0.999	82.6	2.5	23.1
	2	-1684.6	-507.8	1	-36.7	2.2	0.999	80.0	-4.7	16.7
	3	710.4	2443.8	1	-60.6	-2.5	0.999	126.6	5.2	33.8

Table A.2., con't. Test results for delta extensometer in 4-point bending. Sinusoidal inputs.

Delta Extensometer - Sinusoidal Loading Inputs, continued										
File	Grid #	Test Condition			Statistical Summary					
		Strain range ( $\mu\epsilon$ )		Frequency	Mean Diff.	Mean % Error	Pearson's	Max. Diff.	Max. % Error	Std. Dev.
		min.	max.	(Hz)	( $\mu\epsilon$ )	(% max strain)	r	( $\mu\epsilon$ )	(% max strain)	
a47	1	1940.9	3706.1	1	67.1	1.8	0.999	114.7	3.1	17.3
	2	-1901.8	-1027.8	1	-8.9	0.4	0.999	68.8	-3.6	22.6
	3	1445.3	2734.4	1	-192.8	-7.1	0.998	313.0	11.4	52.8
a48*	1	1562.5	3891.6	0.5	53.6	1.4	0.999	97.2	2.5	14.1
	2	-1984.9	-827.6	0.5	3.8	-0.5	0.999	77.4	-9.4	34.8
	3	1164.6	2867.7	0.5	-220.1	-7.7	0.999	434.2	15.1	95.8

\*Note: trial "a48" gives maximum principal strain in the specimen ( $\epsilon_p$ ) as 5032  $\mu\epsilon$ .

Table A.3. Test results for delta extensometer in 4-point bending. Square wave inputs.

Delta Extensometer -- Square Wave Loading Inputs										
File	Grid #	Test Condition			Statistical Summary					
		Strain range ( $\mu\epsilon$ )		Frequency	Mean Diff.	Mean % Error	Pearson's	Max. Diff.	Max % Error	Std. Dev.
		min.	max.	(Hz)	( $\mu\epsilon$ )	(% max strain)	r	( $\mu\epsilon$ )	(% max strain)	
a40	1	618.2	1023.4	2	17.1	1.7	0.997	83.9	8.2	15.3
	2	-533.2	-334.9	2	-33.8	10.1	0.991	69.3	-13.0	12.9
	3	456.0	760.7	2	26.4	3.5	0.990	104.6	13.8	19.6
a41	1	434.6	1217.5	2	16.5	1.4	0.998	107.5	8.8	24.9
	2	-624.0	-239.3	2	-27.8	11.6	0.996	90.2	-14.5	17.2
	3	319.3	906.7	2	-18.4	-2.0	0.996	95.5	10.5	23.2
a43	1	773.5	1951.7	2	26.8	1.4	0.999	125.5	6.4	28.5
	2	-1009.8	-430.7	2	-31.4	7.3	0.997	108.7	-10.8	21.7
	3	574.8	1456.1	2	58.9	4.0	0.997	188.3	12.9	31.4
a44	1	593.5	2153.3	2	33.8	1.6	0.999	122.6	5.7	33.6
	2	-1098.6	-329.6	2	-37.7	11.4	0.998	114.4	-10.4	26.0
	3	441.9	1606.7	2	28.3	1.8	0.998	183.6	11.4	41.9

Operator(s):	gpp, rjp				avg. difference =		20.52209				
Date:	11/16/1999				r =		0.992763				
Sampling Rate (Hz):	5000				max difference =		52.9765				
# Samples:	5000				std. Dev. Of difference =		10.13858				
Filename:	a2.dat				median strain =		421.875				
Gage Length (in.):	0.29				max strain =		541.7969				
Dist. A to B (in.):	0.635				min. strain =		307.6172				
Dist. A to S (in.):	0.7										
Comments:	Acrylic specimen 30 lb +/- 20 @ 5 Hz										
max pin angles (deg) 1,2,3 :	0.014617		0.005799		0.008109						
Xe1	Xe2	Xe3	Xep	Xeq	Xphi	Re1	Re2	Re3	Rep	Req	Rphi
550.663116	-286.941177	393.6273	733.2316	-294.9987	-24.92136	535.9375	-286.9141	402.2461	726.97	-292.7903	-25.64648
550.52152	-286.810899	401.3913	737.4498	-294.0486	-25.19496	537.5977	-287.8906	403.3203	729.1516	-293.8001	-25.641
550.759319	-286.680621	400.4347	737.0475	-294.0385	-25.15415	538.5742	-288.1836	404.2969	730.5416	-294.0833	-25.64818
564.369446	-287.592576	401.0724	748.0746	-296.1751	-24.79855	539.1602	-288.7695	404.3945	731.2282	-294.7048	-25.63784
562.953381	-286.563275	388.5546	739.7382	-296.4418	-24.39671	540.0391	-289.0625	405.2734	732.4887	-294.9887	-25.64445
556.904363	-273.377866	388.714	730.9271	-282.7668	-24.47732	539.3555	-289.0625	405.1758	731.9197	-294.9406	-25.6609
555.392127	-279.840345	404.0824	740.4099	-287.3204	-25.106	539.0625	-289.0625	404.3945	731.2503	-294.9873	-25.64233
556.241774	-286.693559	414.0594	748.9388	-293.2003	-25.46795	538.8672	-289.0625	404.2969	731.0476	-294.9799	-25.64462
549.388721	-289.286286	399.9564	736.5812	-296.5419	-25.19278	538.0859	-288.3789	403.8086	729.9579	-294.2808	-25.64652
564.273179	-285.521024	399.797	746.6238	-294.2577	-24.74342	537.207	-288.0859	403.3203	728.9222	-293.9612	-25.65349
562.760921	-269.495192	401.3913	741.1882	-278.0835	-24.73325	535.6445	-287.207	402.0508	726.7332	-293.0743	-25.64989
550.663116	-256.452257	408.3677	731.6685	-263.2827	-25.24725	533.5938	-286.4258	400.6836	724.1536	-292.2525	-25.65773
544.518155	-272.609059	419.8297	738.7755	-277.7496	-25.92213	531.25	-284.9609	398.9258	720.9067	-290.7635	-25.65662
537.523798	-259.045096	406.1643	721.3406	-264.9119	-25.57654	527.9297	-283.6914	396.4844	716.5975	-289.449	-25.66139
549.807839	-271.332077	405.6954	734.33	-278.2159	-25.27041	524.1211	-281.9336	393.75	711.5944	-287.636	-25.66754
553.302056	-275.084566	401.579	735.8723	-282.6747	-25.04781	520.0195	-280.0781	390.5273	706.0586	-285.7461	-25.66451
541.108373	-273.390774	391.921	720.6136	-280.8545	-25.04753	515.5273	-277.6367	387.1094	699.9266	-283.2599	-25.66277
529.622981	-274.954271	389.23	710.8845	-281.6187	-25.2997	510.2539	-275.1953	383.2031	692.9276	-280.7531	-25.66709
528.722107	-276.387556	378.6254	704.6821	-284.0421	-24.95214	505.0781	-272.5586	379.1016	685.8257	-278.0783	-25.66009
524.938612	-274.967352	370.0745	696.5598	-283.1959	-24.74181	498.9258	-269.4336	374.707	677.6638	-274.8643	-25.66962
516.522378	-261.533683	375.4747	688.8205	-268.5116	-25.1024	492.6758	-266.4063	370.1172	669.348	-271.7569	-25.67568

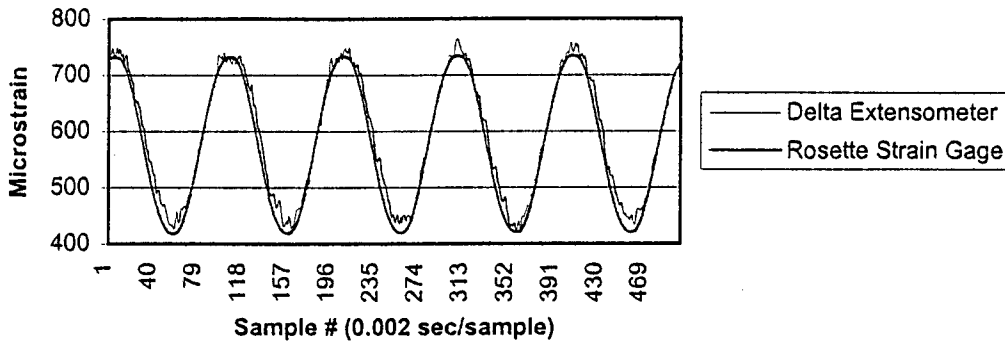
**Column heading definitons:**

- Xe1 = extensometer "grid" 1 strain (reference grid) – calculated
- Xe2 = extensometer "grid" 2 strain – calculated
- Xe3 = extensometer "grid" 3 strain – calculated
- Xep = extensometer principal maximum strain magnitude – calculated
- Xeq = extensometer principal minimum strain magnitude – calculated
- Xphi = extensometer principal strain angle – calculated
- Re1 = rosette strain gage grid 1 strain (reference grid) – measured directly
- Re2 = rosette strain gage grid 2 strain – measured directly
- Re3 = rosette strain gage grid 3 strain – measured directly
- Rep = rosette strain gage principal maximum strain magnitude – calculated
- Req = rosette strain gage principal minimum strain magnitude – calculated
- Rphi = rosette strain gage principal strain angle – calculated

*Figure A.2 Sample data output from delta extensometer four-point bending evaluation.*

*Files were generated in LabVIEW and imported into Microsoft Excel for post-processing.*

Principal Maximum Strain Magnitude Comparison  
Data File a2 (5 Hz sinusoid)



Principal Maximum Strain Magnitude Comparison  
Data File a22 (10 Hz sinusoid)

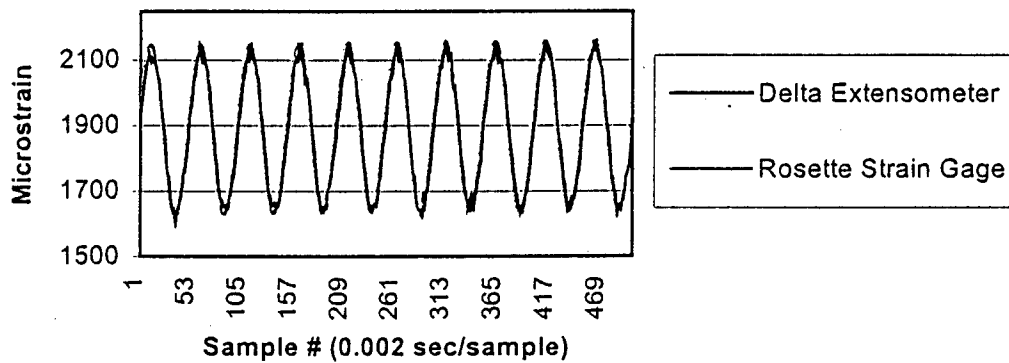


Figure A.3. Example time histories from the delta extensometer four-point bending evaluations. Specific information including range of strains for each grid, and statistical summaries for each grid, can be found in Table A.2.

### Pin angles for walking

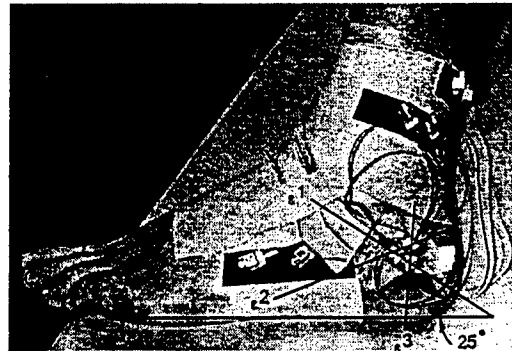
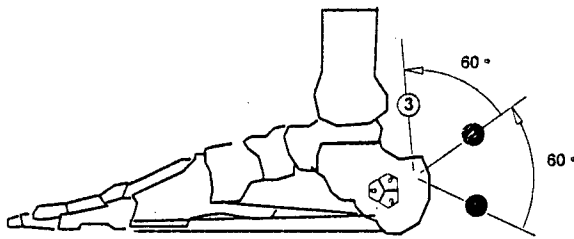
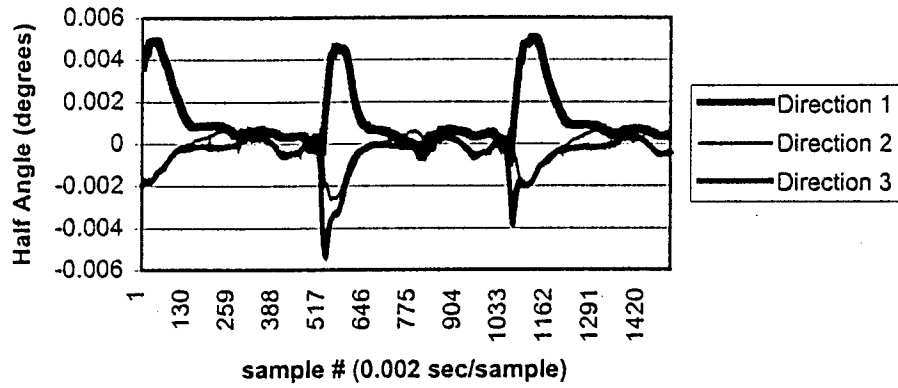


Figure A.4. In vivo pin angles for walking (top) at 5 km/hr on treadmill, and directions 1, 2, and 3 called out in the time history legend, as oriented in human calcaneus (bottom).



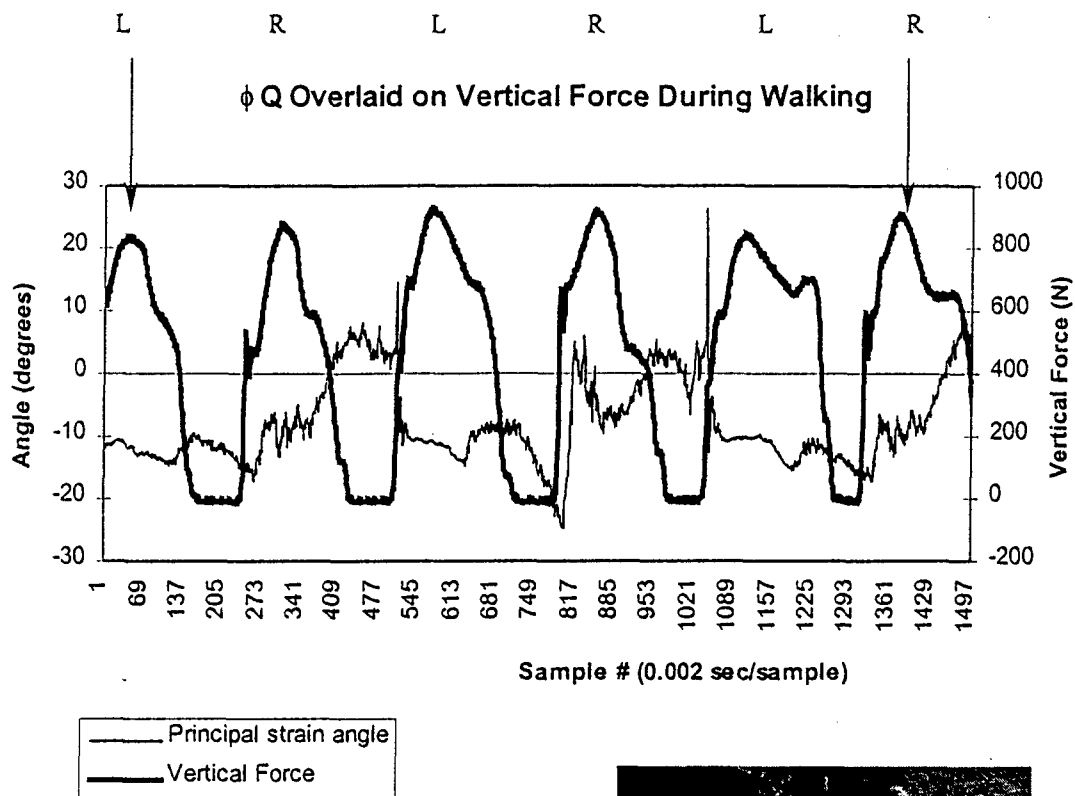


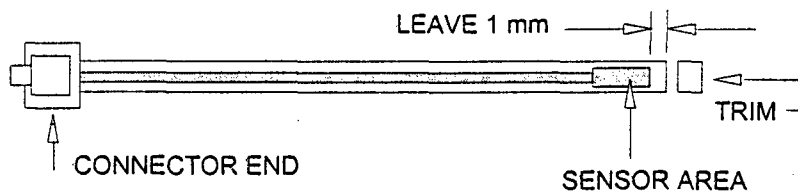
Figure A.5. *In vivo* principal minimum strain angle ( $\phi Q$ ) for human subject walking at 5 km/hr on treadmill overlaid on vertical force. Trial duration is 3 seconds. The angle is measured from the reference grid (direction 1 as indicated in Figure A.4) to the principal minimum strain axis ( $\epsilon Q$ ). This plot was used in conjunction with principal strain magnitudes to generate Figure 4.13 in Chapter 4: Results. Vertical force time history is recorded for both feet, however, the left foot only (indicated above graph as "L") was instrumented with the delta extensometer.

## Appendix B: Procedures

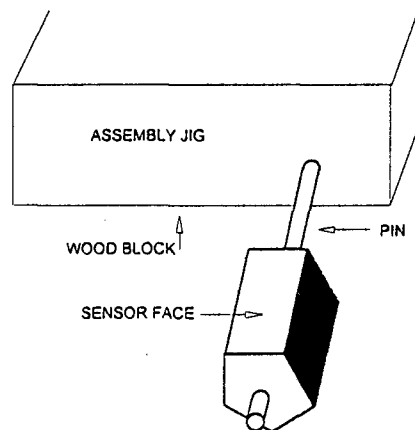
## Delta Extensometer Probe Assembly Procedure

The assembly procedure used for attachment of sensors to the delta extensometer is as follows:

1. Trim end of sensor with X-Acto knife. Trim no closer than 1 mm from sensitive area of sensor (can be seen through Capton film).

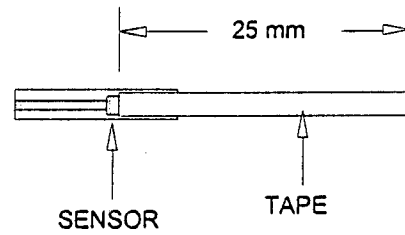


2. Place acrylic body on assembly jig (jig consists of wood block and pin) with the sensor face facing upward.

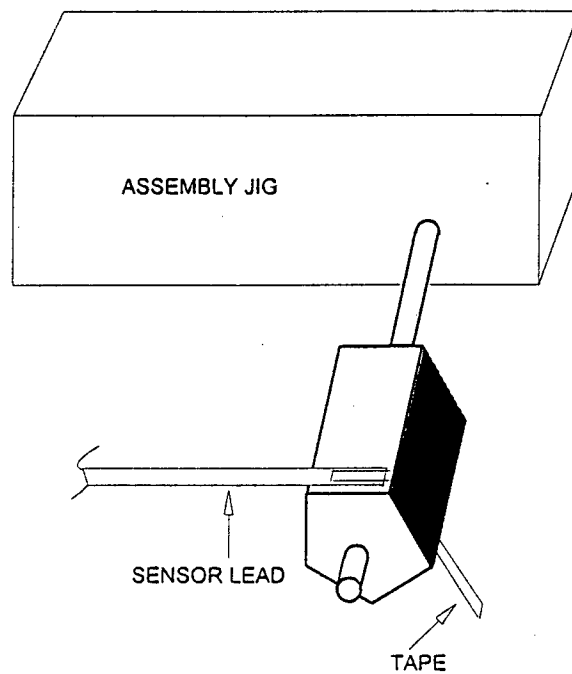


3. Abrade sensor face with wet/dry emory paper. Clean with alcohol.

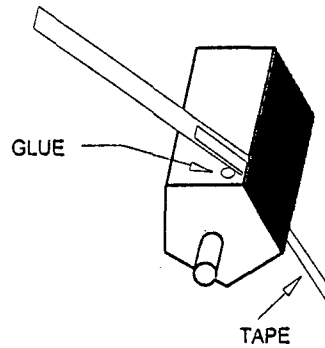
4. Cut thin strip of cellophane tape about 25 mm long and place over trimmed end of sensor.



5. Align sensor over acrylic body, using assembly jig to line up. Tape down to acrylic body in desired location, leaving some tape hanging over to grab later.



6. Lift sensor (hinge on tape) and apply small amount of cyanoacrylate adhesive to area beneath sensor closest to tape hinge. Use hypodermic needle or toothpick to apply glue.



7. Apply pressure to top side of sensor with suitable tool (tongue depressor) or thumb and hold while glue sets. Tip: work under warm light to speed drying time or use accelerator.

8. Peel back and remove tape.

9. Apply small amount of glue over trimmed end of sensor to protect.

## Probe Angle Sensitivity Test Procedure

### Apparatus:

- Troyke Rotary Table with adapter plug

Adapter plug allows target to mount in center of table. Target face is aligned with center of rotation. Target mounts via a 5/64 in. dia. K-wire (stainless steel pin).

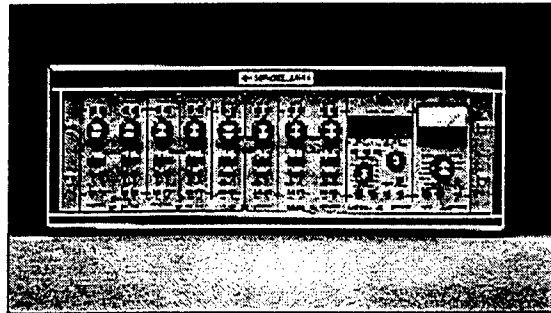
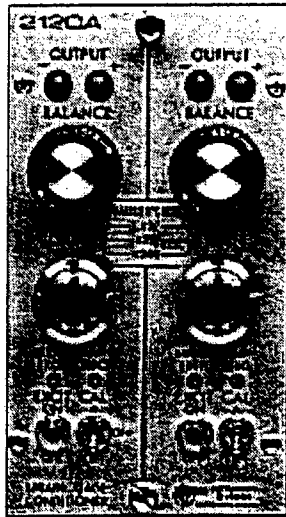
- Vernier Height Gage
- HPB-40 Capacitive Sensor mounted to Vernier height gage arm fixture. Sensor also mounted to 5/64 in. dia. K-wire.
- Axial extensometer (uses HPB-40 probe with linear range of 0 to 0.040 in. = -5 to +5VDC)
- 4100-SL Capacitec signal conditioner
- Hewlett-Packard precision voltmeter

1. Turn on voltmeter and signal conditioner and allow equipment to warm up (2-3 hrs).
2. On level surface, mount probe and target to Vernier height gage and rotary table, respectively. Begin with rotary table set to 0 degrees (target parallel to sensor).
3. Check tightness of vernier height gage clamp, rotary table plug, and rotary vernier scale.
4. Bring probe up to displacement of 0.020 in. (mid range). Set displacement by using sensor output (no external reference necessary).

5. Set rotary table to negative setting, - 5 degrees. Increment rotary table by degrees, minutes to + 5 degrees in 20 minute steps). Record sensor output and rotation angle. Since target face is aligned with center of rotation of table, any deviation from 0.020" displacement will be due to rotation alone (i.e., no translation).

6. Plot angle vs. deviation from baseline output. Fit a curve (2<sup>nd</sup> order) to use as a correction for various angles encountered if necessary.

## Strain Gage Amplifier (Measurements Group 2100) Bridge Balance / Gain Adjust Procedure



1. With excitation OFF (CAL A toggle OFF), specimen unloaded:
2. Adjust excitation to 3 volts for acrylic specimen (to minimize self-heating. An excitation voltage of 5 volts is typically used for metal specimens where gage cooling via conduction is possible). Screwdriver adjust on "BRIDGE EXCIT" control.
3. Adjust screw to amplifier zero until see zero output (adjusting the bias of the amplifier, can go +/- from zero).
4. With excitation ON:
5. Balance bridge to zero output (with large knob at top)
6. Switch CAL A toggle to ON
7. Using GAIN knob, adjust sensitivity until the gage factor value is reached  
Gage factor value sample calculation:  
Assume GF = 2.1
$$\frac{2.0}{2.1} \times 1000 = 952 \text{ microstrain}$$
Adjust sensitivity so with CAL A on, value of 0.952 Volts is obtained
8. Switch CAL A to OFF (leave excitation ON).
9. Readjust bridge balance / readjust zero – ready to take measurement



**Appendix C: Original Drawings**

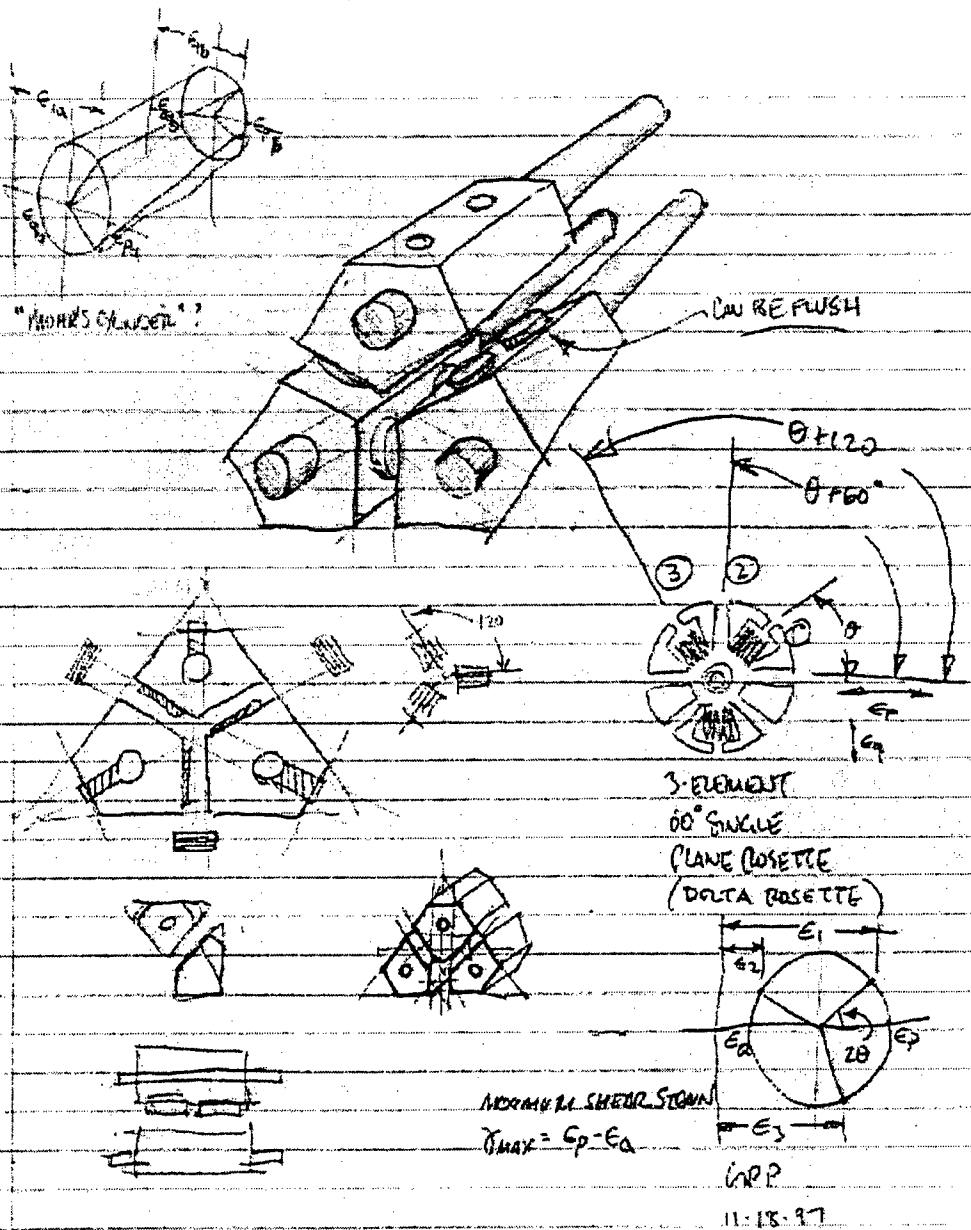


Figure C.1. Original concept sketch for delta extensometer.

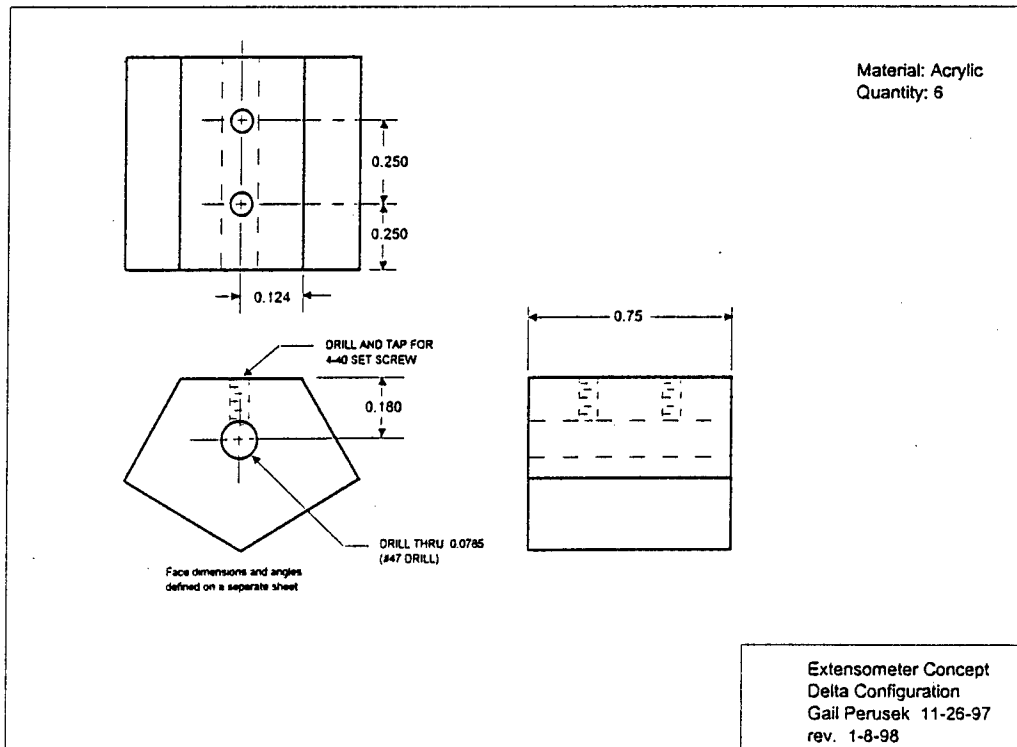
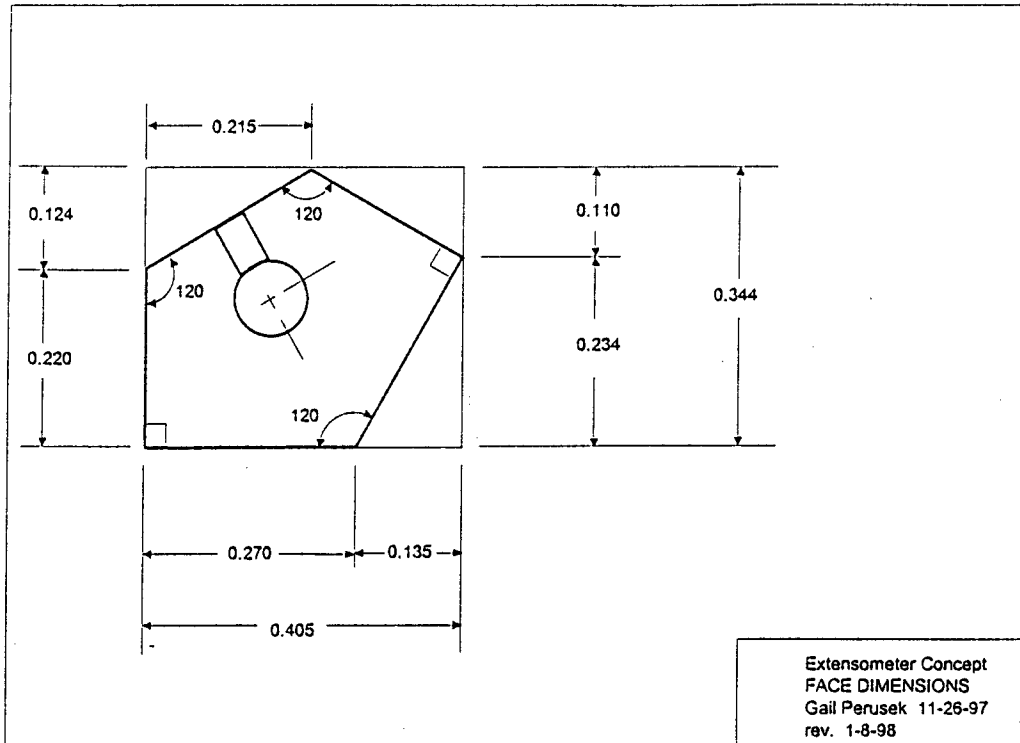
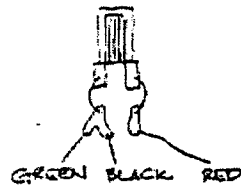
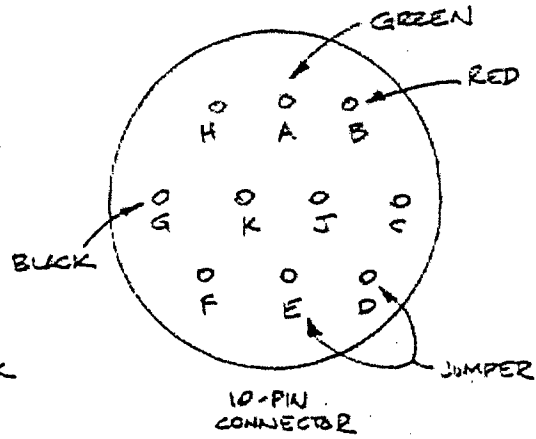
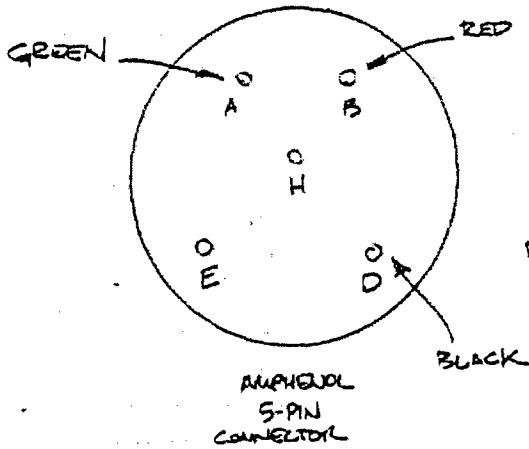


Figure C.2. Delta extensometer acrylic body detail drawings (all dimensions in inches).

QUARTER BRIDGE (3-WIRE) CONNECTOR LAYOUT



FOR 350Ω



FOR 120Ω

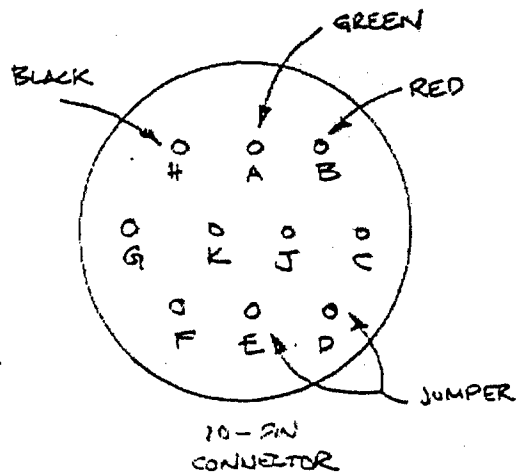
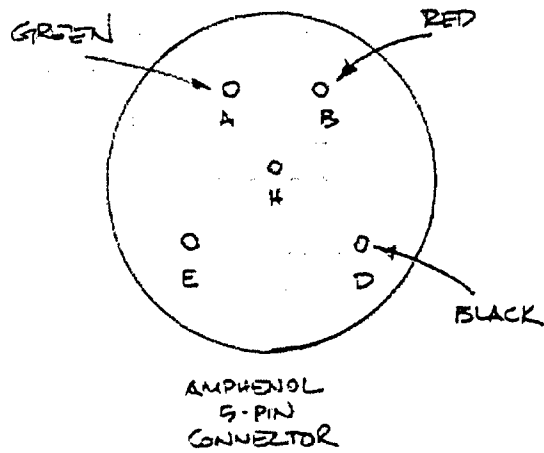


Figure C.3. Connector diagram showing pin-out designations for Amphenol and 10-pin connectors used with the strain gages and Measurements Group 2100 signal conditioning amplifier.

## Appendix D: Mohr's Circle for Strain

## Mohr's Circle for Strain

Although the information contained in this Appendix is found within the body of the thesis text, the equations for Mohr's circle for strain are summarized here for clarity.

Mohr's circle is named after its developer, Otto Mohr, a German engineer (1835 - 1918).

A strain gage rosette or delta extensometer mounted to a specimen (Figure D.1), will provide strain output in the form of resistance or voltage (for strain gage or extensometer, respectively). This output corresponds to measurements of three strain magnitudes,  $\epsilon_1$ ,  $\epsilon_2$ , and  $\epsilon_3$ . The principal strain direction ( $\theta$ ) is unknown at the time of data collection.

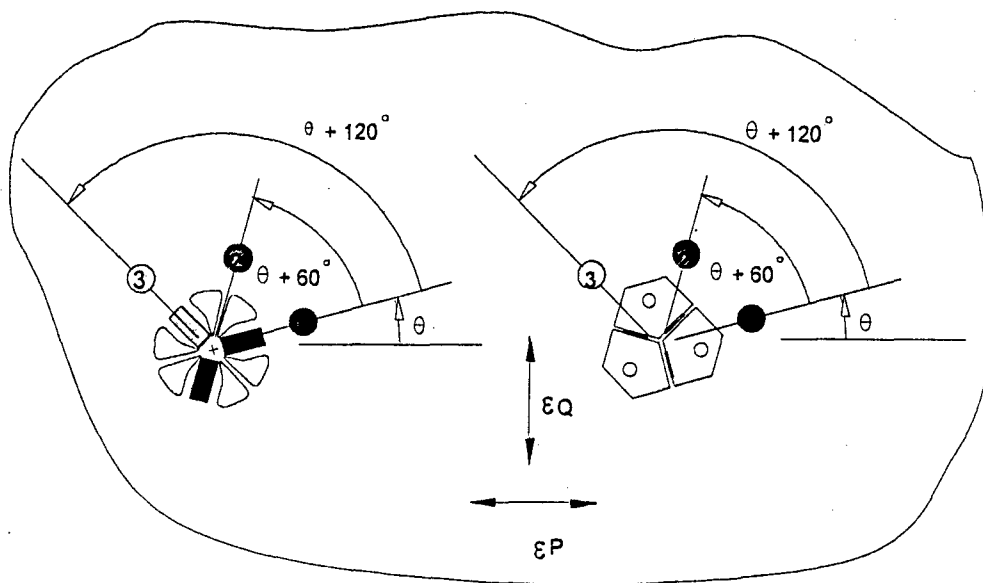


Figure D.1. Delta rosette (at left) installed on a test surface, with Grid 1 at the angle from the major principal strain direction, ( $\theta$ ). Delta extensometer shown at right, with "grid" directions aligned identically with the delta rosette.

From these values, the strain transformation relationships for a planar state of strain are applied to calculate the principal strain magnitudes ( $\epsilon_p, q$ ) and their direction. The direction is indicated as the angle  $\theta$ , and is drawn from the principal maximum or minimum strain axis to a "reference grid", shown as grid 1 in Figure D.1. To determine whether the angle,  $\theta$ , is drawn from the principal maximum or minimum axis, several conditions are checked, described below. Figure D.2 shows the grid directions superimposed on Mohr's circle for strain. The geometry of the circle is the basis for the equations presented below. Note that  $\theta$  as measured on the part is represented as  $2\theta$  on Mohr's circle.

Plane strain refers to situations where the deformations of the material take place within parallel planes, and are the same in each of these planes. The use of strain transformation relationships which assume a state of plane strain is a simplifying assumption in this thesis.

To calculate principal strains ( $\epsilon_p, q$ ) and their direction ( $\theta$ ) for a 60 degree delta rosette, or the delta extensometer, substitute the individual strains  $\epsilon_1$ ,  $\epsilon_2$ , and  $\epsilon_3$  into the following equations:

$$\epsilon_{p,q} = \frac{\epsilon_1 + \epsilon_2 + \epsilon_3}{3} \pm \frac{\sqrt{2}}{3} \sqrt{(\epsilon_1 - \epsilon_2)^2 + (\epsilon_2 - \epsilon_3)^2 + (\epsilon_3 - \epsilon_1)^2}$$

$$\theta = \frac{1}{2} \tan^{-1} \left[ \frac{\sqrt{3}(\varepsilon_3 - \varepsilon_2)}{2\varepsilon_1 - \varepsilon_2 - \varepsilon_3} \right]$$

Where:  $\theta$  is measured from principal axis to reference grid (grid 1).

( $\phi = -\theta$ ;  $\phi$  measured from the reference grid on the strain gage rosette or the extensometer to the principal strain axis)

It is necessary to check for several conditions in order to determine whether the angle  $\phi$  is to the principal maximum or minimum axis ( $\phi_P$  or  $\phi_Q$ , respectively).

The conditions checked are:

- (a) if  $\varepsilon_1 > (\varepsilon_2 + \varepsilon_3) / 2$ , then  $\phi_{P,Q} = \phi_P$
- (b) if  $\varepsilon_1 < (\varepsilon_2 + \varepsilon_3) / 2$ , then  $\phi_{P,Q} = \phi_Q$
- (c) if  $\varepsilon_1 = (\varepsilon_2 + \varepsilon_3) / 2$ , and  $\varepsilon_2 < \varepsilon_1$ , then  $\phi_{P,Q} = \phi_P = -45$  degrees
- (d) if  $\varepsilon_1 = (\varepsilon_2 + \varepsilon_3) / 2$ , and  $\varepsilon_2 > \varepsilon_1$ , then  $\phi_{P,Q} = \phi_P = +45$  degrees
- (e) if  $\varepsilon_1 = \varepsilon_2 = \varepsilon_3$ , then  $\phi_{P,Q}$  is indeterminate (equal biaxial strain)

Maximum shear strain can be written as:

$$\gamma_{\max} = \varepsilon_p - \varepsilon_q$$



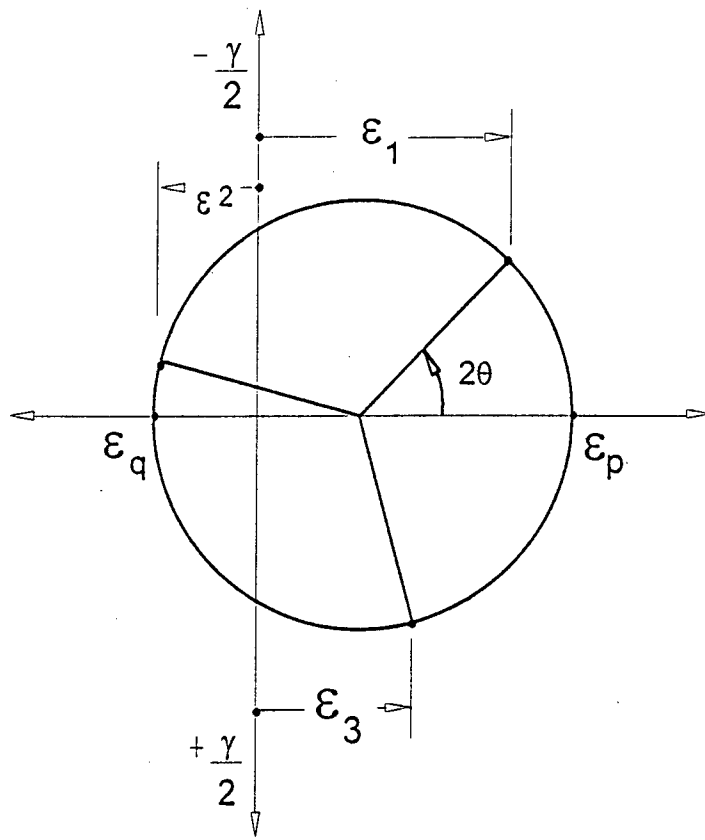


Figure D.2. The rosette grid axes superimposed on Mohr's circle for strain. Note that Grid 2 is to be viewed as +60 degrees (CCW) from Grid 1 in the rosette, and +120 degrees in Mohr's circle.

The Mohr's circle shown above is constructed with positive shear strain plotted downward. This is done so that the positive rotational direction in Mohr's circle is the same (CCW) as for the rosette, while maintaining the usual sign convention for shear (i.e., positive shear corresponds to a reduction in the initial right angle at the origin of the X-Y axes).

**Bibliography**

ASTM Standards E-83-96 (1996) Standard Practice for Verification and Classification of Extensometers. American Society for Testing and Materials, Philadelphia, PA.

Bacon GE, Bacon PJ, Griffiths RK (1979) The orientation of apatite crystals in bone. *J. Appl. Cryst.* 12: 99-103.

Baxter LK (1997) Capacitive Sensors Design and Applications. IEEE Press: Piscataway, NJ.

Biewener AA, Fazzalari NL, Konieczynski DD, Baudinette RV (1996) Adaptive changes in trabecular architecture in relation to functional strain patterns and disuse. *Bone* 19(1): 1-8.

Bishop, O (1995) Understand Electronics. Newnes Butterworth Heinemann, Oxford Press. ISBN 0 7506 2100 1.

Black J (1988) Orthopaedic Biomaterials in Research and Practice. New York: Churchill Livingstone.

Burr DB, Milgrom C, Fyhrie D, Forwood M, Nyska M, Finestone A, Hoshaw S, Saig E, Simkin A. (1996) In Vivo Measurements of Human Tibial Strains During Vigorous Activity. *Bone*, 18(5):05-410.

Buttermann GR, Janevic JT, Lewis JL, Lindquist CM, Wood KB, Schendel MJ (1994) Description and application of instrumented staples for measuring *in vivo* bone strain. *J. Biomechanics* 27: 1087-1094.

Carter DR, Harris WH, Caler WE (1981) The mechanical and biological response of cortical bone to *in vivo* strain histories. In Cowin SC (ed.) Mechanical Properties of Bone, The American Society of Mechanical Engineering, 45:81-92.

Carter DR, Spengler DM (1982) Bone in Clinical Orthopaedics: Biomechanics of Fracture, Edited by G. Sumner-Smith, W.B. Saunders Co., Toronto.

Cavanagh PR, Davis BL, Miller TA (1992) A biomechanical perspective on exercise countermeasures for long-term spaceflight. *Space and Environmental Medicine*, 63: 482-485.

Chang WC, Christensen TM, Pinilla TP, Keaveny TM (1999) Uniaxial yield strains for bovine trabecular bone are isotropic and asymmetric. *Journal of Orthopedic Research*, 17(4):582-5.

Courtney AC, Wachtel EF, Myers ER, Hayes WC. (1995) Age-related reductions in the strength of the femur tested in a fall loading configuration. *Journal of Bone and Joint Surgery*, 77A:387-395.

Courtney AC, Perusek GP, Davis BL, Sferra J, Kambic HE (1997) External impact loading and tibial strains in cadaveric lower limbs. Presented at *International Society of Biomechanics Conference*, Toyko, Japan.

Cowin SC (1997) Posture load-induced bone maintenance – A new hypothesis, NASA Funded Project # 199-26-17-04.

D'Andrea SE (1998) Lower limb response to impact in simulated microgravity and 1G. Ph.D. dissertation. The Ohio State University, Biomedical Engineering Department.

Davis BL, Cavanagh PR, Sommer HJ (1996) Ground reaction forces during locomotion in simulated microgravity. *Aviation Space and Environmental Medicine*, 67(3):235-242.

De Clercq D, Aerts P, Kunnen M (1994) The mechanical characteristics of the human heel pad during foot strike in running: a in vivo cineradiographic study. *J. Biomechanics* 27: 1213-1222.

Evans FG (1973) Mechanical Properties of Bone. Springfield, Illinois: Charles C Thomas.

Foster RL (1989) Linear capacitive reactance sensors for industrial applications. In *Proceedings of the 40<sup>th</sup> Annual Earthmoving Industry Conference*. Peoria, Illinois.

Fukashiro S, Komi PV, Jarvinen M, Miyashita M (1995) *In vivo* achilles tension loading during jumping in humans. *European Journal of Applied Physiology and Occupational Physiology*, 71(5): 453-458.

Goldstein SA, Matthews LS, Kuhn JL, Hollister SJ (1991) Trabecular bone remodeling: an experimental model. *Journal of Biomechanics*, 24(1):135-150.

Greenspan SL, Myers ER, Maitland LA, Resnick NM, Hayes WC (1994) Fall severity and bone mineral density as risk factors for hip fracture in ambulatory elderly. *Journal of the American Medical Association*, 271: 128-133.

Gross TS, Bain SD (1993) Skeletal adaptation to functional stimuli. Chapter 6 in Current Issues in Biomechanics, Mark D. Grabiner, Ed. Human Kinetics Publishers, Champaign, IL., pp. 151-164. ISBN 0-87322-387-X.

Hert J, Liskova M, Landa J (1971) Reaction of bone to mechanical stimuli. Part I. Continuous and intermittent loading of tibia in rabbit. *Folia Morph (Prague)* 19:290-300.

Holman JP (1976) Experimental Methods for Engineers, 3<sup>rd</sup> Edition. McGraw-Hill Kogakusha, Ltd. Publishers., pp. 41-46. ISBN 0-07-029601-4.

Hoshaw SJ, Fyhrie DP, Takano Y, Burr DB, Milgrom C (1997) A method suitable for *in vivo* measurement of bone strain in humans. *J. Biomech.* 30(5):521-524.

Ichiro O, Burr DB, Turner CH, Qiu J, Tu Y, Onyia JE, Duncan RL (1997) Mechanotransduction in bone: osteoblasts are more responsive to fluid forces than mechanical strain. *American Journal of Physiology* 273: (Cell Physiology) C810-C815.

Jaworski ZFG, Uhtoff HK (1986) Reversibility of nontraumaatic disuse osteoporosis during its active phase. *Bone*, 7: 431-439.

Kakurin, LI (1972) Medical investigations carried out according to the flight program of the scientific orbiting satellite station "Salyut." *USSR Ministry of Health and USSR Academy of Science, Moscow.*

Keaveny TM, Hayes WC (1993) Mechanical properties of cortical and trabecular bone. *Bone* 7:285-344.

Keaveny TM, Wachtel EF, Kopperdahl DL (1999) Mechanical behavior of human trabecular bone after overloading. *Journal of Orthopedic Research*, 17 (3): 346-53.

Lanyon LE, Hampson WGJ, Goodship AE, and Shah JS (1975) Bone deformation recorded *in vivo* from strain gauges attached to the human tibial shaft. *Acta Orthopaedica Scandinavia*, (46): 256-268.

Lanyon LE, Baggot DG (1976 -a) Mechanical function as an influence on the structure and form of bone. *Journal of Bone and Joint Surgery*, 58-B(4):436-43.

Lanyon LE, Goodship AE, Baggot DG (1976 -b) The significance of bone strain *in vivo*. *Acta Orthopaedica Belgica*, (42) Suppl. 1: 109-122.

Lanyon LE, Rubin CT (1984) Static vs. dynamic loads as an influence on bone remodelling. *Journal of Biomechanics*, 17(12): 897-90.

Leblanc AD, Schneider VS, Evans HJ, Engelbretson DA, Krebs JM (1990) Bone mineral loss and recovery after 17 weeks of bed rest. *Journal of Bone and Mineral Research*. 5(8):843-850.

Mack PB, LaChance PA, Vose VP, Vogt FB (1967) Bone demineralisation of foot and hand on Gemini-Titan IV, V and VII astronauts during orbital flight. *Am J Roentgenol* 100: 503-11.

McLeod KJ, Bain SD, Rubin CT (1990) Dependence of bone adaptation on the frequency of induced dynamic strains [Abstract] *Transactions of the 36<sup>th</sup> Orthopaedic Research Society*, 36:103.

McNitt R, Gray JL (1993) Kinetic of the lower extremities during drop landings from three heights. *Journal of Biomechanics*, 26(9): 1037-46.

Measurements Group, Strain Gage Selection Procedures, Tech Note 505. (On the web at [www.measurementsgroup.com](http://www.measurementsgroup.com)).

Meyer H (1867) Die Architektur der Spongiosa. *Arch. F. Anat. Und Physiol.* XLVII: 615-628.

Michel MC, Guo XE, Gibson LJ, McMahon TA, Hayes WC (1993) Compressive fatigue behavior of bovine trabecular bone. *J. Biomechanics* 26: 453-463.

Milgrom C, Burr DB, Fyhrie DP, Hoshaw SJ, Nyska M, LieberGall M, Finestone A, Simkin A (1997) A comparison of the effect of shoe gear on human tibial axial strains measured in vivo [Abstract] *Transactions of the 43rd Orthopaedic Research Society*.

Milgrom C, Finestone A, Benjoya N, Simkin A, Ekenman I, Burr DB (1998) Measurement of strain and strain rate developed by jumping exercises *in vivo* in humans [Abstract] *Proceedings of the 17<sup>th</sup> Southern Biomedical Engineering Conference*, Feb. 6-, San Antonio, Texas, 108.

MTS Systems Corporation Product Manual for 632 Series Extensometers, Eden Prairie, MN. (On the web at [www.mts.com](http://www.mts.com)).

Nunamaker DM, Butterweck DM, Provost MT (1990) Fatigue fractures in thoroughbred racehorses: Relationships with age, peak bone strain, and training. *J. Orthoped. Res.* 8:604-611.

Pierson, J.G. (1999) The Art of Practical and Precise Strain Based Measurement. Pierson and Associates, Ltd., Ontario, Canada. 2nd Edition. ISBN 1 895976 00 6.

Qin YX, Rubin CT, McLeod KJ (1998) Nonlinear Dependence of Loading Intensity and Cycle Number in the Maintenance of Bone Mass and Morphology. *J. Orthop. Res.* 16 (4), 482-489.

Rambaut P, Goode A (1985) Skeletal changes during space flight. *The Lancet*, 1050-1052.

Rambaut PC, Smith MC Jr., Mack PB, Vogel JM (1975) Skeletal Response. In: *Biomedical Results of Apollo*. RS. Johnson, L.F. Dietlein, and C.A. Berry (eds.), (Document SP-377). Washington, D.C., pp. 303-322.

Reilly, DT and Burstein, AH (1975) The elastic and ultimate properties of compact bone. *Journal of Biomechanics*, 8:393-405.

Rolf C, Westblad P, Ekenman I, Lundberg A, Murphy N, Lamontagne M, Halvorsen K (1997) An experimental *in vivo* method for analysis of local deformation on tibia, with simultaneous measures of ground reaction forces, lower extremity muscle activity and joint motion. *Scand. J. Med. Sci. Sports* 7: 144-151.

Rubin CT, Lanyon LE (1982) Limb mechanics as a function of speed and gait; A study of functional strains in the radius and tibia of horse and dog. *Journal of Experimental Biology* 101: 187-211

Rubin CT (1984) Skeletal strain and the functional significance of bone architecture. *Calcified Tissue International* 36: S11-S18.

Rubin CT, Lanyon LE (1984) Dynamic strain similarity in vertebrates: an alternative to allometric limb bone scaling. *J. Theor. Biol.* 107: 321-327.

Rubin CT, Lanyon LE (1985) Regulation of bone mass by mechanical strain magnitude. *Calcified Tissue International*, 37: 411-417.

Rubin CT, McLeod KJ, Brand RA, Lanyon LE (1987). Reversal of disuse osteopenia by controlled dynamic loading [Abstract]. *Transactions of the 33<sup>rd</sup> Orthopaedic Research Society*, 33: 351.

Schneider VS. (1990) Space medicine considerations: skeletal and calcium homeostasis. Workshop on Exercise Prescription for Long-Duration Space Flight. *NASA Conference Proceedings 3051* (Eds. B.A. Harris, Jr., and D.F. Stewart), pp. 47-52.

Schneider VS, McDonald J (1984) Skeletal calcium homeostasis and countermeasures to prevent disuse osteoporosis. *Calcified Tissue International*, 36: S 1S 1-S 154.

Scott S, Winter D (1990) Internal forces at chronic injury sites. *Med. Sci. Sports Exerc.* 22: 357-369.

Sedlin ED (1965) A Rheological Model for Cortical Bone. *ACTA Orthopaedica Scandinavica*, S83.

Sessions, N De V, Halloran, BP, Bikle DD, Wronski TJ, Cone CM, Morey-Holton ER (1989) Bone response to normal weight bearing after a period of skeletal unloading. *American Journal of Physiology*, 257: E606-E610.

Skerry TM, Lanyon LE (1995) Interruption of disuse by short duration walking exercise does not prevent bone loss in the sheep calcaneus. *Bone*, 16(2):269-274.

Smith RW Jr, Keiper DA (1965) Dynamic measurement of viscoelastic properties of bone. *American Journal of Medical Electronics* 4(4):156-60.

Swartz SM, Bennett MB, Carrier DR (1992) Bone loading during flight: An in vivo strain analysis of large fruit bats. From *Proceedings of NACOB II, The Second North American Congress on Biomechanics*, Chicago IL.

Szivek JA, Anderson PL, DeYoung DW (1997) *In vivo* strain measurements collected using calcium phosphate ceramic-bonded strain gauges. *J. Invest. Surg.* 10(5):263-273.

Thomas T, Vico L, Skerry TM, Caulin F, Lanyon LE, Alexandre C, Lafage MH (1996) Architectural modifications and cellular response during disuse-related bone loss in calcaneus of the sheep. *Journal of Applied Physiology*, 80(1): 198-202.

Thompson, D'A W (1942) On Growth and Form. Cambridge University Press. The complete revised edition. Dover Publications, New York, NY.

Tilton FE, Degioanni JJC, Schneider VS (1980) Long-term follow up of Skylab bone demineralization. *Aviation, Space, and Environmental Medicine*, 51(11): 1209-1213

Tipton CM (1983) Considerations for exercise prescriptions in future space flights. *Medicine and Science in Sports and Exercise*, 15(5): 441-444.

Turner CH (1989) Yield behavior of bovine cancellous bone. *Journal of Biomechanical Engineering*, 111: 256-260.

Turner CH, Forwood MR, Otter MW (1994) Mechanotransduction in bone: do bone cell act as sensors of fluid flow? *FASEB J.* 8:875-878.

Vaughan CL, Davis BL, O'Conner JC (1992) Dynamics of Human Gait. Champaign Illinois: Human Kinetics Publishers.

Vrijkkotte T (1991) A biomechanical comparison between vertical jumping and jumping in simulated zero-gravity. Unpublished Master's Dissertation Vrije Universiteit, Amsterdam. The Netherlands.

Webster JG (ed.) (1985) *Medical Instrumentation: Application and Design*, 2<sup>nd</sup> Edition. John Wiley & Sons, Inc., New York. ISBN 0 471 12493 1

Whedon GD (1984) Disuse osteoporosis: physiological aspects. *Calcified Tissue International*, 36, S 146-S 150.

Whedon GD, Lutwak L, Rambaut PC, Whittle MW, Smith MC, Reid J, Leach C, Stadler CR, Sanford DD (1977) Mineral and nitrogen metabolic studies, experiment M071. In RS Johnston, LF Dietlein (eds.), *Biomedical Results From Skylab* (pp. 164-174). NASA SP377. NASA, Washington.

Weinbaum S, Cowin SC, Zeng Y (1994) A model for the excitation of osteocytes by mechanical loading-induced bone fluid shear stresses. *J. Biomechanics* 27: 339-360.



Yerby SA, Ehteshami JR, McLain RF (1997) Loading of pedicle screws within the vertebra. *J. Biomechanics* 30: 951-954.

Yettram AL, Camilleri NN (1993) The forces acting on the human calcaneus. *J. Biomed. Eng.* 15: 46-50.

Zernicke RF, Vailis AC, Salem GJ (1990) Biomechanical response of bone to weightlessness. *Exercise and Sport Science Reviews*. 18: 167-192.

### Author Publications and Abstracts From This Research

Perusek GP, Davis BL, Perry JE, Sferra JJ: A multi-axial extensometer for global measurement of bone strain suitable for use *in vivo* in humans. In Proceedings of the 6<sup>th</sup> International Symposium on the 3D Analysis of Human Movement. International Society of Biomechanics, Cape Town, South Africa, (May 1-4, 2000).

G.P. Perusek, B.L. Davis, A.C. Courtney, S.E. D Andrea: An extensometer for global measurement of bone strain suitable for use *in vivo* in humans. Accepted for Publication in Journal of Biomechanics.

B.L. Davis, S.E. D'Andrea, G. Perusek, T. Orlando: Quantifying biomechanical characteristics of jumping exercises in 1G and in simulated and true microgravity. First Biennial Space Biomedical Investigators workshop, League City, Texas, (Jan 11-13, 1999).

S.E. D'Andrea, B.L. Davis, G. Perusek, A. C. Courtney: *In vivo* calcaneal strain during jumping exercises, 45th Annual Meeting of the Orthopaedic Research Society, Anaheim, (Feb 1-4, 1999).

S.E. D Andrea, B.L. Davis and G.P. Perusek: Ground reaction forces during countermovement jumps in simulated and true microgravity. 46th Annual Meeting of the American College of Sports Medicine, Seattle WA, (1999).

S.E. D'Andrea, B.L. Davis, D. Lord, A.C. Courtney, G.P. Perusek: External impact loads on the lower extremity during jumping in simulated microgravity and the relationship to internal bone strain. Submitted to Acta Astronautica, 1997.

Courtney, A.C., Perusek, G.P., Davis, B.L., Sferra, J., and Kambic, H.E. "External impact loading and tibial strains in cadaveric lower limbs." XVI meeting of the International Society of Biomechanics, Tokyo, Japan (1997).

D'Andrea, S.E., Davis, B.L., Courtney, A.C., and Perusek, G.P. "External impact loads on the lower extremity during jumping in simulated microgravity and the relationship to internal bone strain." The 12th Man in Space Symposium, Washington, D.C., (June 8-13, 1997).

Davis, B.L., D'Andrea, S., Lord, D., Courtney, A.C., and Perusek, G.P. "Lower limb response to impact loads in 1G and micro-G." Symposium on the Effects of Microgravity on the Musculoskeletal System, Session G-5 at the 44th Annual Meeting of the American College of Sports Medicine, Denver, CO (May 28-31, 1997).



US006059784A

# United States Patent [19]

Patent Number: 6,059,784

Perusek

[45] Date of Patent: May 9, 2000

[54] CAPACITIVE EXTENSOMETER  
PARTICULARLY SUITED FOR MEASURING  
IN VIVO BONE STRAIN

5,919,192 7/1999 Shouts ..... 606/102

[75] Inventor: Gail P. Perusek, Lakewood, Ohio

[73] Assignee: The United States of America as  
represented by the Administrator of  
the National Aeronautics and Space  
Administration, Washington, D.C.

### OTHER PUBLICATIONS

C.T. Rubin et al. "Regulation of Bone Mass by Mechanical Strain Magnitude." published in *Calcified Tissue International*, 1985, 37:411-417.

S.C. Corwin. "Posture Load-Induced Bone Maintenance—A New Hypothesis." published in NASA-funded Project #199-26-17-04 in 1997.

G.D. Whedon. "Disuse Osteoporosis: Physiological Aspects." published in *Calcified Tissue International* in 1984, 36, S146-S150.

P.C. Rambaut et al. "Skeletal Response." published in 1975 in *Biomedical Results of Apollo*, prepared by R.S. Johnson et al, Document SP-377—Washington, D.C., pp. 303-322.

M.C. Michel et al. "Compressive Fatigue Behavior of Bovine Trabecular Bone." published in 1993—*J. Biomechanics* 26:453-463.

C. Milgrom et al. "A Comparison of the Effect of Shoe Gear on Human Tibial Axial Strains Measured In Vivo" Abstract from ORS 43rd Annual Mtg., Feb. 1997.

[21] Appl. No.: 09/179,355

[22] Filed: Oct. 8, 1998

[51] Int. Cl.<sup>7</sup> ..... A61B 17/56

[52] U.S. Cl. .... 606/54; 606/102

[58] Field of Search ..... 606/54, 102, 57,  
606/59

### [56] References Cited

#### U.S. PATENT DOCUMENTS

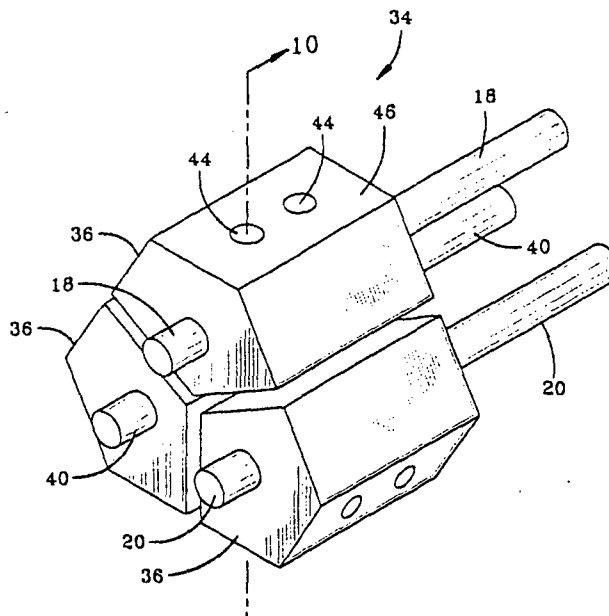
3,577,883	5/1971	Werner .	
3,995,696	12/1976	Kainer et al. .	
4,141,349	2/1979	Ory et al. .	
4,160,325	7/1979	DeNicola .	
4,251,918	2/1981	Duggan .	
4,576,158	3/1986	Boland .....	606/102
4,607,531	8/1986	Meline et al. .	
4,628,583	12/1986	Barnett .	
4,939,445	7/1990	Meline et al. .	
4,964,862	10/1990	Arms .....	606/102
5,289,826	3/1994	Kovacevic .....	606/102
5,334,202	8/1994	Carter .....	606/102
5,360,016	11/1994	Kovacevic .....	606/102
5,402,684	4/1995	Engeler et al. .	
5,425,775	6/1995	Kovacevic et al. ....	606/102
5,456,724	10/1995	Yen et al. .	
5,695,496	12/1997	Orsak et al. .	

*Primary Examiner*—Michael Buiz  
*Assistant Examiner*—Daphna Shai  
*Attorney, Agent, or Firm*—Kent N. Stone

### [57] ABSTRACT

The present invention provides for in vivo measurements of the principal strain magnitudes and directions, and maximum shear strain that occurs in a material, such as human bone, when it is loaded (or subjected to a load). In one embodiment the invention includes a capacitive delta extensometer arranged with six sensors in a three piece configuration, with each sensor of each pair spaced apart from each other by 120 degrees.

7 Claims, 14 Drawing Sheets



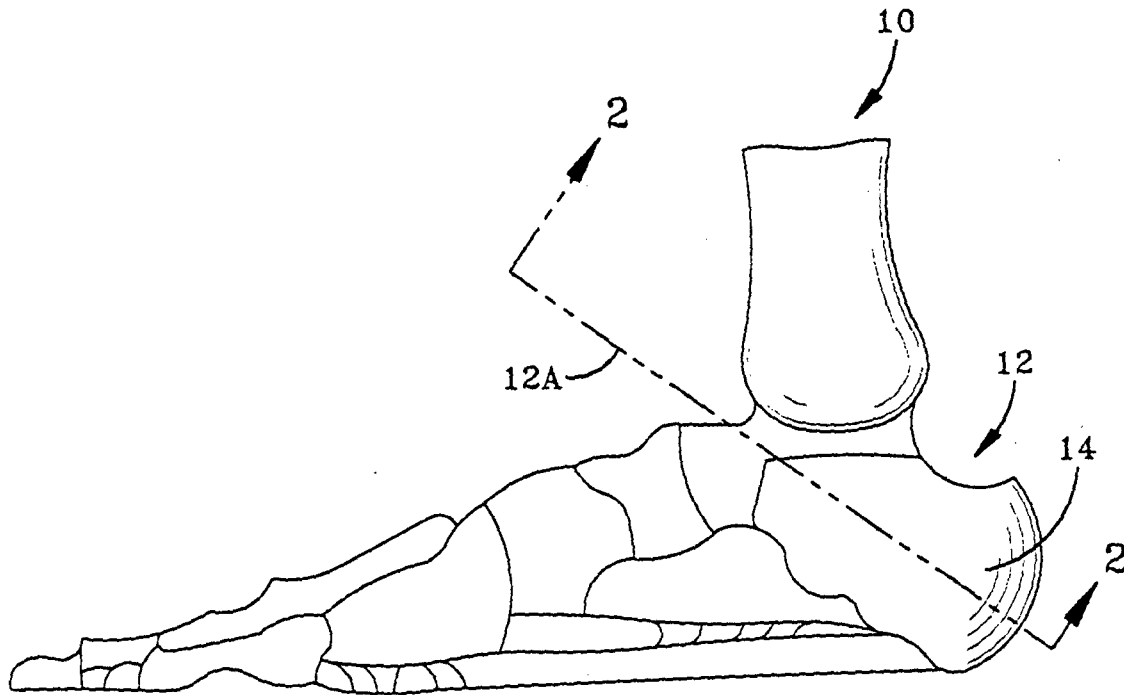


FIG-1(A)

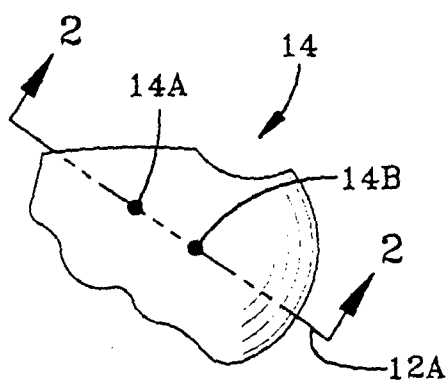


FIG-1(B)

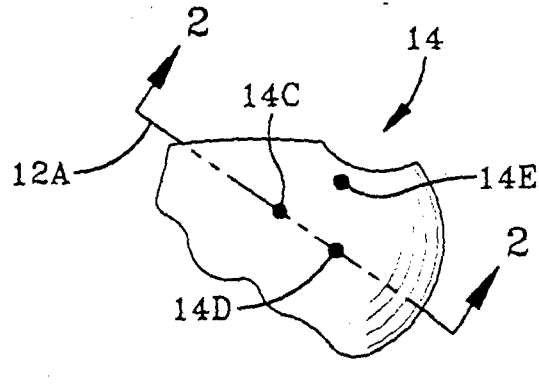


FIG-1(C)

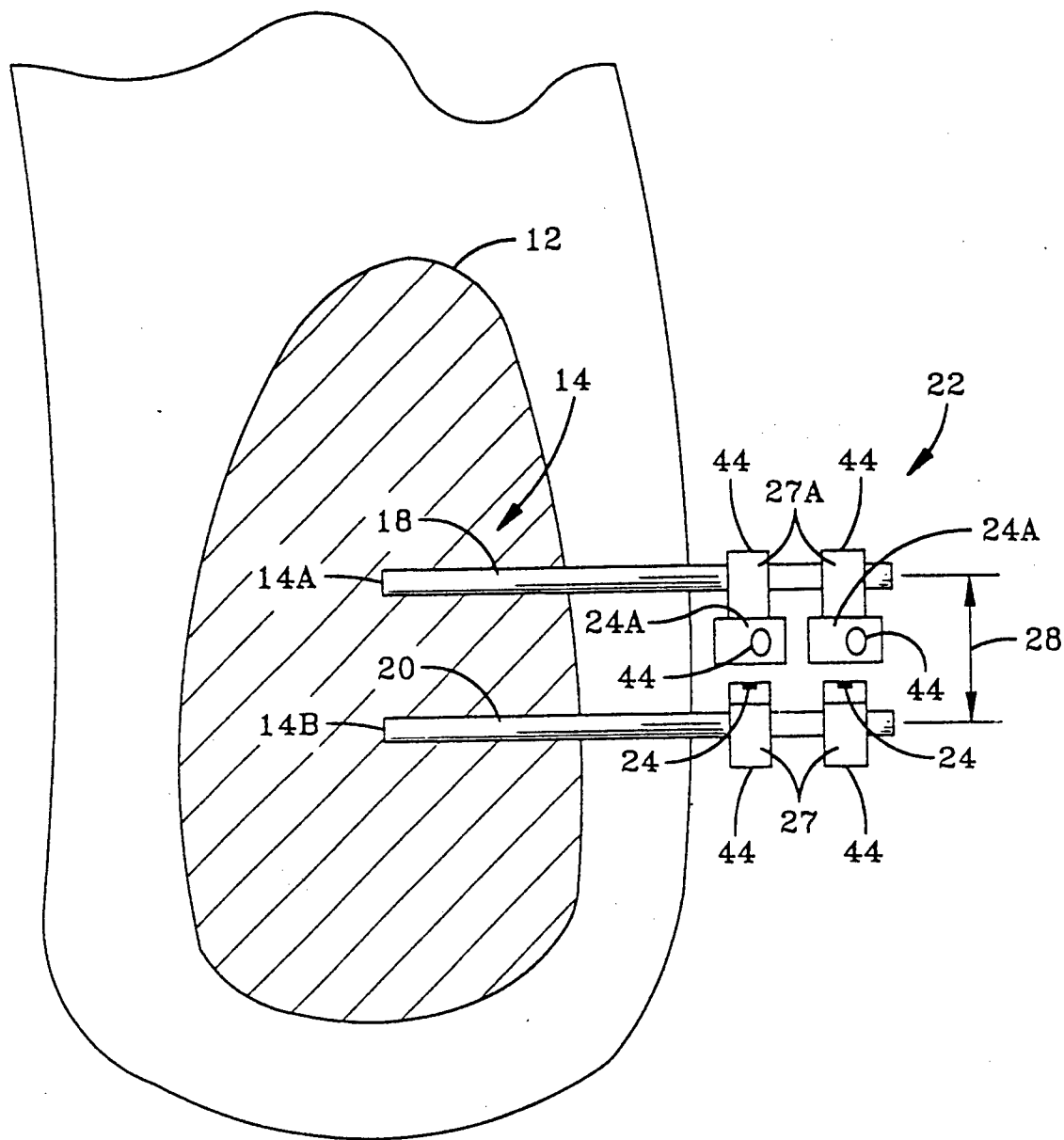


FIG-2  
(SECTION 2-2)

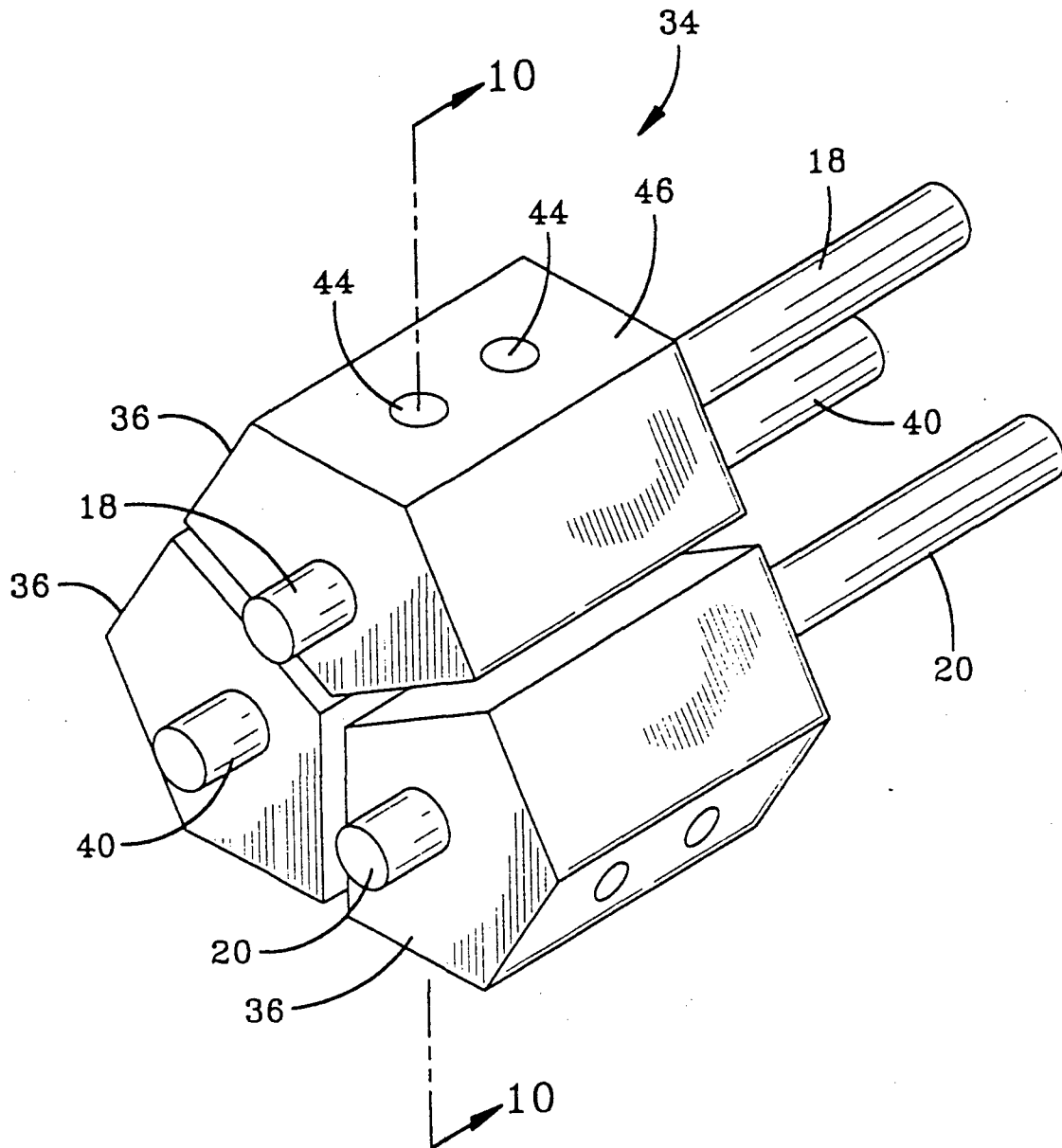


FIG-3

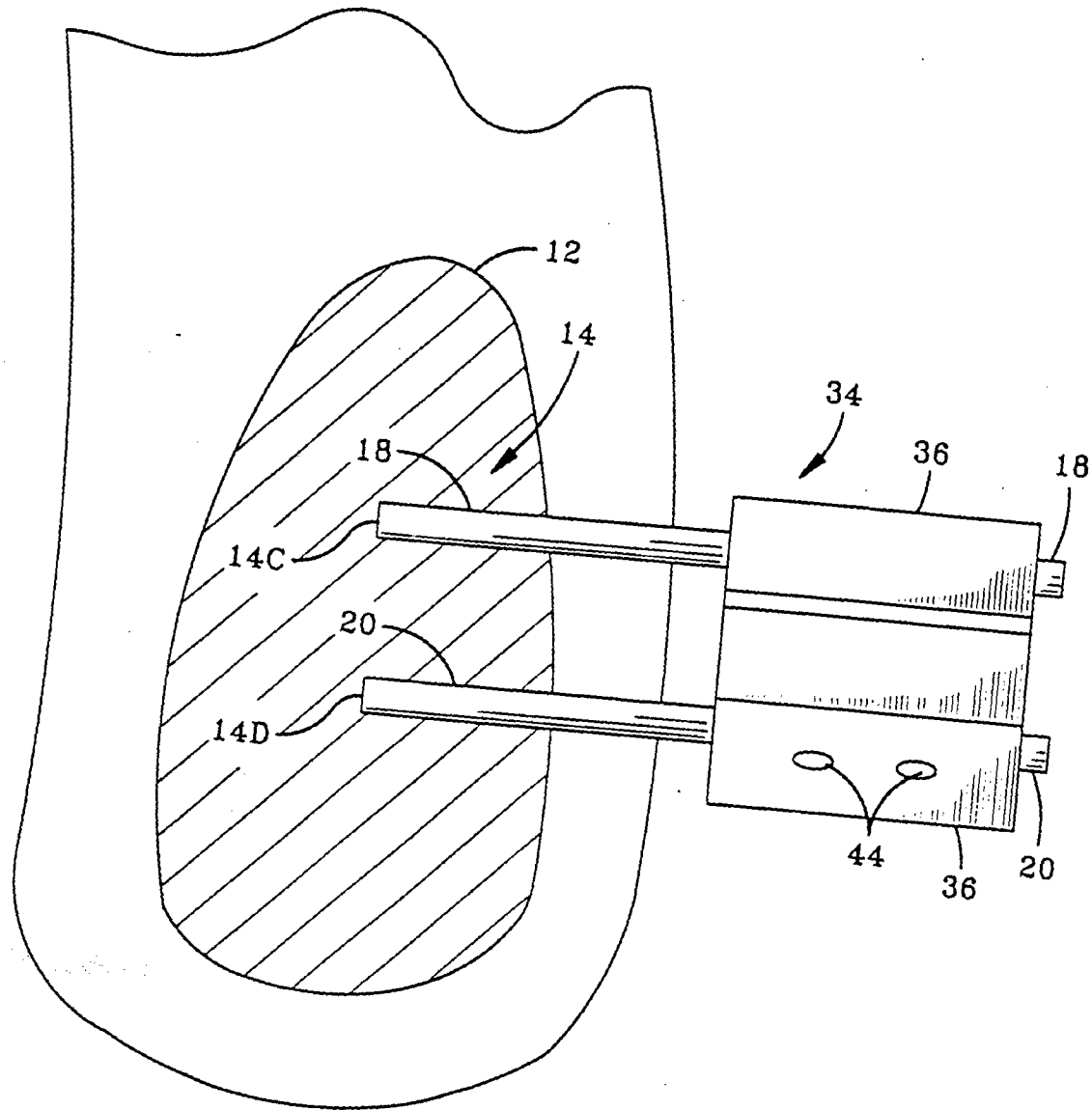


FIG-4

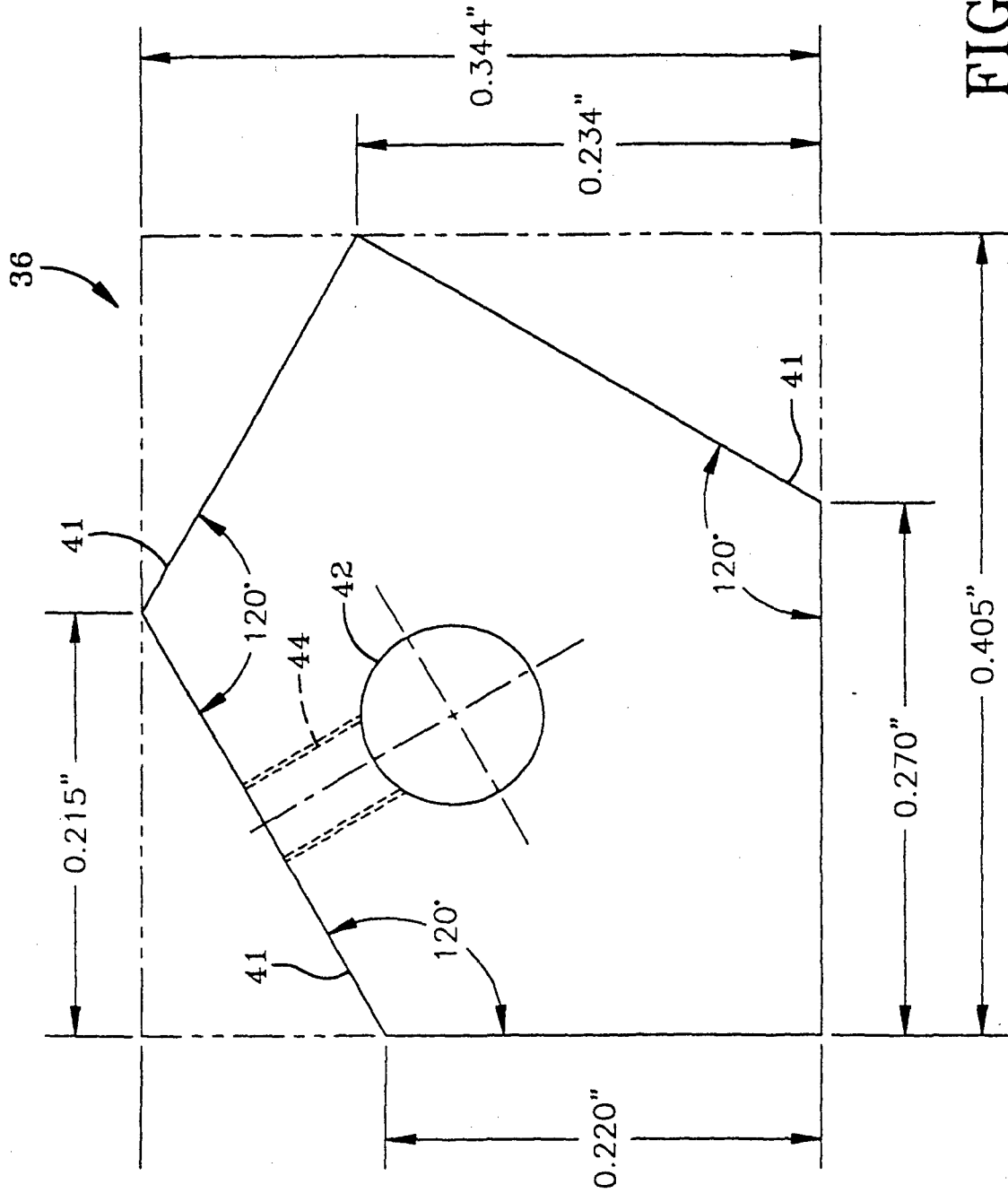


FIG-5



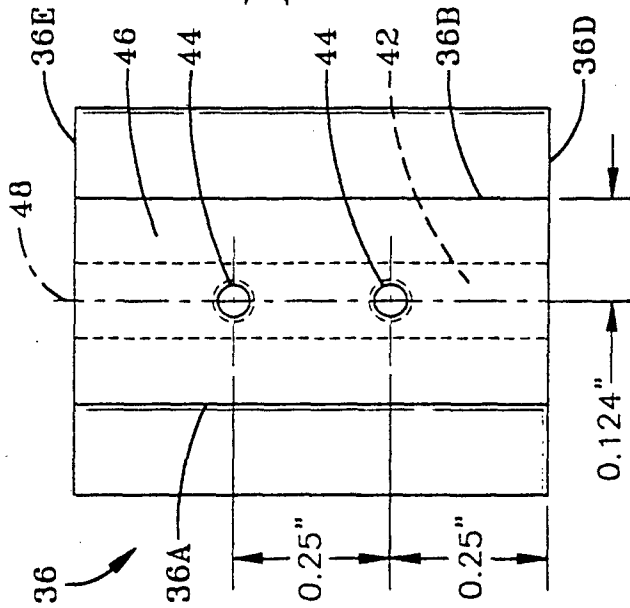


FIG-6(A)

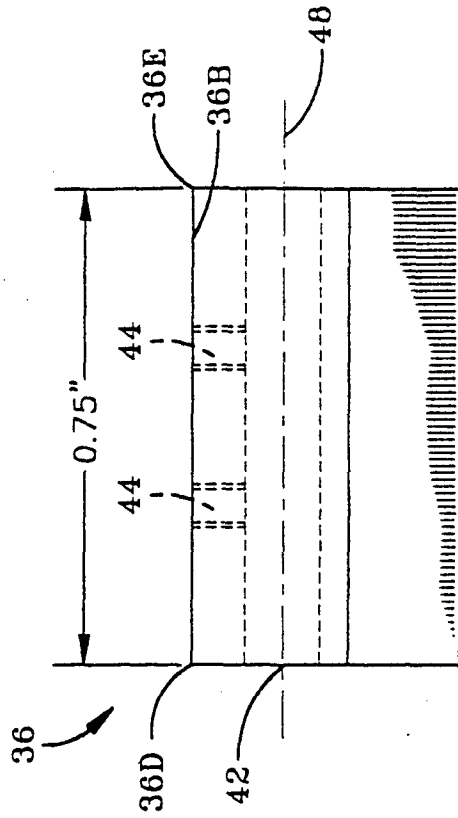


FIG-6(B)

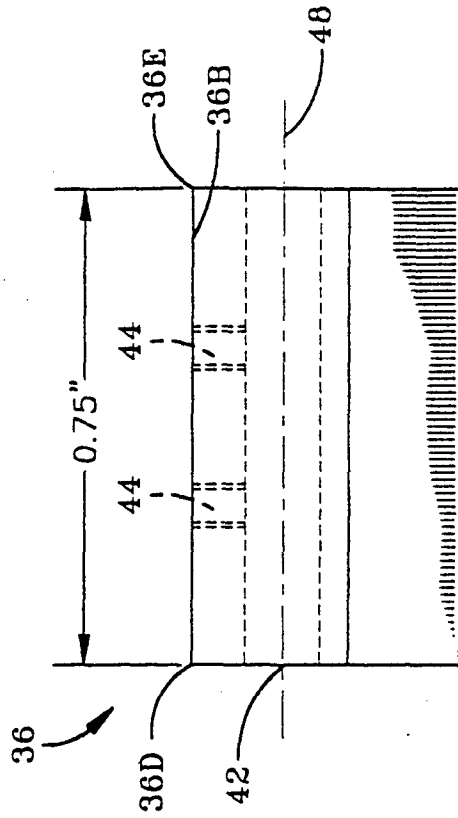


FIG-6(C)

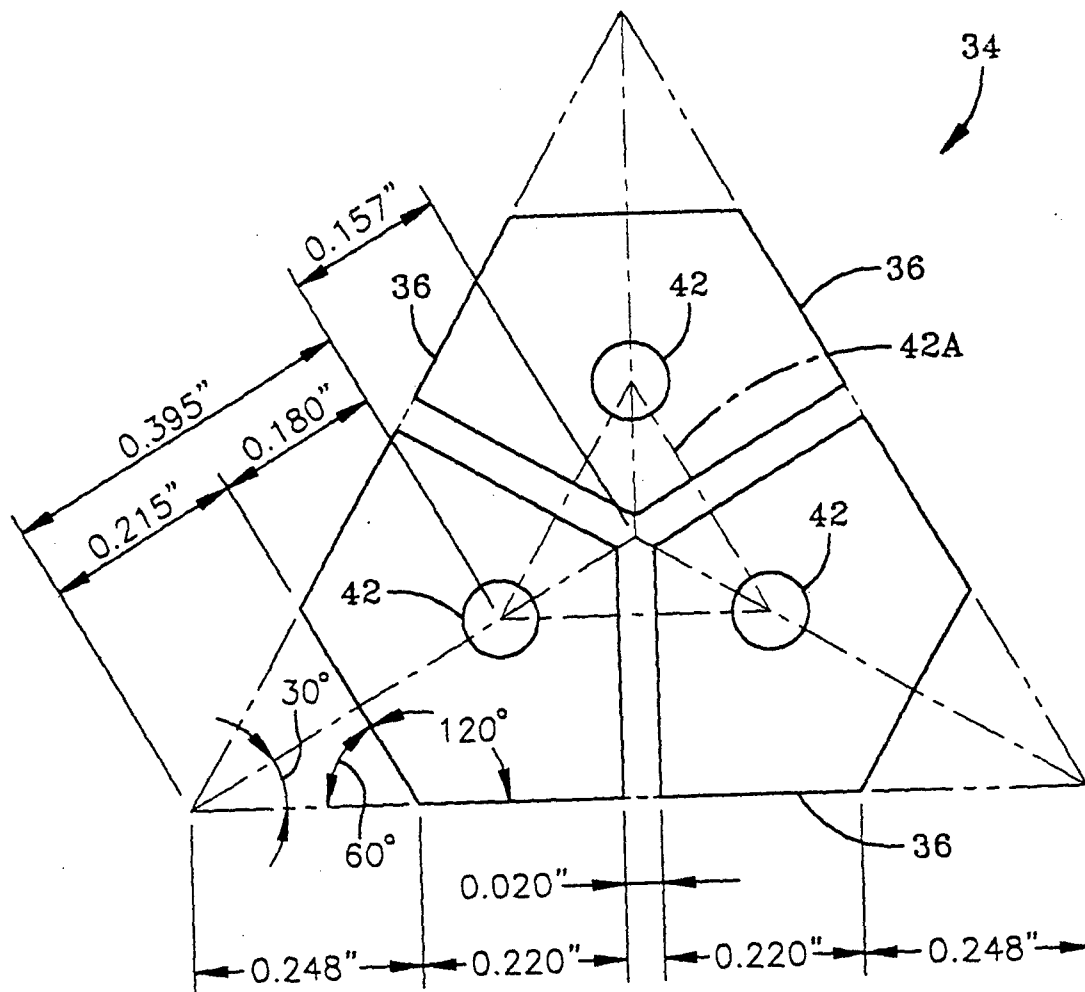


FIG-7(A)

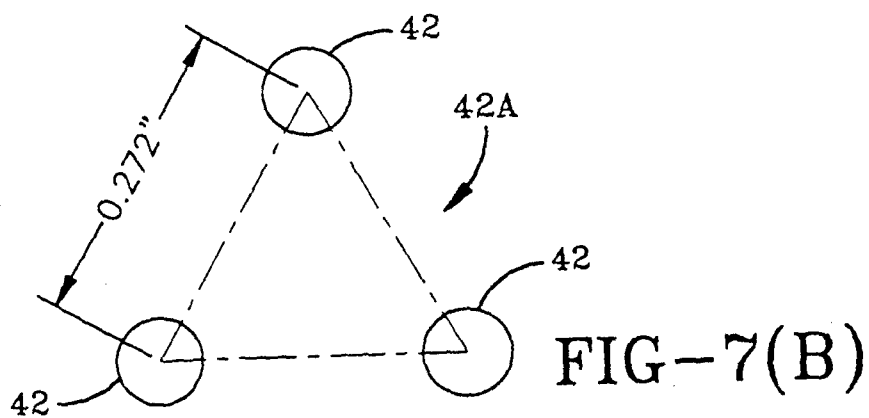


FIG-7(B)

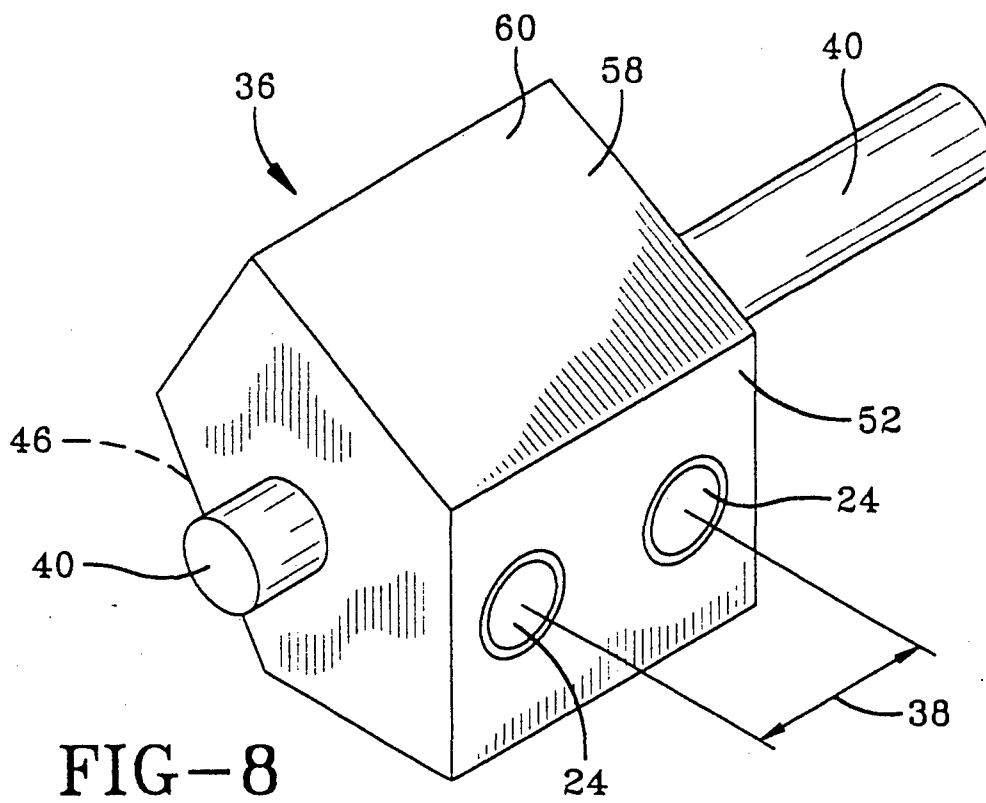


FIG-8

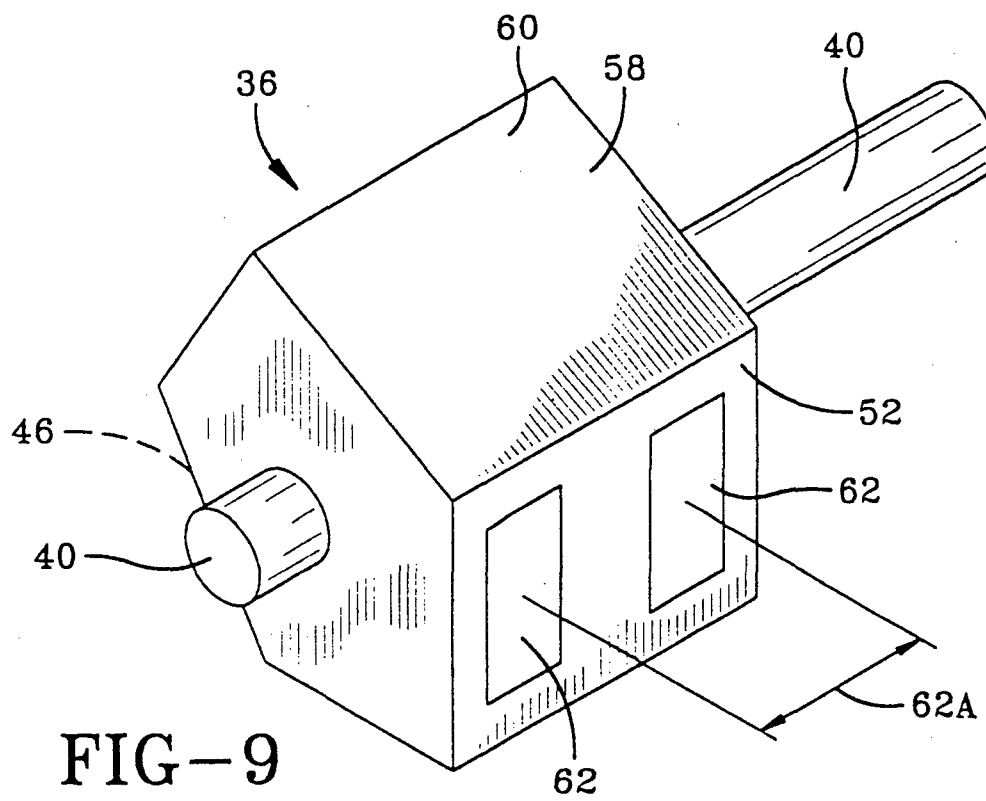


FIG-9

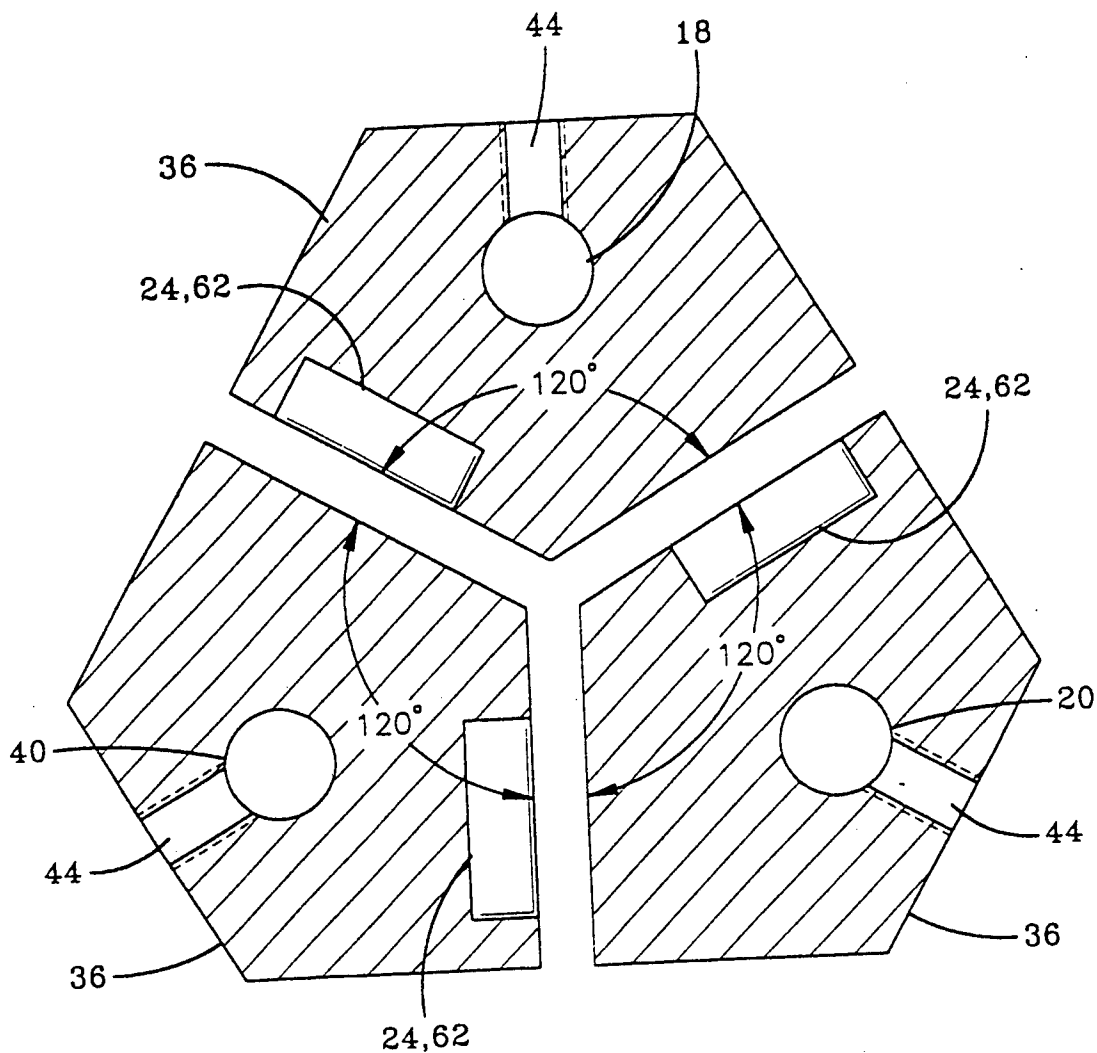


FIG-10  
(SECTION 10-10)

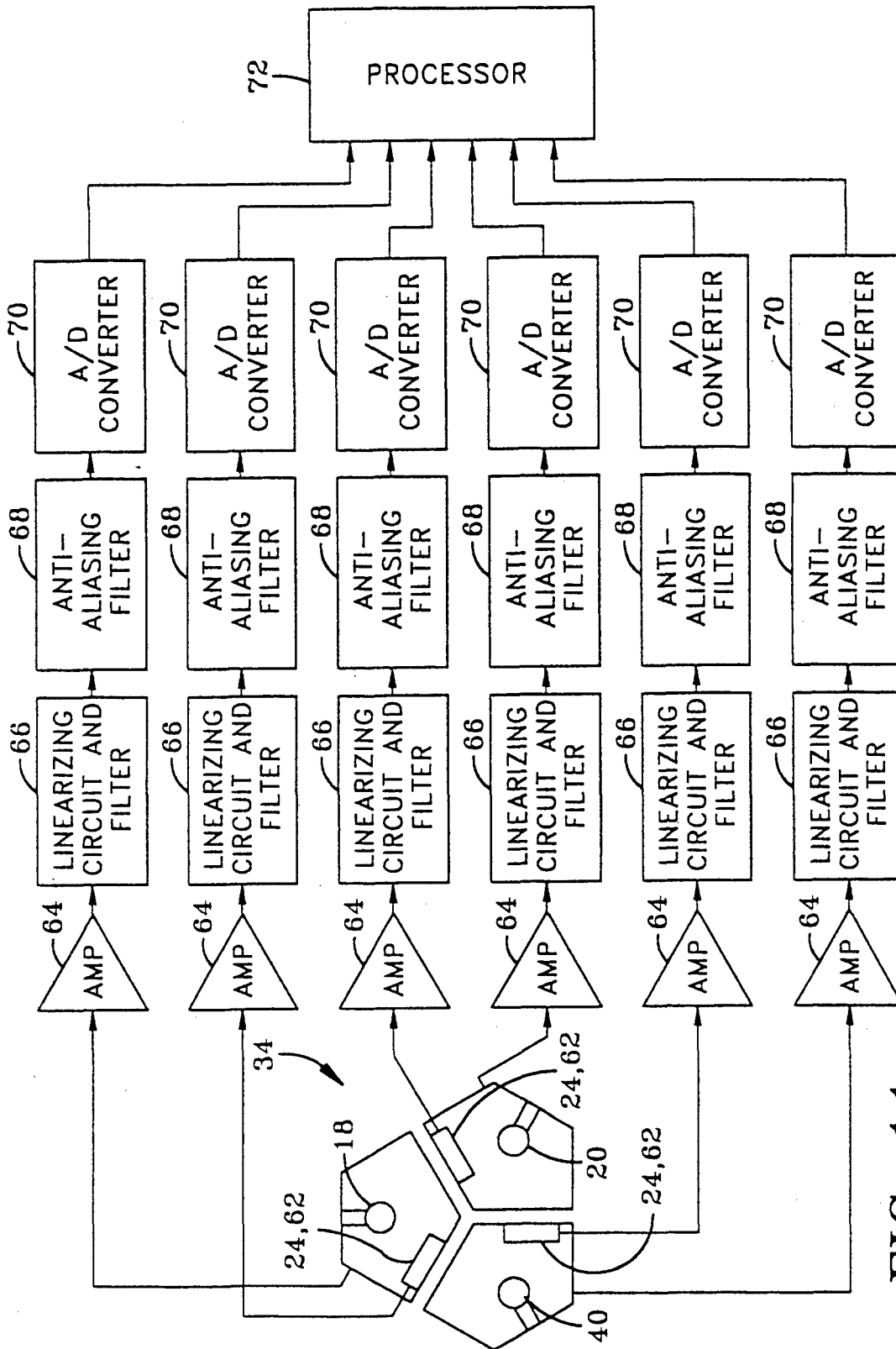
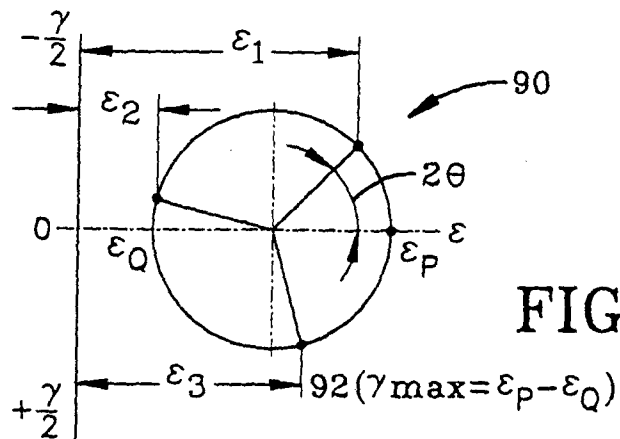
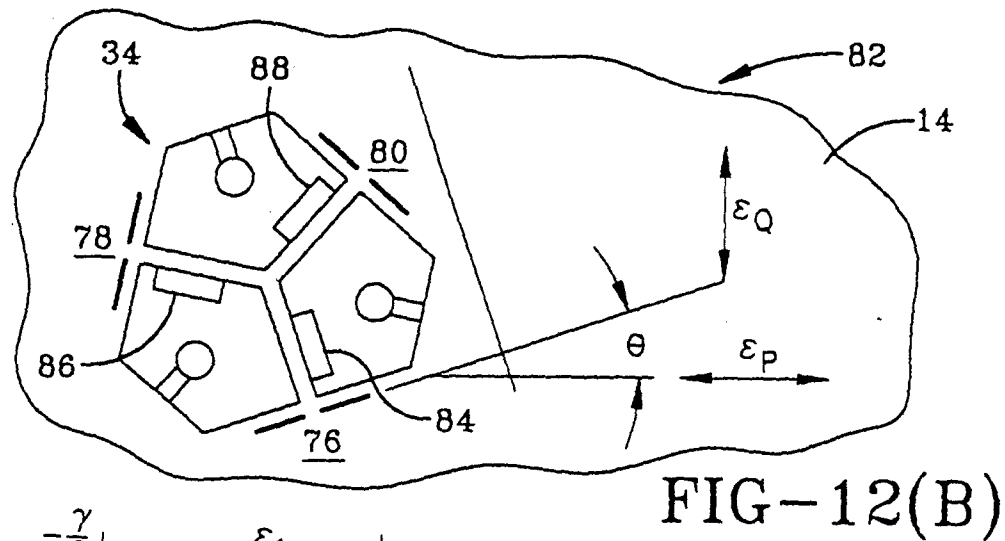
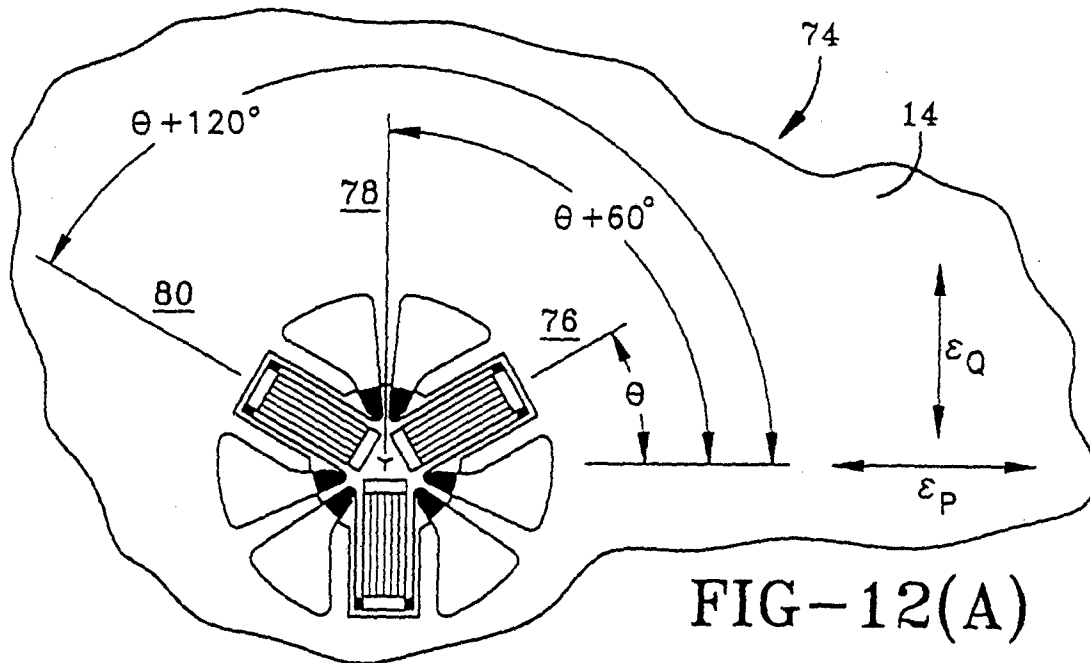


FIG-11



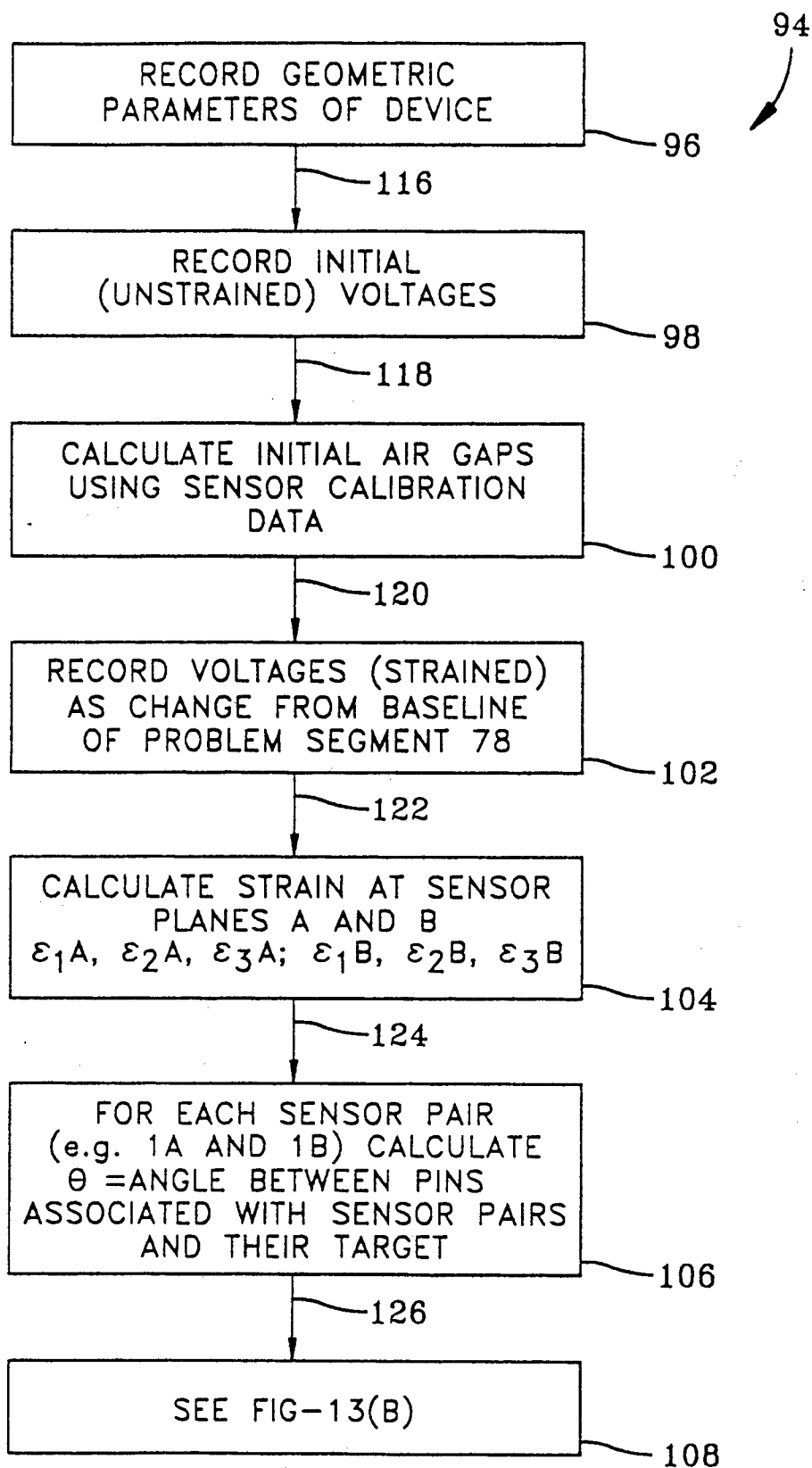


FIG-13(A)

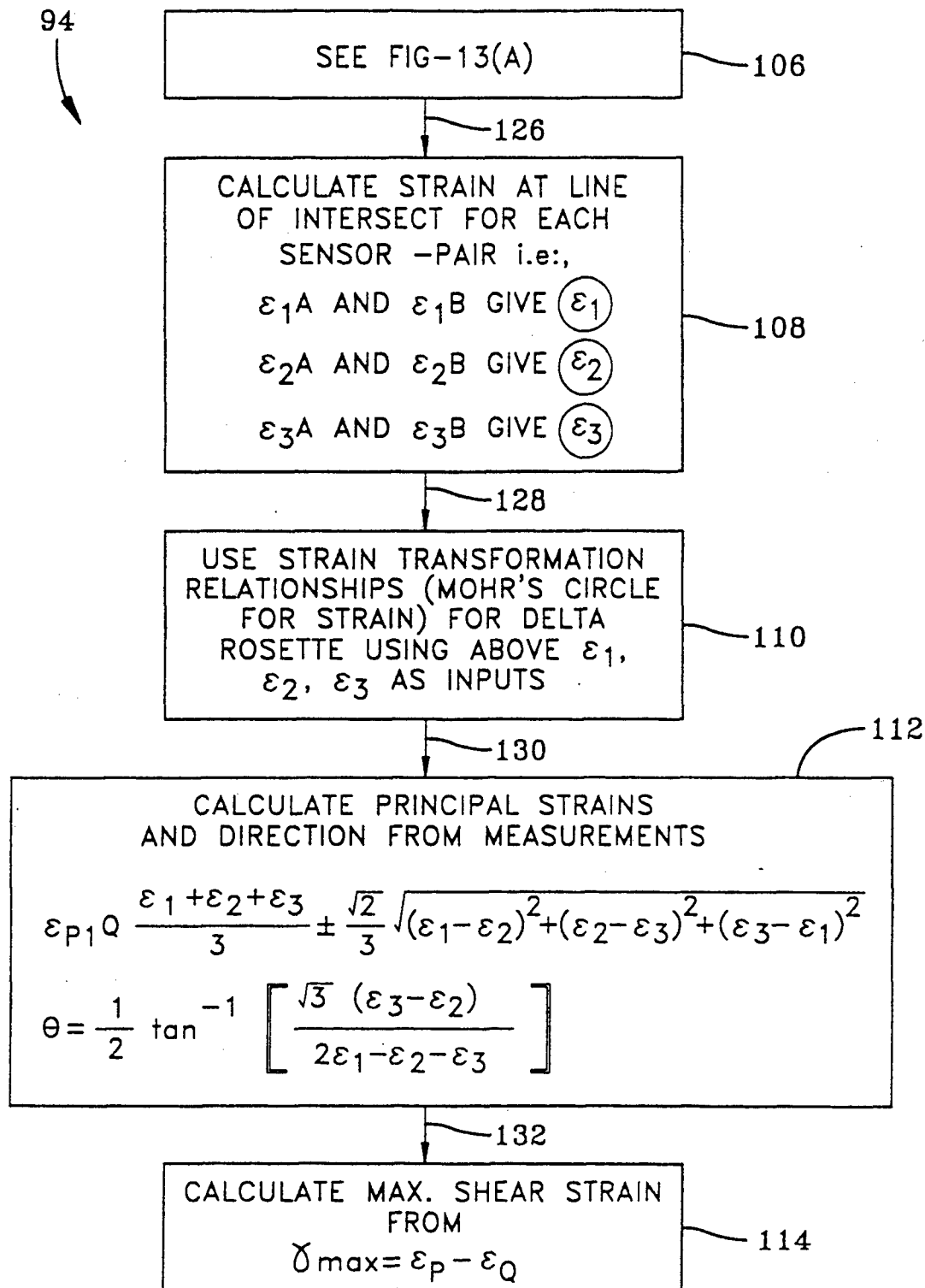


FIG-13(B)



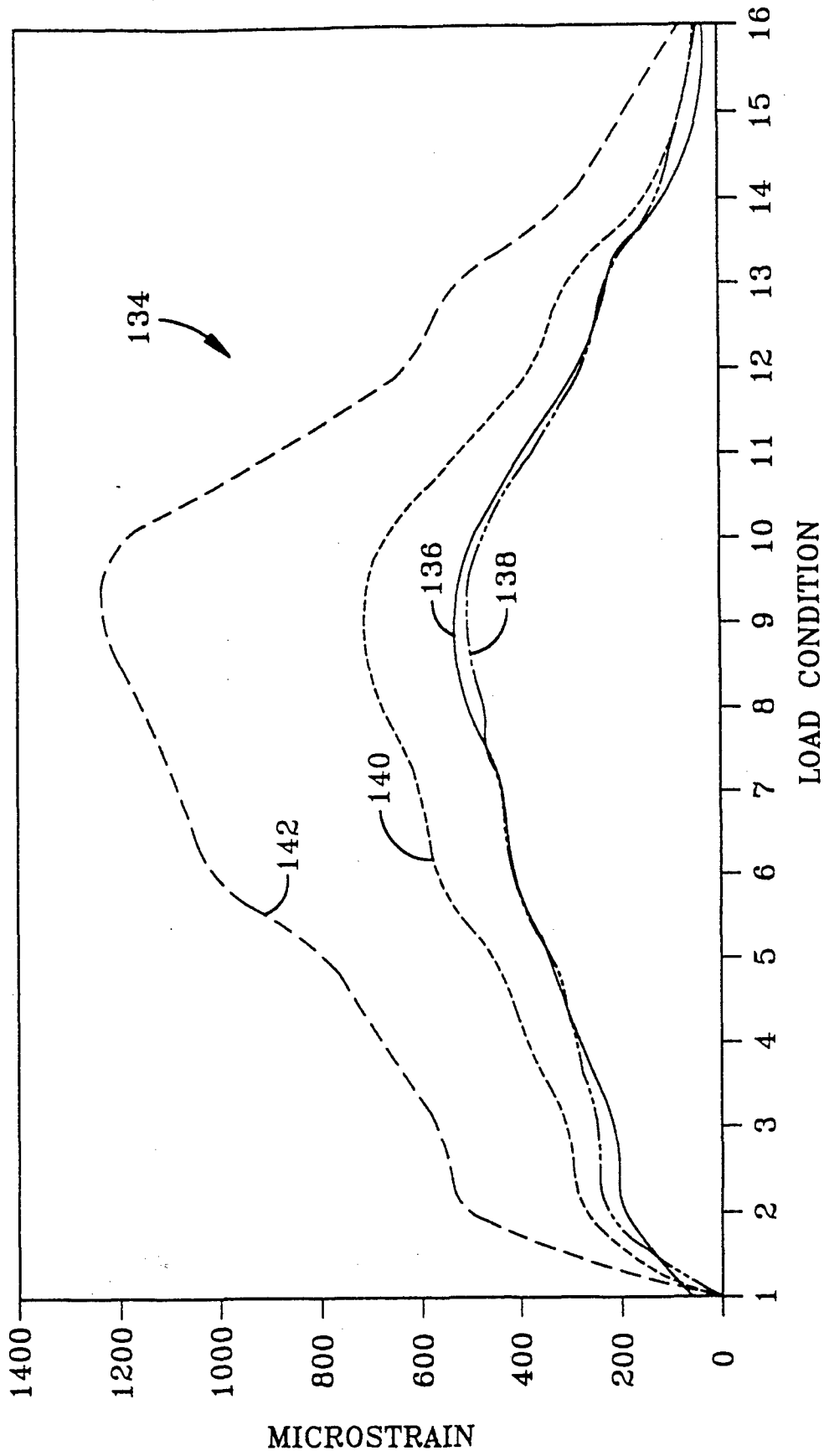


FIG-14

## CAPACITIVE EXTENSOMETER PARTICULARLY SUITED FOR MEASURING IN VIVO BONE STRAIN

### ORIGIN OF THE INVENTION

The invention described herein was made by an employee of the United States Government, and may be manufactured and used by or for the Government for governmental purposes without the payment of any royalties thereon or therefor.

### FIELD OF THE INVENTION

This invention relates to a extensometer for measuring the strain in a specimen. More particularly, the present invention relates to measuring the in vivo bone strain of a mammal. Specifically, the present invention relates to an extensometer, and a method of operation thereof, that measures the principal strain magnitudes and directions, and maximum shear strain that occurs within bones of a human when subjected to strain.

### BACKGROUND OF THE INVENTION

The ability of bone to form optimal structures to support loads and adapt structurally to changing loads is termed the "strain-adaptive remodeling response." The exact nature of the mechanical remodeling signal, or osteogenic stimulus, is not fully understood. However, several mechanical parameters have been proposed, including strain magnitude, frequency, and rate. It is thought that 1 to 2 Hz events during locomotion produce levels of strain on the order of 1000 to 3000 microstrain (or 0.1 to 0.3%), and are osteogenic in nature. These 1 to 2 Hz events are more fully described by Rubin C T and Lanyon L E, in the 1985 technical article "Regulation of Bone Mass by Mechanical Strain Magnitude," published in *Calcified Tissue International*, 37:411-417, which is herein incorporated by reference.

Further, it has been proposed that higher frequency events (15 to 25 Hz) of lower magnitude (100 to 250 microstrain), possibly associated with muscular contractions to maintain posture, are of importance in maintaining bone mass. These 15 to 25 Hz events are more fully described by Cowin, S C, in the 1997 report "Posture Load-Induced Bone Maintenance—A New Hypothesis" disclosed in NASA-funded Project #199-26-17-04, which is herein incorporated by reference. Removing this stimulus in environments such as those encountered during space flight will inhibit the process of bone deposition. It is well documented that bone loss is a physiologic effect of space flight. For example, this bone loss is more fully described by Rambaut P C, Smith M C Jr., Mack P B, Vogel J M, in the 1975 report "Skeletal Response" published in *Biomedical Results of Apollo* prepared by R S. Johnson, L. F. Dietlein, and C. A. Berry (eds.), (Document SP-377), Washington, D.C., pp. 303-322, which is herein incorporated by reference. In addition, this bone loss is also more fully described by Whedon, G. D., in the 1984 technical article "Disuse Osteoporosis: Physiological Aspects," published in *Calcified Tissue International*, 36, S146-S150, which is herein incorporated by reference. Thus, the accurate measurement of strain within this range of frequencies (1-25 Hz) and amplitudes (100-3000 microstrain ( $\mu\epsilon$ )) is important for understanding the relationships between mechanical loading and bone remodeling.

A variety of methods exist for measuring animal bone strain in vitro and in vivo and are described, for example, U.S. Pat. Nos. 5,456,724 and 5,695,496, both of which are

herein incorporated by reference. Local strain in trabecular bone has been measured using optical devices to track the displacement of markers on individual trabeculae such as a method used by Michel M. C., et al in the technical article "Compressive Fatigue Behavior of Bovine Trabecular Bone," published in 1993—*J. Biomechanics* 26:453-463, and herein incorporated by reference.

Global strain has been measured in the tibia using metal-foil type strain gages adapted to intracortical pins that protrude from the skin as disclosed by Milgrom C., et al in "A Comparison of the Effect of Shoe Gear on Human Tibial Axial Strains Measured In Vivo" Abstract from ORS 43rd Annual Mtg., February 1997, and herein incorporated by reference.

The most common method has been to use metal foil type strain gages (for example, unstacked rosettes) bonded directly to the bone cortex. Surface-mounted gages are considered the standard for measuring cortical bone strain in vitro and in animal models in vivo. In humans, however, the use of surface-mounted gages is limited for several reasons: the compatibility of bonding material with living tissue is a problem (cyanoacrylate-based adhesives, which is the standard bonding material, are potentially carcinogenic), the level of invasiveness is high, and proper surface preparation, which is difficult to achieve on bone, is essential for obtaining reliable measurements. Among these methods, gages adapted to intracortical pins offer a less invasive and potentially more reliable way of obtaining in vivo strain data.

Surface-mounted strain gages when arranged in a rosette can provide principal strains and directions, and maximum shear strains within the plane of the gage. However, in the case of bone, where the moduli of cortical and trabecular bone vary greatly, surface strain gages mounted to the bone cortex are questionable indicators of global strain in trabecular bone. Further, if strains due to bending are to be calculated, surface gages must be mounted on opposing faces of the specimen, which is difficult to accomplish in vivo. Intracortical pins, which extend into the trabecular structure, can conceivably be used to follow global deformations and provide a measure of global strain across a section of bone in bending. Assumptions must be made that strain gradients are linear, and that the pins do not themselves deform. Also, as with unstacked strain gage rosettes, a uniform strain field is assumed in planes that contain the gage, as the gage necessarily covers a finite area of the test surface. Macroscopic (or average) strain is what is measured. For this reason, a smaller gage length is better. Since the porosity of the underlying cancellous bone restricts how small the gage length may be, a balance must be achieved between accurately capturing the strain field and sizing the gage length appropriately for a given specimen porosity. This is left to the user to determine for their particular. It is desired that means be provided for measuring in vivo strain encountered by the bones of a human and to do so with accuracy.

### SUMMARY OF THE INVENTION

The present invention is directed to an extensometer, and a method of operation thereof, that measures intracortical pin displacement, from which strain is calculated, and from which, in a preferred embodiment, principal strain magnitudes and directions, maximum shear strain, and strains due to bending may be calculated via strain transformation relationships and geometric parameters of the extensometer.

The extensometer comprises at least two pins adapted to be inserted into the bone; and at least two capacitive sensors

mounted across the pins and providing a variable capacitance whose output is varied by the strain to which the bone is subjected.

In a preferred embodiment, six sensors are arranged into three pairs with each pair being attached to a five (5) sided member and oriented from each other pair by an angle of 120 degrees.

#### BRIEF DESCRIPTION OF THE DRAWINGS

For a better understanding of the nature and objects of the present invention, reference should be made to the following detailed description taken in conjunction with the accompanying drawings, in which like parts are given like reference numbers, and wherein:

FIG. 1 is composed of FIGS. 1(A), 1(B) and 1(C), wherein FIG. 1(A) is a schematic elevational view showing the foot of a human, in particular, the calcaneus of a human serving as a site for in-vivo measurements by the present invention, and wherein FIGS. 1(B) and 1(C) illustrates details of the sites.

FIG. 2 illustrates the in vivo placement of a double sensor extensometer of the present invention.

FIG. 3 illustrates the capacitive delta extensometer of the present invention.

FIG. 4 illustrates the in vivo placement of the capacitive delta extensometer of the present invention.

FIGS. 5 and 6 illustrate further details of the capacitive delta extensometer of FIG. 3.

FIG. 7 is composed of FIGS. 7(A) and 7(B) that illustrate the geometric parameters associated with each intracortical pin lying at the apex of an equilateral triangle which is the basis for placement of the five-sided members making up the capacitive delta extensometer of the present invention.

FIG. 8 illustrates further details of the capacitive delta extensometer of FIG. 4.

FIG. 9 illustrates another embodiment of a capacitive delta extensometer.

FIG. 10 is a cross-sectional view of the capacitive delta extensometer taken along line 10—10 of FIG. 3, and illustrates the orientation of pairs of the sensors thereof displaced from each other by 120 degrees.

FIG. 11 is a block diagram of the electronic equipment for processing the output signals generated by the capacitive delta extensometer of the present invention.

FIG. 12 is composed of FIGS. 12(A), 12(B) and 12(C) that illustrate strain transformations related to the present invention.

FIG. 13 is composed of FIGS. 13(A) and 13(B) and illustrates a flow diagram of the present invention.

FIG. 14 illustrates pilot results obtained from the practice of the double-sensor extensometer configuration of the present invention mounted in an acrylic specimen, with surface-mounted strain gage output plotted as a comparison.

#### DETAILED DESCRIPTION OF THE PREFERRED EMBODIMENTS

Referring now to the drawings, wherein the same reference number indicates the same element throughout, there is shown in FIG. 1 one application of the practice of the present invention. FIG. 1 is composed of FIGS. 1(A), 1(B) and 1(C), wherein FIG. 1(A) is a schematic view of the foot 10 of a human, in particular, the calcaneus 12 of a human serving as a site 14, running along line 12A, for in vivo measurement in accordance with the practice of the present invention

FIG. 1(B) illustrates one measurement site defined by two points 14A and 14B running along the line 12A and associated with two intracortical pins to be described. FIG. 1(C) illustrates another measurement site defined by three points 14C, 14D and 14E, with point 14C intercepting the line 12A and points 14D and 14E straddling the line 12A and with the three defining points 14C, 14D and 14E being associated with three intracortical pins to be described. The measurement site of interest is left to the user's discretion: in this example the line 12A is roughly aligned along the principal orientation of trabeculae in the calcaneus. Although FIGS. 1(B) and 1(C) show typical locations, the intracortical pins may be inserted anywhere that measurement is to be taken in accordance with the present invention.

The measurements of the present invention detect the deformation of the bone, such as the calcaneus 12, and which deformation is converted into electronic signals which are routed to a processor, having routines running therein, for calculating strain in the bone. The strain is detected by extensometers, one arrangement of which may be further described with reference to FIG. 2 which is a view taken along line 2—2 of FIG. 1.

FIG. 2 illustrates a double-sensor extensometer 22 that comprises at least two pins 18 and 20, respectively located at points 14A and 14B, already discussed with reference to FIG. 1(B), adapted to be inserted into the bone; and at least two capacitive sensors 24, made available by Capacitec, Inc., (Ayer, Mass.) with targets 24A mounted across the pins 18 and 20, respectively, and providing a variable capacitance whose output is varied by the strain experienced by bone 12. The targets 24A are conductive and grounded, and provide an adjustment capability so that the initial air gap may be changed. Targets 24A are held in place with set screws 44 (to be further described hereinafter). Sensors 24 are mounted to posts 27 which are insulated from the sensors. Targets 24A are mounted to posts 27A, which incorporate a machined end 29 (not shown) which is cylindrical in cross-section with a flat, against which the target set screw 44 rests. Posts 27 and 27A mount to pins 18 and 20. Posts 27 and 27A are held in place upon pins 18 and 20 by set screws 44 (not visible in view). The double-sensor extensometer 22 preferably has a guard ring 26 (not shown for the sake of clarity) made available from Capacitec Inc., and having a 0.156" inch outer ring preferably surrounding the sensors 24 and minimizing distortion, or fringing effects on the electrostatic field created by the capacitor. The outer edges of intracortical pins 18 and 20 are spaced apart from each other by a gage length 28. The gage length 28 is allowed to change, depending on the user's needs. For example, if the user expects high strain values within site 14, a larger gage length may be desired. On the other hand, if the user is interested in capturing more accurate strains, or the strain field beneath the gage is expected to have high strain gradients, the gage length 28 might need to be smaller. A gage length 28 of 0.524 inches may be a typical value to serve as a place to start these trade-off considerations by the user.

The sensors 24 may each be a non-contact displacement transducer made available from Capacitec, Inc., as their type HPB-75/156B-A-13-B-15-B-D probe. The intracortical pins 18 and 20 may each be comprised of stainless steel K-wire and have a diameter of 0.078 inches.

The double-sensor extensometer 22 has the at least two sensors 24 spaced some distance apart so as to define the angle between pins 18 and 20. Using geometric variables measured from the double-sensor extensometer 22 and displacement data from each of the two sensors 24, it is possible to calculate a corrected strain within the region of bone 12.

5

in a manner as to be described hereinafter with reference to FIG. 14. A further embodiment of the present invention may be further described with reference to FIG. 3.

FIG. 3 illustrates a herein termed "capacitive delta extensometer" 34, which has the benefits of an extensometer, known in the art, which is used to measure axial strain, as well as the additional benefits of providing principal strain magnitudes and direction, maximum shear strain, and strain due to bending. Further details of extensometers may be found in U.S. Pat. Nos. 4,160,325; 4,251,918; 4,607,531; and 4,939,445, all of which are herein incorporated by reference.

The capacitive delta extensometer 34 comprises three (3) identical five-sided members 36 each of which carry a pair of capacitive sensors 38 (not shown in FIG. 3) spaced apart from each other and oriented with respect to each pair by a value of 120 degrees, as will be further described hereinafter with reference to FIG. 10. The capacitive delta extensometer 34 carries three intracortical pins 18, 20 and 40.

The capacitive delta extensometer 34 is shown in FIG. 4 in a pictorial view as being embedded in the calcaneus bone 12 shown in cross-section of the foot 10. The intracortical pin 40 of FIG. 3 is out of view for the cross-section of FIG. 4, but all three pins 18, 20 and 40 are present and their placement is that of FIG. 1(C) having defining points 14C, 14D and 14E. The capacitive delta extensometer 34 may be further described with reference to FIG. 5.

FIG. 5 illustrates typical dimensions of the five-sided member 36, three of which members make up the capacitive delta extensometer 34 of the present invention. Although FIG. 5 illustrates the typical dimensions in great detail, the dimensions shown in FIG. 5 should not be considered as limiting features of the invention in any manner whatsoever.

The five-sided member 36 allows for the ability to orient the sensors 38 of the capacitive delta extensometer 34 by a preferred 120 degrees. More particularly, the five-sided member 36 has three corners identified with the reference number 41 and showing the angle of 120 degrees. These three corners may be used to obtain the desired orientation of 120 degrees between each pair of the sensors 38 to be described hereinafter with reference to FIG. 10. The five-sided member 36 has first and second apertures 42 and 44 respectively serving as the aperture through which either of the intracortical pins 18, 20 or 40 extends and the aperture through which set screw 44, is inserted so as to affix each of the five-sided members 36 to its related intracortical pin 18, 20 or 40. The five-sided member 36 may be further described with reference to FIG. 6 which is composed of

FIG. 6(A) shows a side 46, also shown in FIG. 3 along with apertures 44, of the five-sided member 36 which is herein termed "the set screw side." More particularly, side 46 is the side of the five-sided member 36 in which set screws (not shown) are inserted and screwed into aperture 44 having screw threads and a centerpoint which corresponds to the axis 48 of the five-sided member 36. The reference number 44 may be used in an interchangeable manner to identify "apertures 44" and "set screws 44." FIG. 6(A) further illustrates that each of the apertures 44 for the set screws are spaced apart from each other by a predetermined distance, such as 0.25 inches and with one of the apertures 44 spaced from a front edge of the five-sided member 36 by the same 0.25 distance. The axis 48 is also the axis for the aperture 42 and the axis 48 and is located at a predetermined distance such as 0.180 from top edges 36A and 36B which are also shown in FIG. 6(B). The distance the

6

pins 18, 20 and 40 are spaced apart from each other is similar to the gage length 28 of FIG. 2. FIG. 6(A) also shows outer edges 36D and 36E of the five-sided member 36 and which outer edges are shown in FIG. 6(C) having a typical separation of 0.75 inches.

The five-sided member 36 of FIGS. 5 and 6 provides for the proper alignment of the sensors 38 and also provides for the proper air gaps within a linear range of the sensors 38 so as to provide for proper operation of the capacitive delta extensometer 34. The capacitive delta extensometer 34 is mated to the three intracortical pins 18, 20 and 40 by way of aperture 42 with each pin positioned at the apex of an equilateral triangle provided by the three five-sided members 36 which may be further described with reference to FIG. 7 composed of FIGS. 7(A) and 7(B).

FIG. 7(A) illustrates three five-sided members separated from each other by a typical distance of 0.020 inches and arranged to form the capacitive delta extensometer 34 and also having typical dimensions shown therein, as well as interconnecting dimensional lines so as to indicate appropriate angles thereof. FIG. 7(A) shows an equilateral triangle 42A interconnecting the apertures 42. From the dimensions shown in FIG. 7(A), it may be determined that the sides of equilateral triangle 42A may each have a typical value of 0.272 inches as shown in FIG. 7(B).

From the parameters shown in FIGS. 7(A) and 7(B) and using a typical diameter of 0.078 inches for each of the intracortical pins 18, 20 and 40, it may be determined the gage length, that is the separation between pins 18, 20 and 40 is 0.350 inches (0.272+0.078).

In the assembly procedure for the capacitive delta extensometer 34, it is desired that a drilling guide be provided and used to ensure accurate placement of pins 18, 20 or 40 into specimen, such as site 14, and so that the pins 18, 20 and 40 are parallel to one another. Once the pins 18, 20 and 40 are in place, the five (5)-sided members 36 may be mounted to the pins 18, 20 and 40 and properly aligned. The arrangement shown in FIG. 7 may be used as a template for making a drill and placement guide for the capacitive delta extensometer 34. The capacitive delta extensometer 34 having the typical dimensions of FIGS. 5, 6 and 7 may be further described with reference to FIG. 8.

FIG. 8 illustrates one of three five-sided members 36 of capacitive delta extensometer 34 as having a face 52, that is its sensor face, positioned in the direction of the opposing target face, such as 58. The direction in which the five-sided member 36 is placed into the specimen 14 is not critical so long as the pins 18, 20 and 40 are long enough to extend into specimen 14. The five-sided member 36 further has a target face 58, as well as the set-screw side 46 of FIG. 6(A). The sensor face 52 has attached thereto two sensors 24, that is, a sensor pair, placed at a predetermined distance 38 apart from each other, and having a typical value of 0.50 inches. The sensor face 52 is positioned in the direction of the next five-sided member's 36 target face 58. The sensors 24 used in this embodiment of the capacitive delta extensometer 34 are disk-shaped "button probes," with a sensor O.D. of 0.075" and a linear range of 0.050", typical. The target face 58 has mounted to it a thin, conductive material 60 such as aluminized mylar (or aluminum tape) which is grounded. The conductive material 60 acts as one-half of the capacitor for each of sensor 24 opposing it in a manner similar to 24A in FIG. 2.

The function of each sensor pair comprised of the two sensors 24 is to define two points on the intracortical pin, such as pins 18, 20 and 40, such that the position of either

pin 18, 20 or 40 in two-dimensional (2D) space at any point along its length may be calculated. The displacement of pin 20 relative to pin 40, for example, is defined in the plane containing pins 20 and 40, and the displacement of pins 20 and 18, for example, is defined in the plane containing pins 20 and 18. In this way, the pin displacement measurement is analogous to measuring  $\%$  elongation of a single uniaxial gage element contained in a strain gage rosette arrangement known in the art. For such calculations, it is assumed that none of the pins 18, 20 and 40 deforms rather, their movement is defined as a translation plus a rotation within planes as described above. A further embodiment of the capacitive delta extensometer 34 may be further described with reference to FIG. 9.

FIG. 9 is similar to FIG. 8 with the exception that the capacitive sensors 24 of FIG. 8 have been replaced by rectangular shaped thin sensors 62 separated from each other by a distance 62A having values similar to those of 38 of FIG. 8. The rectangular faces measure 0.039 by 0.157 inches, typical, and have a thickness=0.0063 inches nominal. Both of the capacitive delta extensometer 34 embodiments of sensor 24 or 62 of FIGS. 8 and 9 may be further described with reference to FIG. 10, which is a view taken along line 10—10 of FIG. 3.

FIG. 10 illustrates the sensors 24 or 62 oriented 120 degrees with respect to each other. It should be recognized that each of the sensors 24 or 62 on each of the three five-sided members 36 cooperates with its other sensors 24 or 62 (not shown in FIG. 10 but shown in FIGS. 8 and 9) making up its pair and each pair of sensors of each of the five-sided member 36 is oriented by the desired 120 degrees. The sensor, such as sensor 24, is mounted to an insulated base to the intracortical pin 18, 20 or 40, which may be accomplished by making the five-sided member 36 out of a non-conductive material, whereas the other half of the capacitor, that is, surface 60, is conductive and grounded. Sensors are typically mounted in place using cyanoacrylate-based adhesive.

#### Operation of the Present Invention

The operation of the present invention may be described with reference to FIG. 11 which is a block diagram of the electronics used to process the displacement output of the sensors 24 or 62 arranged 120 degrees apart from each other, as discussed with reference to FIG. 10 and as generally illustrated in FIG. 11 for the capacitive delta extensometer 34. Each of the six (6) sensors provides an electrical output signal corresponding to the displacement that it senses and each of which electrical signal is routed to a serial arrangement comprising an amplifier 64, preferably a linearizing circuit and low pass filter 66, preferably an anti-aliasing filter 68, and an analog-to-digital converter 70. Each of the serial arrangements for each of the six (6) sensors is routed to a processor 72.

Each of the sensor amplifiers 64 uses a linear capacitive reactance technique for converting the displacement of the variable capacitor of each of the capacitive sensors 24 or 62 to a voltage output which results in increased sensitivity with decreasing sensor area. Each of the sensors 24 or 62 detects a strain that is resolved to  $\pm$ four (4) to  $\pm$ eight (8)  $\mu$ e for a 0.524 inch gage length device or  $\pm$ 15  $\mu$ e for a 0.272 inch gage length device. This  $\pm$ 4  $\mu$ e is obtained by using sensors that are calibrated within the range of 0.040 inches, for example, and an amplifier having output in the range of 0-10V with  $\pm$ 0.001 volt resolution.

The separation, such as 38 of FIG. 8, of the sensors 24 may be selected to be 0.500, inches but can be changed by mounting the sensors closer or further apart. The capacitive

delta extensometer 34 maintains an air gap (separation between the five-sided members 36), shown in FIG. 7, throughout the strain measurements and this air gap may be set to about 0.020 inches. The amplifier 64 preferably contains the linearizing circuit and low pass filter.

The A/D converter 70 may be made available from National Instruments as their AT-M10-16E-10 type. Each of the A/D converters 70 provides a digital representation that is routed to a processor 72 which may be a PC.

Operating routines within the processor 72 accept the measurements from each of the sensor paths and calculate the strain reading due to specimen deformation. Basically the routines provide a line which is defined by a space between two (2) points, with each line corresponding to each intracortical pin. The two (2) points defining the position are determined by the sensors mounted at their known points along the length. The data reduction program incorporates calculations of the effective strain in the region of the bone based on strain time-history paths and sensor geometry variables. Strain-transformation relationships are used to calculate the principal strain directions and magnitudes and maximum shear strains in the specimen. The strain transformations related to the present invention may be further described with reference to FIG. 12 composed of FIGS. 12(A), 12(B) and 12(C).

FIG. 12(A) illustrates a delta rosette orientation, known in the art, for a sensor installed on a test surface, such as site 14, with a first grid 76 at an angle  $\Theta$  from the major principal strain direction,  $\epsilon_p$ . FIG. 12(A) further illustrates a strain direction,  $\epsilon_Q$  which is perpendicular to  $\epsilon_p$  and also illustrates second and third grids 78 and 80 respectively.

FIG. 12(B) illustrates the rosette grid axes of FIG. 12(A) resulting in an orientation 82 related to the capacitive delta extensometer 34 of FIG. 10. The orientation 82 is analogous to the sensor of the capacitive delta extensometer 34 of FIG. 3. From FIG. 12(B) it should be noted that, for example, the second grid 78 is to be viewed as  $+60^\circ$  (CCW) from grid 76 in the rosette of FIG. 12(A), and  $+120^\circ$  in Mohr's circle of FIG. 12(B). FIG. 12(B) further illustrates the capacitive delta extensometer 34 as carrying sensors indicated by reference numbers 84, 86 and 88, wherein 84 represents a sensor-pair aligned with the first grid 76 of FIG. 12(A), 86 represents a sensor-pair aligned with the second grid 78 of FIG. 12(A), and 88 represents a sensor-pair aligned with the third grid 80 of FIG. 12(A).

FIG. 12(C) illustrates the parameters of the Mohr's circle, generally identified by reference number 90, for strain and including strains  $\epsilon_1$ ,  $\epsilon_2$  and  $\epsilon_3$ , as well as maximum shear strain 92 shown as  $\gamma_{max} = \epsilon_p - \epsilon_Q$  determined by operating routines being run in the processor 72. It is important to note that the plane containing strains as represented by Mohr's circle for strain in FIG. 12(C) is chosen by the user, and is a plane different than those planes containing sensors. The strains represented in FIG. 12(C) are developed through a procedure described below. The overall operation 94 of the routines running in the processor 72 are shown in FIG. 13 which is comprised of FIGS. 13(A) and 13(B).

The overall operation 94 is comprised of program segments 96-114, wherein program segment 96 of FIG. 13(A) records (from manual inputs) geometric parameters of FIGS. 5-9 of the device being used, such as the capacitive delta extensometer 34, and then passes control to program segment 98 by way of signal path 116.

Program segment 98 records the initial (unstrained) voltage of all six sensors, such as those of FIG. 11 and then passes control to program segment 100 by way of signal path 128.

Program segment 100 calculates the initial air gaps using sensor calibration data supplied by manufacturer or determined by user and then passes control to program segment 102 by way of signal path 120.

Program segment 102 records voltages (strained) as a change from baseline, that is, from the initially recorded voltages of program segment 98, and then passes control to program segment 104 by way of signal path 122.

Program segment 104 calculates strain at the planes for the three pairs of sensors. For example, with reference to FIG. 12(B), it is seen that one plane, defined as A, would be common to all three sensors 84, 86 and 88 and that another plane, defined as B, would be common to the other three sensors (not shown in FIG. 12(B)) associated with the three sensors 84, 86 and 88. The strain,  $\epsilon$ , at the planes A and B may be defined as  $\epsilon_1A, \epsilon_2A, \epsilon_3A$ ;  $\epsilon_1B, \epsilon_2B, \epsilon_3B$ . After segment 104 performs its calculations, program segment 104 passes control to program segment 106 by way of signal path 124.

Program segment 106 for each sensor pair calculates  $\Theta$ =angle, shown in FIG. 12(A), between pins 18, 20 or 40, associated with a particular sensor pair, and their target face by using sensed displacements and geometric parameters obtained in program segment 96. After these calculations, program segment 106 passes control to program segment 108 of FIG. 13(B) by way of signal path 126.

Program segment 108 calculates strain at the line of interest, for each sensor pair 84, 86 or 88. These calculations yield the following results: i.e.,  $\epsilon_1A$  and  $\epsilon_1B$  yields  $\epsilon_1$ ,  $\epsilon_2A$  and  $\epsilon_2B$  yields  $\epsilon_2$ , and  $\epsilon_3A$  and  $\epsilon_3B$  yields  $\epsilon_3$ , wherein  $\epsilon_1$ ,  $\epsilon_2$  and  $\epsilon_3$  are shown in FIG. 12(C). After such calculations, program segment 108 passes control to program segment 110 by way of signal path 128.

Program segment 110 uses strain transformation relationships, such as Mohr's circle for strain, known in the art and shown in FIG. 12(C), for a delta rosette, also known in the art, using program segment 108 quantities  $\epsilon_1$ ,  $\epsilon_2$ ,  $\epsilon_3$  as inputs. After such calculations, program segment 110 passes control to program segment 112 by way of signal path 130.

Program segment 112 calculates principal strains  $\epsilon_{p,Q}$  and direction  $\Theta$  from measurements given below by expressions (1) and (2), known in the art:

$$\epsilon_{p,Q} = \frac{\epsilon_1 + \epsilon_2 + \epsilon_3}{3} \pm \frac{\sqrt{2}}{3} \sqrt{(\epsilon_1 - \epsilon_2)^2 + (\epsilon_2 - \epsilon_3)^2 + (\epsilon_3 - \epsilon_1)^2} \quad 1$$

$$\Theta = \frac{1}{2} \left[ \frac{\sqrt{3}(\epsilon_1 - \epsilon_2)}{2\epsilon_1 - \epsilon_2 - \epsilon_3} \right] \quad 2$$

After program segment 112 completes its calculations it passes control to program segment 114 by way of signal path 132.

Program segment 114 calculates maximum shear strain from;  $\gamma_{max} = \epsilon_p - \epsilon_Q$ . The completion of the calculations of program segment 114 corresponds to the completion of the routines 94.

#### Practice of the Invention

In the practice of the invention, testing was performed using the double-sensor extensometer 22 of FIG. 2 and the results 134 are shown in FIG. 14 represented by plots 136, 138, 140 and 142. FIG. 14 illustrates pilot results obtained from a double-sensor extensometer 22 mounted in an acrylic specimen, with a surface-mounted strain gage output plotted as a comparison. FIG. 14 has a Y axis indicated in microstrain ( $\mu\epsilon$ ), and an X axis indicated by load condition ON-25N-ON (where N=Newtons). The positive-slope and negative-slope regions of each of the plots 136, 138, 140 and 142 along the X-axis of FIG. 14 respectively represent loading and unloading conditions. The specimen was subjected to cantilevered bending.

Plot 136 represents the predicted strain at the surface 22 obtained from the double-sensor extensometer 22, such as at

the surface of the calcaneus 14 of FIG. 1(A). Plot 138 represents the measured strain at the surface obtained with a surface-mounted metal-foil strain gage known in the art. Plot 140 represents the measured strain at the double-sensor extensometer's 22 inboard sensors, that is the one closest to the specimen surface. Plot 142 represents the measured strain at the double-sensor extensometer's 22 outboard sensor, that is the one furthest away from the specimen surface.

From the pilot study summarized by FIG. 14, in particular from plots 136 and 138, it is seen that the practice of the present invention provides measurement of the strains which occur in planes which do not contain sensors. This technique could be used to estimate strains occurring within a specimen, such as bone.

It is understood that the invention is not limited to the specific embodiments herein illustrated and described but may be otherwise without departing from the spirit and scope of the invention. Although the capacitive delta extensometer has been described for use to provide in vivo measurements of bone strain, it should be recognized that strain measurements in other materials, for example, porous metals, plastic and ceramics, where surfaces with high porosity make it impractical to use surface-mounted strain gauges are contemplated by the practice of the present invention.

It should now be appreciated that the practice of the present invention provides various embodiments of capacitive sensors that can measure the in vivo strain encountered by the bone of a mammal, such as a human being.

What I claim is:

1. A capacitive extensometer adapted to be inserted into the bone of a mammal system for sensing the in vivo strain of said bone, said extensometer comprising:

- (a) three pins adapted to be inserted into said bone; and
- (b) six (6) capacitive sensors mounted across said three pins and each providing a variable capacitance whose value is varied by the strain to which said bone is subjected, wherein said six (6) capacitive sensors are grouped into pairs with each pair being arranged on a five (5) sided member having a sensor face along which said pair is attached and spaced apart from each other.

2. The capacitive extensometer according to claim 1, wherein there are three five (5) sided members which are arranged so that three pins are each positioned at an apex of an equivalent triangle.

3. The capacitive extensometer according to claim 1, wherein said six (6) sensors are grouped into three pairs with each of the three pairs attached to said sensor face of three respective five-sided members and each of the attached pair is oriented 120 degrees from each other.

4. The capacitive extensometer according to claim 3, wherein each of said six (6) sensors generates an electrical signal.

5. The capacitive extensometer according to claim 4, wherein each electric signal is received by a serial arrangement comprising an amplifier and analog-to-digital converter.

6. The capacitive extensometer according to claim 5, wherein said serial arrangement further comprises a linearizing circuit and a low pass filter interposed between said amplifier and said analog-to-digital converter.

7. The capacitive extensometer according to claim 6, wherein said electrical signal after passing through said serial arrangement is delivered to a processor.



DEPARTMENT OF THE ARMY  
US ARMY MEDICAL RESEARCH AND MATERIEL COMMAND  
504 SCOTT STREET  
FORT DETRICK, MD 21702-5012

REPLY TO  
ATTENTION OF

MCMR-RMI-S (70-1y)

15 May 03

MEMORANDUM FOR Administrator, Defense Technical Information Center (DTIC-OCA), 8725 John J. Kingman Road, Fort Belvoir, VA 22060-6218


SUBJECT: Request Change in Distribution Statement

1. The U.S. Army Medical Research and Materiel Command has reexamined the need for the limitation assigned to technical reports written for this Command. Request the limited distribution statement for the enclosed accession numbers be changed to "Approved for public release; distribution unlimited." These reports should be released to the National Technical Information Service.

2. Point of contact for this request is Ms. Kristin Morrow at DSN 343-7327 or by e-mail at Kristin.Morrow@det.amedd.army.mil.

FOR THE COMMANDER:

Encl

  
PHYLLIS M. RINEHART  
Deputy Chief of Staff for  
Information Management

ADB266022	ADB265793
ADB260153	ADB281613
ADB272842	ADB284934
ADB283918	ADB263442
ADB282576	ADB284977
ADB282300	ADB263437
ADB285053	ADB265310
ADB262444	ADB281573
ADB282296	ADB250216
ADB258969	ADB258699
ADB269117	ADB274387
ADB283887	ADB285530
ADB263560	
ADB262487	
ADB277417	
ADB285857	
ADB270847	
ADB283780	
ADB262079	
ADB279651	
ADB253401	
ADB264625	
ADB279639	
ADB263763	
ADB283958	
ADB262379	
ADB283894	
ADB283063	
ADB261795	
ADB263454	
ADB281633	
ADB283877	
ADB284034	
ADB283924	
ADB284320	
ADB284135	
ADB259954	
ADB258194	
ADB266157	
ADB279641	
ADB244802	
ADB257340	
ADB244688	
ADB283789	
ADB258856	
ADB270749	
ADB258933	